UNIVERSITY OF PARMA

FACULTY OF ENGINEERING

DOCTORATE IN CIVIL ENGINEERING – XVIII CYCLE

STRUCTURAL MECHANICS – ICAR/09

THREE-DIMENSIONAL NUMERICAL MODELING OF REINFORCED CONCRETE BEHAVIOR

Supervisor:
Prof. ROBERTO CERIONI
Co-supervisor:
Prof. IVO IORI
Doctorate coordinator:
Prof. PAOLO MIGNOSA

Author:
ANDREA MORDINI

March 2006

To Lorenzo,
wishing his life to be moved, like mine,
by research and discovery.

“…il cemento armato non si tradisce!”

Prof. Ivo Iori during a lecture.

TABLE OF CONTENTS

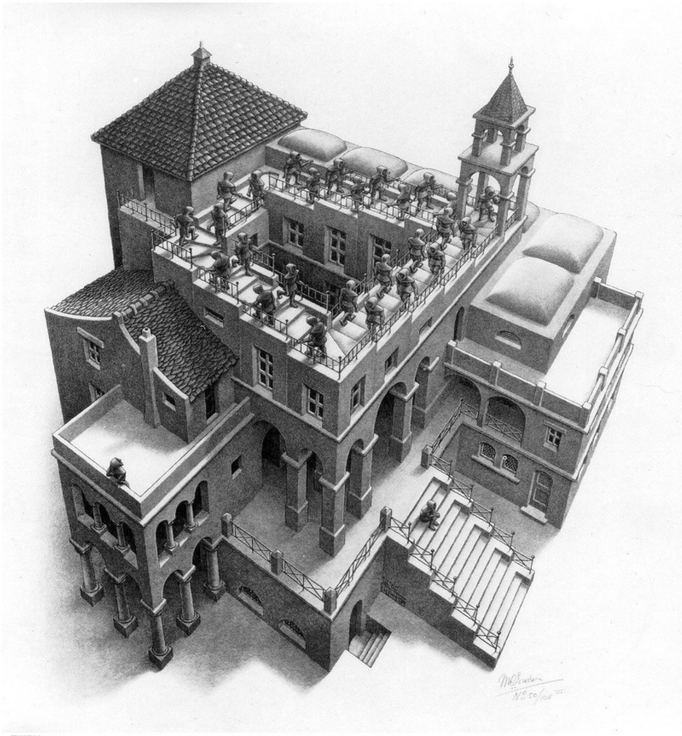

Maurits Cornelis Escher, Ascending and Descending, 1960.

CHAPTER 1 – THE THREE-DIMENSIONAL PROBLEM

Reinforced concrete (RC) structures exhibit a complex behavior even for low load levels. Non-linear compressive stress-strain relations, tensile cracking, post cracking softening and interaction effects between concrete and reinforcing bars are the main sources of a highly non-linear and complicated response. In order to capture the real structural behavior, sophisticated numerical tools are necessary to take into account all the remarkable phenomena and to perform the time-consuming non-linear calculations.

In this doctorate dissertation, the three-dimensional (3D) constitutive model for non-linear analysis of RC structures 3D-PARC – Three-Dimensional Physical Approach for Reinforced Concrete, is presented. The 3D study started some years ago with the author's graduate thesis which laid the foundations of the model [34]. That work was an extension of PARC, a numerical model for membrane elements subjected to plane stress (Figure 1.1) developed at the Department of Civil Engineering of the University of Parma [8, 9]. The PARC formulation is based on some previous works [25, 14].

In the author's graduate thesis, the model was implemented in TRE, a computer code which can analyze the behavior of a single material point and therefore, also of simple structures subjected to uniform stress. The good results achieved were an encouragement to keep on working on this topic.

The research carried out during the doctorate, deepens the investigation of the model theory and the development of numerical tools to provide efficacy and power to its application. Starting from the work already done, a new approach is developed and implemented. However, the basic philosophy does not change: the model remains as close as possible to the physical reality, without using numerical devices which are often "unphysical". The starting point for the model formulation is the study of physical phenomena (concrete subjected to multiaxial stresses, aggregate bridging and interlock, tension stiffening, dowel action) through single basic studies which are assembled to build the model.

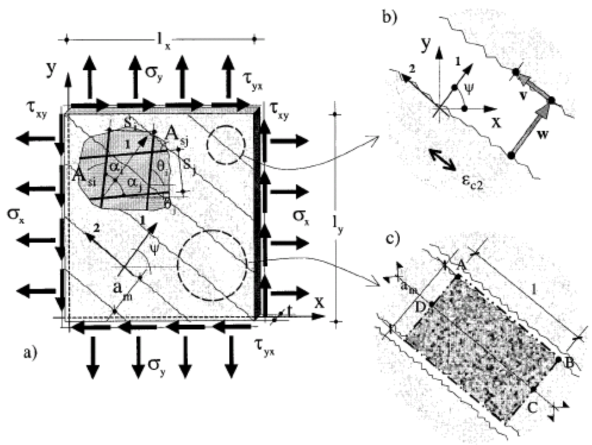

Figure 1.1 – The basic plane element investigated by PARC.

The developed theory is implemented in a FORTRAN code which can be used within the commercial Finite Element (FE) code ABAQUS [1]. In this way, the model can be used to analyze structures subjected to complex stress states. In fact, the FE formulation gives the possibility to model a wide range of structures independently on the geometry.

Subsequently, the theory formulation as well as the numerical implementation are validated by some significant comparisons with experimental tests taken from the literature.

During a six-month collaboration with the Institute of Structural Engineering (IKI) of the University of Natural Resources and Applied Life Sciences – BOKU in Vienna, the software package SARA, which includes the RC-oriented FE code ATENA and the statistical module FREET, was also used. This research program produced the FE analysis of RC corbels reported in Chapter 5.

CHAPTER 2 – STATE OF THE ART

2.1 – INTRODUCTION

In the following chapter, an overview on the state of the art of the three-dimensional (3D) modeling of reinforced concrete (RC) is presented. First of all, the main differences between the basic formulations for reinforcements and cracks are discussed [41]. Secondly, some important numerical models for RC are illustrated. All of these models were created to work in Finite Element (FE) programs and some of them are implemented within worldwide famous commercial codes such as ABAQUS, ADINA, ANSYS and ATENA. The theory implemented within ATENA is presented in chapter 5.

2.1.1 – Reinforcement modeling

Generally, it is possible to describe the reinforcement behavior in two different ways, by using discrete or smeared reinforcements (Figure 2.1).

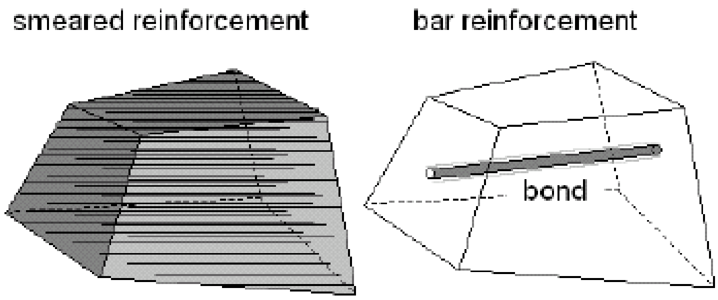

Figure 2.1 – Different reinforcement models.

In the discrete approach, concrete and reinforcement bars are modeled with different elements. Therefore, two different meshes are created and superposed, each one having its own elements and integration points (Figure 2.2). Usually, the concrete mesh is not affected by reinforcements because the bar elements are not forced to share their nodes with concrete elements: The reinforcement node displacements are constrained to the concrete node displacements.

One of the main drawbacks for this approach is the difficulty in modeling the steel-concrete interface phenomena. To solve this problem, it is possible to use special interface elements to create the connection between steel and concrete or to insert suitable numerical corrections in concrete behavior in order to simulate these effects. Nevertheless, the discrete approach is easier to use in the model creation phase, especially for structural elements in which reinforcing bars have a complex spatial distribution.

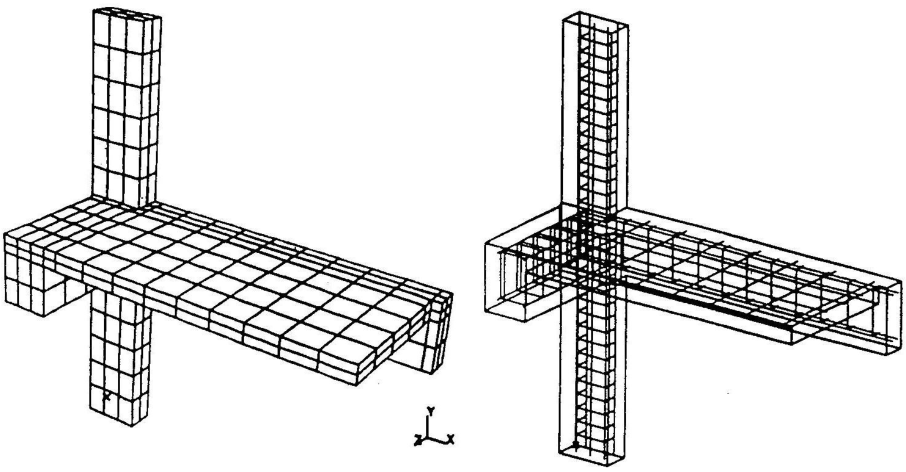

Figure 2.2 – An example of mesh superposition.

On the contrary, considering smeared reinforcements means to model the RC like a single continuum equivalent material whose properties are given by the sum of different contributes (such as concrete, reinforcing bars and interface effects). In this formulation, the effects of the bars are smeared along their interaxes. Usually, this approach has a good response in structures where reinforcing bars are spatially not too concentrated.

Generally, the different methods of modeling the reinforcements have a little influence on results.

2.1.2 – Crack modeling

There are two main ways of modeling the concrete behavior after cracking and the choice between them depends on the investigated problem (Figure 2.3).

If the problem is dominated by a few number of cracks, it is usually better to adopt a discrete crack approach. When the crack arises, there is a separation of the mesh in the cracked zone and in this discontinuity, new interface elements with variable stiffness are inserted to simulate the crack opening. Two major drawbacks can be mentioned: the FE mesh connectivity changes during the analysis and the crack lips are constrained to follow the FE sides. In order to avoid these problems, remeshing operations can be implemented and, with special procedures, the crack can be allowed to propagate also inside the FE. These properties, however, make this approach suitable only in particular cases, such as the study of fracture propagation in pre-notched specimens since the notch provides good information about the fracture position and propagation.

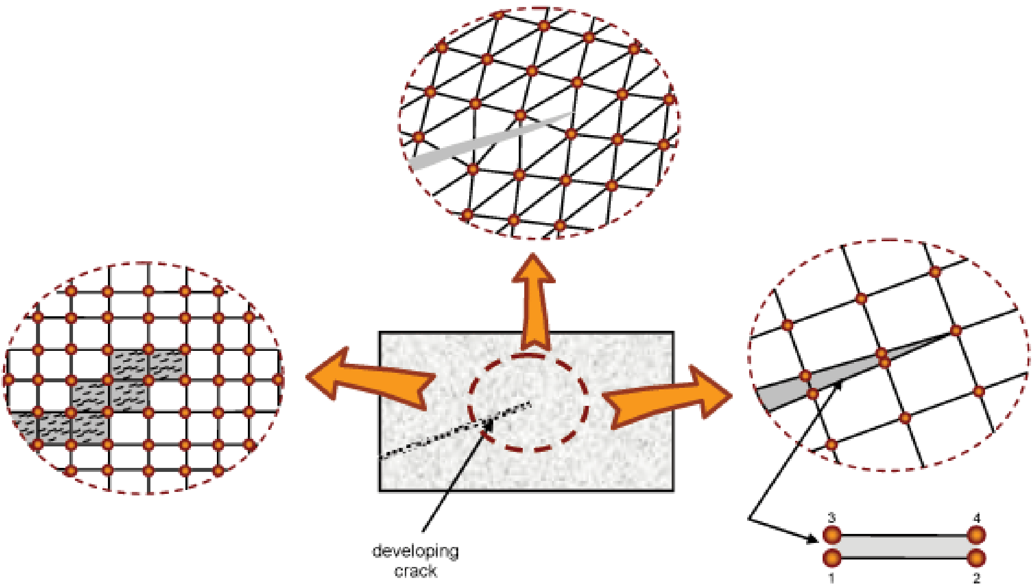

Figure 2.3 – Different crack models in the FE framework.

On the contrary, in presence of a high number of cracks, a smeared crack approach is more convenient. The material is described like an equivalent continuum with the constitutive relation modified by considering cracking, interface phenomena and reinforcing bars. When cracking occurs, a new local coordinate system in which is easier to describe the material and the interface behavior is defined according to cracking direction. A cracked material constitutive matrix is written in this system and then it is transferred to the global coordinate system to create the global stiffness matrix.

This approach allows to maintain the same mesh for the whole analysis and allows the cracks to open in any direction. As drawback, it has been noted that the mesh size influences the load which causes the crack propagation. Moreover, the shear strength of some structural elements can be overestimated.

Smeared crack models can adopt fixed or rotating crack formulation. In the former case, the crack direction remains the same for the whole analysis even if the principal directions change whereas, in the latter case, the crack orientation changes according to the principal directions.
The main difference between these approaches lies in the necessity, for fixed crack, to calculate the contributes due to the shear transferred across the crack by the aggregate interlock. This contribution is usually calculated by a Shear Retention Factor, a numerical coefficient computed in various ways, taking into account the shear stresses as a fraction of the stresses in the uncracked case. Therefore, the rotating approach is generally easier to use and to insert in computer codes but it can be considered partially “unphysical” since, in the empirical reality, the crack is not free to change its orientation. It has to be mentioned however, that the rotating approach describes better particular situations with various crack patterns. For example, in a bended beam that will have shear failure, if every integration point can crack only once, the fixed approach cannot give reliable results. In fact, the first cracks are caused by the bending moment (vertical crack). Then, as the load increases, shear diagonal cracks open on the previous ones, dominating the structural behavior. In this case, the crack rotation allows to capture the most important crack pattern while the fixed cracks maintain their initial vertical orientation giving a bad description of the subsequent shear cracks.
One improvement of the fixed approach is the multi-directional cracking approach in which the material is allowed to crack more than once. Each crack is free to open in any direction and remains fixed after the formation. This approach involves the strain decomposition of total strain into concrete and crack strain. The strain of the subsequent cracks is added to the previous ones.

2.2 – ABAQUS MODEL

This FE code describes the RC through the fixed smeared crack and the discrete reinforcements approaches [1]. It is intended that the modeling is accomplished by combining standard elements, using plain concrete model, with bar elements, using an uniaxial strain theory with standard metal plasticity constitutive models. The reinforcements can be singly defined or embedded in oriented surfaces as shown in Figure 2.4.

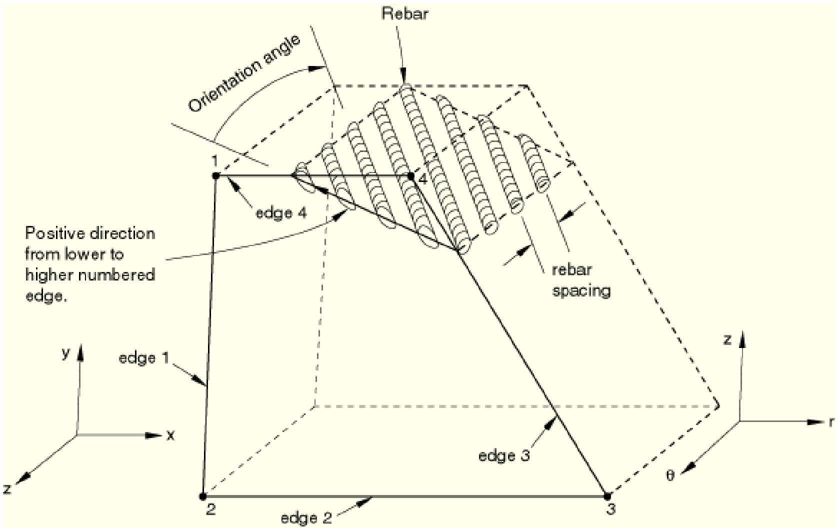

Figure 2.4 – Reinforcing bar layer in solid elements.

This modeling approach allows the concrete behavior to be independent on the reinforcing bars. Effects associated with the steel-concrete interface can be considered by modifying some aspects of the plain concrete behavior to mimic them, such as the "tension stiffening" formulation simulating the load transfer across cracks through the bars.

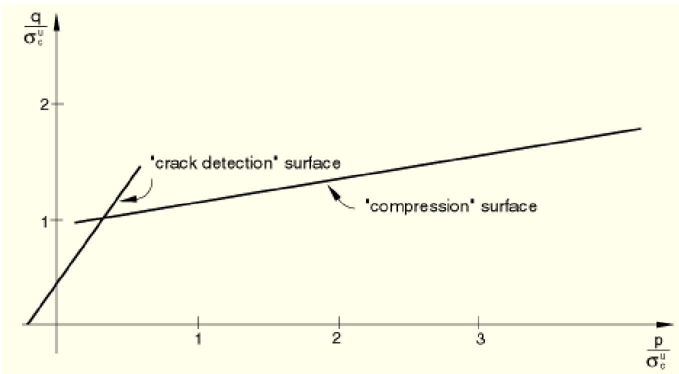

Figure 2.5 – Concrete failure surface in p-q plane.

The model consists of a compressive yield/flow surface to model the concrete response in predominantly compressive stress states, together with damaged elasticity to represent cracks occurring at calculation points.

Cracking is assumed to be the most important and dominating aspect; it occurs when the stress reaches the crack detection surface (Figure 2.5) which is a linear relationship between the equivalent pressure stress p and the Mises equivalent deviatoric stress q. When a crack is detected, its orientation is stored for subsequent calculations made for convenience in a local coordinate system (Figure 2.6).

Subsequent cracks at the same point are restricted to be orthogonal to this direction since stress components associated with an open crack are not included in the definition of the failure surface used for detecting the additional cracks. In a 3D case, no more than three cracks can occur at the same point, two in a plane stress case and one in an uniaxial stress case. Furthermore, cracks are irrecoverable: they remain for the rest of the calculation but no permanent strain is associated with cracking. That means that the cracks can close completely when the stress across them becomes compressive.

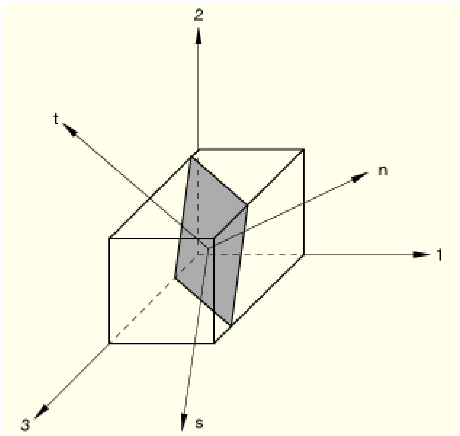

Figure 2.6 – Global and local coordinate systems.

When the principal stress components are dominantly compressive, the response of the concrete is modeled by an elastic-plastic theory, using a simple form of yield surface written in terms of the first two stress invariants (Figure 2.5). Associated flow and isotropic hardening are used.

This model significantly simplifies the real behavior: for example, the simple yield surface, without the third stress invariant, does not match all data very accurately and when concrete is subjected to very high pressure stress, it exhibits inelastic response which is not included in the model. Therefore, it has a good response for relatively monotonic loadings under fairly low confining pressures (less than four to five times the uniaxial compressive strength). In spite of these limitations, the model provides useful predictions for a variety of problems involving inelastic loading of concrete. The limitations are introduced for the sake of computational efficiency.

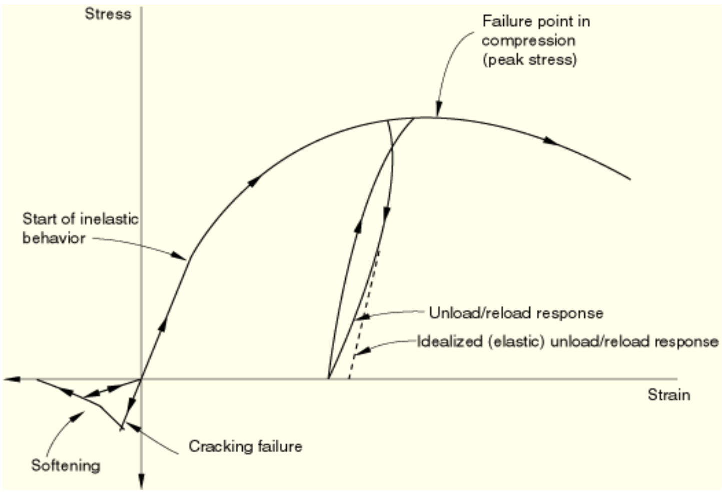

Figure 2.7 – Uniaxial constitutive law for concrete.

Figure 2.7 shows the uniaxial concrete behavior. If the load is removed in the compressive range after inelastic straining has occurred, an idealized elastic response is used. In multiaxial stress states, these observations can be generalized through the concept of failure surfaces and of ultimate strength in stress space.

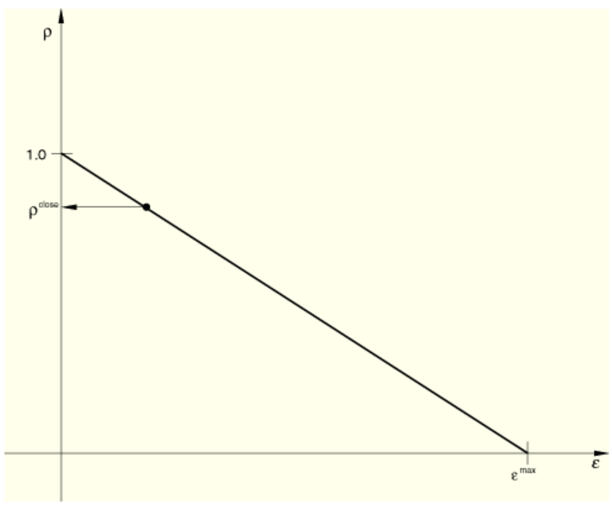

Figure 2.8 – Shear retention modeling.

This model makes no attempt to predict cyclic response or reduction in the elastic stiffness caused by inelastic straining since the model is intended for application to relatively monotonic loading cases. Nevertheless, the model should predict the response in such cases with a reasonable accuracy.

As the concrete cracks, its shear modulus is reduced by a multiplying factor defined as a function of the opening strain across the crack (Figure 2.8). It is also possible to specify a reduced shear modulus for closed cracks.

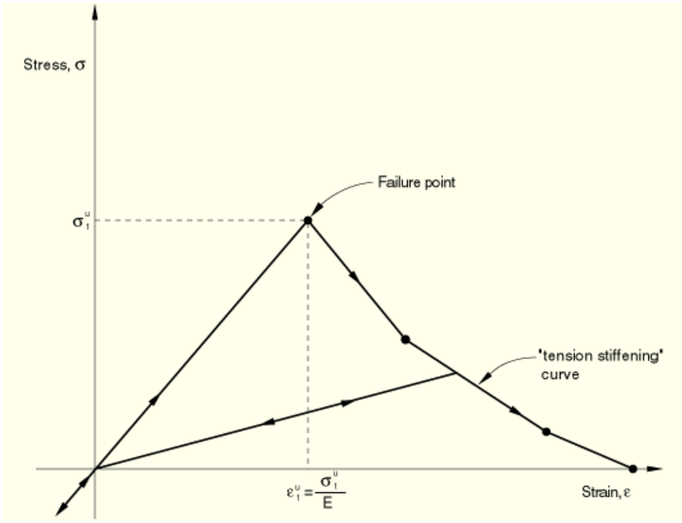

Figure 2.9 – Post failure stress-strain relation.

The post-failure behavior for direct straining across the cracks is modeled with "tension stiffening", which allows to define the strain-softening behavior for cracked concrete. This formulation also allows concrete-reinforcement interaction to be simulated in a simple manner. It is possible to specify tension stiffening by means of a post-failure stress-strain relation (Figure 2.9) or by applying a fracture energy cracking criterion based on crack width.

In cases with little or no reinforcement, the stress-strain relation often introduces mesh sensitivity in the analysis results when a few discrete cracks form in the structure; on the contrary, if cracks are evenly distributed, mesh sensitivity is less of a concern. Generally, a higher tension stiffening makes the numerical solution easier.

The fracture energy cracking criterion is based on the assumption that the fracture energy required to form a unit area of crack surface is a material property. Following this approach, the concrete brittle behavior is characterized by a stress-displacement response rather than a stress-strain response. The implementation of this stress-displacement concept in a FE model requires the definition of a characteristic length associated with an integration point. The characteristic crack length is based on the element geometry: for beams and trusses the integration point length is used; for shell and planar elements the square root of the integration

point area is used; for solid elements the cube root of the integration point volume is used.
To validate the model, the collapse of a RC slab (Mc Neice slab) is simulated. The problem geometry is shown in Figure 2.10. A square slab is supported in the transversal direction at its four corners and loaded by a point load at its center. The slab is reinforced in two directions at 75% of its depth. The reinforcement ratio (volume of steel to volume of concrete) is 8.5×10^{-3} in each direction. Symmetry conditions allow to model one quarter of the slab. A 3×3 mesh of 8-node shell elements is used. No mesh convergence studies were performed, but the reasonable agreement between the analysis results and the experimental data suggests that the mesh is adequate to predict the overall structural response with usable accuracy. The two-way reinforcement is modeled using a rebar layer.

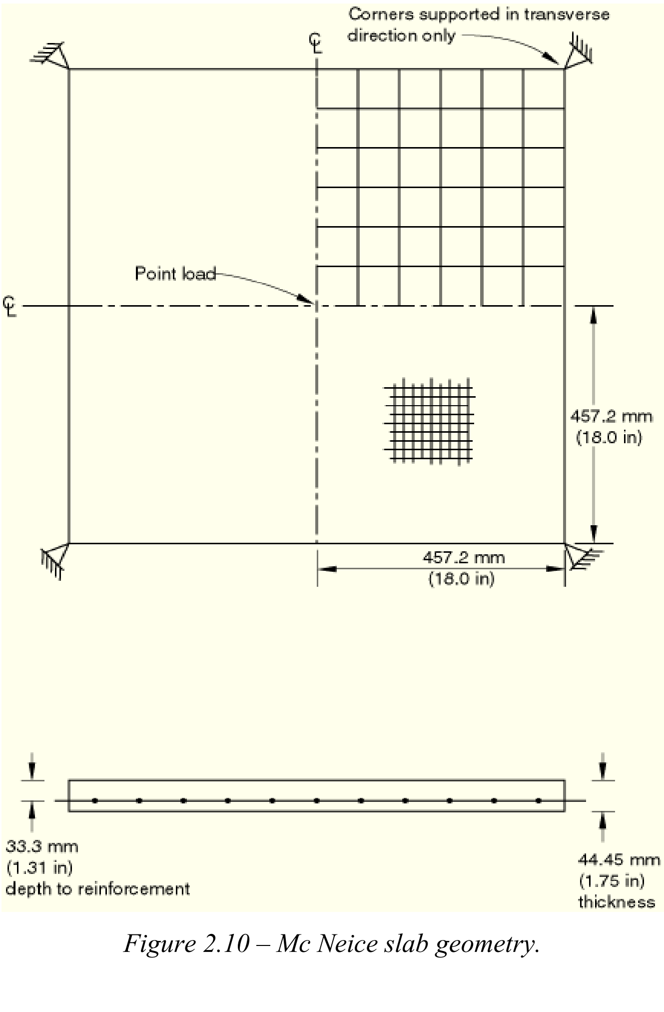

Figure 2.10 – Mc Neice slab geometry.

In this example, the tension stiffening is modeled with three different values to illustrate its effect on the global response. Since the problem is dominated by bending, the response is highly influenced by the material behavior normal to the crack planes. Therefore, the shear behavior in the plane of the cracks is not important. Consequently, the choice of the shear retention has no significant influence on the results. Since considerable non-linearity is expected in the response, including the possibility of unstable regimes as the concrete cracks, the modified Riks method is used with automatic incrementation.

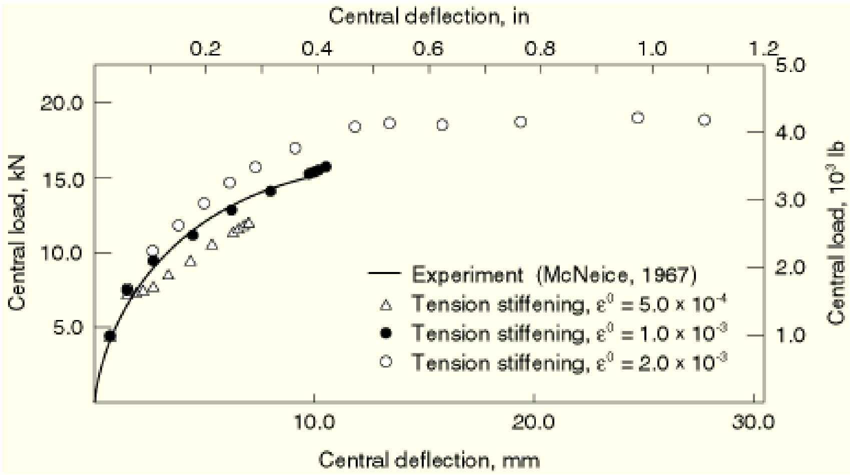

Figure 2.11 – Load-deflection response.

The numerical and experimental results are compared in Figure 2.11 on the basis of load versus deflection at the center of the slab. The strong effect of the tension stiffening assumption is very clear in the plot. The numerical analysis provides also other interesting outcomes such as the crack pattern of the lower slab surface depicted in Figure 2.12.

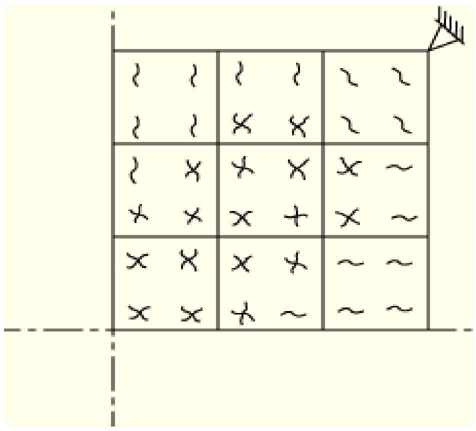

Figure 2.12 – Crack pattern on lower slab surface.

2.3 – ADINA MODEL

In the following section, the model for RC presented by Bathe, Walczac, Welch and Mistry [6] and implemented in the FE code ADINA is presented [3].

The paper describes the main properties of a good code: the model should be as simple as possible and it should be well built on theory and reliable from the numerical point of view. To fully describe the material behavior three features are requested:

- a stress-strain relation to include the high concrete non-linearity;
- a failure surface to define tensile and compressive failure;
- a suitable technique to implement the post-cracking and crushing behavior.

The concrete model can be employed both with 2D and 3D solid elements, with small displacement as well as large displacement formulation but, in all cases, small strains are assumed. Moreover, the model can be also used for other brittle materials like a wide variety of rocks.

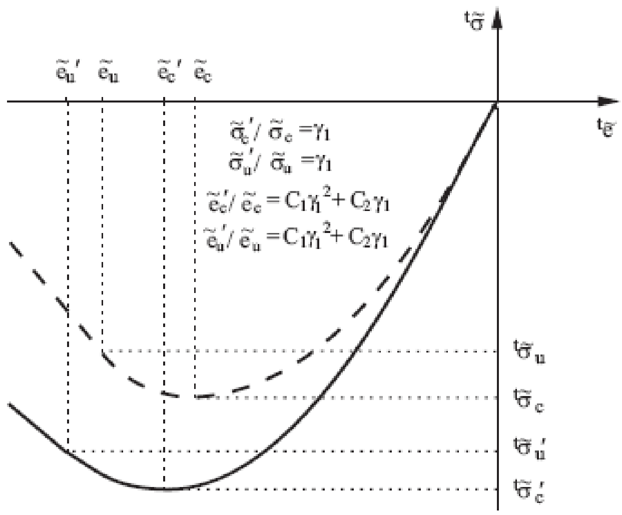

Figure 2.13 – Compressive stress-strain behaviors.

Figure 2.13 shows the compressive stress-strain relation for uniaxial and multiaxial stress conditions. The latter is derived from the former taking into account the multiaxial stress state. Furthermore, different curve parameters are used depending on whether the material is in loading or unloading conditions.

In order to evaluate the loading and unloading conditions, for each integration point a stress-based loading scalar is defined: if the scalar is increasing, the condition is "loading" whereas if the scalar is smaller than the maximum value already reached during the analysis, the condition is “unloading”. For unloading and reloading conditions (up to the stress state from which unloading occurred), the initial elastic modulus is used. For strain states beyond the ultimate compressive strain, it is assumed that stresses are linearly released to zero.

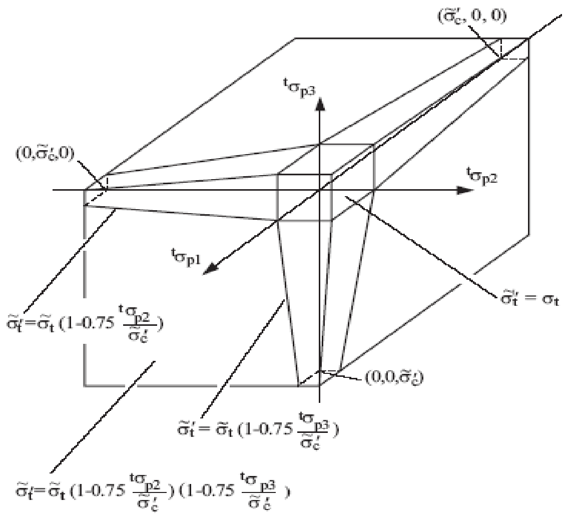

Figure 2.14 – Tensile failure envelope.

The material is considered orthotropic with respect to the principal stress directions. If cracking occurs in any direction, that direction is fixed from that point onward in calculating. The Poisson ratio is assumed to be constant under tensile stresses and variable in the compressive region in order to capture the dilatancy.

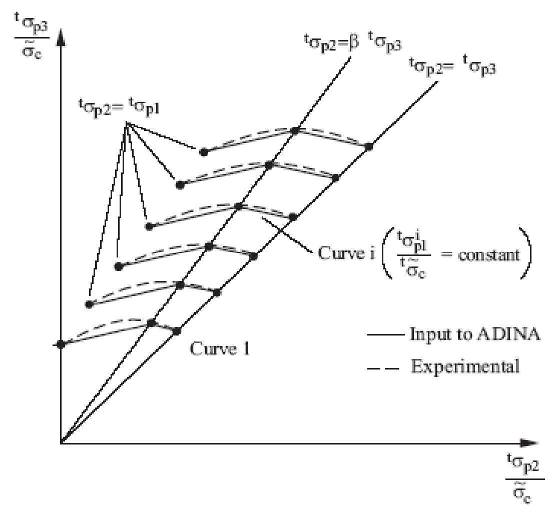

Figure 2.15 – Triaxial compressive failure envelope.

The failure envelopes, based on principal stresses, are shown in Figure 2.14 (tensile fields) and Figure 2.15 (compressive field). The compressive failure surface is created by using 24 different values for the principal stresses. By changing these values, it is possible to adopt the same model for many different materials.

Starting from the current stress state, it is possible to establish the stress-strain laws taking into account the multiaxial stress conditions and to check whether tensile or crushing failure occurs. Tensile failure occurs if a tensile principal stress exceeds the tensile strength which depends on compressive stresses in other principal directions. The other tensile principal stresses do not effect the cracking.

After cracking, it is assumed that a failure plane develops perpendicularly to the corresponding principal stress direction. Therefore, the normal and shear stiffnesses across the failure plane are reduced and plane stress conditions are assumed. The 2D failure envelope is derived from the 3D one. These stiffness reductions are considered by using two constants η_n and η_s following the Shear Retention Factor concept. Typically, η_n=0.0001 and η_s=0.5. The factor η_n is not exactly equal to zero in order to avoid the possibility of a singular stiffness matrix. The factor η_s depends on a number of physical factors and it must be chosen carefully. For the concrete model in ADINA, η_n and η_s are both input parameters.

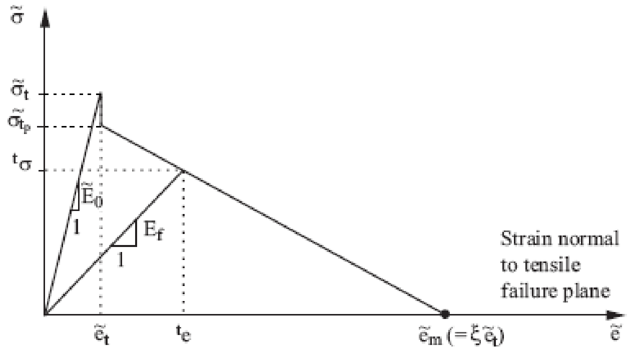

Figure 2.16 – Uniaxial tensile behavior.

Figure 2.16 shows the material behavior in the direction normal to the tensile failure plane. ξ is an user-defined variable which determines the amount of tension stiffening. To obtain a mesh independent solution, the fracture energy G_f can be directly provided and therefore, ξ is evaluated at each integration point based on the FE size (Figure 2.17).

The shear moduli in the tensile failure plane also depend on the strain normal to that plane: the moduli are written with the parameter η_f which follows the law in Figure 2.18.

In each solution step, the crack is checked in order to verify whether the failure is still active. The failure is considered inactive if the normal strain across the plane becomes negative or less than the strain at which the last failure occurred; otherwise it is active.

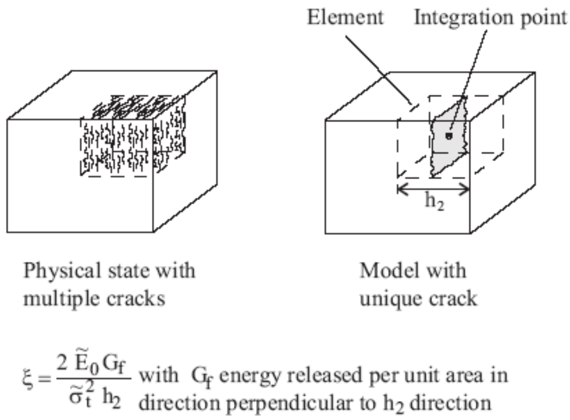

Figure 2.17 – Parameter ξ calculation.

After the first crack onset, the coordinate system is redefined and the stresses in the crack directions are used to evaluate the stress-strain matrix, instead of using the principal stresses and corresponding directions. A subsequent failure plane is assumed to form perpendicularly to the direction of the first failure plane whenever a normal stress along the original failure plane reaches the tensile strength. Therefore, at any integration point, the direction of the third tensile failure plane is fixed after the second cracking.
If the material crushes in compression, it is assumed that the material becomes isotropic and strain-softens in all directions with very small elastic modulus values.
In ADINA, many material properties can be defined as temperature-dependent including the strains due to the temperature effects.

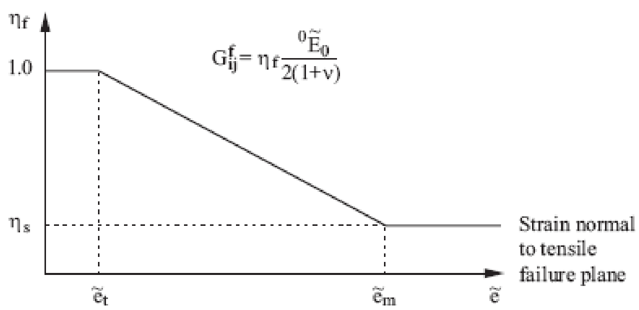

Figure 2.18 – Parameter η_f calculation.

The model is applied at first to simple structures with different load combinations in order to verify the basic formulation. Afterwards, more complex structures are investigated. The significant study of the RC containment Sandia pressure vessel is presented.
This investigation is part of the US Nuclear Regulatory Commission program on containments. The structure is analyzed prior to experimental tests by ten different groups,

four from the USA and six from Europe. One of the analysis is carried out with ADINA by using an axisymmetric model.

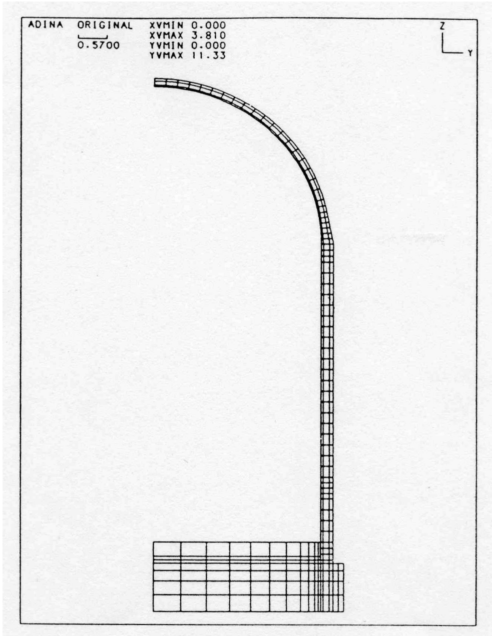

Figure 2.19 – Sandia pressure vessel FE mesh.

The concrete properties are derived from published results, but the agreement with the ADINA default values is satisfactory with the exception of the high triaxial compressive region. The axisymmetric approach presents some modeling problems: the main vertical and hoop reinforcements can be modeled easily, but at the bottom of the wall some diagonal seismic reinforcements are designed. Therefore, this reinforcement set is inserted as equivalent extra vertical and hoop reinforcements. The soil is modeled as a set of spring elements. Since the bottom plate is relatively thick, the spring stiffness is supposed not to have a great influence on the structural behavior. The FE mesh is shown in Figure 2.19.

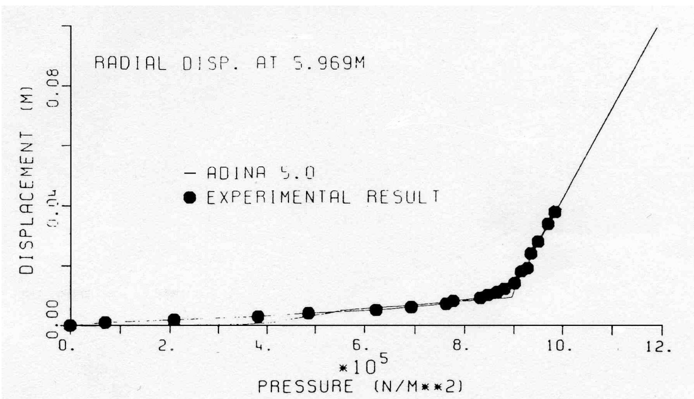

Figure 2.20 – Comparison with experimental results for Sandia pressure vessel.

The one-sixth scale specimen was built at Sandia National Laboratories and tested in July 1987. The test was performed with a first cycle up to 1.15 times the design pressure. Afterwards, after returning to zero, the pressure was increased again up to failure. The initial cycle is not simulated within ADINA.

In Figure 2.20 the comparison between experimental and numerical results regarding the radial displacement, the most significant movement, is shown. The correlation is very high even if the experimental ultimate load is lower due to excessive leakage. Moreover, the numerical analysis allows to follow all the crack patterns and the deformed shapes up to failure as reported in Figure 2.21.

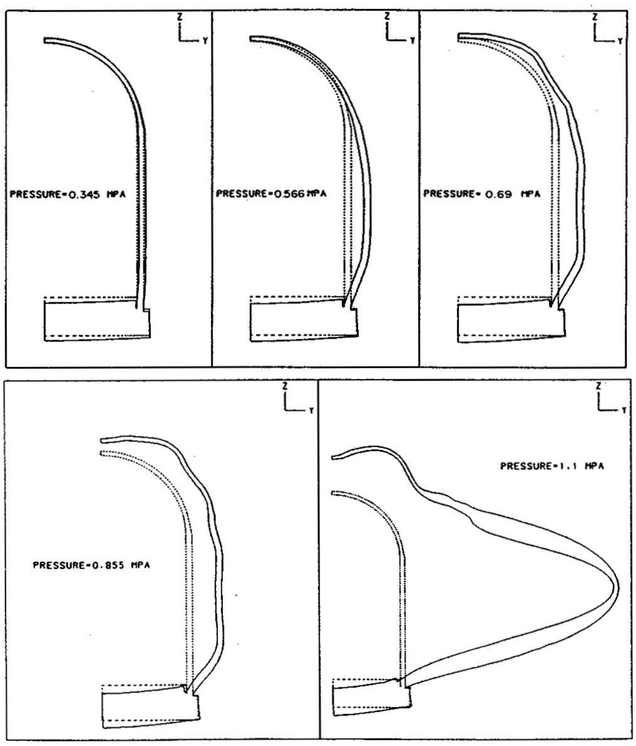

Figure 2.21 – Sandia pressure vessel deformed shape for several analysis steps.

2.4 – ANSYS MODEL

The FE code ANSYS models RC with smeared cracking and smeared reinforcement approaches [4].

In concrete modeling, the 3D element SOLID65 is used (Figure 2.22). This element allows the presence of four different materials, one matrix material and a maximum of three independent reinforcing materials. Since SOLID65 is capable of cracking in tension and crushing in compression, it can be used to model RC or other materials such as reinforced composites (e.g. fiberglass), and geological materials (e.g. rock). The element is defined by eight nodes having three translational degrees of freedom at each node.

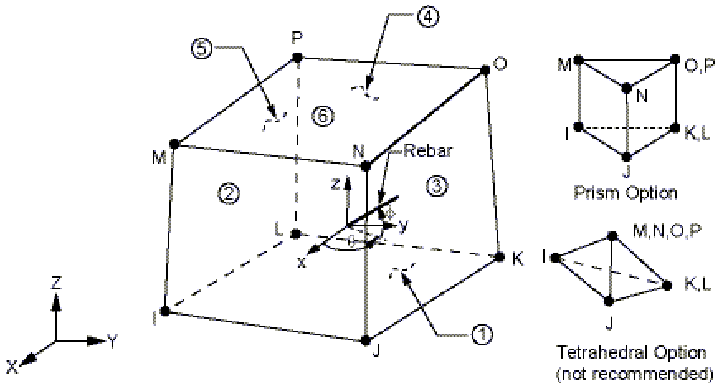

Figure 2.22 – SOLID65 geometric properties.

Concrete is capable of directional integration point cracking and crushing besides incorporating plastic and creep behavior. The reinforcement, which also incorporates creep and plasticity, has uniaxial stiffness only and it is assumed to be smeared throughout the element. Directional orientation is accomplished through user specified angles.

In concrete, which is assumed to be initially isotropic, cracking is permitted in three orthogonal directions at each integration point and it is modeled through an adjustment of material properties which effectively treats the cracking as a smeared crack band, rather than discrete cracks.

Then, a unique matrix is written for both materials as follows:

$$[D]=\left(1-\sum_{i=1}^{N_r}V_i\right)[D_c]+\sum_{i=1}^{N_r}V_i\,[D_{ri}]\,, \tag{2.1}$$

where N_r is the number of reinforcing materials, V_i is the ratio of the volume of i^{th} reinforcing

material to the total volume of element, $[D_c]$ is the constitutive matrix for concrete and $[D_{ri}]$ is the constitutive matrix for the i^{th} reinforcement.
The concrete description is based on the Rate Independent Plasticity which is characterized by the irreversible straining occurring in the material when a certain level of stress is reached. The plastic strains are assumed to develop instantaneously, independently on time.
The failure criterion is described by the Willam and Warnke formulation [47]. This material model predicts either elastic, cracking or crushing behavior. If elastic behavior is predicted, the concrete is treated as a linear elastic isotropic material. If cracking or crushing behavior is predicted, the elastic stress-strain matrix is adjusted in a different way for each failure mode.
The 3D failure surface can be written as

$$\frac{F}{f_c} - S \geq 0\,, \tag{2.2}$$

where F is a function of the principal stress state, S is a failure surface, f_c is the uniaxial compressive strength (Figure 2.23).

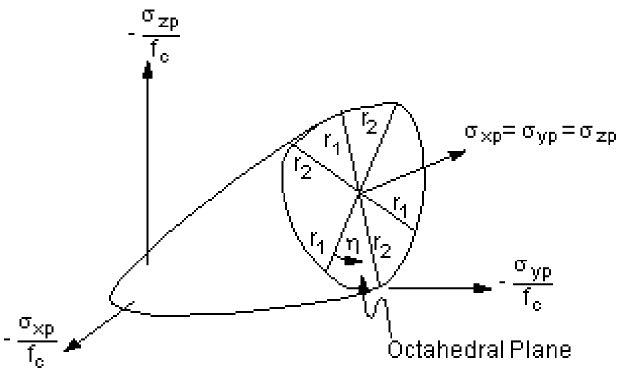

Figure 2.23 – The 3D failure surface.

Five input parameters, which can be temperature dependent, are requested to define the failure surface. For small values of the hydrostatic stress, instead, the failure surface can be specified by using some constant relations between parameters with a minimum of two constants: the uniaxial tensile and compressive strength. For high values of the hydrostatic stress, five parameters are required.
Four different domains are investigated based on the principal stress signs (triaxial compression, triaxial tension and two mixed cases) and in each domain different formulations for F and S are written. The failure surface is closed and can predict failure also under high

hydrostatic pressure.

If the material at an integration point fails in uniaxial, biaxial, or triaxial compression, the material is assumed to crush. Crushing is defined as the complete deterioration of the material structural integrity. Therefore, the stiffness at that integration point can be ignored.

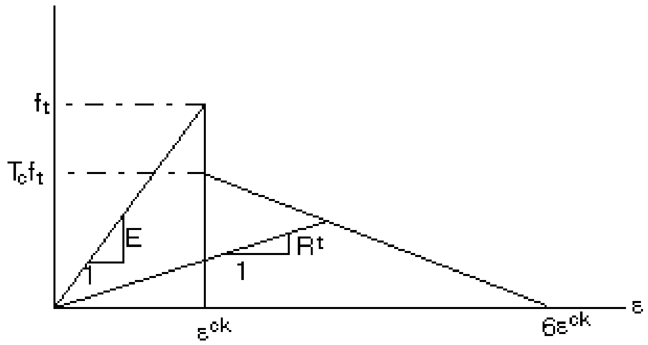

Figure 2.24 – Tensile post cracking behavior.

The presence of a crack at an integration point is represented through modification of the stress-strain relations by introducing a plane of weakness in the direction normal to the crack face. The constitutive matrix for a material cracked in one direction is

$$\left[D_c^{ck}\right]=\frac{E}{1+\nu}\begin{bmatrix} R^t\dfrac{1+\nu}{E} & 0 & 0 & 0 & 0 & 0 \\ & \dfrac{1}{1-\nu} & \dfrac{\nu}{1-\nu} & 0 & 0 & 0 \\ & & \dfrac{1}{1-\nu} & 0 & 0 & 0 \\ & & & \dfrac{\beta_t}{2} & 0 & 0 \\ & symm. & & & \dfrac{1}{2} & 0 \\ & & & & & \dfrac{\beta_t}{2} \end{bmatrix}. \tag{2.3}$$

The stress-strain relation refers now to a coordinate system parallel to the principal stress directions with the first axis perpendicular to the crack face. Then, in order to build the global stiffness matrix, a coordinate transformation is needed. In the same way, it is possible to write the stress-strain matrix for cracking in two and three directions.

Figure 2.24 shows the post cracking behavior in the direction perpendicular to the crack and defines the R^t factor. The crack is allowed to close: in this case, all the compressive stresses normal to the crack plane are transferred, whereas a different shear transfer coefficient is specified.

A shear transfer coefficient βt is introduced representing a shear strength reduction factor for subsequent loads inducing sliding across the crack face.

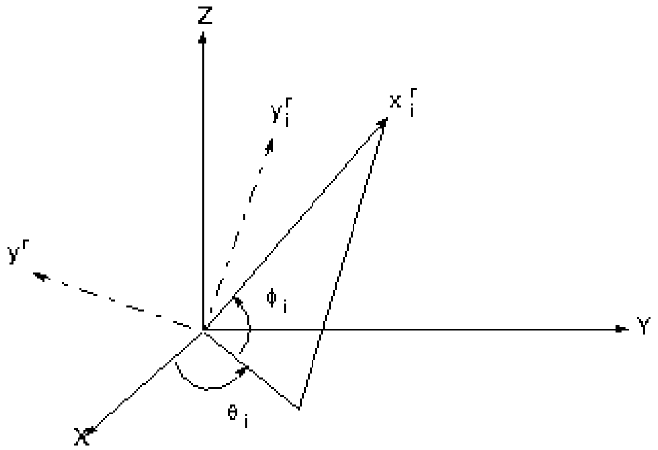

Figure 2.25 – Reinforcement orientation.

Reinforcing bars are assumed to work in axial direction only. Their orientation is specified as shown in Figure 2.25. A creep and plasticity non-linear behavior can be defined.

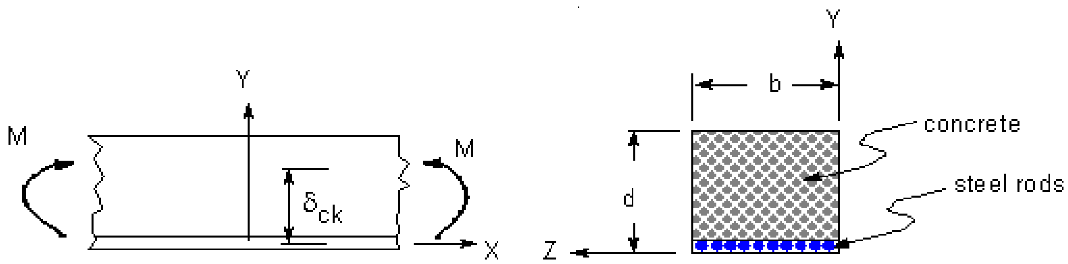

Figure 2.26 – Verification beam geometry.

In ANSYS documentation, a verification example taken from Timoshenko [44], is presented. A concrete beam reinforced with steel rods is subjected to pure bending load (Figure 2.26). The analysis evaluates the crack depth from the bottom surface, the maximum steel tensile stress and the maximum concrete compressive stress, assuming that the concrete tensile strength is zero.

In order to match the reference assumptions, the simulation adopts a zero Poisson coefficient and an infinite crushing strength for concrete. Moreover, constraint equations are used along the beam depth to conveniently apply the load and match the plane cross-section hypothesis.

The FE discretization is shown in Figure 2.27.

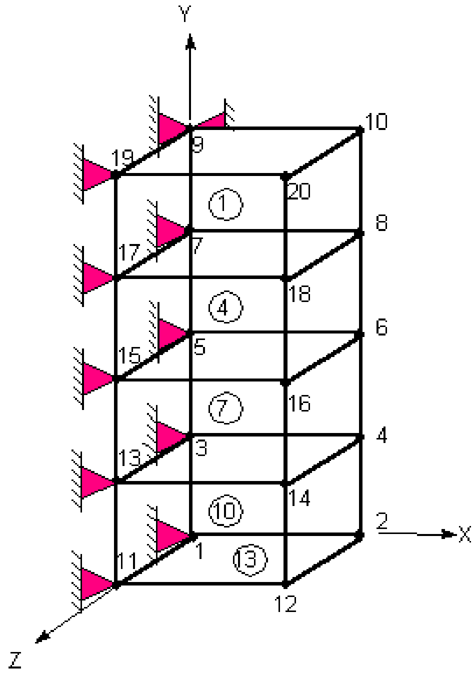

Figure 2.27 – FE model.

Result comparison is reported in Table 2.1. The agreement is very high.

	Target	***ANSYS***	***Ratio***
crack depth	*3.49*	*3.32 – 4.18*	*-*
stress in steel	*387.28*	*387.25*	*1.000*
stress in concrete	*-18.54*	*-18.49*	*0.997*

Table 2.1 – Result comparison.

2.5 – BALAN, SPACONE AND KWON MODEL

This model was developed at the University of Colorado at Boulder by Balan, Spacone and Kwon [5] and validated through the study of simple concrete-only specimens under different confinements. Later, the model was modified by Kwon and Spacone [28] and applied to concrete confined by steel and fiber reinforced polymer jackets and to RC columns.

The model is based on hypoplastic formulation and can be applied to concrete structures under monotonic or cyclic, proportional or non-proportional loading.

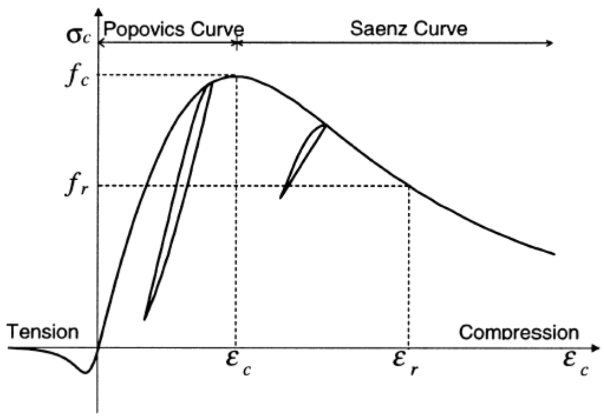

Figure 2.28 – Stress-equivalent uniaxial strain relation.

The stress-strain curves are based on equivalent uniaxial strain concept and are divided in two different fields. In the ascending branch, the Popovics formulation is used [38] whereas after the peak, the Saenz curve [42] is preferred (Figure 2.28). This choice is determined by the fact that the results from the ascending branch of the Saenz curves are satisfactory only if the initial modulus is greater than two times the secant modulus at peak. In the calculation the total secant modulus is used.

The stress-strain curves depend on the current stress state through the stress and strain relative to the peak. In order to find them, a failure surface is required. The failure surface of this study is derived by the Willam and Warnke one [47] and it is a combination of the Rankine and the Mohr-Coulomb criteria according to the Menetrey and Willam formulation [33]. Moreover, a cap surface is added to capture the failure near the hydrostatic axis (Figure 2.29).

The strain parameters for the stress-strain curves are obtained by using a similar failure surface in the strain space where the strain parameters replace the stress ones.

Since the model is capable of describing also the unloading, a suitable load function written with strain variables is defined.

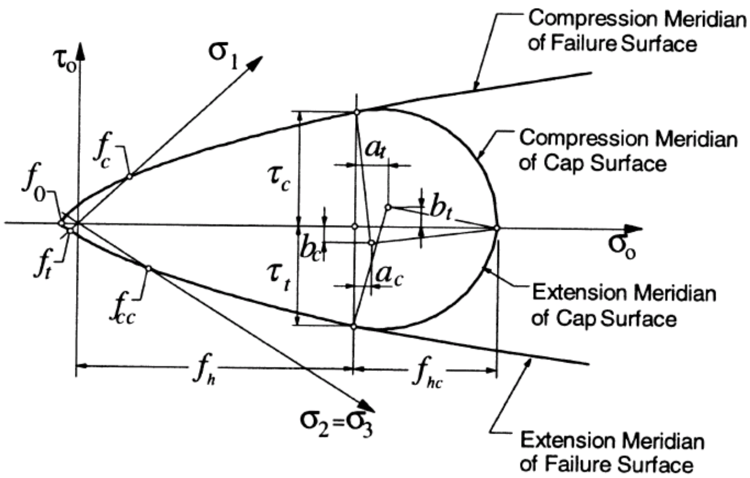

Figure 2.29 – Failure surface in Rendulic plane.

The model is implemented in the FE program FEAP as a stand alone routine. In the first stage, the model is applied, for its validation, to simple uniaxial, biaxial and triaxial concrete-only tests, all carried out at the University of Colorado at Boulder.

The first validation is performed on uniaxial tests of concrete specimens under constant lateral confinement. The final aim of these tests is to show the transition from brittle-softening to ductile-hardening behavior as the lateral confinement increases. With an accurate estimation of the cap and post peak parameters, a good agreement between experimental and numerical results is achieved and the transition is clearly visible (Figure 2.30).

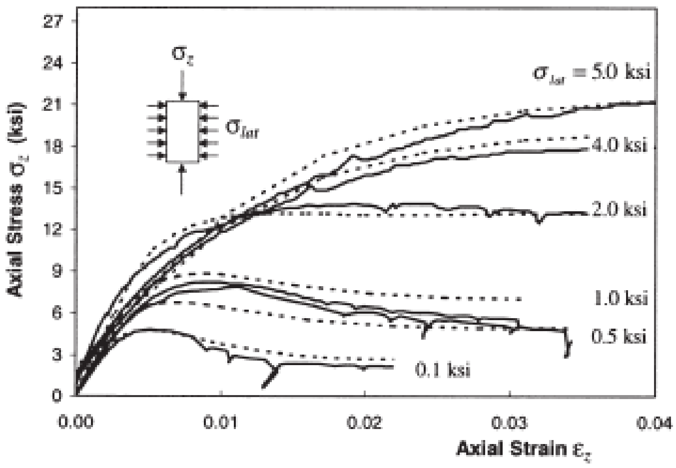

Figure 2.30 – Constant confinement compression tests.

The second application of the model is the study of concrete specimens under cyclic axial load and lateral confinement. The comparison between experimental and numerical results for three different cases is shown in Figure 2.31. The model is able to capture the changes in peak stress and strain, the post peak response and the loading-unloading behavior. A numerical mixed control is used to trace the stress path with an imposed axial displacement and constant lateral confining stress.

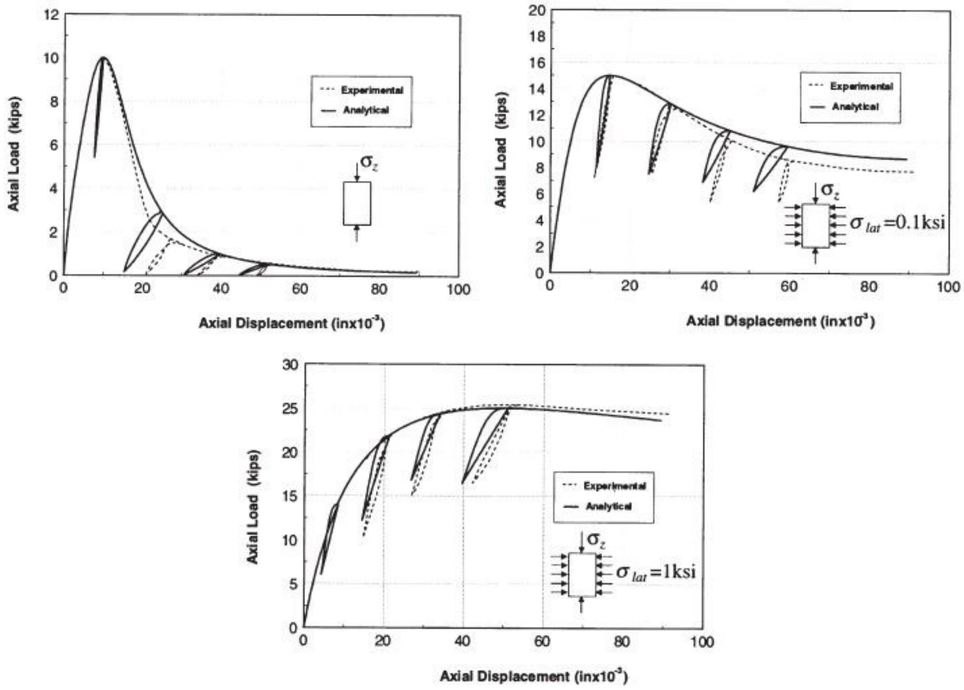

Figure 2.31 – Cyclic confined compression test results.

The model is also applied to the cases of biaxial proportional and triaxial non-proportional loading. The results for the latter case are reported in Figure 2.32. This is an important test since the most demanding stress histories in concrete analysis are those with non-proportional loading. The specimen is at first loaded along the hydrostatic axis up to 26 ksi and then, the stresses were modified by cyclic loading on the corresponding deviatoric plane. The agreement between experimental and numerical results is good.

In the second stage, the model is modified by Kwon and Spacone with some theoretical enhancements and inserting the effect of steel reinforcing bars.

In the previous version of the model, the eccentricity of the failure surface (defining the out of roundness of the deviatoric section) was defined as e=0.52 whereas in this version the eccentricity is written as a function of the brittleness.

Moreover, in order to describe simple shear (only shear strain applied) and pure shear (only shear stresses applied), an additional term containing the octahedral stress is added to the volumetric stress definition. This modification, coupling normal and shear response, represents the volumetric stress induced by the deviatoric stress.

Finally, the effects of reinforcing bars are introduced using truss elements (superposed on solid element concrete mesh) with a simple uniaxial, bilinear, strain-hardening constitutive law. Perfect bond is assumed.

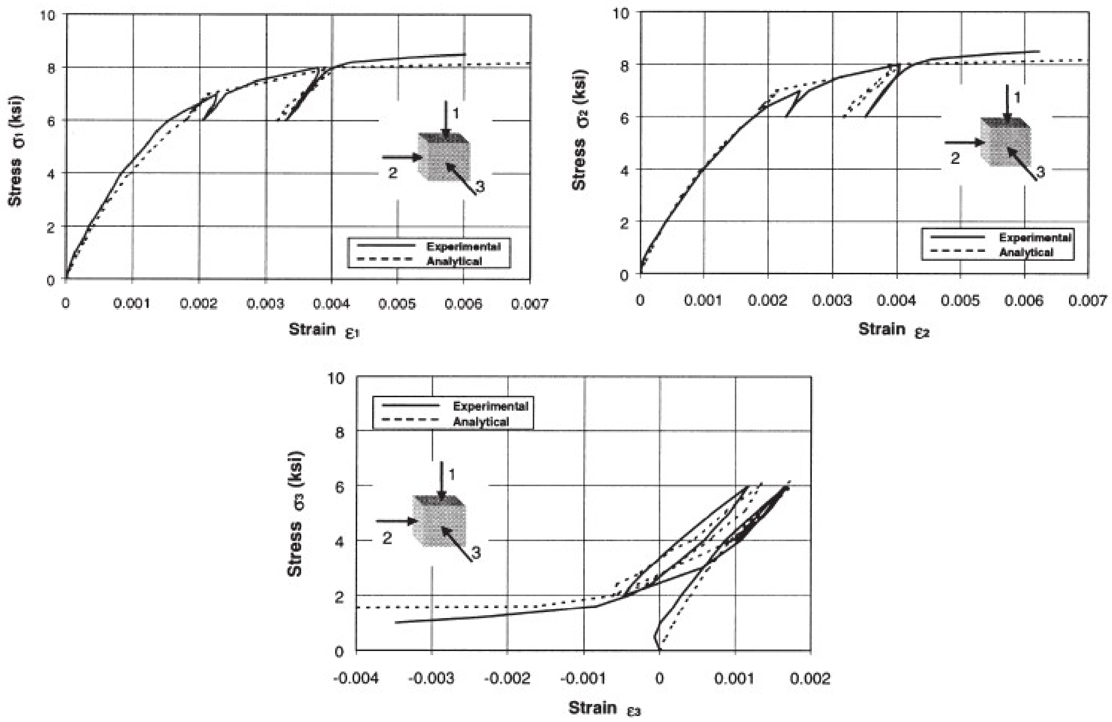

Figure 2.32 – Triaxial non-proportional loading test results.

The smeared crack approach is used in this model since it can better describe the crack pattern of structures with heavily distributed reinforcements. In this case, the shear stiffness of the structural element can be overestimated due to the stress locking in commonly used elements but the problem can be avoided using fine meshes. The crack directions are allowed to rotate with the principal strain directions during the analysis. The principal stress axes are not coaxial with the principal strain ones and the cracks are supposed to open normally to the principal strain directions.

The model is applied, at first, to axially loaded cylindric concrete specimens confined by steel and fiber reinforced polymer (FRP) jackets in order to highlight the different confinement mechanism. The steel confinement increases with the vertical load up to yielding and then, the confining stress remains constant. On the contrary, the FRP jacket is elastic up to the failure point and then, the confining stress increases with the vertical load. The good agreement between experimental and numerical results shows that the model is able to capture this difference (Figure 2.33).

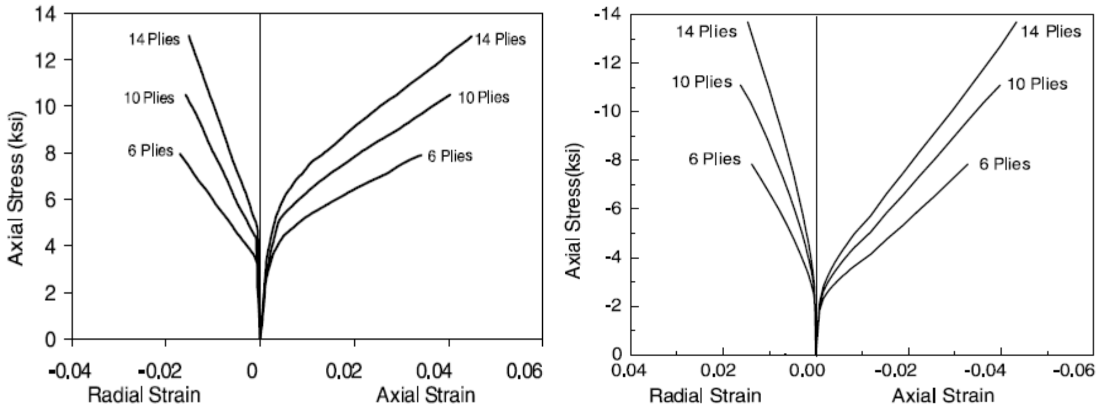

Figure 2.33 – Experimental (left) and numerical (right) results.

Finally, three RC columns from an experimental program of the University of California at San Diego are investigated. The specimens, a one-third replica of real bridge piers build in the mid '60s, are clamped at both ends and subjected to a constant axial load and to a cyclic lateral displacement (Figure 2.34).

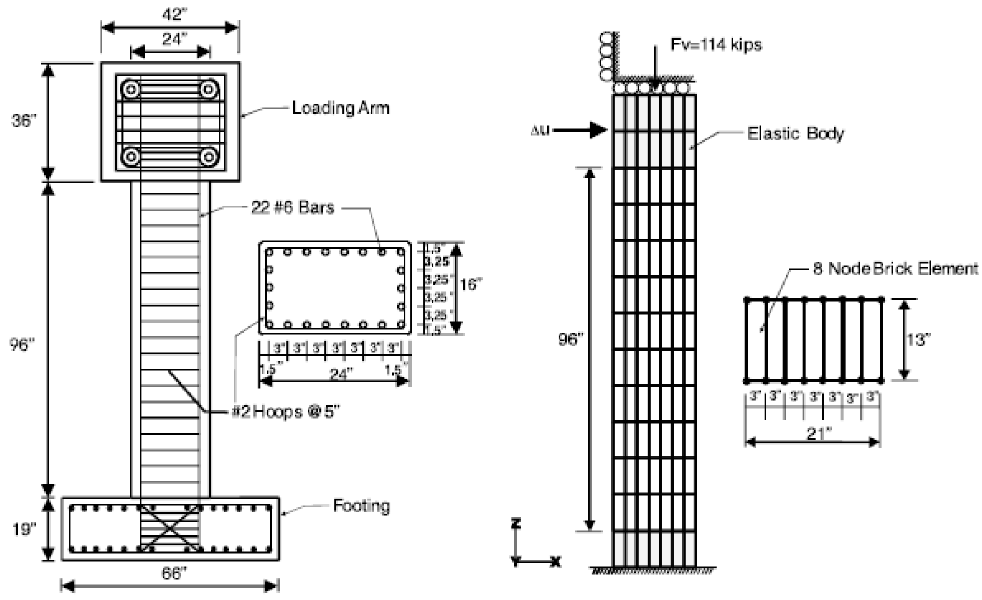

Figure 2.34 – Test configuration and FE mesh.

In order to reduce the computational time and since the final objective of the study is to capture the failure mode of the columns, only the monotonic loading envelope is followed in the simulations. The numerical outcomes are in very good agreement with the experimental tests as shown in Figure 2.35.

The first column R1 is designed in order to avoid the shear failure: it has higher hoop strength with respect to the longitudinal reinforcement strength. The failure mode and the ultimate load are captured by the model as well as the longitudinal steel bars yielding together with the presence of the compressive strut in concrete.

The column R3 is designed with a concrete with lower properties which leads to a shear failure when the flexural strength is still not achieved. The failure sequence presents at first the crushing of the main concrete strut (point A) and then, the sudden shear failure (point B). In both cases, the model is able to capture the structural behavior.

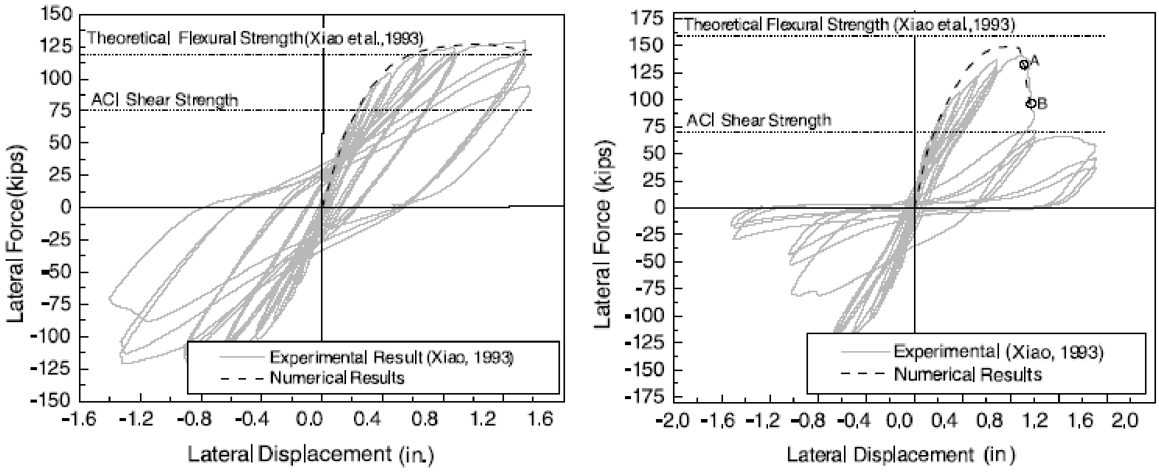

Figure 2.35 – Column R1 (left) and R3 (right) result comparisons.

CHAPTER 3 – THE PROPOSED MODEL 3D-PARC

3.1 – BASIC HYPOTHESES

The proposed model 3D-PARC – Three-Dimensional Physical Approach for Reinforced Concrete, describes the mechanical behavior of a three-dimensional (3D) reinforced concrete (RC) element subjected to general stresses. It is based on fixed, multi-directional cracking and smeared reinforcement approaches and it is formulated in terms of global material stiffness matrix.

In relation to the RC physical conditions, the proposed model is able to simulate three different phases:

- uncracked material;
- singly cracked material;
- doubly or multi-cracked material.

In the uncracked phase, perfect bond is assumed between concrete and reinforcements. Therefore, the two materials behave in parallel and their stiffness contributes are added.

In the singly cracked phase, the materials in the crack and between the cracks are considered as working in series. The modeling procedure involves a strain decomposition: the total strain is divided into the strain of the material between the cracks and in the crack. While the RC between the cracks is modeled as uncracked but damaged by the presence of the crack, the material in the crack includes all the phenomena generated by the cracking such as aggregate bridging and interlock, tension stiffening and dowel action. Finally, the flexibilities of the two materials are added together.

In the doubly or multi-cracked phase, each crack is assumed to work in series with the material between the cracks.

Cracking is assumed to arise when the principal tensile strain exceeds the strain tensile limit and the crack pattern is considered as immediately fully developed with a crack spacing a_m constant during the loading process.

The proposed model is structured in a modular framework. All the mechanical phenomena are analyzed separately on the basis of their properties and physical state. Afterwards, all the contributes are assembled to create the equivalent, non-linear, continuum material which exhibits, in the mean sense, the behavior of the sum of the contributes. In this way, each part of the model can be freely modified and updated.

For each phase, the stress-strain relation adopted, in the global coordinate system *x*-*y*-*z*, is:

$$\left\{\sigma^{xyz}\right\}=\left[D^{xyz}\right]\left\{\varepsilon^{xyz}\right\}, \tag{3.1}$$

where

$$\left\{\sigma\right\}=\left\{\sigma_x \quad \sigma_y \quad \sigma_z \quad \tau_{xy} \quad \tau_{xz} \quad \tau_{yz}\right\}^T \text{ and } \left\{\varepsilon\right\}=\left\{\varepsilon_x \quad \varepsilon_y \quad \varepsilon_z \quad \gamma_{xy} \quad \gamma_{xz} \quad \gamma_{yz}\right\}^T, \tag{3.2}$$

being $[D^{xyz}]$ the material stiffness matrix which takes into account all the stiffness contributes. This matrix is formulated in terms of secant values and assumes different forms in each phase as the strain field evolves. The secant formulation usually improves the numerical reliability in non-linear problem solution.

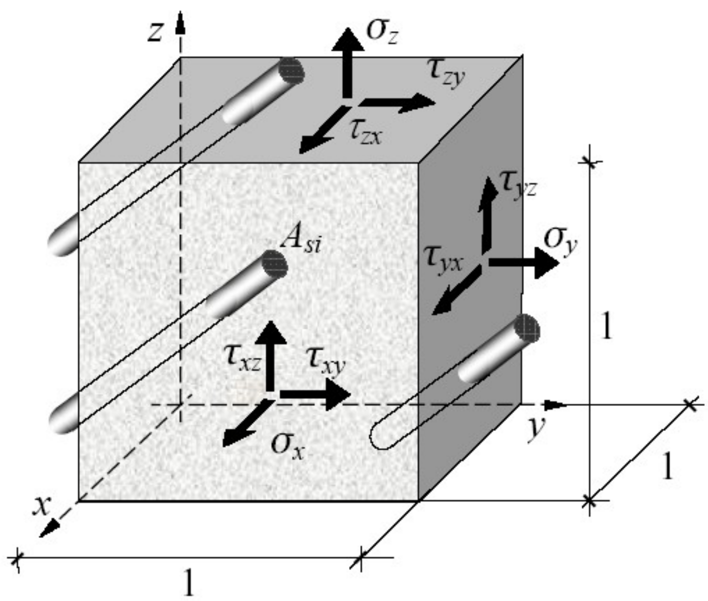

Figure 3.1 – Solid unitary RC element.

The 3D-PARC theory formulation refers to a unitary solid RC element reinforced by ordinary steel bars arranged in layers (Figure 3.1).

For each layer, a local coordinate system *x'-y'-z'* is defined and all the steel bars are parallel and oriented along the x'-axis. Each bar is characterized by a cross-sectional area A_{si}, a diameter Φ_i, a spacing p_{1i} and p_{2i} along the y' and z'-axis respectively and an orientation defined by the angles θ_{1i} and θ_{2i} (Figure 3.2).

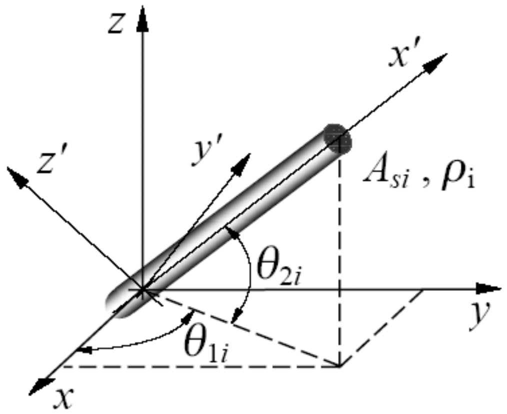

Figure 3.2 – Local steel coordinate system.

The effect of each bar is smeared on the concrete area p_{1i} by p_{2i} . Therefore, the steel geometric ratio for the i^{th} steel layer is defined as

$$\rho_i = \frac{A_{si}}{p_{1i} p_{2i}} . \tag{3.3}$$

In the same way, it is possible to define any number of steel layers, each of them having its own local system, steel ratio and diameter.

3.2 – UNCRACKED MATERIAL

In the uncracked phase, concrete and steel are supposed to behave as two materials in parallel. Since perfect bond is assumed, both concrete and steel strains are equal to the total strain:

$$\left\{\varepsilon^{xyz}\right\}=\left\{\varepsilon_c^{xyz}\right\}=\left\{\varepsilon_s^{xyz}\right\}. \tag{3.4}$$

Afterwards, the equilibrium is imposed. The total stress is the sum of the stresses in the concrete and in the steel:

$$\left\{\sigma^{xyz}\right\}=\left\{\sigma_c^{xyz}\right\}+\left\{\sigma_s^{xyz}\right\}=\left[D_c^{xyz}\right]\left\{\varepsilon_c^{xyz}\right\}+\left[D_s^{xyz}\right]\left\{\varepsilon_s^{xyz}\right\}=\left[D^{xyz}\right]\left\{\varepsilon^{xyz}\right\}, \tag{3.5}$$

where

$$\left[D_s^{xyz}\right]=\sum_{i=1}^{N_r}\left[D_{si}^{xyz}\right], \tag{3.6}$$

being $\left[D_c^{xyz}\right]$ the stiffness matrix of the concrete, $\left[D_{si}^{xyz}\right]$ the stiffness matrix of the i^{th} steel layer and N_r the total number of reinforcing layers.
Therefore, the global material stiffness matrix is

$$\left[D^{xyz}\right]=\left[D_c^{xyz}\right]+\left[D_s^{xyz}\right]. \tag{3.7}$$

In the following pages, the procedures adopted to model the two contributes are described in detail.

3.2.1 – Concrete contribute

Concrete is modeled as an incrementally linear material, orthotropic with respect to the principal strain directions *1-2-3*. The orientation of the crack system *1-2-3* with respect to the global system *x-y-z* is defined by the ψ_i angles (Figure 3.3).
The following material stiffness matrix is adopted [21]:

$$\left[D_c^{123}\right]=\begin{bmatrix}\left[D_{c\ direct}^{123}\right] & [0]\\ [0] & \left[D_{c\ shear}^{123}\right]\end{bmatrix}, \tag{3.8}$$

where

$$\left[D_{c\ direct}^{123}\right]=\frac{1}{\Phi}\begin{bmatrix} E_{c1}\left(1-\mu_{23}^{2}\right) & \sqrt{E_{c1}E_{c2}}\left(\mu_{13}\mu_{23}+\mu_{12}\right) & \sqrt{E_{c1}E_{c3}}\left(\mu_{12}\mu_{23}+\mu_{13}\right) \\ & E_{c2}\left(1-\mu_{13}^{2}\right) & \sqrt{E_{c2}E_{c3}}\left(\mu_{12}\mu_{13}+\mu_{23}\right) \\ symm. & & E_{c3}\left(1-\mu_{12}^{2}\right) \end{bmatrix} \tag{3.9}$$

and

$$\left[D_{c\ shear}^{123}\right]=\begin{bmatrix} G_{12} & 0 & 0 \\ & G_{13} & 0 \\ symm. & & G_{23} \end{bmatrix}. \tag{3.10}$$

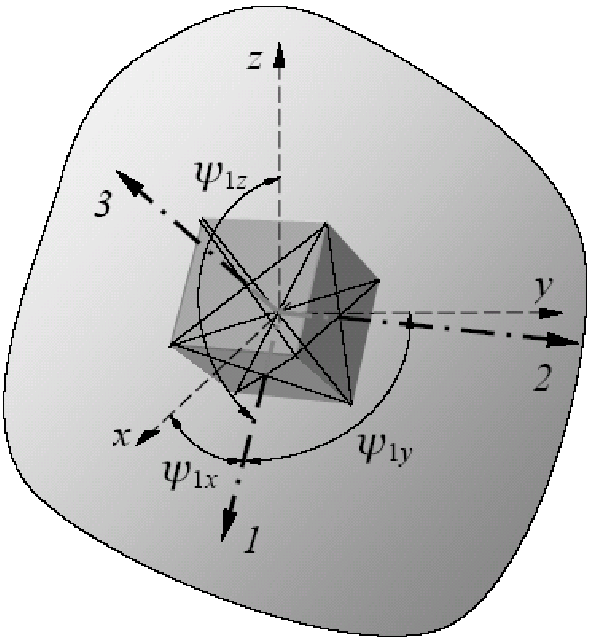

Figure 3.3 – Global and principal strain coordinate systems.

The coefficients are

$$\begin{aligned} &\Phi=1-\mu_{12}^{2}-\mu_{13}^{2}-\mu_{23}^{2}-2\mu_{12}\mu_{13}\mu_{23} \\ &\mu_{12}^{2}=\nu_{1}\nu_{2} \\ &\mu_{13}^{2}=\nu_{1}\nu_{3} \\ &\mu_{23}^{2}=\nu_{2}\nu_{3} \end{aligned} \tag{3.11}$$

and

$$
\begin{aligned}
G_{12} &= \frac{1}{4\Phi}\left[E_{c1}+E_{c2}-2\mu_{12}\sqrt{E_{c1}E_{c2}}-\left(\sqrt{E_{c1}}\mu_{23}+\sqrt{E_{c2}}\mu_{13}\right)^2\right]\\
G_{13} &= \frac{1}{4\Phi}\left[E_{c1}+E_{c3}-2\mu_{13}\sqrt{E_{c1}E_{c3}}-\left(\sqrt{E_{c1}}\mu_{23}+\sqrt{E_{c3}}\mu_{12}\right)^2\right]\\
G_{23} &= \frac{1}{4\Phi}\left[E_{c2}+E_{c3}-2\mu_{23}\sqrt{E_{c2}E_{c3}}-\left(\sqrt{E_{c2}}\mu_{13}+\sqrt{E_{c3}}\mu_{12}\right)^2\right]
\end{aligned}
\tag{3.12}
$$

being E_{ci} and ν_i the secant elastic modulus and the Poisson coefficient relative to i^{th} direction respectively. Since E_{ci} and ν_i are non-linear functions of the strain field, the material stiffness matrix varies during the loading process.

In general, the principal stress and strain directions are not coaxial. The concrete behavior is evaluated by means of the principal strains and therefore, the principal stresses are approximately computed, as a function of the strains, along the principal strain directions.

3.2.2 – Elastic moduli and Poisson coefficients

The concept of equivalent uniaxial strain is used [21] to evaluate the E_{ci} and ν_i in the three directions as a function of the strain field. If the material was loaded in one direction only, its strain would be the equivalent uniaxial strain. In other words, the strain in each direction is purified from the strains caused by the stresses in the perpendicular directions. In this way, it is possible to make each direction independent and to write a stress-equivalent uniaxial strain law for each direction.

The i^{th} equivalent uniaxial strain can be defined as

$$\varepsilon_{iu} = \frac{\sigma_i}{E_{ci}}. \tag{3.13}$$

The principal stresses are related to the principal strains through the matrix (3.9). Therefore, the equivalent uniaxial strains $\{\varepsilon_u\}$ can be computed from the current strain state.

In matrix form:

$$\{\varepsilon_u\} = [E]\{\varepsilon\}. \tag{3.14}$$

where the matrix $[E]$ is obtained by dividing each row of the matrix (3.9) by the modulus E_{ci}:

$$[E]=\frac{1}{\Phi}\begin{bmatrix} \left(1-\mu_{23}^2\right) & \sqrt{\frac{E_{c2}}{E_{c1}}}\left(\mu_{13}\mu_{23}+\mu_{12}\right) & \sqrt{\frac{E_{c3}}{E_{c1}}}\left(\mu_{12}\mu_{23}+\mu_{13}\right) \\ \sqrt{\frac{E_{c1}}{E_{c2}}}\left(\mu_{13}\mu_{23}+\mu_{12}\right) & \left(1-\mu_{13}^2\right) & \sqrt{\frac{E_{c3}}{E_{c2}}}\left(\mu_{12}\mu_{13}+\mu_{23}\right) \\ \sqrt{\frac{E_{c1}}{E_{c3}}}\left(\mu_{12}\mu_{23}+\mu_{13}\right) & \sqrt{\frac{E_{c2}}{E_{c3}}}\left(\mu_{12}\mu_{13}+\mu_{23}\right) & \left(1-\mu_{12}^2\right) \end{bmatrix}, \tag{3.15}$$

where Φ and μ_{ij} are defined in (3.11).

In the numerical implementation, the elastic moduli of the matrix [E] are taken from the previous iteration because the moduli of the current iteration have not been calculated yet.

From the equivalent uniaxial strains, through suitable constitutive laws, the secant moduli E_{ci} can be derived.

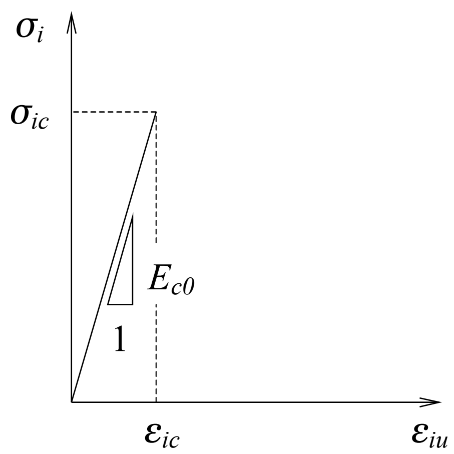

Figure 3.4 – Concrete tensile law.

In the tensile field, a linear elastic behavior is assumed (Figure 3.4), whereas, in the compressive field, the Saenz curve [42] is adopted (Figure 3.5):

$$\sigma_i=\frac{E_{c0}\varepsilon_{iu}}{1+\left(R+R_E-2\right)\frac{\varepsilon_{iu}}{\varepsilon_{ic}}-\left(2R-1\right)\left(\frac{\varepsilon_{iu}}{\varepsilon_{ic}}\right)^2+R\left(\frac{\varepsilon_{iu}}{\varepsilon_{ic}}\right)^3}, \tag{3.16}$$

where

$$R_E=\frac{E_{c0}}{E_s},\ E_s=\frac{\sigma_{ic}}{\varepsilon_{ic}},\ R=R_E\frac{R_\sigma-1}{\left(R_\varepsilon-1\right)^2}-\frac{1}{R_\varepsilon},\ R_\sigma=\frac{\sigma_{ic}}{\sigma_{if}}\text{ and }R_\varepsilon=\frac{\varepsilon_{if}}{\varepsilon_{ic}}, \tag{3.17}$$

being E_{c0} the initial elastic modulus, σ_{ic} and ε_{ic} the peak stress and the related strain in the i^{th} direction, σ_{if} and ε_{if} the coordinates of a point on the descending branch. The following values are chosen: $\sigma_{if}=\sigma_{ic}/4$ and $\varepsilon_{if}=4\ \varepsilon_{ic}$.

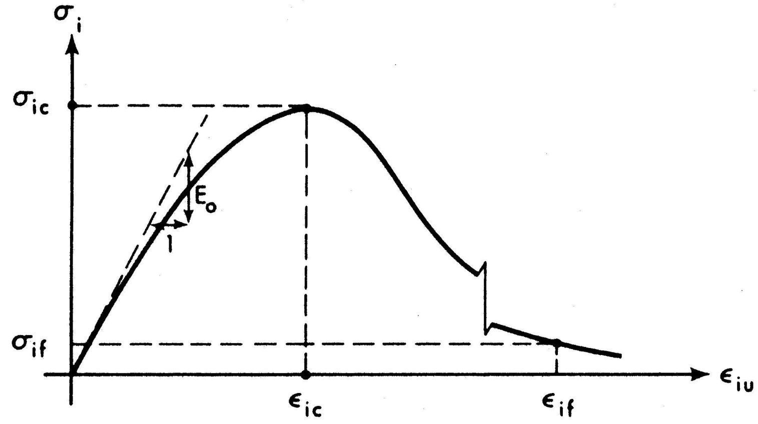

Figure 3.5 – Concrete compressive law.

The Poisson coefficient ν_i is computed, in each direction, as a function of the ratio between the principal stress and the peak stress [3]:

$$\nu_i = \begin{cases} \nu_0 & \text{when } R \le R_{lim} \\ \nu_f - \left(\nu_f - \nu_0\right)\sqrt{1-\left(\dfrac{R-R_{lim}}{1-R_{lim}}\right)^2} & \text{when } R > R_{lim} \end{cases} \tag{3.18}$$

where

$$R = \frac{\sigma_i}{\sigma_{ic}},\ R_{lim} = 0.7 \text{ and } \nu_f = 0.42\,. \tag{3.19}$$

Using a variable Poisson coefficient, it is possible to capture the dilatancy phenomenon which, as observed in experimental tests, becomes important for high values of compressive stresses (about 80% of the ultimate strength). Where the dilatancy has a low influence, a constant Poisson coefficient can be used.

3.2.3 – Stress failure surface

The failure surface in the stress space defines the stress states which cause the concrete failure. The surface used in 3D-PARC, proposed by Balan, Spacone and Kwon [5], is based on the previous works of Menetrey and Willam [33] and Willam and Warnke [47]. Moreover, a new cap surface is proposed in order to close the surface in the high hydrostatic stress region.

The Balan-Spacone-Kwon surface (Figure 3.6) presents some major advantages from the numerical point of view since it can be written as a parabola and therefore, it provides the required values in closed form. On the contrary, for the previous Willam-Warnke surface, an iterative Newton-Raphson solving procedure was required to find the concrete strength values.

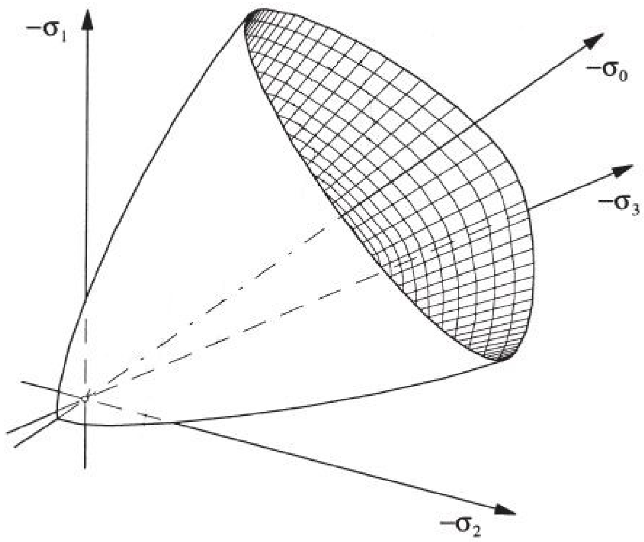

Figure 3.6 – The 3D failure surface.

In the principal stress space, the concrete strength, identified with the vector $\{\sigma_c\}$, can be evaluated as it follows. Starting from the current principal stress values, the corresponding point in the principal stress space is found. Then, a straight line by the origin and by this point is drawn until it intersects the failure surface: the coordinates of the intersection are (σ_{1c}, σ_{2c}, σ_{3c}).

The surface is written as a function of three invariants: the octahedral stresses σ_o and τ_o and the Lode angle θ:

$$\begin{aligned} \sigma_o &= \frac{\sigma_1+\sigma_2+\sigma_3}{3} \\ \tau_o &= \frac{1}{3}\left[(\sigma_1-\sigma_2)^2+(\sigma_2-\sigma_3)^2+(\sigma_3-\sigma_1)^2\right]^{0.5} \\ \cos\theta &= \frac{2\sigma_1-\sigma_2-\sigma_3}{2\sqrt{3}J_2^{0.5}} \end{aligned} \tag{3.20}$$

where

$$J_2 = \frac{1}{6}\left[\left(\sigma_1-\sigma_2\right)^2+\left(\sigma_2-\sigma_3\right)^2+\left(\sigma_3-\sigma_1\right)^2\right]^{0.5}. \tag{3.21}$$

J_2 is the second invariant of the deviatoric stress tensor.

The Rendulic plane is defined as a plane passing by the isotropic line σ_1=σ_2=σ_3 and localized by a value of θ (Figure 3.7). The deviatoric plane is defined as a plane perpendicular to the isotropic line and localized by a value of σ_o (Figure 3.8).

The surface is a parabola in the Rendulic plane. After calculating the current value of θ, the procedure is carried out in the Rendulic plane and therefore, the problem variables are σ_o and τ_o only. The parabola is described by the equation

$$\tau_o^2 + A\left(\frac{\tau_o}{\sqrt{2}}r\left(e,\theta\right)+\sigma_o\right)+B=0, \tag{3.22}$$

where

$$A=\frac{f_c^2-f_t^2}{9f_t}\left(2+\alpha\right) \text{ and } B=-\frac{2}{9}f_c^2, \tag{3.23}$$

being e the eccentricity and α the fragility defined as the ratio between the uniaxial tensile and compressive strength:

$$\alpha=\frac{f_t}{f_c}. \tag{3.24}$$

The eccentricity indicates how much the intersection of the surface with a deviatoric plane differs from the circular shape.

The polar radius $r(e, \theta)$ is written as

$$r\left(e,\theta\right)=\frac{a\eta^2+b^2}{a\eta+b\sqrt{a\left(\eta^2-1\right)+b^2}}, \tag{3.25}$$

where

$$a=1-e^2,\ b=2e-1 \text{ and } \eta=2\cos\theta. \tag{3.26}$$

This parabola has an intersection with the σ_o-axis in the equi-triaxial tension point for

$$f_o = -\frac{B}{A} = \frac{2f_t}{\left(1-\alpha^2\right)\left(2+\alpha\right)} \tag{3.27}$$

and provides a biaxial compressive strength equal to

$$f_{cc} = \frac{f_c}{4}\left[\left(1-\alpha^2\right)+\sqrt{\left(1-\alpha^2\right)^2+16}\right]. \tag{3.28}$$

In order to capture the material failure for the stress states near the hydrostatic axis, a cap surface is formulated. Balan, Spacone and Kwon [5] propose a cap surface written in the stress space as a function of the invariants. In 3D-PARC, a different solution is proposed: the cap surface is defined directly in the Rendulic plane by a parabola. This curve has the main axis parallel to the τ_o-axis, it is tangent to the surface in the point with σ_o=-f_h and it passes by the equi-triaxial compression point with σ_o=-f_{ccc} (Figure 3.7). In this way, with an easy numerical formulation, the continuity and the smoothness of the 3D domain is assured.

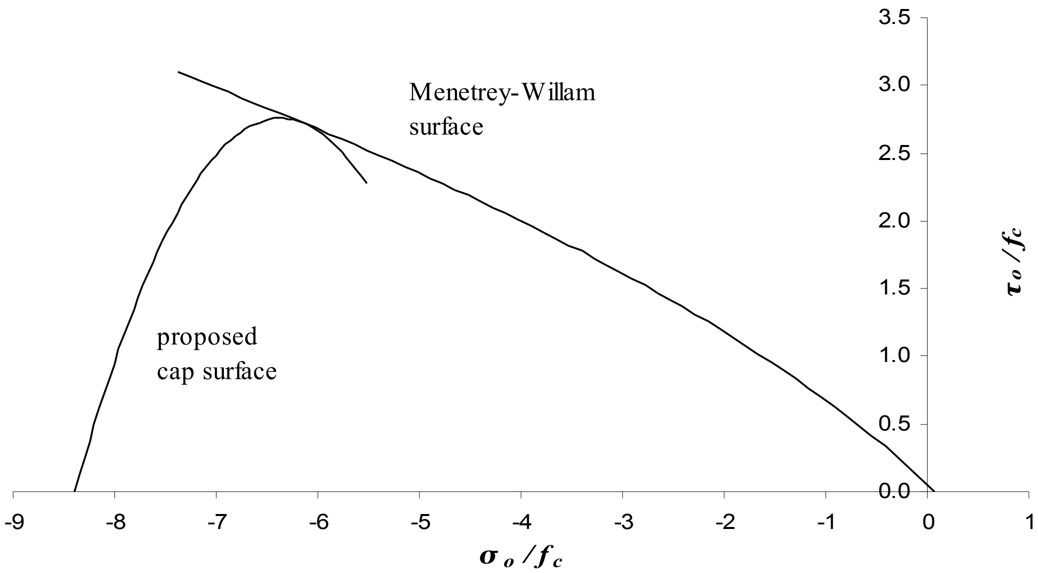

Figure 3.7 – The two parabolas defining the failure surface in the Rendulic plane.

The cap is defined as

$$\tau_o = D\sigma_o^2 + E\sigma_o + F\,, \tag{3.29}$$

where

$$D = \frac{k\left(f_{ccc} - f_h\right) - \tau^*}{\left(f_{ccc} - f_h\right)^2},\ E = k + 2Df_h \text{ and } F = Ef_{ccc} - Df_{ccc}^2, \tag{3.30}$$

being τ^* the surface value for σ_o=-f_h and k the surface first derivative in the same point.
The parameters f_{ccc} and f_h are tuned in order to obtain a good agreement with the Willam-Warnke surface. f_{ccc} and f_h can be written as functions of the material fragility, of the uniaxial compressive strength and of the Lode angle:

$$\begin{aligned} \frac{f_{ccc}}{f_c} &= 102.86\alpha^2 + 11.498\alpha + 6.8738 \\ \frac{f_h}{f_{ccc}} &= \left(-0.0974\theta^2 - 0.1432\theta + 0.9\right)\left(0.1662\theta^2 - 0.487\theta + 0.813\right) \end{aligned} \tag{3.31}$$

The coordinates of the intersection between the current stress state line and the surface can be written as:

$$\begin{Bmatrix} \sigma_{1c} \\ \sigma_{2c} \\ \sigma_{3c} \end{Bmatrix} = \sigma_o^{int} + \sqrt{2}\tau_o^{int} \begin{Bmatrix} \cos\theta \\ \cos\left(\theta - 2\pi/3\right) \\ \cos\left(\theta + 2\pi/3\right) \end{Bmatrix}, \tag{3.32}$$

where $\left(\sigma_o^{int}, \tau_o^{int}\right)$ are the coordinates of the intersection point in the Rendulic plane.

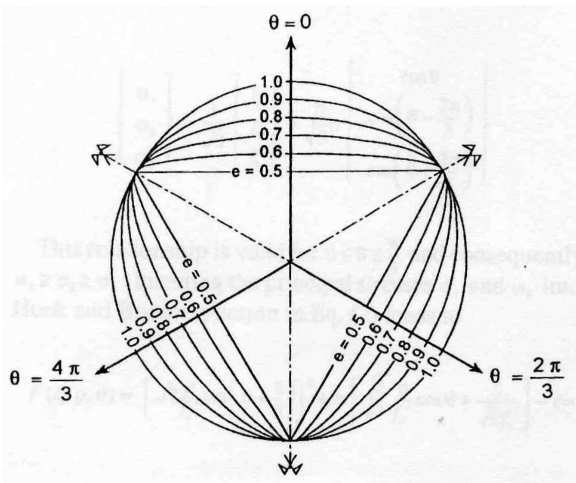

Figure 3.8 – Deviatoric sections for different values of e.

The failure surface is fully defined by three parameters, the uniaxial tensile strength f_t, the uniaxial compressive strength f_c and the eccentricity e. The influence of the eccentricity on the deviatoric section can be seen in Figure 3.8.

In general, the uniaxial parameters f_t and f_c are well known or easy to estimate. On the contrary, the effect of the eccentricity is less investigated even if it strongly influences the surface. This effect can be clearly detected by plotting the intersection of the failure surface with the σ_3=0 plane, obtaining a biaxial failure domain.

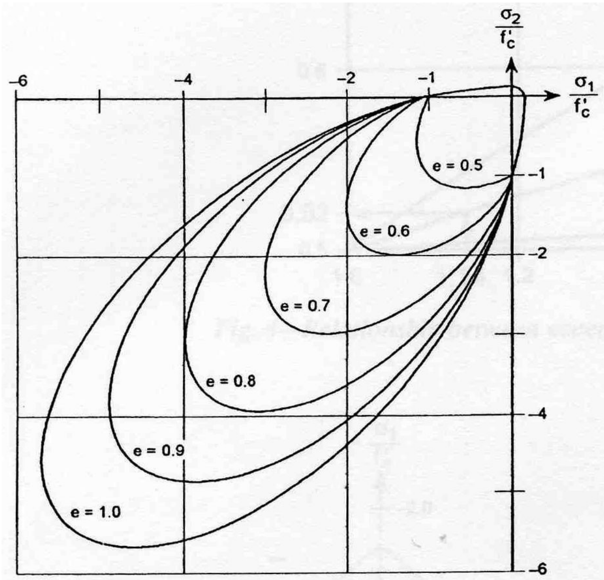

Figure 3.9 – Biaxial failure domain as a function of e.

In order to preserve the convexity and smoothness of the elliptic deviatoric section of the surface, the eccentricity must be kept in the range 0.5<e≤1. Drawing the biaxial domain for f_c=10.35 f_t and varying e in this range, the biaxial compression field is strongly influenced: the biaxial compressive strength f_{cc} varies between f_c for e=0.5 and 5.31 f_c for e=1 (Figure 3.9).

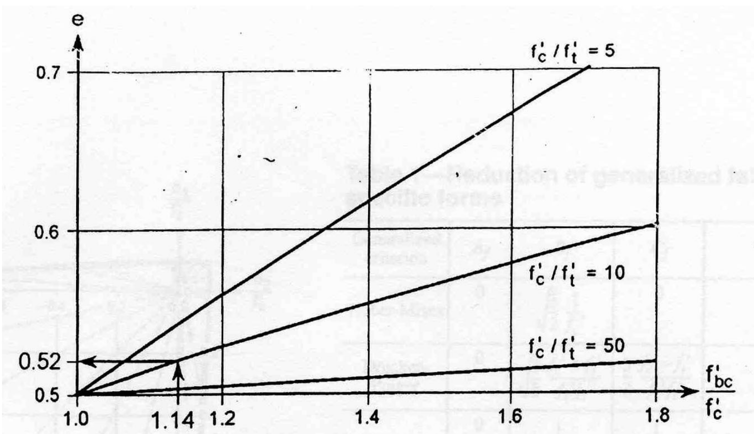

Figure 3.10 – Relationship between e and f_{cc}.

Therefore, it is clear that the eccentricity should be chosen carefully. The diagram in Figure 3.10 allows to chose the eccentricity value starting from the required biaxial compressive strength and the f_c/f_t ratio. For example, if f_{cc}/f_c=1.14 and f_c/f_t=10, a suitable value for e is 0.52. This value generally provides very good agreement with experimental results.
Another possibility is introduced by Kwon and Spacone [28]: the eccentricity is computed as a function of the fragility α. This allows the failure surface to be written as a function of two parameters only. The proposed equation for the eccentricity is

$$e=\frac{2+\alpha}{4-\alpha}\,. \tag{3.33}$$

With a fragility α=0.1, an eccentricity e= 0.54 is obtained.

3.2.4 – Peak strain calculation

To define the peak strains $\{\varepsilon_c\}$, related to the $\{\sigma_c\}$ in the equivalent uniaxial curves, two different procedures can be applied.
The more general technique requires a surface in the principal strain space [5]. This surface has the same form as the one built in the stress space with the stress variables replaced by the corresponding strain variables:

$$\begin{aligned}
\varepsilon_o &= \frac{\varepsilon_{1u}+\varepsilon_{2u}+\varepsilon_{3u}}{3} \\
\gamma_o &= \frac{1}{3}\left[\left(\varepsilon_{1u}-\varepsilon_{2u}\right)^2+\left(\varepsilon_{2u}-\varepsilon_{3u}\right)^2+\left(\varepsilon_{3u}-\varepsilon_{1u}\right)^2\right]^{0.5} \\
\cos\theta &= \frac{2\varepsilon_{1u}-\varepsilon_{2u}-\varepsilon_{3u}}{2\sqrt{3}J_2^{0.5}}
\end{aligned} \tag{3.34}$$

where

$$J_2=\frac{1}{6}\left[\left(\varepsilon_{1u}-\varepsilon_{2u}\right)^2+\left(\varepsilon_{2u}-\varepsilon_{3u}\right)^2+\left(\varepsilon_{3u}-\varepsilon_{1u}\right)^2\right]^{0.5}. \tag{3.35}$$

J_2 is the second invariant of the deviatoric strain tensor. Then, the procedure to find the $\{\varepsilon_c\}$ is analogous to the one used in the stress case.
A simpler procedure uses equations fitting the experimental data. The ε_{ic} is provided as a function of the σ_{ic} and of two parameters of the uniaxial stress-strain curve: the compressive

strength f_c and the related peak strain ε_{cp}. Darwin and Pecknold [20] propose, after biaxial studies:

$$\frac{\varepsilon_{ic}}{\varepsilon_{cp}} = \begin{cases} -1.6\left(\dfrac{\sigma_{ic}}{f_c}\right)^3 + 2.25\left(\dfrac{\sigma_{ic}}{f_c}\right)^2 + 0.35\left(\dfrac{\sigma_{ic}}{f_c}\right) & \text{when } \sigma_{ic} \le f_c \\ \dfrac{\sigma_{ic}}{f_c} R - (R-1) & \text{when } \sigma_{ic} > f_c \end{cases} \tag{3.36}$$

where the coefficient R is derived from experimental investigations. The suggested value is R=3. The equation (3.36) is plotted in Figure 3.11.

In 3D-PARC, both procedures are implemented.

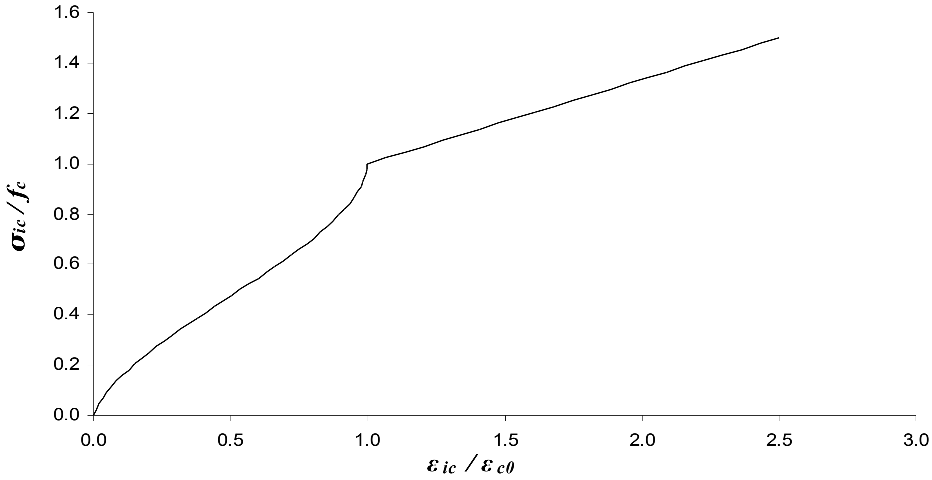

Figure 3.11 – Darwin-Pecknold curve for peak strains.

3.2.5 – Concrete failure fields

One of the main problems of the presented formulation is the simultaneous failure. In fact, the peak stress σ_{ic} is modified, for each curve, according to the current stress state, namely, the curve peak in one direction is influenced by the stresses in other directions. But for stress ratios close to uniaxial loading, the curve peaks, and consequently the elastic moduli, are reduced in all directions. Therefore, it is not possible to evaluate in which direction the failure occurs. This situation is clearly unphysical.

In order to solve this problem, the failure surface is divided by a cone into two failure fields in which the failure mode is assigned. The cone has its vertex in the origin of the 3D stress space and the intersection with a biaxial plane (one principal stress equal to zero) is a line identified by the stress ratio

$$\alpha_{\lim} = \frac{\sigma_1}{\sigma_2} = -\frac{f_t}{f_c} = -\alpha \tag{3.37}$$

depending on the fragility α (3.24). Then, the cone trace is transferred in the Rendulic plane identified by the current Lode angle and the position of the current stress state is checked.
Figure 3.12 shows the Menetrey-Willam surface, the proposed cap surface and the cone defining the failure fields.

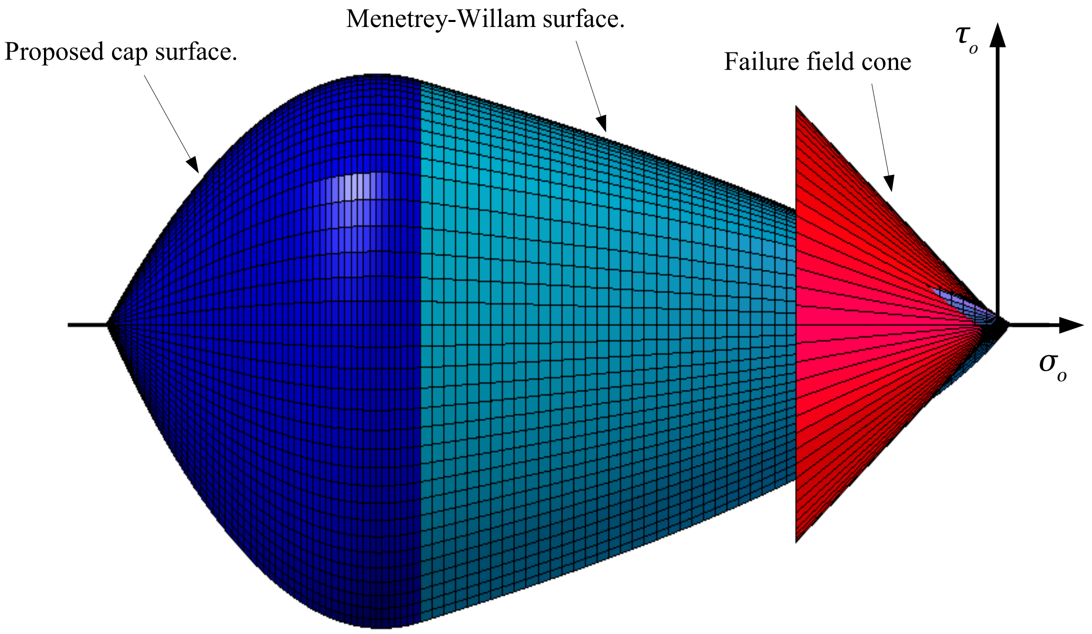

Figure 3.12 – The failure surface and the cone defining the failure fields.

If the point of the current stress state is inside the cone, the failure is considered compressive, whereas, if the point is external, the failure is considered tensile (Figure 3.13).
Furthermore, this approach allows to assign the stress-strain curves in order to avoid the elastic modulus decrement and the consequent simultaneous failure in all directions. In general, the curve of the most loaded direction is assigned also to other directions. In this way, when the failure is occurring in the most loaded direction, in the other directions the failure is still faraway.
If the failure is tensile, the curves in compressive directions are computed by recalculating the $\{\sigma_c\}$ with a modified version of the current stress state. In particular, the compressive stresses are modified in the following way:

$$\sigma_{i\ mod} = -\frac{\sigma_i}{\alpha_{\lim}} = \frac{\sigma_i}{\alpha}. \tag{3.38}$$

By this method, the output for the compressive directions guarantees that the failure is not achieved in those directions.

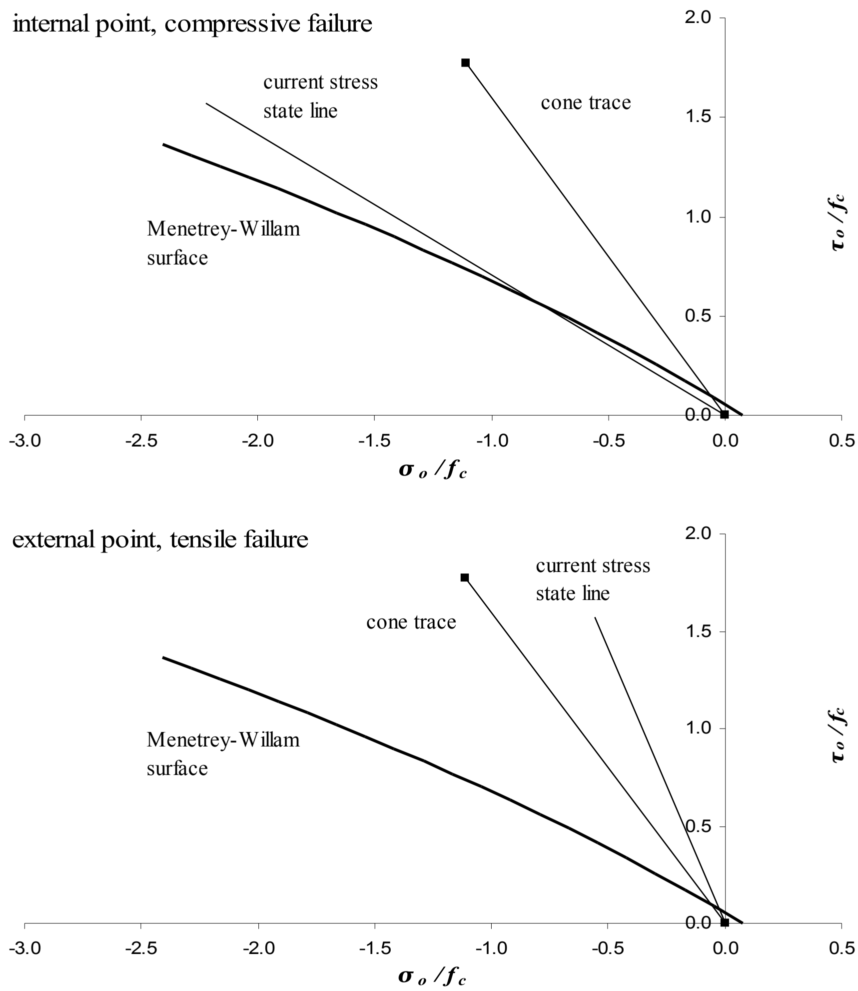

Figure 3.13 – Compressive and tensile failure fields.

The failure is always checked along the directions *1* (tensile failure) and *3* (compressive failure). Both failures are checked on the strains: the tensile failure occurs when the first principal uniaxial strain ε_{1u} exceeds the tensile strain ε_{1c}:

$$\varepsilon_{1u} > \varepsilon_{1c} = \frac{\sigma_{1c}}{E_{c0}}. \tag{3.39}$$

The compressive failure occurs when the third principal uniaxial strain ε_{3u} exceeds the concrete ultimate strain ε_{ult}:

$$|\varepsilon_{3u}| > |\varepsilon_{ult}| . \tag{3.40}$$

The ultimate strain value can be chosen by the user. In the Eurocode 2 [13], for uniaxial load cases, the peak strain is 0.002 and the ultimate strain is 0.0035, with a ratio

$$r = \frac{0.0035}{0.002} = 1.75 . \tag{3.41}$$

In the proposed model, the Eurocode approach is extended to the multiaxial stress states and therefore, the ultimate strain is computed as 1.75 times the peak strain. The ultimate strain is computed along the direction *3* since that is the most compressed one:

$$\varepsilon_{ult} = 1.75\varepsilon_{3c} . \tag{3.42}$$

If the ultimate strain is reached, the material softens in all directions.

The stress combinations provide several different cases:

A) $\sigma_1 \geq 0$, $\sigma_2 \geq 0$, $\sigma_3 \geq 0$

The failure is tensile. For all directions the linear curve limited to σ_{1c} is adopted.

B) $\sigma_1 \geq 0$, $\sigma_2 \geq 0$, $\sigma_3 < 0$

B1) The current stress state point is external, the failure is tensile. For both directions *1* and *2*, the linear curve limited to σ_{1c} is adopted. For direction *3*, the σ_{3c} is computed by using the modification (3.38).

B2) The current stress state point is internal, the failure is compressive. For both directions *1* and *2*, the linear curve limited to σ_{1c} is adopted. For direction *3*, the σ_{3c} is computed without modification.

C) $\sigma_1 \geq 0$, $\sigma_2 < 0$, $\sigma_3 < 0$

C1) The current stress state point is external, the failure is tensile. For direction *1*, the linear curve limited to σ_{1c} is adopted. For both directions *2* and *3*, the σ_{ic} is computed by using the modification (3.38). The stress-strain law for direction *3* is used also for direction *2*.

C2) The current stress state point is internal, the failure is compressive. For directions *1*, the linear curve limited to σ_{1c} is adopted. For both directions *2* and *3*, the σ_{ic} is computed without modification. The stress-strain law for direction *3* is used also for direction *2*.

D) $\sigma_1 < 0$, $\sigma_2 < 0$, $\sigma_3 < 0$

The failure is compressive. For all the directions, the σ_{ic} is computed without modification. The stress-strain law for direction *3* is used for all directions.
A summary is reported in Table 3.1.

Case	$\boldsymbol{\sigma_1}$	$\boldsymbol{\sigma_2}$	$\boldsymbol{\sigma_3}$	***Failure***	***Direction 1***	***Direction 2***	***Direction 3***
A	≥0	≥0	≥0	*tensile*	*linear* (σ_{1c})	*linear* (σ_{1c})	*linear* (σ_{1c})
B1	≥0	≥0	<0	*tensile*	*linear* (σ_{1c})	*linear* (σ_{1c})	*Saenz* ($\sigma_{3c\,mod}$)
B2	≥0	≥0	<0	*compressive*	*linear* (σ_{1c})	*linear* (σ_{1c})	*Saenz* (σ_{3c})
C1	≥0	<0	<0	*tensile*	*linear* (σ_{1c})	*Saenz* ($\sigma_{3c\,mod}$)	*Saenz* ($\sigma_{3c\,mod}$)
C2	≥0	<0	<0	*compressive*	*linear* (σ_{1c})	*Saenz* (σ_{3c})	*Saenz* (σ_{3c})
D	<0	<0	<0	*compressive*	*Saenz* (σ_{3c})	*Saenz* (σ_{3c})	*Saenz* (σ_{3c})

Table 3.1 – Curve assignment summary.

3.2.6 – Reinforcement contribute

The constitutive model for the steel is the simple bilinear elastic-plastic curve equal in tension and compression shown in Figure 3.14.

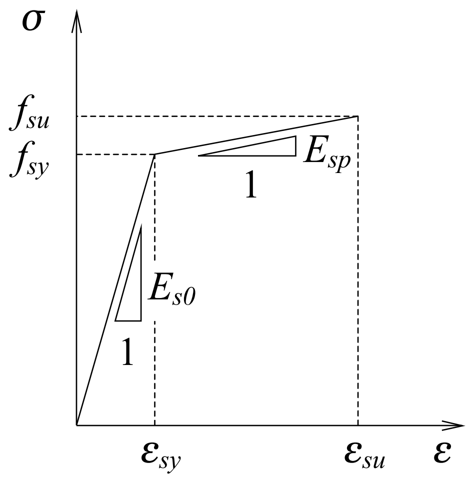

Figure 3.14 – Uniaxial law for ordinary steel reinforcements.

The elastic modulus is

$$E_s = \begin{cases} E_{s0} & \text{when } \varepsilon_s \le \varepsilon_{sy} \\ E_{s0} + \left(E_{sp} - E_{s0}\right)\dfrac{\varepsilon_s - \varepsilon_{sy}}{\varepsilon_s} & \text{when } \varepsilon_s > \varepsilon_{sy} \end{cases} \tag{3.43}$$

where E_{s0} is the initial elastic modulus, E_{sp} is the plastic modulus, ε_s is the current bar strain and ε_{sy} is the yielding strain.

The current bar strain in the local system *x'-y'-z'* is computed from the total strain in the global system *x-y-z* through the transformation [19]

$$\left\{\varepsilon_s^{x'y'z'}\right\} = \left[T_\varepsilon\right]\left\{\varepsilon_s^{xyz}\right\} = \left[T_\varepsilon\right]\left\{\varepsilon^{xyz}\right\}, \tag{3.44}$$

where $[T_\varepsilon]$ is the strain transformation matrix.

Since the steel bars exhibit stiffness along their axes only, their constitutive matrix for the i^{th} steel layer can be written, in the local system, as

$$\left[D_{si}^{x'y'z'}\right] = \rho_i \begin{bmatrix} E_{si} & 0 & 0 & 0 & 0 & 0 \\ & 0 & 0 & 0 & 0 & 0 \\ & & 0 & 0 & 0 & 0 \\ & & & 0 & 0 & 0 \\ & symm. & & & 0 & 0 \\ & & & & & 0 \end{bmatrix}. \tag{3.45}$$

Subsequently, the steel matrix is written for each layer in the global system through the transformation

$$\left[D_{si}^{xyz}\right] = \left[T_\varepsilon\right]^T \left[D_{si}^{x'y'z'}\right]\left[T_\varepsilon\right]. \tag{3.46}$$

3.3 – SINGLY CRACKED MATERIAL

In 3D-PARC, the fixed, multi-directional cracking approach is adopted. When the tensile failure occurs, the crack opens perpendicularly to the *1*-axis which is the direction of the maximum tensile strain. This direction will be kept fixed from now on in the calculation. In the theoretical formulation, up to now, the system *1-2-3* has been the principal strain system while from now on it will identify the first crack system.

When the strain tensile limit is achieved, the crack pattern develops with a constant crack spacing a_m (Figure 3.15).

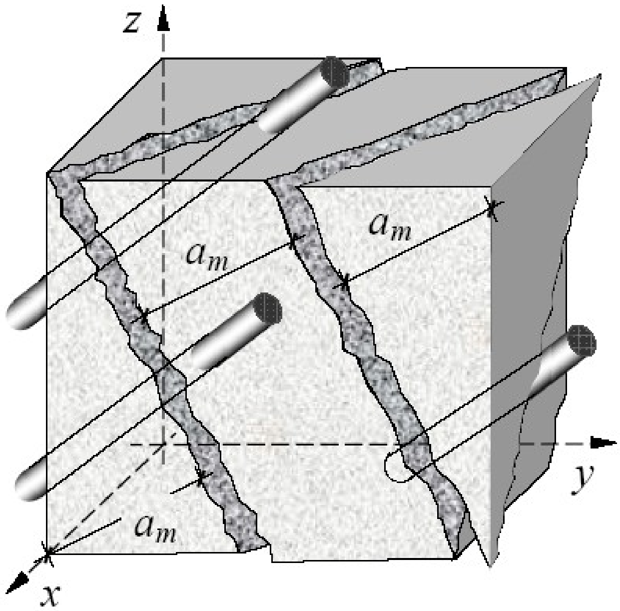

Figure 3.15 – Solid cracked RC element.

After cracking, the strain is decomposed into two contributes, the first related to the concrete between the cracks and the second related to the crack:

$$\left\{\varepsilon^{xyz}\right\} = \left\{\varepsilon_c^{xyz}\right\} + \left\{\varepsilon_{cr}^{xyz}\right\}. \tag{3.47}$$

The stiffness matrix is calculated separately for each material by using different constitutive models and techniques, and eventually, the material contributes are superimposed.

This technique allows a more general approach to the problem since every constitutive model can be developed totally independently on others. If a better method to model the cracking or the uncracked RC is proposed, it can be easily inserted in 3D-PARC by substituting only the related part of the code. Moreover, it is possible to consider the effect of subsequent cracking phenomena by simply adding the effect of the new cracks. Furthermore, the subsequent cracks are not forced to develop in a fixed direction but they are free to arise in the real maximum tensile strain direction after the first failure.

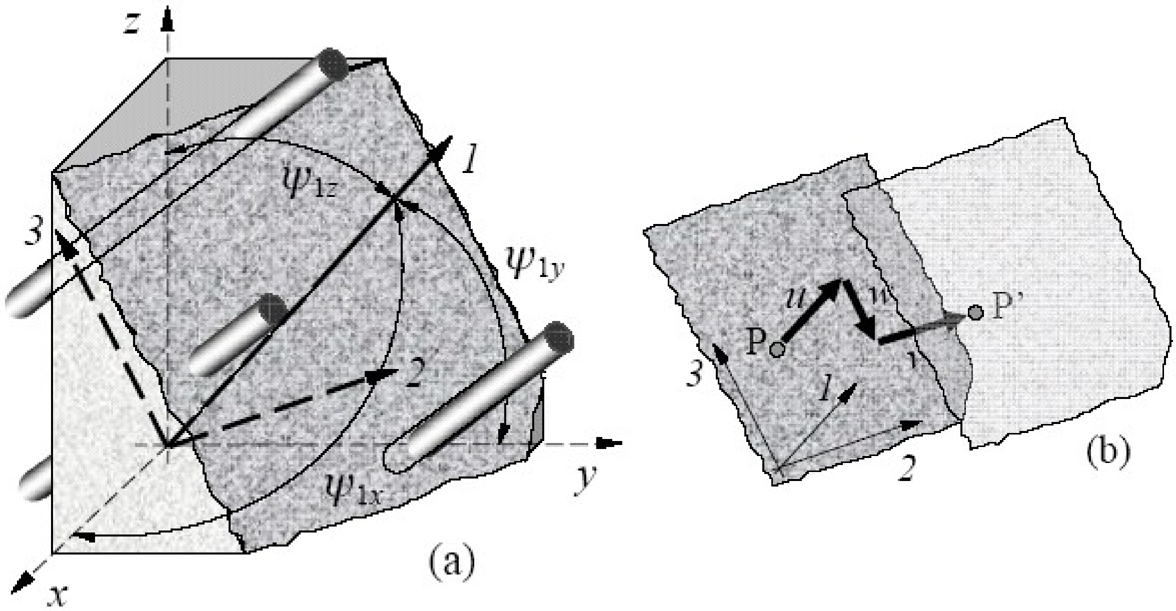

Figure 3.16 – Principal strain system (a) and crack displacement (b) definition.

Three different coordinate systems are used: the global system *x-y-z*, the local steel system *x'-y'-z'* and the local crack system *1-2-3* (Figure 3.16-a). The reinforcing bar position is fully defined by two angles, θ_{1i} and θ_{2i} in the system *x-y-z*, and α_{1i} and α_{2i} in the system *1-2-3*. In the crack system, *u* is the crack opening along the *1*-axis, *v* is the crack slip along the *2*-axis and *w* is the crack slip along the *3*-axis (Figure 3.16-b).
The equilibrium in the crack can be written as

$$\left\{\sigma^{xyz}\right\}=\left\{\sigma^{xyz}_{cr}\right\}=\left\{\sigma^{xyz}_{ccr}\right\}+\left\{\sigma^{xyz}_{scr}\right\}=\left(\left[D^{xyz}_{ccr}\right]+\left[D^{xyz}_{scr}\right]\right)\left\{\varepsilon^{xyz}_{cr}\right\}=\left[D^{xyz}_{cr}\right]\left\{\varepsilon^{xyz}_{cr}\right\}, \qquad (3.48)$$

where $\left[D^{xyz}_{cr}\right]$ is the stiffness matrix of the crack contributes, $\left[D^{xyz}_{ccr}\right]$ is the stiffness matrix of the concrete contributes in the crack and $\left[D^{xyz}_{scr}\right]$ is the stiffness matrix of the steel contributes in the crack.
The equilibrium of the RC between the cracks can be written as

$$\left\{\sigma^{xyz}\right\}=\left\{\sigma_c^{xyz}\right\}+\left\{\sigma_s^{xyz}\right\}=\left[D_c^{xyz}\right]\left\{\varepsilon_c^{xyz}\right\}+\left[D_s^{xyz}\right]\left\{\varepsilon_s^{xyz}\right\}. \tag{3.49}$$

From equation (3.48), the crack strain is obtained:

$$\left\{\varepsilon_{cr}^{xyz}\right\}=\left[D_{cr}^{xyz}\right]^{-1}\left\{\sigma^{xyz}\right\} \tag{3.50}$$

and from equation (3.49), the concrete strain is derived:

$$\left\{\varepsilon_c^{xyz}\right\}=\left[D_c^{xyz}\right]^{-1}\left(\left\{\sigma^{xyz}\right\}-\left[D_s^{xyz}\right]\left\{\varepsilon_s^{xyz}\right\}\right). \tag{3.51}$$

Imposing the strain in the steel between the cracks to be equal to the total strain, which is equal to the mean steel strain, it is possible to insert equations (3.50) and (3.51) in the compatibility equation (3.47). Afterwards, the total strain is obtained:

$$\left\{\varepsilon^{xyz}\right\}=\left([I]+\left[D_c^{xyz}\right]^{-1}\left[D_s^{xyz}\right]\right)^{-1}\left(\left[D_c^{xyz}\right]^{-1}+\left[D_{cr}^{xyz}\right]^{-1}\right)\left\{\sigma^{xyz}\right\}. \tag{3.52}$$

Therefore, the global material stiffness matrix is

$$\left[D^{xyz}\right]=\left(\left([I]+\left[D_c^{xyz}\right]^{-1}\left[D_s^{xyz}\right]\right)^{-1}\left(\left[D_c^{xyz}\right]^{-1}+\left[D_{cr}^{xyz}\right]^{-1}\right)\right)^{-1}, \tag{3.53}$$

where [I] is the identity matrix.
In the following pages, the contributes of each matrix are discussed in detail.

3.3.1 – Material between the cracks

The material between the cracks is considered uncracked. Therefore, the modeling techniques are assumed to be the same as already presented for the uncracked phase.
In order to consider the damage effect due to the crack, a penalty coefficient ξ is introduced as a function of the crack opening u. The coefficient is applied on the stress-strain curve peaks reducing the value of σ_{ic} and, consequently, of E_{ci}. No modification is inserted in the ε_{ic}.
The penalty coefficient is [7]

$$\xi=\frac{0.9}{\sqrt{1+400\varepsilon_1}}=\frac{0.9}{\sqrt{1+400\dfrac{u}{a_m}}}. \tag{3.54}$$

The effect of the coefficient on the compressive stress-strain curve is shown in Figure 3.17.

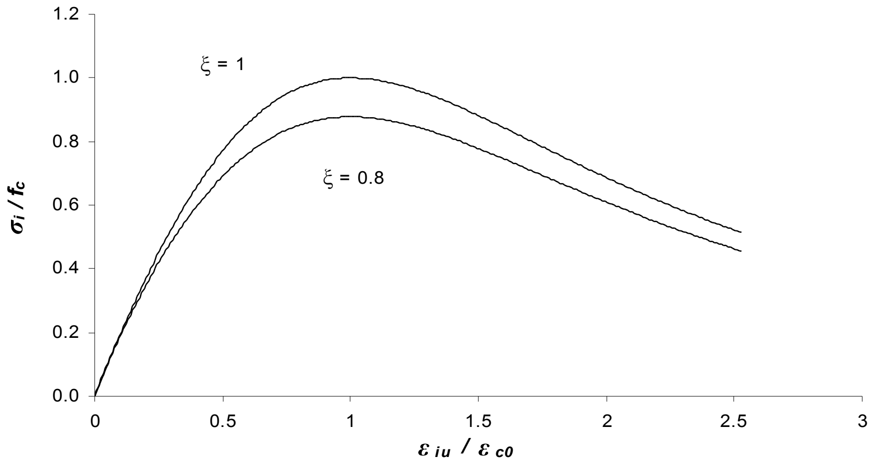

Figure 3.17 – Penalization effect on the compressive stress-strain curve.

3.3.2 – Material in the crack

The material in the crack is described in the local crack system *1-2-3*. Since after cracking this system is kept fixed, in general, it no longer coincides with the principal strain system. The crack contribute comes from the sum of concrete and steel effects.

Since the crack is not capable of transferring all the stress and strain components, the stress and strain fields in the crack system are defined as

$$\begin{aligned}&\left\{\sigma_{cr}^{123}\right\}=\left\{\sigma_1 \quad \tau_{12} \quad \tau_{13}\right\}^T\\&\left\{\varepsilon_{cr}^{123}\right\}=\left\{\varepsilon_1 \quad \gamma_{12} \quad \gamma_{13}\right\}^T=\left\{\frac{u}{a_m} \quad \frac{v}{a_m} \quad \frac{w}{a_m}\right\}^T\end{aligned} \tag{3.55}$$

In (3.55), the strain variables are written as a function of the crack displacements u, v and w. a_m is the crack spacing measured along the *1*-axis.

The stress-strain relation can be written assuming that the two materials behave in parallel:

$$\left\{\sigma_{cr}^{123}\right\}=\left[D_{cr}^{123}\right]\left\{\varepsilon_{cr}^{123}\right\}=\left(\left[D_{ccr}^{123}\right]+\left[D_{scr}^{123}\right]\right)\left\{\varepsilon_{cr}^{123}\right\}, \tag{3.56}$$

where

$$\left[D_{scr}^{123}\right]=\sum_{i=1}^{N_r}\left[D_{scri}^{123}\right], \tag{3.57}$$

being $\left[D_{scri}^{123}\right]$ the stiffness matrix of the i^{th} steel layer in the crack and N_r the total number of reinforcing layers.

The concrete matrix contains the contributes related to the aggregate bridging and interlock whereas the steel matrix contains the axial force, the tension stiffening and the dowel action contributes for each reinforcing layer.

3.3.3 – Crack spacing

The distance between the cracks is calculated according to Eurocode 2 [13]:

$$a_m = 50 + 0.25\, k_1\, k_2 \frac{\Phi_m}{\rho} \quad [\mathrm{mm}] \tag{3.58}$$

where Φ_m is the mean bar diameter and ρ is the ratio of the reinforcement area to the effective concrete area.

The coefficient k_1 depends on the bar type:

$$k_1 = \begin{cases} 0.8 & \text{for high-bond bars} \\ 1 & \text{for normal bars} \end{cases} \tag{3.59}$$

and k_2 depends on the shape of the strain diagram:

$$k_2 = \begin{cases} 0.5 & \text{for bending} \\ 1 & \text{for tension} \\ 0.5(\varepsilon_1 + \varepsilon_2)/\varepsilon_1 & \text{for tension with eccentricity} \end{cases} \tag{3.60}$$

The effective concrete area is the zone in which the effect of steel bars is not negligible and it can be estimated as a circle with diameter equal to 14 Φ centered in the bar.

In the proposed model the following values are used: k_1=0.8, k_2 =1 and ρ=1.

3.3.4 – Aggregate bridging and interlock contributes

The aggregate bridging, namely the normal stresses transferred between the crack lips (Figure 3.18), is modeled in the CEB Model Code 90 [12] by a bilateral law as a function of the crack opening (Figure 3.19).

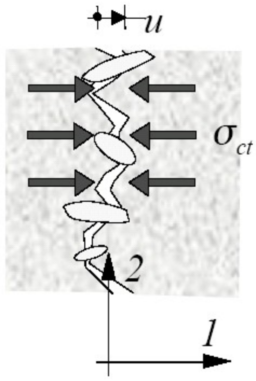

Figure 3.18 – Aggregate bridging modeling in the plane 1-2.

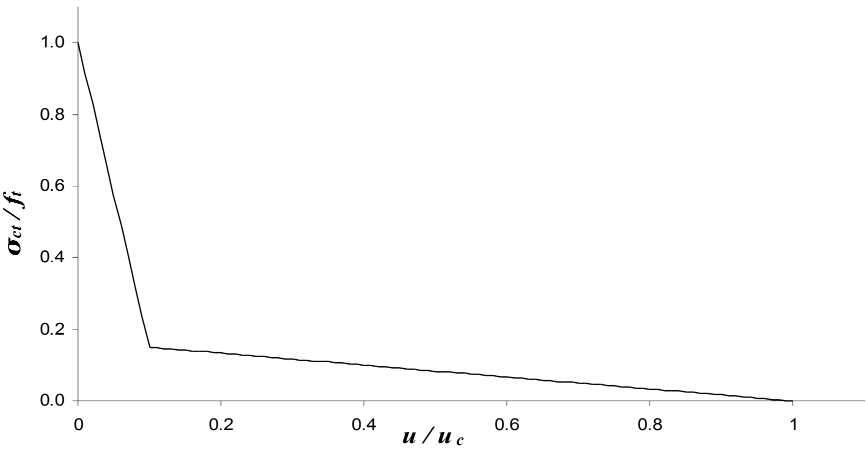

Figure 3.19 – CEB Model Code 90 σ-u law.

The analytical form of the law is

$$\sigma_{ct} = \begin{cases} f_t\left(1 - \dfrac{0.85u}{u_1}\right) & \text{when } 0 \le u \le u_1 \\ \dfrac{0.15 f_t}{u_1 - u_c}\left(u - u_c\right) & \text{when } u_1 \le u \le u_c \\ 0 & \text{when } u_c \le u \end{cases} \tag{3.61}$$

where

$$u_c = \alpha_F \frac{G_F}{f_t},\ u_1 = 2\frac{G_F}{f_t} - 0.15u_c,\ \alpha_F = 8,\ G_F = G_{F0}\left(\frac{f_c}{10}\right)^{0.7} \text{ and } G_{F0} = 0.025\frac{\text{Nmm}}{\text{mm}^2}, \tag{3.62}$$

being G_F the concrete fracture energy, u_1 the crack opening for σ_{ct}=0.15 f_t and u_c the crack opening for σ_{ct}=0.

Since in the numerical implementation a smooth curve is preferable, the following law [31] is adopted in 3D-PARC (Figure 3.20):

$$\sigma_{ct} = \frac{f_t}{1+\left(\frac{u}{u_0}\right)^p}, \tag{3.63}$$

where u_0 is the crack opening corresponding to σ_{ct}=0.5 f_t and p is a coefficient defining the curve shape. In this work, p=1 is used.

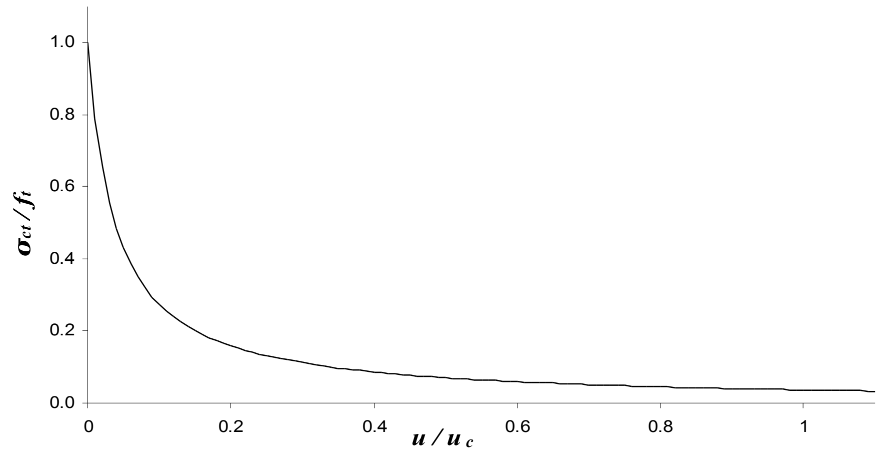

Figure 3.20 – Adopted σ-u law.

The value of u_0 is chosen according to the Model Code 90 law by imposing the same area under the curve, namely the fracture energy, in the range from u=0 to u=u_c.

Therefore, u_0 can be expressed as a function of u_1:

$$u_0 = 0.3771 u_1, \tag{3.64}$$

The stress due to the bridging effect is defined as

$$\sigma_1 = \sigma_{ct} = c_t \varepsilon_1 \tag{3.65}$$

and therefore, the bridging coefficient is

$$c_t = \frac{\sigma_{ct}}{\varepsilon_1} = \sigma_{ct}\frac{a_m}{u}\,. \tag{3.66}$$

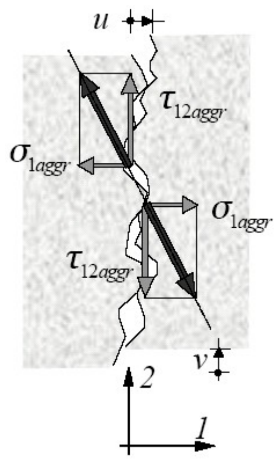

Figure 3.21 – Aggregate interlock modeling in the plane 1-2.

In 3D-PARC, the aggregate interlock, namely the shear tangential stresses transferred between the crack lips (Figure 3.21), is modeled according to Gambarova [23]. This approach was developed through theoretical studies and experimental comparisons for elements subjected to plane stresses. Nevertheless, in the proposed model, these results are also used in the 3D case due to the lack of appropriate investigations.
The stresses due to the aggregate interlock can be written as

$$\begin{aligned} \sigma_{1aggr} &= -c_{uv}a_m\gamma_{12} - c_{uw}a_m\gamma_{13} \\ \tau_{12aggr} &= c_v a_m \gamma_{12} \\ \tau_{13aggr} &= c_w a_m \gamma_{13} \end{aligned} \tag{3.67}$$

The four coefficients are defined as functions of the crack opening and the crack slips:

$$\begin{gathered} c_v = \tau^*\left(1-\sqrt{\frac{2u}{D_{\max}}}\right)\frac{a_3 + a_4\left|\dfrac{v}{u}\right|^3}{1+a_4\left(\dfrac{v}{u}\right)^4}\frac{a_m}{u} \text{ and } c_w = \tau^*\left(1-\sqrt{\frac{2u}{D_{\max}}}\right)\frac{a_3 + a_4\left|\dfrac{w}{u}\right|^3}{1+a_4\left(\dfrac{w}{u}\right)^4}\frac{a_m}{u}, \\ c_{uv} = \frac{a_1 a_2}{u^{2q}}\left(1+\left(\frac{v}{u}\right)^2\right)^{-q} c_v v \text{ and } c_{uw} = \frac{a_1 a_2}{u^{2q}}\left(1+\left(\frac{w}{u}\right)^2\right)^{-q} c_w w \end{gathered} \tag{3.68}$$

where

$$a_1 a_2 = 0.62,\ a_3 = \frac{2.45}{\tau^*},\ a_4 = 2.44\left(1 - \frac{4}{\tau^*}\right),\ \tau^* = 0.27 f_c \text{ and } q = 0.25, \tag{3.69}$$

being D_{max} the maximum aggregate size.

Finally, the concrete matrix in the crack system is obtained:

$$\left[D_{ccr}^{123}\right] = \begin{bmatrix} c_t & -c_{uv} & -c_{uw} \\ 0 & c_v & 0 \\ 0 & 0 & c_w \end{bmatrix}. \tag{3.70}$$

3.3.5 – Reinforcement and dowel action contributes

The steel matrix is computed in the local coordinate system *x'-y'-z'*. The bar length between two cracks can be calculated through the angles α_{1i} and α_{2i} as shown in Figure 3.22:

$$l_{si} = \frac{a_m}{\cos\alpha_{1i}\cos\alpha_{2i}}. \tag{3.71}$$

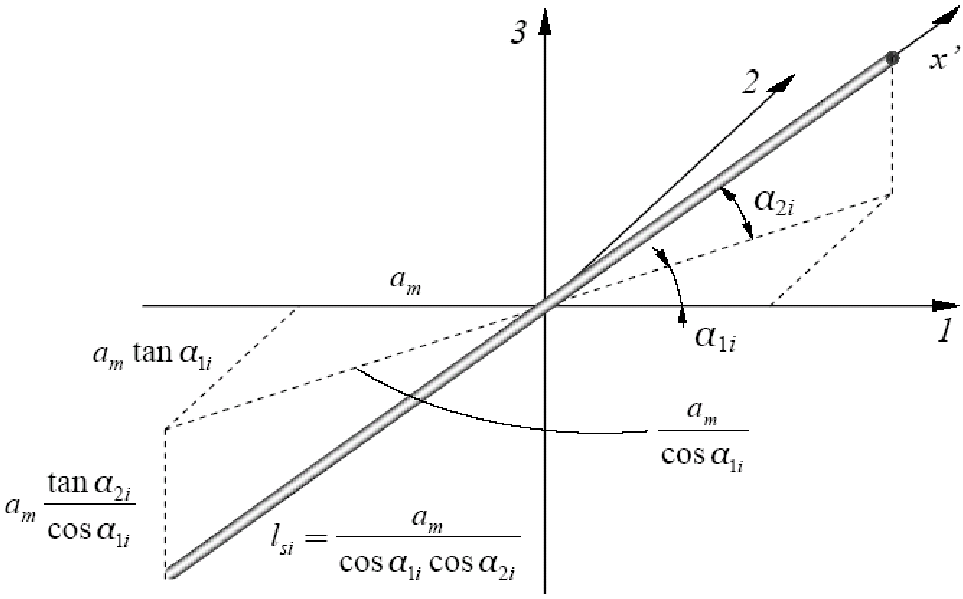

Figure 3.22 – Bar length between two cracks.

The stress and strain fields in the steel system are defined as

$$\begin{aligned} \left\{\sigma_{cr}^{x'y'z'}\right\} &= \left\{\sigma_{x'} \quad \tau_{x'y'} \quad \tau_{x'z'}\right\}^T \\ \left\{\varepsilon_{cr}^{x'y'z'}\right\} &= \left\{\varepsilon_{x'} \quad \gamma_{x'y'} \quad \gamma_{x'z'}\right\}^T = \left\{\frac{\delta}{l_s} \quad \frac{\eta_1}{l_s} \quad \frac{\eta_2}{l_s}\right\}^T \end{aligned} \tag{3.72}$$

In equation (3.72), the strain variables are written as functions of the crack displacements in the steel system x'-y'-z'. In particular, δ is the displacement along the x'-axis, η_1 along the y'-axis and η_2 along the z'-axis.
The steel forces due to the axial stiffness of the bar and to the dowel action are modeled in the steel system (Figure 3.23-a) and then smeared obtaining the corresponding stresses (Figure 3.23-b).
The axial contribute of the i^{th} steel layer is computed as

$$\sigma_{x'} = \sigma_{scri} = \frac{N_{scri}}{p_{1i}p_{2i}} = \frac{A_{si}}{p_{1i}p_{2i}} E_{scri}\varepsilon_{scri} = \rho_i E_{scri} g_i \frac{\delta}{l_s} = \rho_i E_{scri} g_i \varepsilon_{x'}, \tag{3.73}$$

where N_{scri} is the steel axial force in the crack.
The tension stiffening coefficient g_i is defined as the ratio:

$$g_i = \frac{\varepsilon_{scri}}{\dfrac{\delta}{l_{si}}}, \tag{3.74}$$

where ε_{scri} is the steel strain in the crack.
The tension stiffening formulation is discussed in detail in the next section.

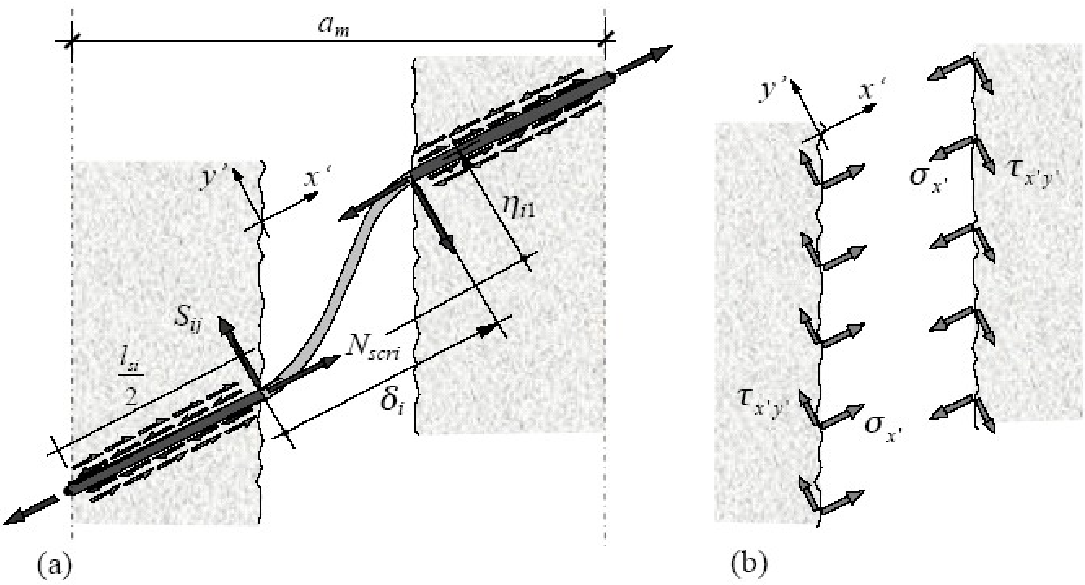

Figure 3.23 – Steel contributes modeling in the crack, in the plane x'-y'.

The dowel action contribute is modeled according to Walraven and Reinhardt [46]. In the following equations, the index i indicates the i^{th} steel layer while the index $j=1,2$ indicates the direction of the tangential stresses.

For the i^{th} steel layer, the dowel force orthogonal to the bars is smeared along the interaxes and the related stresses are obtained:

$$\tau_{x'y'} = \tau_{i1} = \frac{S_{i1}}{p_{1i} p_{2i}} \text{ and } \tau_{x'z'} = \tau_{i2} = \frac{S_{i2}}{p_{1i} p_{2i}} . \tag{3.75}$$

The force S_{ij} is calculated as a function of the crack displacements δ_i, η_{i1} and η_{i2}:

$$S_{ij} = 10.73 f_c^{0.38} \Phi_i^{1.75} \frac{1}{(\delta_i + 0.2)} \eta_{ij}^{0.36} . \tag{3.76}$$

Substituting (3.76) into (3.75), after some mathematical passages, the tangential stresses are obtained:

$$\tau_{ij} = 13.66 f_c^{0.38} \Phi_i^{-0.25} \rho_i \frac{l_{si}}{(\delta_i + 0.2)\eta_{ij}^{0.64}} \frac{\eta_{ij}}{l_{si}} = \rho_i d_{ij} \gamma_{ij} , \tag{3.77}$$

where

$$d_{ij} = 13.66 f_c^{0.38} \Phi_i^{-0.25} \frac{l_{si}}{(\delta_i + 0.2)\eta_{ij}^{0.64}} . \tag{3.78}$$

Finally, the stiffness matrix for the i^{th} layer in the steel system is

$$\left[D_{scri}^{x'y'z'}\right] = \rho_i \begin{bmatrix} g_i E_{scri} & 0 & 0 \\ & d_{i1} & 0 \\ symm. & & d_{i2} \end{bmatrix} . \tag{3.79}$$

Afterwards, all the matrices $\left[D_{scri}^{x'y'z'}\right]$ are transferred to the crack system and summed to obtain the matrix $\left[D_{scr}^{123}\right]$ according to (3.57). Subsequently, the steel contribute is added to the concrete one to obtain the crack matrix according to (3.56).

3.3.6 – Tension stiffening

The tension stiffening is implemented in 3D-PARC by following a numerical approach. The stiffening contribute provided by the concrete between two cracks is taken into account by increasing the value of the mean steel strain.

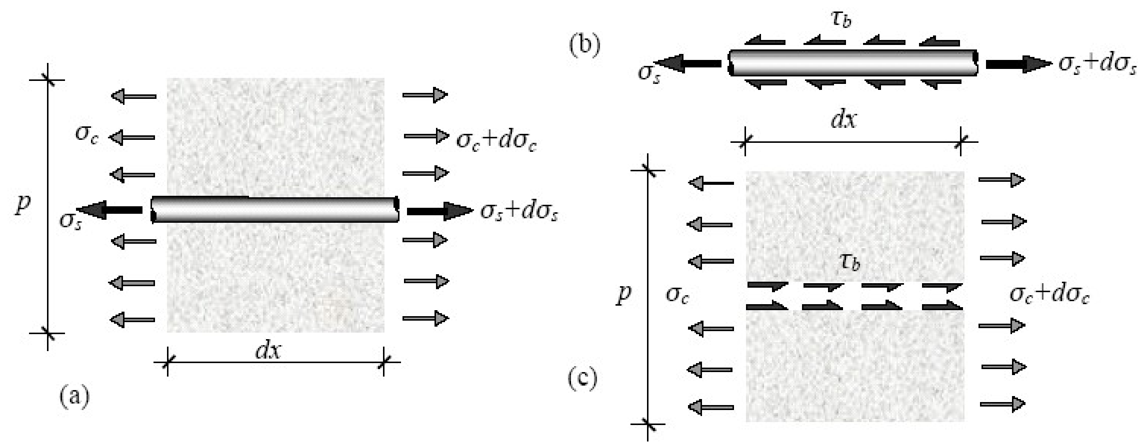

Figure 3.24 – Equilibrium conditions of a RC portion (a), of a steel bar (b) and of concrete (c).

The equilibrium equations governing the problem are:

- section equilibrium (Figure 3.24-a):

$$\frac{d\sigma_c}{dx}+\rho\frac{d\sigma_s}{dx}=0; \tag{3.80}$$

- steel bar equilibrium (Figure 3.24-b):

$$\frac{d\sigma_s}{dx}=\frac{4}{\Phi}\tau\left(s\left(x\right)\right); \tag{3.81}$$

- concrete equilibrium (Figure 3.24-c):

$$\frac{d\sigma_c}{dx}=-\rho\frac{4}{\Phi}\tau\left(s\left(x\right)\right). \tag{3.82}$$

The compatibility equation is

$$s=u_s-u_c, \tag{3.83}$$

where s is the slip and u_s and u_c are the steel and concrete displacement respectively. After the differentiation, the (3.83) becomes

$$\frac{ds}{dx}=\varepsilon_s-\varepsilon_c. \tag{3.84}$$

Combining the previous equations, the solving equation is obtained:

$$\frac{d^2 s(x)}{dx^2} = \frac{4}{\Phi E_s}\left(1 + \frac{E_s}{E_c}\rho\right)\tau\left(s(x)\right). \tag{3.85}$$

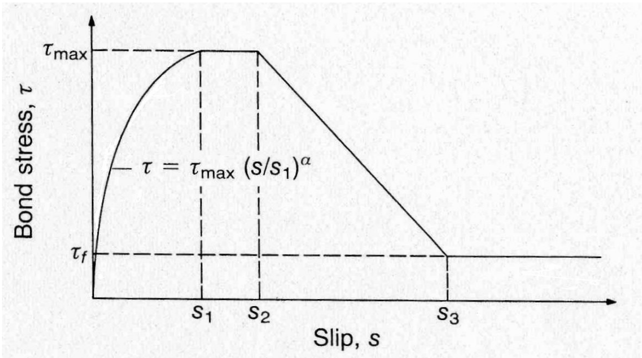

Figure 3.25 – CEB Model Code 90 bond-slip law.

The bond-slip law is taken from the CEB Model Code 90 [12] and is shown in Figure 3.25:

$$\tau = \begin{cases} \tau_{max}\left(\dfrac{s}{s_1}\right)^{\alpha} & \text{when } 0 \le s \le s_1 \\ \tau_{max} & \text{when } s_1 \le s \le s_2 \\ \tau_{max} - \left(\tau_{max} - \tau_f\right)\dfrac{s - s_2}{s_3 - s_2} & \text{when } s_2 \le s \le s_3 \\ \tau_f & \text{when } s_3 \le s \end{cases} \tag{3.86}$$

The parameters depend on bond conditions and confinement as reported in Table 3.2.

Parameter	***Unconfined concrete[(1)]***		***Confined concrete[(2)]***	
	Good bond conditions	***All other bond conditions***	***Good bond conditions***	***All other bond conditions***
s_1 *[mm]*	*0.6*	*0.6*	*1.0*	*1.0*
s_2 *[mm]*	*0.6*	*0.6*	*3.0*	*3.0*
s_3 *[mm]*	*1.0*	*2.5*	*Clear rib spacing*	*Clear rib spacing*
α	*0.4*	*0.4*	*0.4*	*0.4*
τ_{max} *[MPa]*	$2.0\sqrt{f_c}$	$1.0\sqrt{f_c}$	$2.5\sqrt{f_c}$	$1.25\sqrt{f_c}$
τ_f *[MPa]*	$0.15\,\tau_{max}$	$0.15\,\tau_{max}$	$0.40\,\tau_{max}$	$0.40\,\tau_{max}$

Table 3.2 – Bond-slip law parameters.

[(1)] Failure by splitting of the concrete. [(2)] Failure by shearing of the concrete between the ribs.

In 3D-PARC, the problem is solved in a numerical way by using the Finite Difference Method (FDM). Following this approach, the solution is calculated in a finite number of points and the accuracy can be improved by increasing the number of points (Figure 3.26).

First of all, a set of points, usually equi-spaced, is chosen. The x-axis is intended to be the steel bar axis having its origin in the middle point between the cracks and the point $x=l_s/2$ coinciding with the middle of the crack. The derivatives of the solving function in the i^{th} point are written by using the values of the function in the same point and in some other points next to it. In particular, the second derivative of $s(x)$ in the i^{th} point can be written as

$$\frac{d^2 s(x)}{dx^2} = \frac{s_{i-1} - 2s_i + s_{i+1}}{\Delta x^2}. \tag{3.87}$$

The equation (3.85) written in the i^{th} point is

$$s_{i-1} - 2s_i + s_{i+1} = k\Delta x^2 \tau_i, \tag{3.88}$$

where

$$k = \frac{4}{\Phi E_s}\left(1 + \frac{E_s}{E_c}\rho\right). \tag{3.89}$$

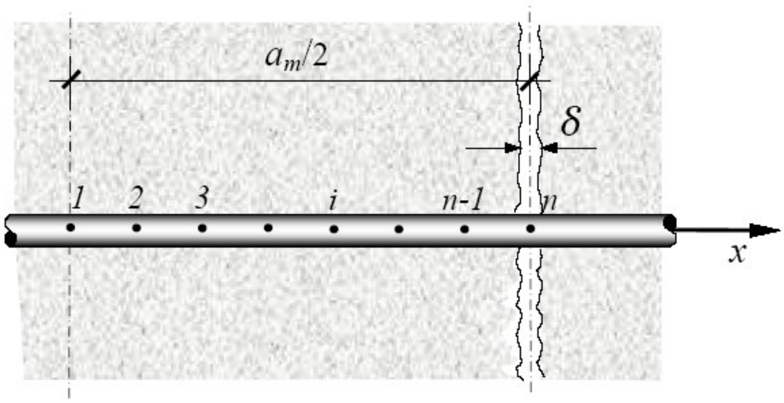

Figure 3.26 – FDM discretization.

By using the boundary conditions $s(0)=0$ and $s(l_s/2)=\delta/2$, the following solving system is obtained:

$$\begin{bmatrix} 1 & 0 & 0 & \dots & 0 \\ 1 & -2 & 1 & \dots & 0 \\ & & \dots & & \\ 0 & \dots & 1 & -2 & 1 \\ 0 & \dots & 0 & 0 & 1 \end{bmatrix} \begin{Bmatrix} s_1 \\ s_2 \\ \dots \\ s_{n-1} \\ s_n \end{Bmatrix} = \begin{Bmatrix} 0 \\ k\Delta x^2 \tau_2 \\ \dots \\ k\Delta x^2 \tau_{n-1} \\ \delta/2 \end{Bmatrix}. \tag{3.90}$$

Since the tangential stress in a point is a function of the slip in that point, an iterative procedure is required. The convergence rate is quite fast.

After computing the $s(x)$, all the other unknown functions can be calculated in a similar manner. By applying the FDM approximation, the (3.82) can be written as

$$\sigma_{c,\,i} - \sigma_{c,\,i+1} = \rho \frac{4}{\Phi} \Delta x \tau_i \,. \tag{3.91}$$

By using the approximated boundary conditions $\sigma(l_s/2)=\sigma_{ct}$, the following solving system is obtained:

$$\begin{bmatrix} 1 & -1 & 0 & \dots & 0 \\ 0 & 1 & -1 & \dots & 0 \\ & & \dots & & \\ 0 & \dots & 0 & 1 & -1 \\ 0 & \dots & 0 & 0 & 1 \end{bmatrix} \begin{Bmatrix} \sigma_{c,1} \\ \sigma_{c,2} \\ \dots \\ \sigma_{c,n-1} \\ \sigma_{c,n} \end{Bmatrix} = \begin{Bmatrix} \rho \frac{4}{\Phi} \Delta x \tau_1 \\ \rho \frac{4}{\Phi} \Delta x \tau_2 \\ \dots \\ \rho \frac{4}{\Phi} \Delta x \tau_{n-1} \\ \sigma_{ct} \end{Bmatrix}. \tag{3.92}$$

Subsequently, the concrete strain is computed by the tensile field of the concrete constitutive law. Since the proposed model adopts a linear elastic curve, the concrete strain is expressed as

$$\varepsilon_{c,\,i} = \frac{\sigma_{c,i}}{E_{c0}} \,. \tag{3.93}$$

Finally, the equation (3.84) provides the steel strain in the bar. The FDM gives

$$\varepsilon_{s,\,i} = \varepsilon_{c,\,i} + \frac{1}{2\Delta x}\left(s_{i+1} - s_{i-1}\right). \tag{3.94}$$

By imposing the symmetry in x=0 and x=l_s/2, the solving system is

$$\begin{Bmatrix} \varepsilon_{s,1} \\ \varepsilon_{s,2} \\ \dots \\ \varepsilon_{s,n-1} \\ \varepsilon_{s,n} \end{Bmatrix} = \begin{Bmatrix} \varepsilon_{c,1} \\ \varepsilon_{c,2} \\ \dots \\ \varepsilon_{c,n-1} \\ \varepsilon_{c,n} \end{Bmatrix} + \frac{1}{2\Delta x} \begin{bmatrix} 0 & 2 & 0 & \dots & 0 \\ -1 & 0 & 1 & \dots & 0 \\ & & \dots & & \\ 0 & \dots & -1 & 0 & 1 \\ 0 & \dots & 0 & -2 & 0 \end{bmatrix} \begin{Bmatrix} s_1 \\ s_2 \\ \dots \\ s_{n-1} \\ s_n \end{Bmatrix}. \tag{3.95}$$

The steel strain distribution along the bar is now defined. Afterwards, the mean steel strain from the tension stiffening formulation is compared with the global mean steel strain computed as the global strain in the bar direction. The tension stiffening distribution is corrected to assure the mean strain equality:

$$\varepsilon_{s,mean}^{global} = \varepsilon_{s,mean}^{ts} + \Delta\varepsilon_s \,. \tag{3.96}$$

The mean value of the tension stiffening strain distribution is computed by

$$\varepsilon_{s,mean}^{ts} = \frac{1}{n-1}\left(\frac{\varepsilon_{s,1}}{2} + \sum_{i=2}^{n-1} \varepsilon_{s,i} + \frac{\varepsilon_{s,n}}{2} \right). \tag{3.97}$$

After these procedures, the steel strain along the bar is obtained (Figure 3.27). $\varepsilon_{s,n}=\varepsilon_{scri}$ is the steel strain of the i^{th} reinforcing layer in the crack. Therefore, the tension stiffening coefficient g_i is computed according to (3.74).

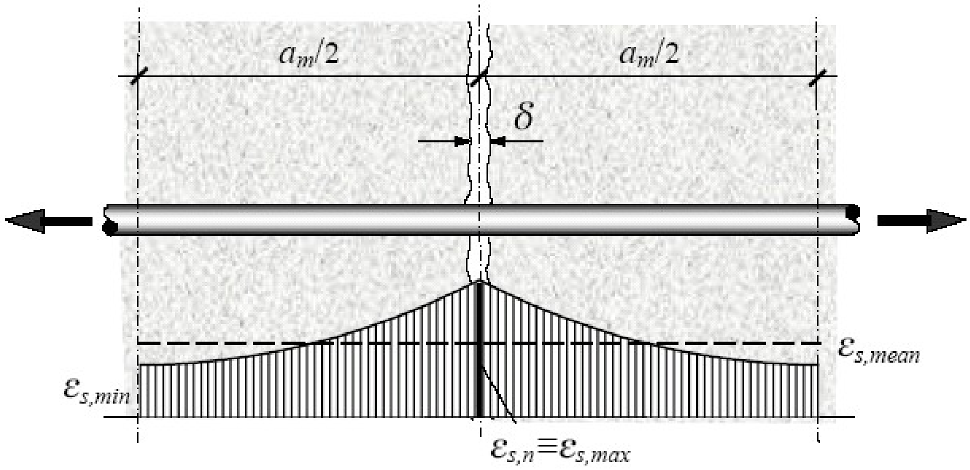

Figure 3.27 – Steel strain distribution.

3.4 – DOUBLY CRACKED MATERIAL

After the first crack formation, the material between the cracks still works as an uncracked material. The principal strain directions are recomputed independently on the first crack orientation. Due to the modular framework of the model, when a new crack arises in the principal strain system, its effect can be easily inserted.

After the second cracking, the strain is decomposed into three contributes, the first related to the concrete between the cracks and the others related to the cracks:

$$\left\{\varepsilon^{xyz}\right\}=\left\{\varepsilon_{c}^{xyz}\right\}+\left\{\varepsilon_{cr1}^{xyz}\right\}+\left\{\varepsilon_{cr2}^{xyz}\right\}. \tag{3.98}$$

As previously explained for the singly cracked material, the starting point is the equilibrium. The equilibrium in the first crack can be written as

$$\left\{\sigma^{xyz}\right\}=\left\{\sigma_{cr1}^{xyz}\right\}=\left\{\sigma_{ccr1}^{xyz}\right\}+\left\{\sigma_{scr1}^{xyz}\right\}=\left(\left[D_{ccr1}^{xyz}\right]+\left[D_{scr1}^{xyz}\right]\right)\left\{\varepsilon_{cr1}^{xyz}\right\}=\left[D_{cr1}^{xyz}\right]\left\{\varepsilon_{cr1}^{xyz}\right\}, \tag{3.99}$$

where $\left[D_{cr1}^{xyz}\right]$ is the stiffness matrix of the first crack contributes, $\left[D_{ccr1}^{xyz}\right]$ is the stiffness matrix of the concrete contributes in the first crack and $\left[D_{scr1}^{xyz}\right]$ is the stiffness matrix of the steel contributes in the first crack.

In the same way, the equilibrium in the second crack can be written as

$$\left\{\sigma^{xyz}\right\}=\left\{\sigma_{cr2}^{xyz}\right\}=\left\{\sigma_{ccr2}^{xyz}\right\}+\left\{\sigma_{scr2}^{xyz}\right\}=\left(\left[D_{ccr2}^{xyz}\right]+\left[D_{scr2}^{xyz}\right]\right)\left\{\varepsilon_{cr2}^{xyz}\right\}=\left[D_{cr2}^{xyz}\right]\left\{\varepsilon_{cr2}^{xyz}\right\}. \tag{3.100}$$

The equilibrium between the cracks can be written as

$$\left\{\sigma^{xyz}\right\}=\left\{\sigma_{c}^{xyz}\right\}+\left\{\sigma_{s}^{xyz}\right\}=\left[D_{c}^{xyz}\right]\left\{\varepsilon_{c}^{xyz}\right\}+\left[D_{s}^{xyz}\right]\left\{\varepsilon_{s}^{xyz}\right\}. \tag{3.101}$$

From equations (3.99) and (3.100), the crack strains are obtained:

$$\left\{\varepsilon_{cr1}^{xyz}\right\}=\left[D_{cr1}^{xyz}\right]^{-1}\left\{\sigma^{xyz}\right\} \text{ and } \left\{\varepsilon_{cr2}^{xyz}\right\}=\left[D_{cr2}^{xyz}\right]^{-1}\left\{\sigma^{xyz}\right\} \tag{3.102}$$

and from equation (3.101), the concrete strain is derived:

$$\left\{\varepsilon_c^{xyz}\right\}=\left[D_c^{xyz}\right]^{-1}\left(\left\{\sigma^{xyz}\right\}-\left[D_s^{xyz}\right]\left\{\varepsilon_s^{xyz}\right\}\right). \tag{3.103}$$

Imposing the strain in the steel between the cracks to be equal to the total strain, which is equal to the mean steel strain, it is possible to insert equations (3.102) and (3.103) in the compatibility equation (3.98). Afterwards, the total strain is obtained:

$$\left\{\varepsilon^{xyz}\right\}=\left([I]+\left[D_c^{xyz}\right]^{-1}\left[D_s^{xyz}\right]\right)^{-1}\left(\left[D_c^{xyz}\right]^{-1}+\left[D_{cr1}^{xyz}\right]^{-1}+\left[D_{cr2}^{xyz}\right]^{-1}\right)\left\{\sigma^{xyz}\right\}. \tag{3.104}$$

Therefore, the global material stiffness matrix is

$$\left[D^{xyz}\right]=\left(\left([I]+\left[D_c^{xyz}\right]^{-1}\left[D_s^{xyz}\right]\right)^{-1}\left(\left[D_c^{xyz}\right]^{-1}+\left[D_{cr1}^{xyz}\right]^{-1}+\left[D_{cr2}^{xyz}\right]^{-1}\right)\right)^{-1}, \tag{3.105}$$

where $[I]$ is the identity matrix.

The multi-cracking procedure is realized by simply adding the flexibility of the subsequent crack. With analogous procedures, it is possible to insert any number of subsequent cracks even if the first ones remain the most important since they characterize the structural behavior.

CHAPTER 4 – APPLICATIONS

4.1 – INTRODUCTION

Since the beginning, the proposed model 3D-PARC – Three-Dimensional Physical Approach for Reinforced Concrete, was formulated in order to be implemented from the computational point of view. The first version of the model, developed in the author's graduate thesis, was implemented in the code TRE [34], a FORTRAN code able to evaluate the behavior of a material portion. Therefore, only very simple structures subjected to uniform stress states can be analyzed with TRE.

Subsequently, in order to provide the model with more flexibility, the work was focused on the Finite Element (FE) implementation. The commercial FE code ABAQUS [1] allows the user to design his own material constitutive model by using an UMAT (User MATerial) FORTRAN subroutine. In this way, the model 3D-PARC is implemented in the FE framework allowing the analysis of more complex structures.

The leading philosophy does not change since the single material point analyzed by TRE becomes the integration point analyzed by 3D-PARC. To verify the model and its numerical implementation, comparisons with literature experimental results are carried out.

The following chapter describes, at first, the main solving procedures used in FE codes for non-linear problems, the ABAQUS solving techniques and the role of 3D-PARC within it. Secondly, the applications of 3D-PARC to some significant, well documented, experimental cases are presented.

4.2 – NON-LINEAR PROBLEM SOLVING PROCEDURES

Reinforced Concrete (RC) structures exhibit a complex behavior due to the highly non-linear response of both uncracked and cracked material. The structural equation system can be written as

$$[K]\{u\}=\{F\}, \tag{4.1}$$

where $[K]$ is the stiffness matrix, $\{u\}$ is the displacement vector and $\{F\}$ is the external force vector. The numerical problem is faced by using iterative and incremental solving techniques. This means that the external actions are not fully applied but are divided in a suitable number of increments. For each increment, the problem is linearized and solved with an iterative process until a convergence criterion is satisfied. For each iteration, a linear problem is solved and a new structural configuration is found.

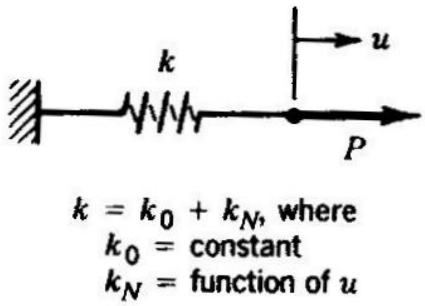

Figure 4.1 – Uniaxial example problem.

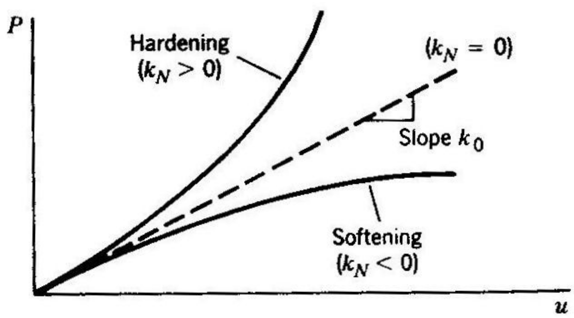

Figure 4.2 – Hardening and softening behavior.

In the following section, some solving techniques are presented in the simple one-degree of freedom case shown in Figure 4.1. The same concepts can be applied to any multi-degree of freedom case [19]. A non-linear, softening spring is defined. The spring stiffness is a function of the displacement u and an external load P is applied (Figure 4.2). In this study, the option of softening behavior is chosen as it is the most common for RC structures.

4.2.1 – Secant method

Starting from the origin, the load P_A is applied and the corresponding configuration u_A is searched (Figure 4.3). With the initial stiffness k_0, the point a, related to the load P_A and to the configuration u_1, is found. Starting from the new configuration u_1, the load P_1 is computed by using the constitutive model of the structure. Being the load P_1 rather far from P_A, a new stiffness $k_0 + k_{N1}$ is computed with u_1, and the procedure is repeated from the beginning. The new stiffness provides the point b and the new configuration u_2 as a new starting point. The convergence is achieved when the difference P_A-P_i differs from zero by a tolerance set by the user.

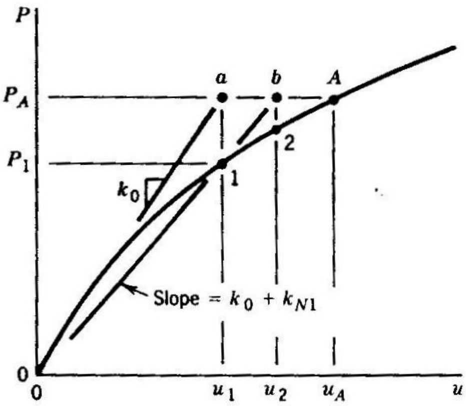

Figure 4.3 – Secant technique.

4.2.2 – Newton-Raphson method

Starting from the load P_A related to the configuration u_A, the load is incremented up to P_B and the configuration u_B is searched (Figure 4.4). The tangent stiffness is calculated in u_A (graphically it is the line tangent to the curve in the point A) and the configuration u_1, related to the load P_B, is found. With u_1, the load P_1 is computed: P_1 is the part of the load equilibrated by the structure in the configuration u_1, whereas the load P_B-P_1 is the part of the load which is not equilibrated. Starting from u_1, the new tangent stiffness is computed in the point 1 and then the procedure is repeated. The convergence is achieved when the unbalanced load P_B-P_i differs from zero by a tolerance set by the user. The convergence rate is quadratic but the tangent stiffness needs to be calculated for each iteration.

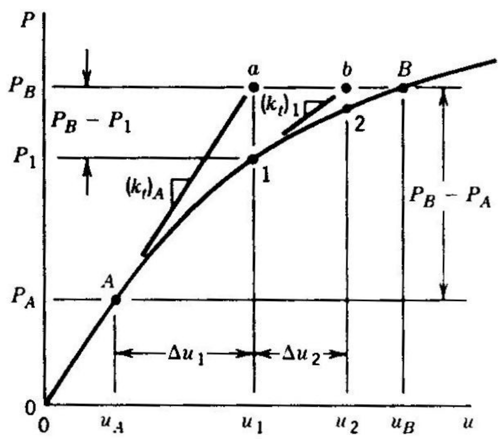

Figure 4.4 – Newton-Raphson technique.

4.2.3 – Modified Newton-Raphson method

This method differs from the previous one because the tangent stiffness is not updated for each iteration but remains constant during the whole increment or, alternatively, it is updated only from time to time during the increment (Figure 4.5). In this way, the computational cost is strongly reduced. In fact, the calculation of the tangent stiffness for each iteration can be a big numerical effort. The convergence rate depends on the updating frequency, but obviously it decreases with respect to the Newton-Raphson method.

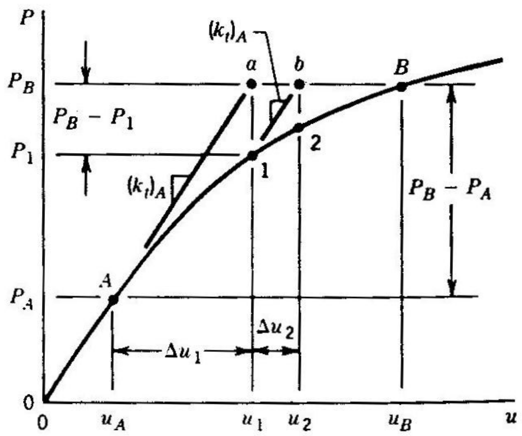

Figure 4.5 – Modified Newton-Raphson technique.

4.2.4 – Quasi-Newton method

This method implements the first two iterations with the Newton-Raphson approach using the initial tangent (Figure 4.6). In this way, the points 1 and 2 on the curve are found. Subsequently, starting from these two points, the secant stiffness (line passing by 1 and 2) is evaluated. From that point onward, the same secant stiffness is used. The convergence rate is superlinear.

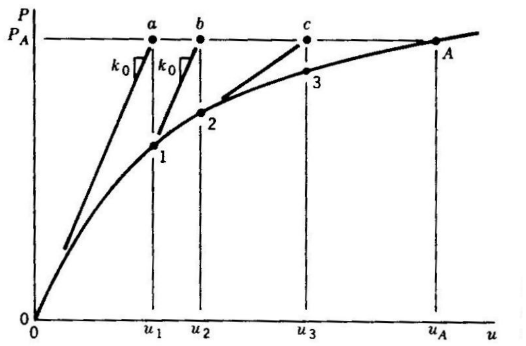

Figure 4.6 – Quasi-Newton technique.

4.2.5 – Initial stiffness method

Using the above mentioned methods, numerical problems can arise in particular situations. In the Newton-Raphson method, despite a very fast convergence rate, problems can occur near the material curve peaks when the tangent is close to zero. The secant formulation, on the contrary, has a slower convergence rate but in general, it is more stable from the numerical point of view. Nevertheless, problems can be found in the post-cracking phase when some elements of the stiffness matrix can be zero.

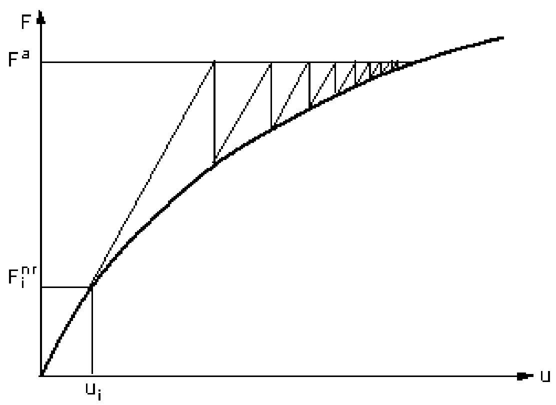

Figure 4.7 – Initial stiffness technique.

In order to avoid these numerical problems, a different approach can be implemented. In the FE formulation, for each integration point, the stress vector for the internal force calculation, and the Jacobian matrix for the stiffness computation are required. In other words, the Jacobian matrix determines only the slope which is used to approach the solution. Therefore,

the Jacobian matrix can be considered only a numerical tool which can be defined by the user. For softening structures, however, it should be always stiffer than the one related to the current structural configuration, otherwise the equilibrium point could be unattainable.
In the initial stiffness method, the Jacobian matrix, computed at the beginning of the analysis, is maintained during the whole calculation (Figure 4.7). In this case, the Jacobian matrix is the linear elastic matrix.
Obviously, due to the fact that the matrix is stiffer than the secant, the computational time is highly increased since much more iterations are necessary to achieve the convergence. Therefore, this numerical tool should be used carefully and only when the other methods are unsuitable.

4.3 – NUMERICAL PROCEDURES IN ABAQUS

4.3.1 – Non-linear problems in ABAQUS

The final aim of non-linear analyses is to evaluate a realistic response, up to failure, of structures under generic loads, taking into account the physical reality of the material constitutive laws and of the geometric characteristics (Figure 4.8).

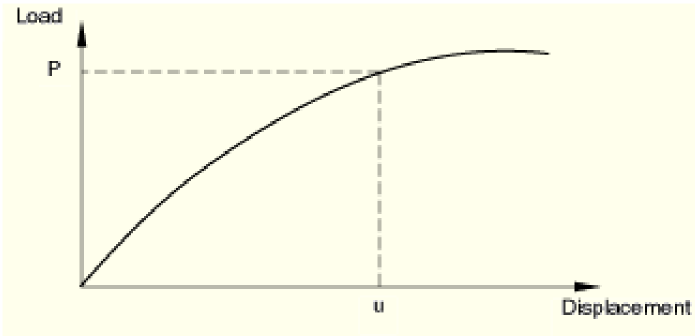

Figure 4.8 – Non-linear response example.

Since the problem is non-linear, an incremental and iterative procedure is required [1]. “Incremental” means that the external load is divided into small parts gradually added one by one and the equilibrium configuration is searched for each increment. “Iterative” means that several iterations are usually required to find the solution. The non-linear problem is solved as a repeated linear problem.

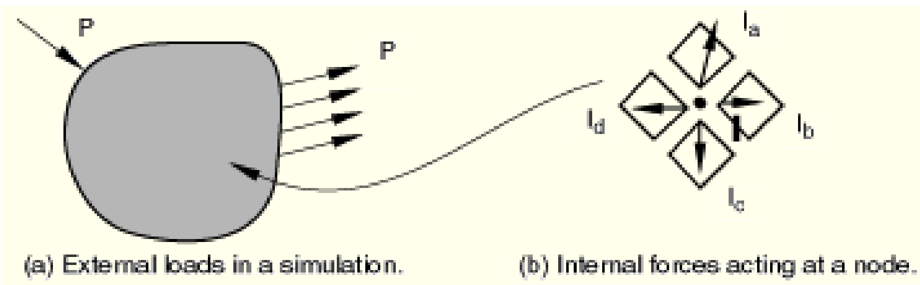

Figure 4.9 – External and internal forces.

The simulation time history consists of steps. In each step, different loads, boundary conditions and solving procedures can be defined. Each step is divided into increments in order to follow the non-linear response. The size of the increment can be fixed as well as automatically determined. At the end of each increment the structure is in approximate equilibrium. An iteration is an attempt at finding an equilibrium solution within an increment.

If the convergence criteria are not satisfied, another increment is required.
Figure 4.9 shows the external and internal forces acting on a body. The internal forces at a node are caused by the stresses in the elements connected to the node. The equilibrium is satisfied when external forces *P* and internal forces *I* balance each other at every node:

$$P - I = 0\,. \tag{4.2}$$

Starting from the configuration u_0, a load increment ΔP is applied. In the first iteration, the structure stiffness matrix K_0, related to the configuration u_0, and the increment ΔP are used to compute a displacement correction c_a. The structure configuration is updated to u_a by using c_a (Figure 4.10).

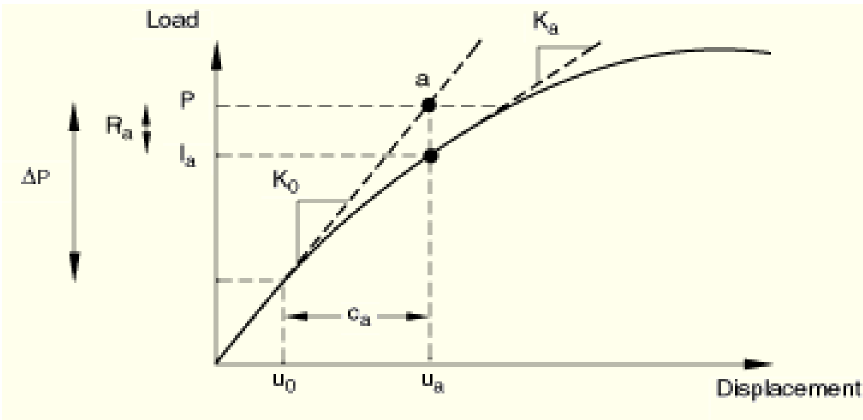

Figure 4.10 – First iteration.

Then, ABAQUS computes the internal forces I_a in this new configuration and subsequently, the force residue for the iteration, which is the difference between the external and the internal forces:

$$R_a = P - I_a\,. \tag{4.3}$$

If R_a is zero for every degree of freedom and for every node in the model, the point *a* is an equilibrium point laying on the curve. Since the problem is non-linear, the residue is never zero but it is compared with a tolerance value. Therefore, if the residue is lower than a specified value, the equilibrium is considered achieved and the point is accepted as an equilibrium point.
However, ABAQUS performs a convergence check also on the displacement correction c_a which should be small compared to the total displacement increment

$$\Delta u_a = u_a - u_0 \,. \tag{4.4}$$

Both the convergence criteria must be satisfied to consider the equilibrium achieved. The tolerance values can be specified by the user.

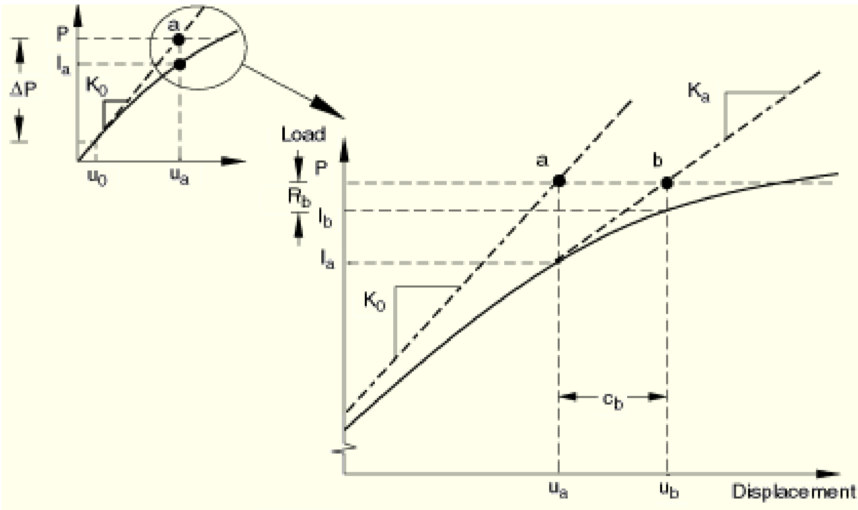

Figure 4.11 – Second iteration.

On the contrary, if the convergence is not attained, another iteration is carried out in order to reduce the residue (Figure 4.11). Starting from the current structure configuration u_a, the stiffness K_a is assembled. Afterwards, by using K_a and the residue R_a, a new displacement correction c_b is computed determining the new point b which is closer to the equilibrium point. A new residue is calculated by using the internal force I_b related to the configuration u_b:

$$R_b = P - I_b \,. \tag{4.5}$$

Then, a new convergence check is performed on the residue R_b and on the displacement correction

$$\Delta u_b = u_b - u_0 \,. \tag{4.6}$$

If necessary, a further iteration is performed with the same procedure.

It can be concluded that for every increment a global system of equations is assembled and solved. Therefore, the computational cost of each iteration is close to the cost of a complete linear analysis. For this reason, the computational expense of a non-linear analysis is potentially many times greater than the cost of a linear analysis.

4.3.2 – The code 3D-PARC in the Finite Element framework

The FE code ABAQUS allows the user to define a constitutive model by inserting a FORTRAN subroutine called UMAT (User MATerial) describing the integration point behavior.

The variables passed in are the material properties and the variables corresponding to the current state of the structure. The output variables are the stresses, used to compute the internal forces, and the Jacobian matrix, used to calculate the element stiffness matrix.

3D-PARC requires the following input material properties for concrete: the uniaxial tensile strength f_t, the uniaxial compressive strength f_c, the strain ε_{cp} corresponding to f_c in the uniaxial stress-strain curve, the initial elastic modulus E_{c0} and the initial Poisson coefficient ν_0. For each steel layer, the following properties are required: the elastic modulus E_{s0}, the plastic modulus E_{sp}, the yielding strength f_{sy}, the ultimate strength f_{su}, the bar diameter Φ and the angles defining the bar orientation θ_{1i} and θ_{2i}.

For each iteration and for each integration point, the procedure starts with the total strain $\{\varepsilon\}+\{\Delta\varepsilon\}$ which is the input variable defining the current state (Figure 4.12). $\{\varepsilon\}$ is the total strain at the beginning of the increment while $\{\Delta\varepsilon\}$ is the trial strain increment. ABAQUS searches for the $\{\Delta\varepsilon\}$ correction required to satisfy the convergence within each increment.

The output variables from the subroutine are the total stress $\{\sigma\}$ and the Jacobian matrix $[D]$. Since the model is formulated in terms of secant values, the total stress at the end of each iteration is computed as

$$\{\sigma\}=[D]\left(\{\varepsilon\}+\{\Delta\varepsilon\}\right). \tag{4.7}$$

The stress is used to compute the internal forces by integration over the element and then, the internal forces over the structure by an assemblage procedure. The internal forces are the part of the external load equilibrated through the current structural deformation. The Jacobian matrix is used to compute the element stiffness matrix by integration over the element and then, the structure stiffness matrix by an assemblage procedure.

Now, the solving system can be written by using the global stiffness matrix and the residual forces computed as the difference between the external and the internal forces. The residue is the part of the load which is not equilibrated by the internal stress.

After the solving procedures, the displacement increment $\{\Delta q\}$ is found. The displacement increment for each element and then the strain increment for each integration point can now

be computed. The whole procedure can be repeated up to the convergence.
Several different FE can be used with 3D-PARC. In this work, the 20-node quadratic reduced integration solid element C3D20R is preferred.

$$\{\varepsilon\}+\{\Delta\varepsilon\}$$

$$\downarrow$$

$$\boxed{\text{3D-PARC}}$$

$$\{\sigma\} \qquad\qquad [D]$$

$$\{f_{int,i}\}=\int_{V_i}[B]^T\{\sigma\}dV \qquad\qquad [K_i]=\int_{V_i}[B]^T[D_i][B]dV$$

$$\{f_{int}\}=\sum_{i=1}^{N_{el}}[L_i]\{f_{int,i}\} \qquad\qquad [K]=\sum_{i=1}^{N_{el}}[L_i]^T[K_i][L_i]$$

$$[K]\{\Delta q\}=\{f_{ext}\}-\{f_{int}\}$$

$$\downarrow$$

$$\{\Delta q\}\ \mathit{and}\ \{\Delta\varepsilon\}$$

Figure 4.12 – The code 3D-PARC in the FE framework.

4.3.3 – Numerical procedure for strain decomposition

After the crack formation, an iterative procedure is required, within the code 3D-PARC, in order to achieve an exact strain decomposition fulfilling both compatibility and equilibrium (Figure 4.13).

The starting point is the total strain vector $\{\varepsilon\}$ which needs to be divided in concrete strain $\{\varepsilon_c\}$ and in crack strain $\{\varepsilon_{cr}\}$. After $\{\varepsilon_{cr}\}$ is defined, $\{\varepsilon_c\}$ is computed by a subtraction. In this way, the compatibility is imposed. From these strains, three constitutive matrices for steel, concrete and crack are computed. Then, the three matrices are used to build the total constitutive matrix [D] and to compute the stresses between the cracks (steel and concrete) and in the crack. Moreover, through the [D] matrix, the total stress {σ} is obtained.

Afterwards, the equilibrium of the stress in the crack and between the cracks is checked. If the equilibrium is satisfied, the [D] matrix and the total stress {σ} are taken as output. If not, a new crack strain {ε_{cr}} is defined by using the crack stiffness matrix and the total stress. In fact, the stress in the crack as well as the stress between the cracks must be equal to the total stress.

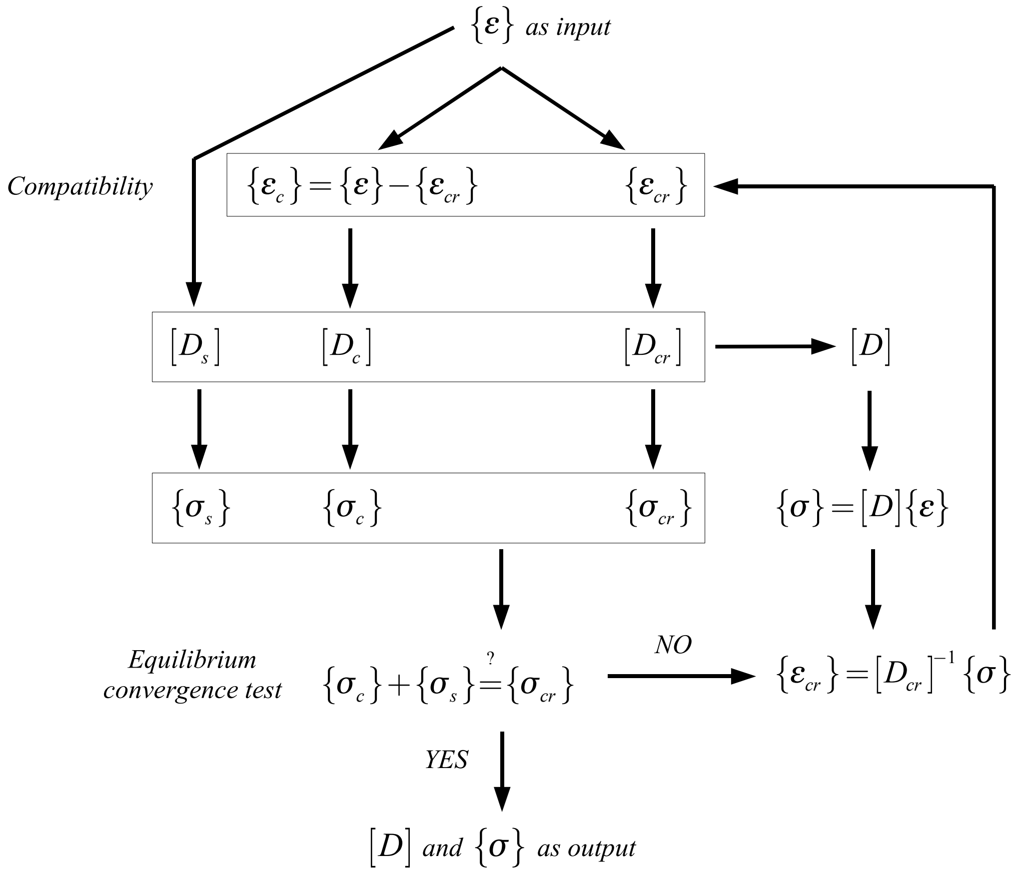

Figure 4.13 – Strain decomposition procedure.

4.4 – PLAIN CONCRETE BIAXIAL TESTS

4.4.1 – Experimental program

As first validation, the proposed model 3D-PARC is applied to plain concrete specimens subjected to biaxial stresses. The final aim of this evaluation is a deep investigation of the concrete constitutive model by using well known and reliable experimental data [27].

Since the development of an universal failure domain is a highly interesting topic, many different experimental studies were performed on concrete subjected to biaxial stresses.

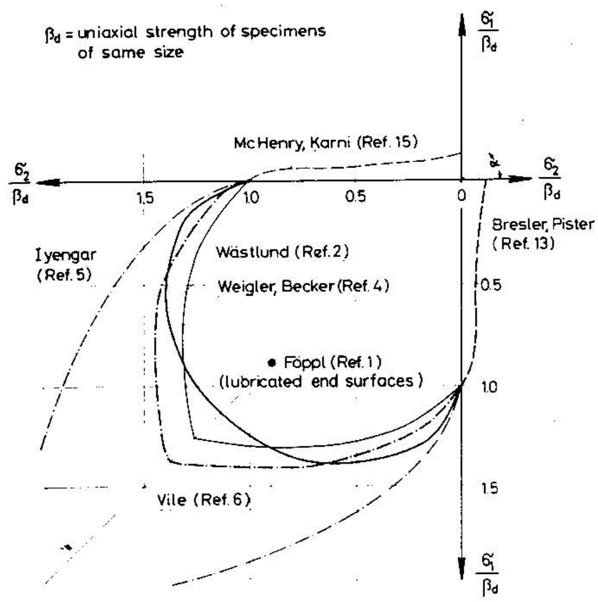

Figure 4.14 – Summary of previous experimental results.

In general, the obtained results present a great discrepancy since many difficulties were encountered in obtaining a suitable test setup. In this kind of tests, the experimental setup should be chosen carefully due to the fact that it is very important to obtain a well defined and uniform biaxial stress state inside the specimen. One of the major problems is the effect of the friction between the bearing plates and the specimen which could produce a confinement modifying the stress state along the concrete edges and increasing the ultimate strength. Many different solutions were tried to avoid this problem, like lubricants, surface treatments or soft packing between the surfaces, but, in general, the results were not reliable: for equal biaxial compressive stresses, the ultimate strength varies from 80% up to 350% of the uniaxial compressive strength (Figure 4.14). On the contrary, in the mixed tensile-compressive fields the agreement was good. Finally, the concrete specimen size and shape had a strong influence on the results.

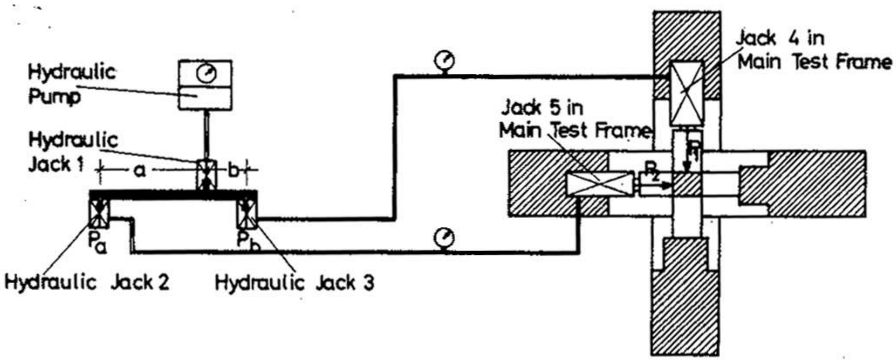

Figure 4.15 – Experimental setup.

In this experimental study, square plates loaded in their plane were used since it seems to be a suitable specimen shape and brush bearing platens were adopted in order to reduce the confinement effect. These platens consisted of a series of closely spaced, small, steel bars which, due to their flexibility, can follow the concrete deformation without giving appreciable restraining effects. In order to avoid buckling instability, shorter steel bars were used with higher concrete strength while, in case of tensile stress, the bars were glued to the concrete edges.

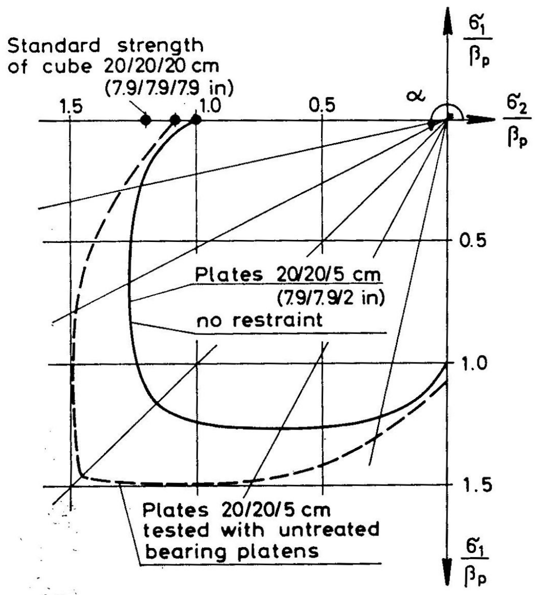

Figure 4.16 – Untreated and brush bearing platens results.

20x20x5-cm plain concrete specimens were subjected to stress combinations in biaxial tensile, tensile-compressive and biaxial compressive fields in order to draw a complete failure

domain. For each field, four different stress ratios were chosen and six specimen were tested. Three different types of concrete having different uniaxial compressive strengths were used. The maximum aggregate size was 15 mm. The experimental setup is shown in Figure 4.15.
In order to test the experimental setup, several preliminary tests varying the specimen size and shape were performed with and without the brush platens. The difference between restrained and unrestrained specimen is highlighted in Figure 4.16. Moreover, when the brush bearing platens were used, the shape of the specimen did not influence the results.
In the figures, the strength values are defined as a fraction of the uniaxial compressive strength in order to compare the results obtained from the three different types of concrete.

4.4.2 – Results and comparisons

The experimental crack patterns are reported in Figure 4.17. For biaxial compressive combinations, numerous microcracks parallel to the free surface of the specimen arose during the loading procedure and eventually, a major crack developed with an angle in the range 18-27 deg to the free surface.

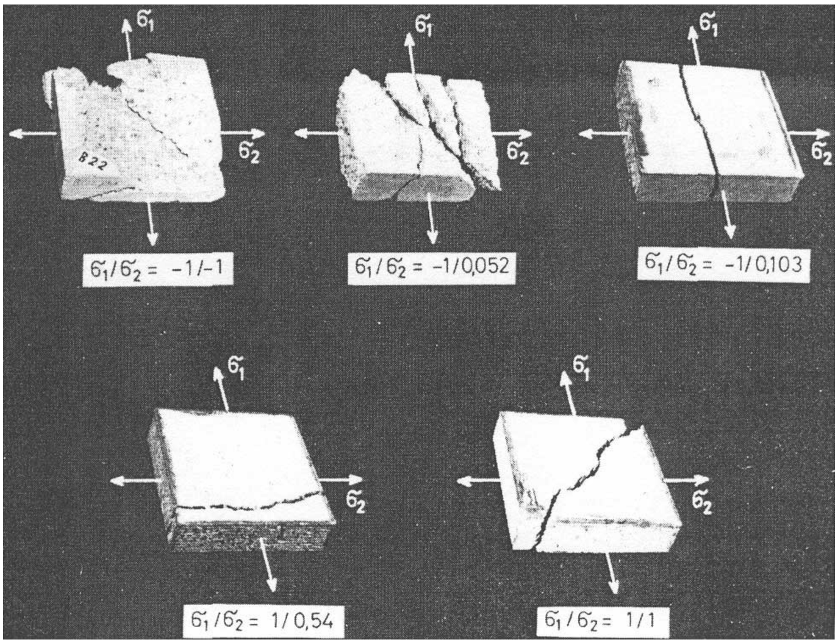

Figure 4.17 – Experimental failure modes.

For mixed tensile-compressive combinations, the specimens behaved in the same way as long as the ratio σ_1/σ_2 was less than 1/15. For larger tensile stresses, a single, well defined crack perpendicular to the maximum stress brought the specimen to the failure. For biaxial tensile combinations, no preferred crack directions were observed, but the crack was always perpendicular to the free surface.

In general, the strength data were slightly affected by the different uniaxial compressive strength but, for example, in the mixed tensile-compressive field, the concrete strength decreased as the uniaxial strength increased.

The concrete strength under biaxial compression was 16% larger than under uniaxial compression. This increment is very low if compared to the outcomes of other experimental programs. In the mixed tensile-compressive field the results were in good agreement with previous investigations. Finally, in the biaxial tension field, the strength was almost independent of the stress ratio σ_1/σ_2 and equal to the uniaxial tensile strength.

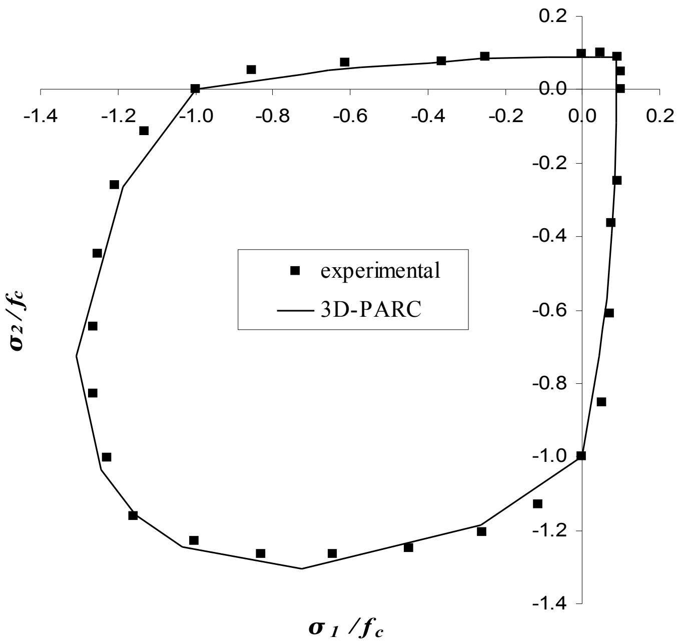

Figure 4.18 – Experimental and numerical biaxial failure domain.

In Figure 4.18, 3D-PARC is applied to obtain the biaxial failure domain. As already mentioned, the triaxial failure surface is highly influenced by the eccentricity *e*, whose value, for these biaxial tests, is chosen to be e=0.52. The numerical simulation reproduces the experimental data with high accuracy.

Furthermore, the stress-strain behavior for several biaxial stress combinations is simulated. Figure 4.19 and Figure 4.20 represent two significant cases for biaxial compression. In the first one the specimen is subjected to equal biaxial stresses. In the second one, the stress combination provides the highest concrete strength.

It can be noted that the ultimate strength as well as the peak strain can be captured very well in the most loaded direction. On the contrary, the strains in the perpendicular directions are detected with less accuracy.

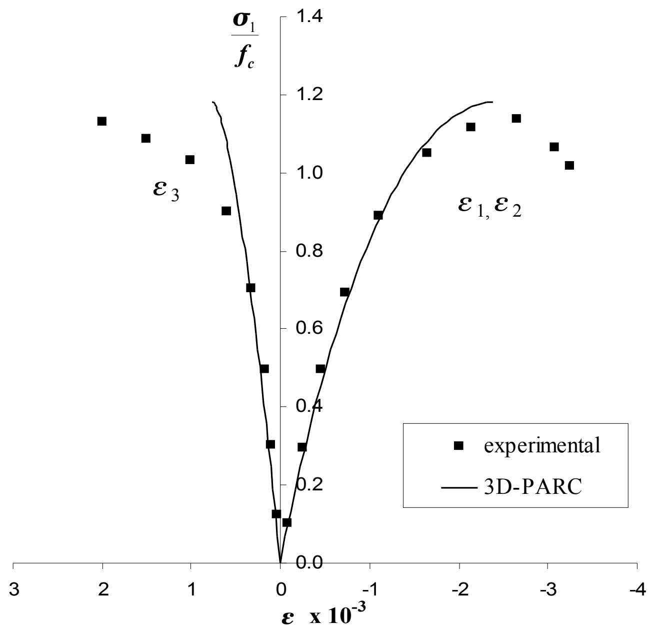

Figure 4.19 – Stress-strain curves for σ_1/σ_2=-1/-1.

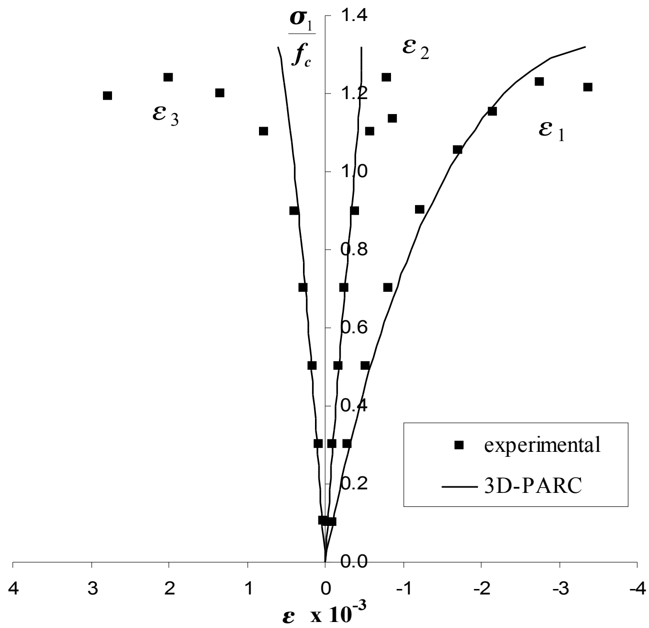

Figure 4.20 – Stress-strain curves for σ_1/σ_2=-1/-0.52.

Finally, one case extracted from the mixed tensile-compressive region is reported in Figure 4.21. As it can be clearly seen from the curve shapes, the tensile stress has a high influence on the specimen response, with a strong reduction of the concrete strength. In this case, all the strain can be captured in a very accurate way.

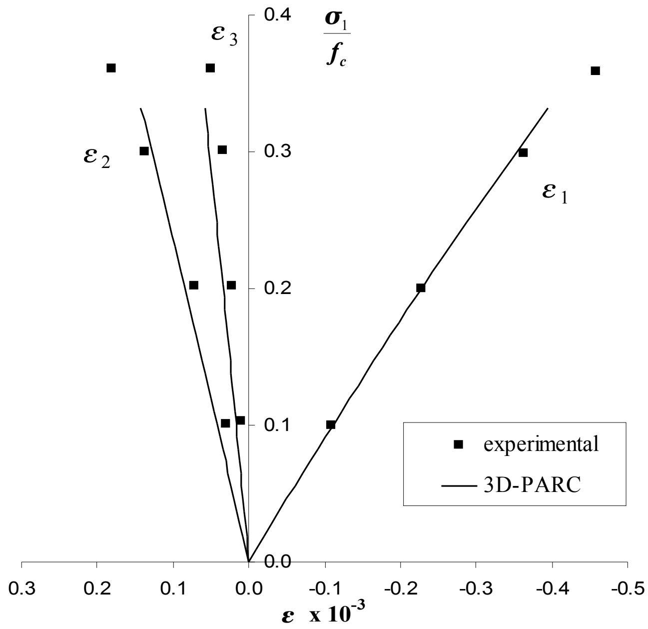

Figure 4.21 – Stress-strain curves for σ_1/σ_2=-1/0.204.

4.5 – PLAIN CONCRETE TRIAXIAL TESTS

4.5.1 – Experimental program

In 1968 and 1969, an experimental study on plain concrete behavior under triaxial stresses was carried out at the Centre d'Etudes Scientifiques et Techniques (CEST, Grenoble) for the Compagnie Industrielle de Travaux (CITRA, Paris) [30].

The final objective of the research was the investigation of deformability under service loads and of failure strength of the thick concrete walls used in nuclear reactor containment vessels. For the deformability investigation, the experimental tests were performed on 140-mm side cubes, at three different temperatures, up to 50 MPa in all the three directions, whereas, for the study of the ultimate strength, 70-mm side cubes up to 200 MPa were used.

The specimens were cast by choosing the same material used for an already built vessel: a CPAC-325 cement with silico-calcareous gravel characterized by a maximum aggregate size of 15 mm. The nominal uniaxial compressive strength values varied between 30 and 45 MPa. Figure 4.22 shows the experimental facilities.

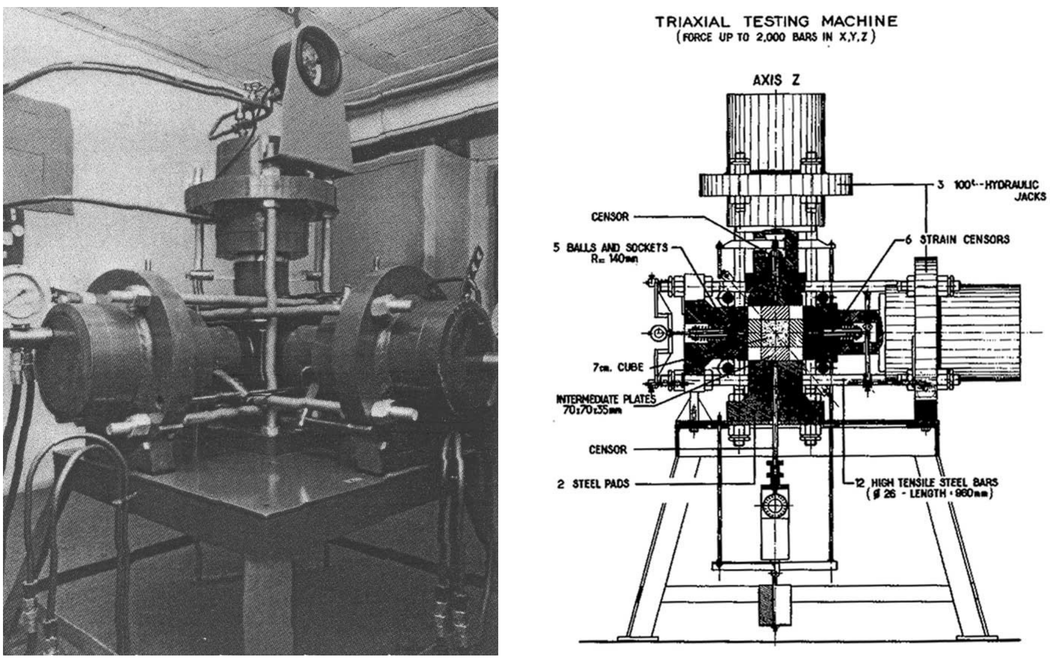

Figure 4.22 – Testing machine (left) and experimental setup (right).

In order to avoid any friction effect, two different systems were used: the specimen was lubricated with talc or an aluminum pad was inserted between the concrete and the loading plate surfaces. Each pad consisted of four aluminum sheets with interposed talc lubrication.

4.5.2 – Results and comparisons

Figures from 4.23 to 4.28 show the experimental results related to the 3D failure surface by varying the σ_1 stress component. The intersections between the failure surface and several planes σ_1/f_c are reported in the plane σ_2/f_c-σ_3/f_c . All the diagrams are symmetrical with respect to the bisecting line. Two different series are plotted for the experimental results: the "experimental 1" refers to the specimen lubricated with talc and the "experimental 2" to those lubricated with aluminum pads.

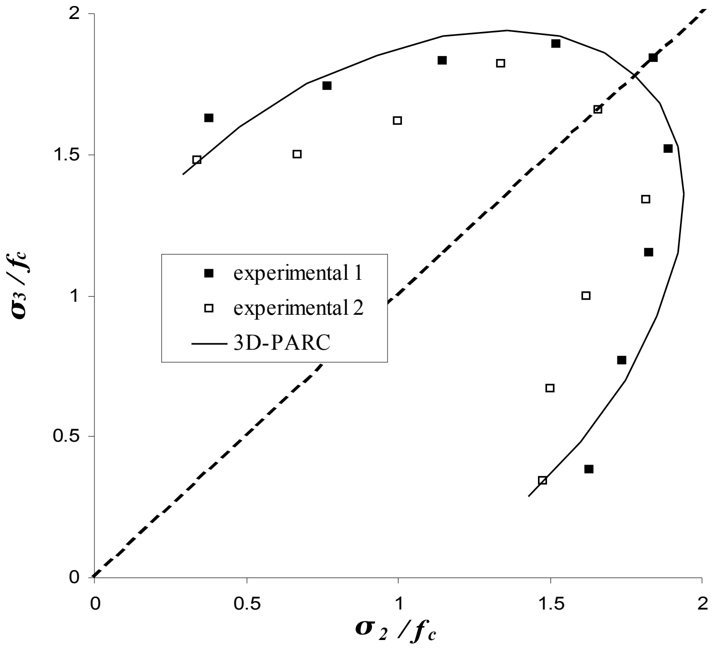

Figure 4.23 – Experimental and numerical (e=0.58) failure domain for σ_1=0.

In order to obtain a good result fitting, in the numerical simulation, the eccentricity value is not constant but it needs to be increased with the confining stress value. The starting value is 0.58 for σ_1=0 and then the value is increased up to 0.7 for the subsequent cases.

Figure 4.23 can be compared with Figure 4.18 in order to understand the different confinement effect. They both refer to the case with σ_1=0, but they provide very different results. In particular, the Launay-Gachon failure domain is greatly overestimated possibly because of the confinement effect of the supports. As already mentioned about the biaxial experimental program, if the experimental setup is not carefully arranged, the bearing platens can have a remarkable restraining effect.

Moreover, the increment of eccentricity, required by the transversal stress increment, could be another consequence of this phenomenon. Therefore, it can be concluded that probably the talc and the aluminum pads are not sufficient to prevent the confinement effect and the related strength increment.

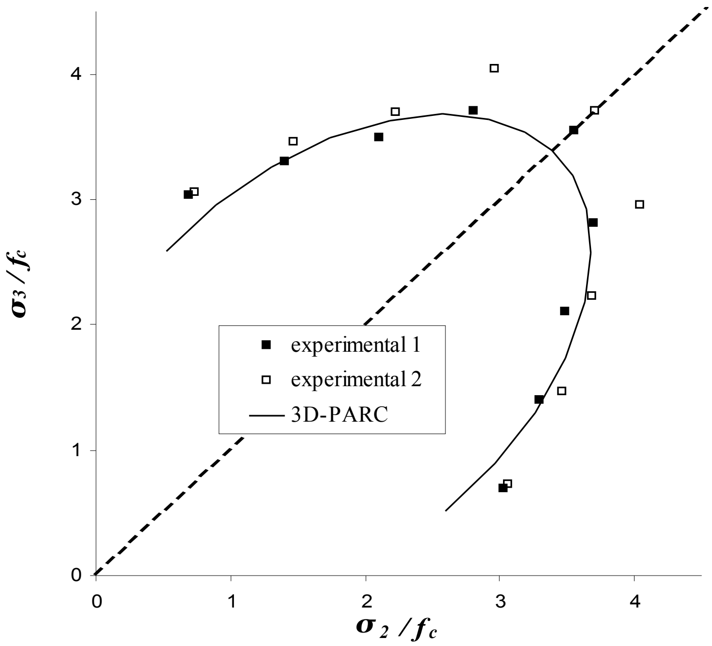

Figure 4.24 – Experimental and numerical (e=0.65) failure domain for σ_1=0.2 f_c.

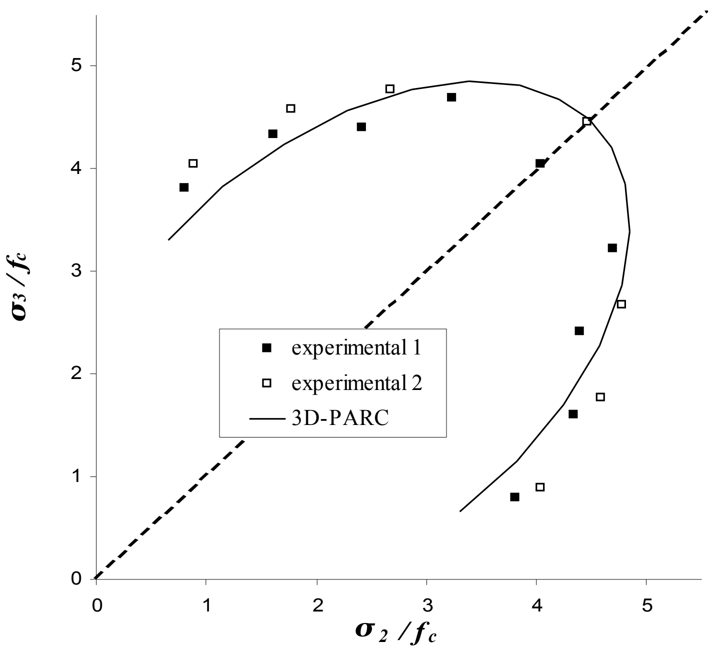

Figure 4.25 – Experimental and numerical (e=0.7) failure domain for σ_1=0.4 f_c.

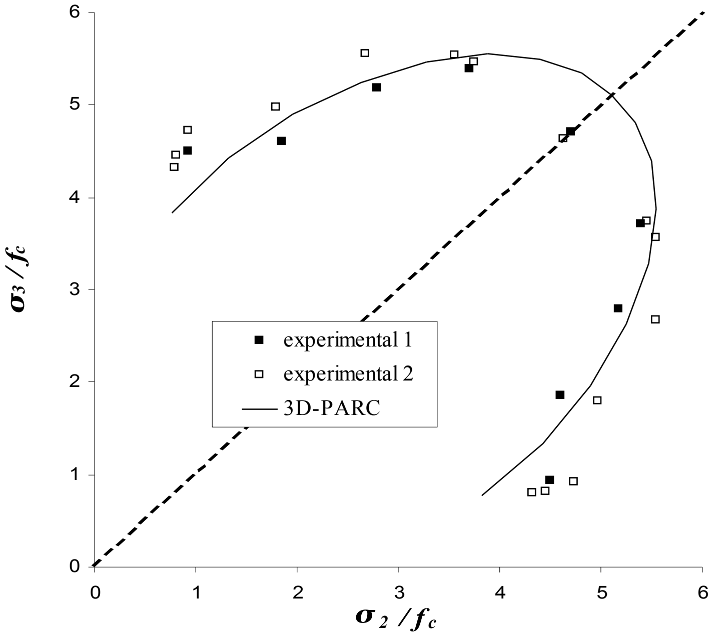

Figure 4.26 – Experimental and numerical (e=0.7) failure domain for σ_1=0.6 f_c.

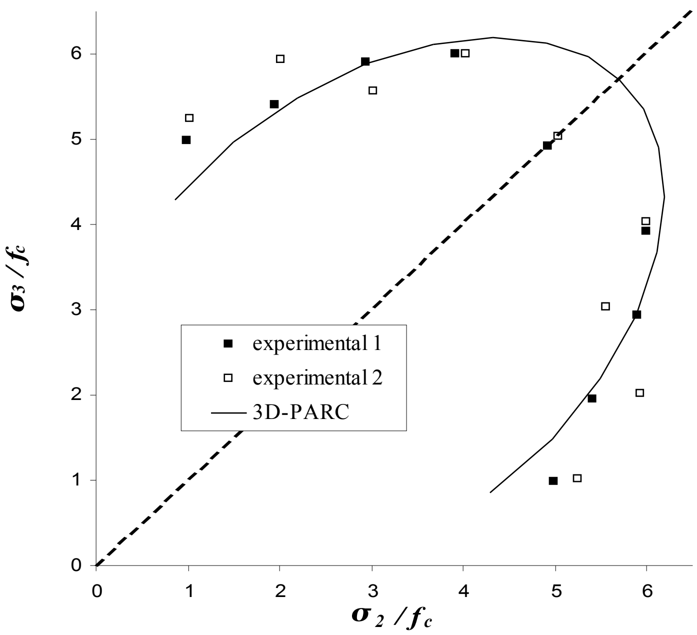

Figure 4.27 – Experimental and numerical (e=0.7) failure domain for σ_1=0.8 f_c.

In Figure 4.29, the failure surface is shown in the Rendulic plane passing by the axis σ_3/f_c and the isotropic line $\sigma_1/f_c=\sigma_2/f_c=\sigma_3/f_c$. Two different intersection curves are obtained, being defined by $\sigma_1=\sigma_2\leq\sigma_3$ and $\sigma_1\leq\sigma_2=\sigma_3$. These two curves are typical of the concrete behavior and can be utilized as parametric functions to define any type of concrete. A constant value of e=0.7 is used.

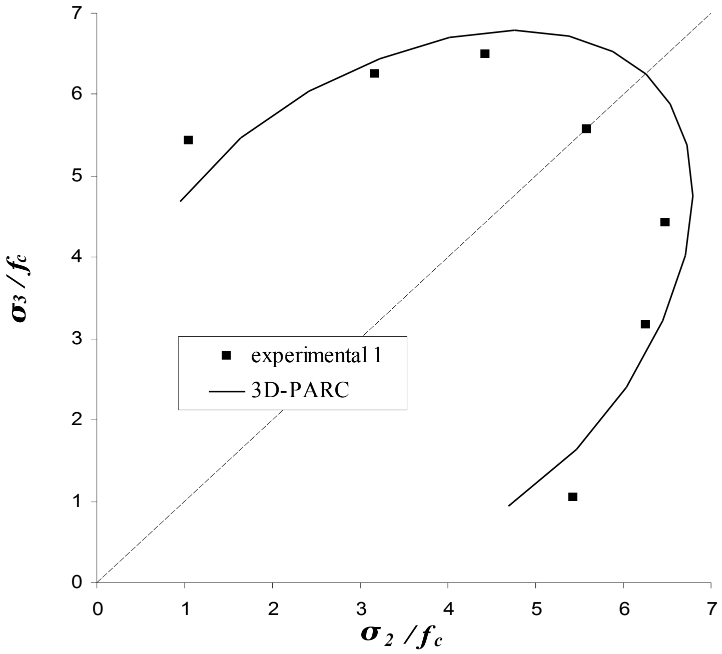

Figure 4.28 – Experimental and numerical (e=0.7) failure domain for σ_1=f_c.

The proposed model is in good agreement with the experimental results. In general, it is able to capture with satisfactory accuracy the failure domain in the 3D stress space including the confinement effects due to transversal stresses. Moreover, by directly changing the eccentricity, it is possible to add flexibility and reliability to its application to a wide range of experimental tests.

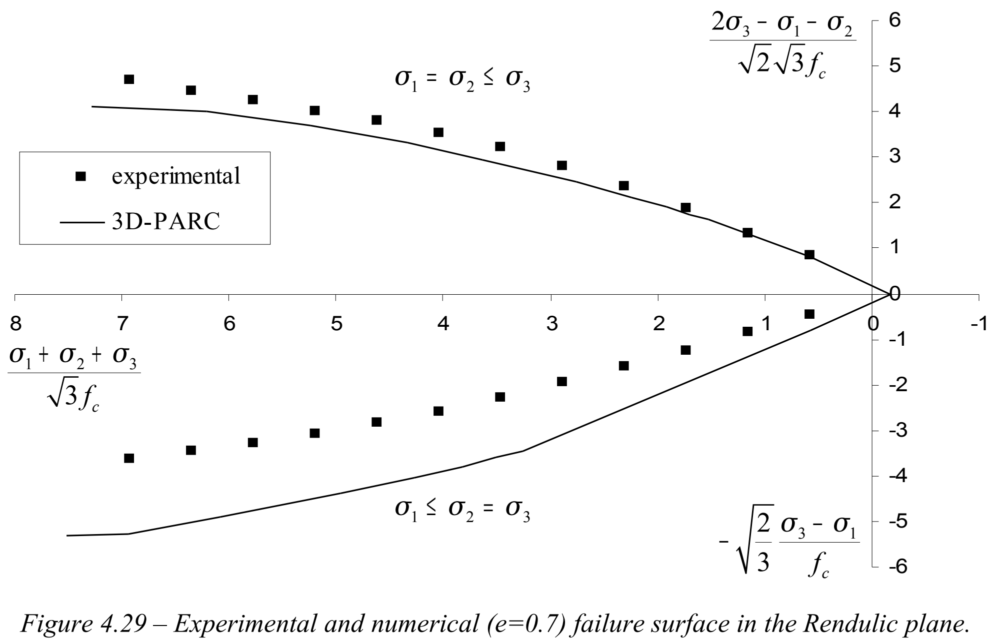

Figure 4.29 – Experimental and numerical (e=0.7) failure surface in the Rendulic plane.

4.6 – VECCHIO-COLLINS SHEAR PANELS

4.6.1 – Experimental program

In the following section, the proposed model 3D-PARC is applied to RC membrane elements subjected to plane stress states.
The experimental program was carried out in the '80s at the University of Toronto and it is a very important reference for the study of plane elements [45]. The importance of this kind of experiments lies in the fact that, as shown in Figure 4.30, a wide range of civil structures can be idealized as an assemblage of membrane elements, as underlined by the authors.

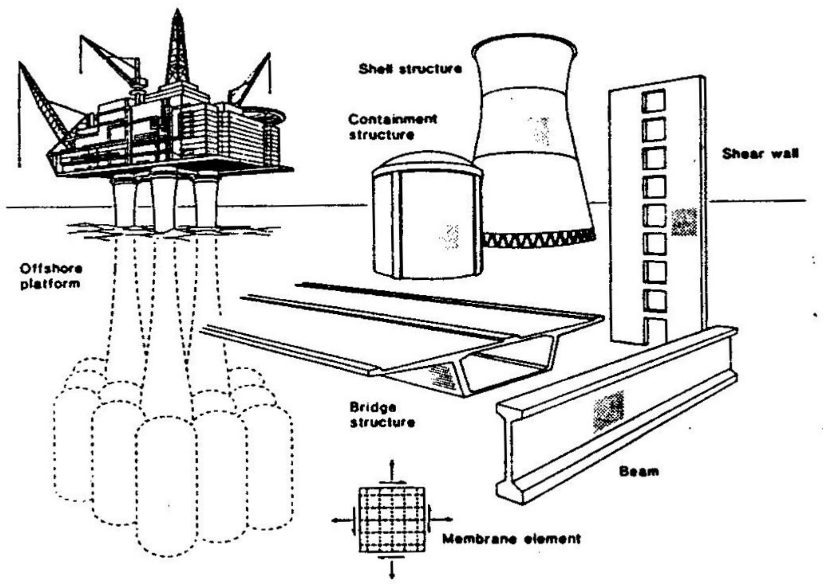

Figure 4.30 – The importance of membrane elements.

The paper presents also the modified compression-field theory for the prediction of the membrane element behavior. This model is based on the compression-field theory and implements the continuum equivalent approach.
This experimental program, involving 30 panels, is worldwide famous since, after testing the first 15 panels, an international competition was called in order to predict the response of some of the remaining panels.
The competition, a partial blind test, being the response of the first 15 panels known, underlined the difficulties in predicting the right response and the lack of a well established common and reliable theoretical background. 43 different leading researcher from 13 countries attempted to predict the behavior of four panels and very different numerical

techniques were used ranging from simple manual calculations to high sophisticated FE analysis. None of the competitors was able to predict the ultimate load remaining within an error range of 15% for any of the four panels. For one of the elements, the ratio of the lowest to the highest prediction was one to six. It has to be noted, however, that the panels chosen for the competition were the most difficult to predict since their behavior was strongly dependent on the stress-strain concrete characteristics.

This experimental program is chosen to test the proposed model since it gives the possibility to deeply investigate the basic assumptions of the theory and its numerical implementation.

The panels were 890-mm square and 70-mm thick, reinforced with two steel layers running parallel to the edges. The two layers were welded together. The reinforcing bars were 50-mm equally spaced with a clear cover of 6 mm. The maximum aggregate size was 6 mm.

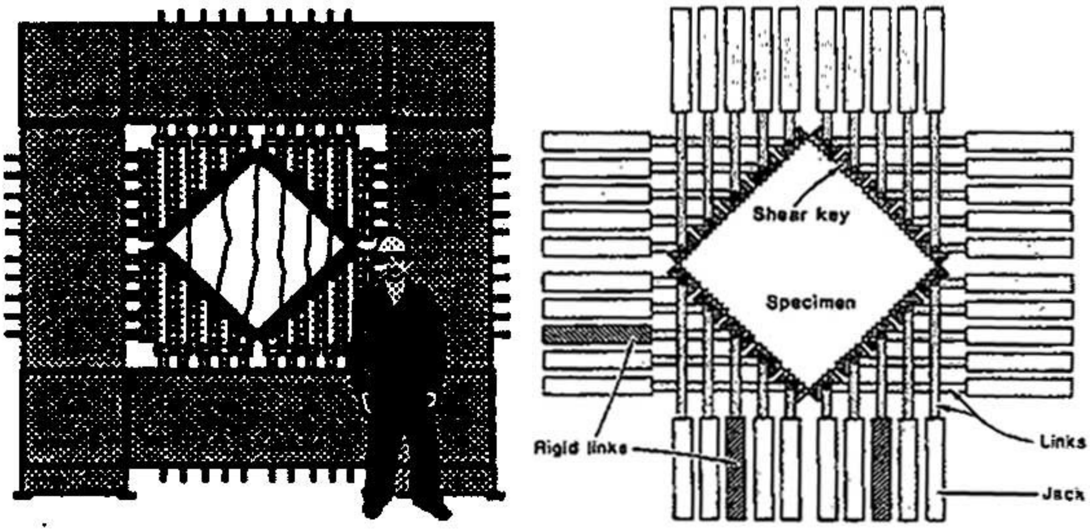

Figure 4.31 – Testing machine (left) and experimental setup (right).

The specimens were tested in the special membrane element tester reported in Figure 4.31. Most of the panels were subjected to pure shear loading conditions but some of them were tested with various combination of shear, tension and compression. In addition to the loading conditions, some other variables were changed such as the concrete strength and the percentage of longitudinal and transversal reinforcement.

In order to transmit the loads to the specimen, five shear keys were cast on the panel along each side. Each shear key was connected to hydraulic jacks by a network of links. Three links were rigid in order to support the specimen. This system allowed to apply every combination of external loads. The out-of-plane displacements were constrained. The experimental setup was inserted in a steel frame which held the specimen.

4.6.2 – Results and comparisons

Ten panels with different failure modes are investigated by 3D-PARC. The properties of the investigated panels are reported in Table 4.1. All the specimens are subjected to pure shear load with the exception of the PV23 which is also compressed along both *x* and *y* directions with the ratios σ_x, σ_y, τ_{xy}=-0.39, -0.39, 1.

In the selected specimens, the steel ratio, the steel yielding strength and the concrete compressive strength are varied in order to obtain different failure modes. The longitudinal steel ratio ρ_x is kept constant in all the specimens with the exception of PV16. The transversal steel ratio ρ_y varies from 0.045 to 0.0179. Only three panels are fully symmetrical: PV16, PV23 and PV27.

Figures from 4.32 to 4.41 show the comparisons with the experimental outcomes in terms of shear stress-shear strain.

Panel	f_c ***[MPa]***	ε_{cp}	ρ_x	f_{syx} ***[MPa]***	ρ_y	f_{syy} ***[MPa]***
PV10	*14.5*	*0.0027*	*0.0179*	*276*	*0.0100*	*276*
PV11	*15.6*	*0.0026*	*0.0179*	*235*	*0.0131*	*235*
PV12	*16.0*	*0.0025*	*0.0179*	*469*	*0.0045*	*269*
PV16	*21.7*	*0.002*	*0.0074*	*255*	*0.0074*	*255*
PV19	*19.0*	*0.0022*	*0.0179*	*458*	*0.0071*	*299*
PV20	*16.9*	*0.0018*	*0.0179*	*460*	*0.0089*	*297*
PV21	*19.5*	*0.0018*	*0.0179*	*458*	*0.0130*	*302*
PV22	*19.6*	*0.002*	*0.0179*	*458*	*0.0152*	*420*
PV23	*20.5*	*0.002*	*0.0179*	*518*	*0.0179*	*518*
PV27	*20.5*	*0.0019*	*0.0179*	*442*	*0.0179*	*442*

Table 4.1 – Investigated panel properties.

The panels PV10, PV11 and PV12 are under-reinforced and present a ductile response. The failure is reached by the steel yielding of both layers. In fact, the steel layers are not symmetrical and, as it is clear from the figures, they yield for different load levels.

The panel PV16 is under-reinforced in both directions. The failure is caused by simultaneous steel yielding in both directions.

The panels PV19, PV20 and PV21 fail because of the steel yielding. The steel layers are not symmetrical in terms of steel ratio and yielding strength and therefore, the failures are not simultaneous. The stress-strain curves show a highly ductile response.

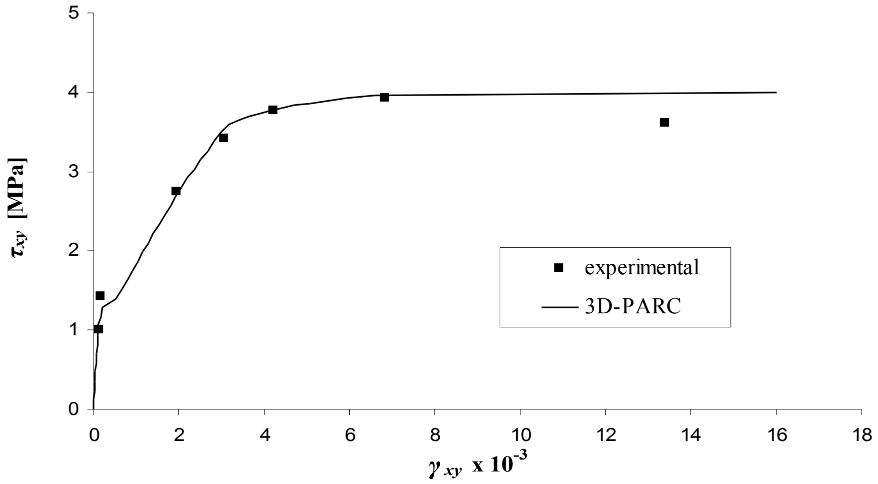

Figure 4.32 – Result comparison for panel PV10.

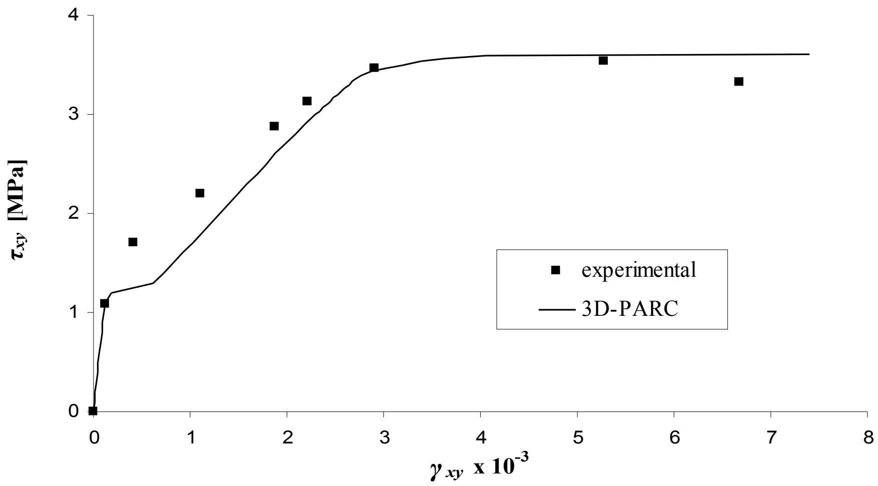

Figure 4.33 – Result comparison for panel PV11.

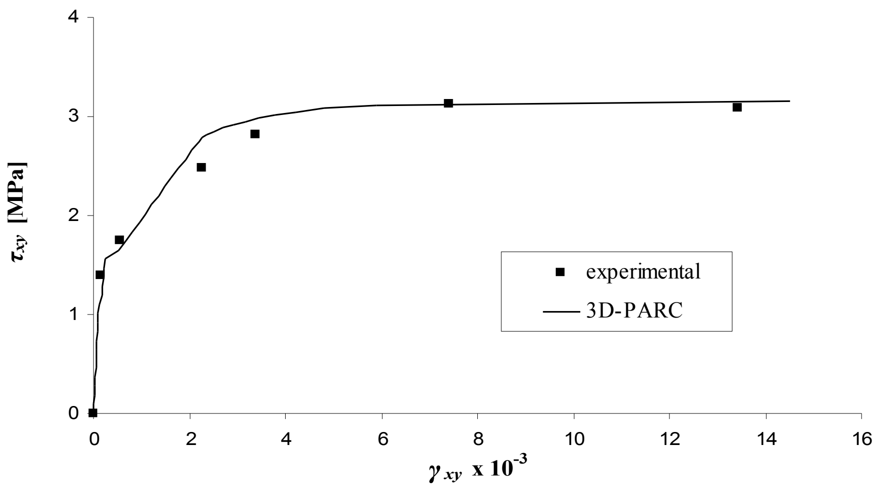

Figure 4.34 – Result comparison for panel PV12.

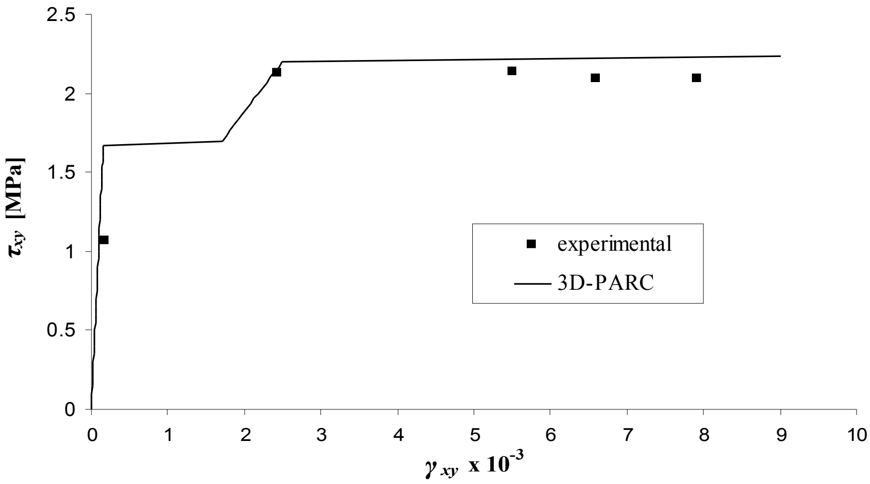

Figure 4.35 – Result comparison for panel PV16.

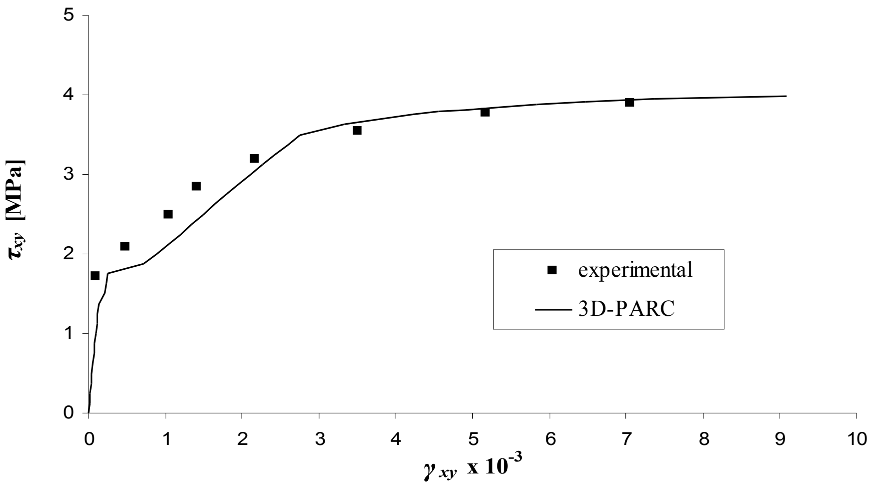

Figure 4.36 – Result comparison for panel PV19.

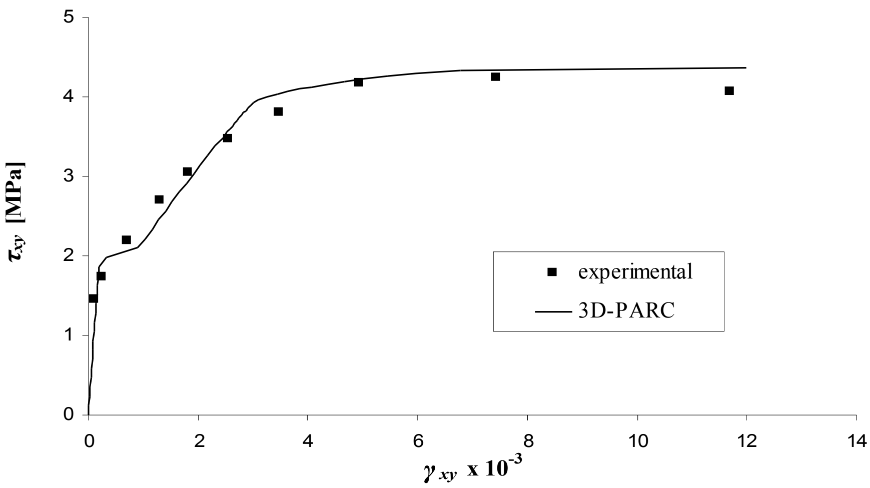

Figure 4.37 – Result comparison for panel PV20.

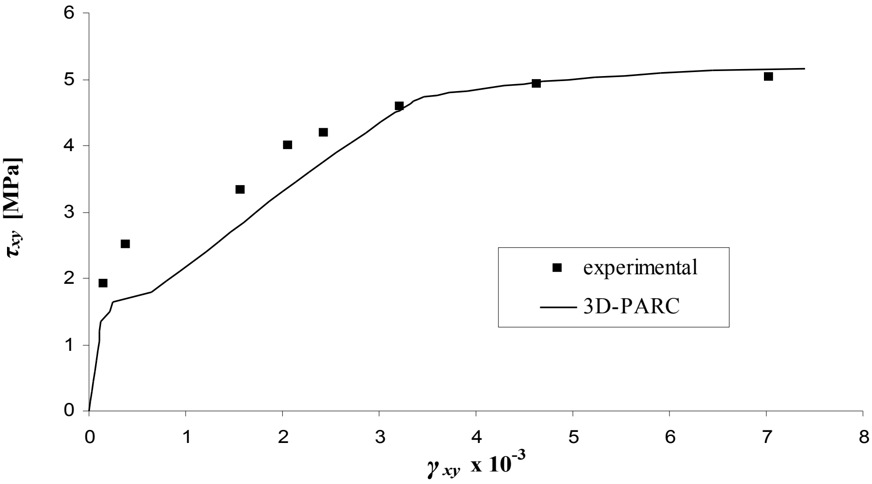

Figure 4.38 – Result comparison for panel PV21.

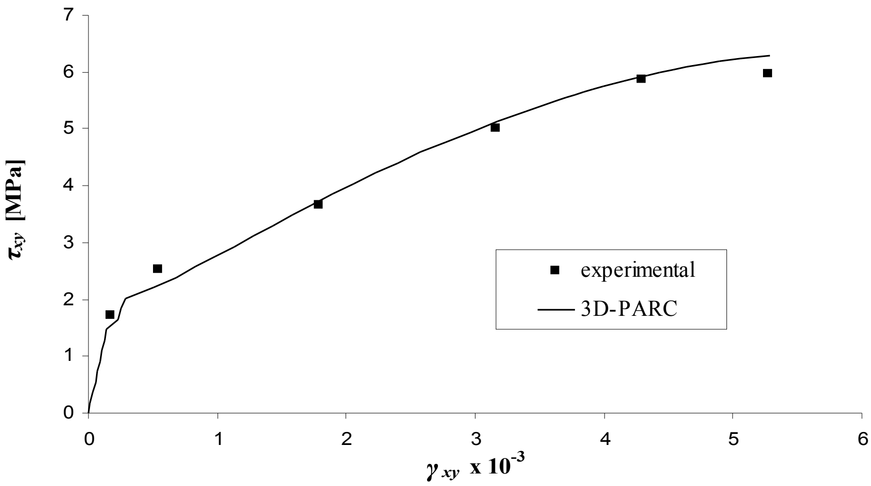

Figure 4.39 – Result comparison for panel PV22.

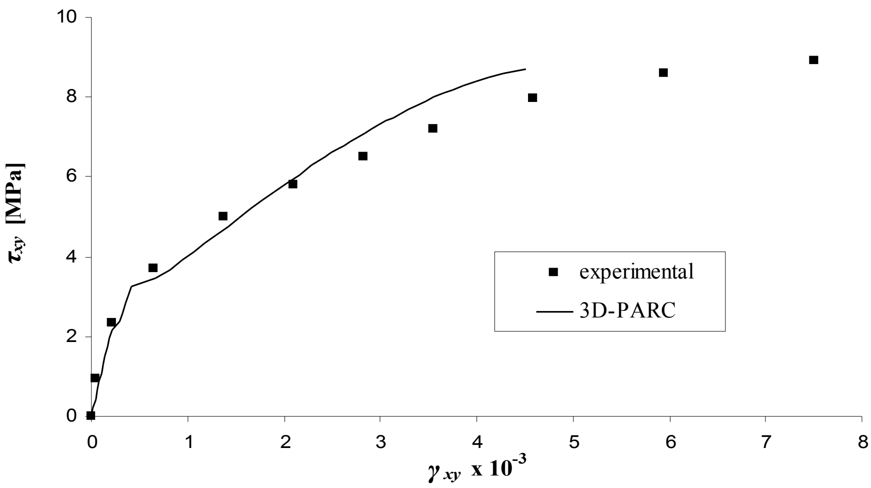

Figure 4.40 – Result comparison for panel PV23.

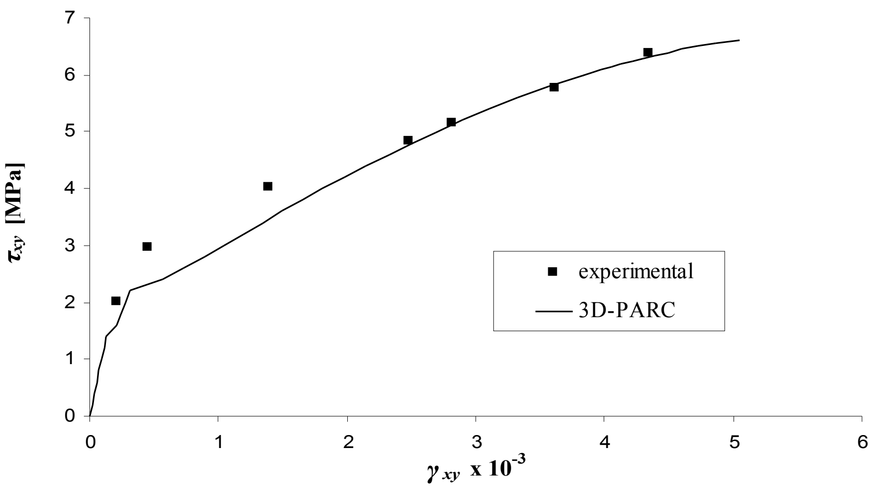

Figure 4.41 – Result comparison for panel PV27.

The panels PV22, PV23 and PV27 exhibit a similar response even if they are different in steel ratio, yielding strength and loading conditions. The PV23 and PV27 are fully symmetrical, while the PV22 is not symmetrical neither in steel ratio nor in yielding strength. All the three panels are over-reinforced and the failure is reached by crushing of the concrete between the cracks. This behavior can be clearly seen in the smooth response of the curves.

The PV23 and PV27 differ only in the steel yielding strength, but, due to the brittle failure mode, they can be considered identical. Therefore, the effect of the combined shear and compressive stresses causes, in the PV23, an increment in the ultimate load as well as in the deformation. The response of PV23 is not easy to capture, probably due to the confining effect of the compression. However, the proposed model is able to capture the ultimate load value as well as the failure mode, but the computed behavior remains stiffer than the real one.

In conclusions, it can be stated that 3D-PARC provides very good results in the panel investigation. The numerical simulations are generally able to capture with high accuracy the ultimate load, the deformability and the failure mode of the specimens.

4.7 – PANG-HSU SHEAR PANELS

4.7.1 – Experimental program

In the '90s, the University of Houston carried out a wide experimental program on membrane elements subjected to tension-compression [7] as well as shear loads [37].

A careful examination of the previous tests in literature led the authors to the following conclusions: the small size of the specimens previously used had a strong influence on the results. Furthermore, a large amount of data is necessary to investigate the 2D softening. Finally, since the outcomes used to present a high scattering, a reliable testing technique should be found and implemented. In order to fulfill these requirements, a high capacity test facility, the "universal panel tester" was built (Figure 4.42).

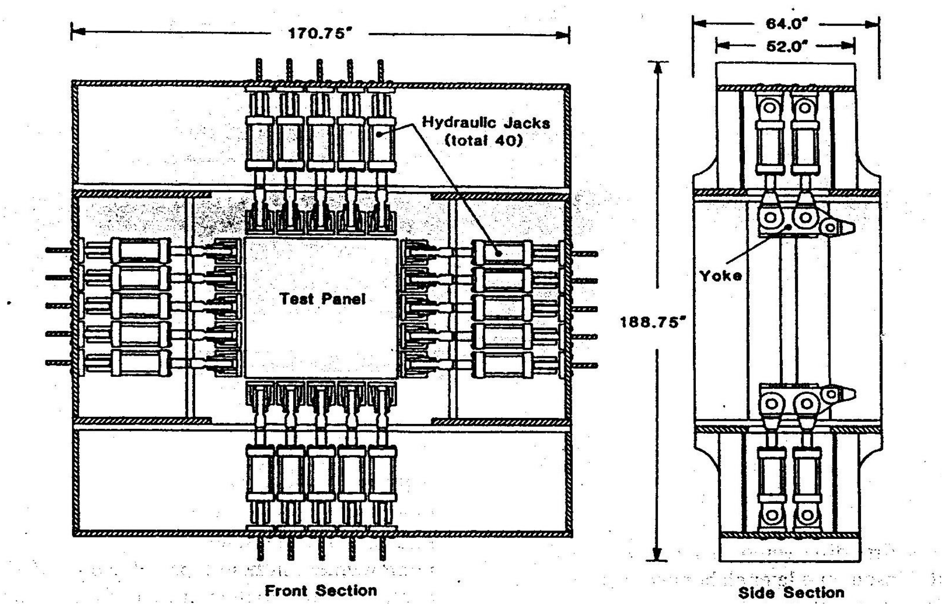

Figure 4.42 – Testing facility.

The main objectives of the experimental program were:

- the exploration of the strain measuring techniques for cracked concrete;
- the study of the variables influencing the constitutive model of cracked concrete;
- the understanding of the involved physical phenomena and the improvement of the mathematical description of the constitutive laws.

In the shear program, 13 panels (1400x1400x178 mm) were investigated. The reinforcements were arranged at 45 deg with respect to the loading directions *x* and *y*. The concrete properties were maintained approximately constant with a uniaxial compressive strength of 42 MPa. The steel nominal yielding strength was 420 MPa. During the experimental tests, three variables were varied:

- the percentage of reinforcements;
- the ratio of transversal to longitudinal steel;
- the load path.

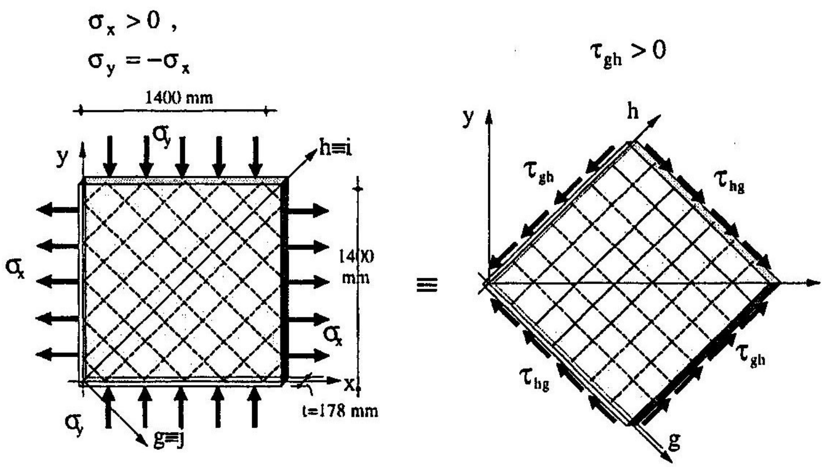

Figure 4.43 – Specimen geometry and load equivalence.

The specimens were divided into three series: the A series consisted of four fully symmetrical panels, while the B panels presented a different amount of reinforcements in the two directions. The series A and B were subjected to pure shear: the specimens were loaded along the directions *x* and *y* by equal stresses which provided a pure shear stress state (Figure 4.43). The panels C were identical to the A panels but a different load path was applied.

Panel	f_c ***[MPa]***	ε_{cp}	ρ_x	f_{syx} ***[MPa]***	ρ_y	f_{syy} ***[MPa]***
A2	*41.2*	*0.0021*	*0.01193*	*463*	*0.01193*	*463*
A3	*41.6*	*0.0019*	*0.01789*	*445*	*0.01789*	*445*
A4	*42.4*	*0.0022*	*0.02982*	*470*	*0.02982*	*470*
B1	*45.2*	*0.0021*	*0.01193*	*463*	*0.00596*	*445*
B2	*44.1*	*0.0024*	*0.01789*	*445*	*0.01193*	*463*
B3	*44.9*	*0.0022*	*0.01789*	*445*	*0.00596*	*445*
B4	*44.7*	*0.0021*	*0.02982*	*470*	*0.00596*	*445*
B5	*42.8*	*0.0022*	*0.02982*	*470*	*0.01193*	*463*
B6	*43.0*	*0.0022*	*0.02982*	*470*	*0.01789*	*445*

Table 4.2 – Investigated panel properties.

In order to transmit the load to the specimen, the reinforcing bars were welded to 20 anchor inserts cast at the edges of the panels. Each anchor insert was connected to a hydraulic jack.

4.7.2 – Results and comparisons

Nine panels with different properties and failure modes are simulated through 3D-PARC. The panels properties are reported in Table 4.2.

The numerical results are compared to the experimental outcomes in terms of shear stress-shear strain curves from Figure 4.44 to Figure 4.52.

The panels A2 and A3 exhibit simultaneous steel failures. This can be clearly seen from the stress-strain curve. After a first uncracked linear stage, common for all the specimens, the cracking produces an immediate strain increment. The subsequent stage is characterized by a linear response, since the concrete is far from the failure and remains within the linear behavior. Finally, the steel yielding strength is reached at the same load level in both the reinforcing layers leading to a sudden strain increment.

On the contrary, the panel A4, presents the failure of the concrete between the cracks. The stress-strain curve after cracking exhibits a smooth behavior and the ultimate load is reached with a softening response.

All the B panels are asymmetrically reinforced and present an under-reinforced behavior. The failure is caused by the yielding of the transversal layer followed by the yielding of the longitudinal layer (B1, B2 and B3) or by the yielding of the transversal layer followed by the concrete crushing (B4, B5 and B6).

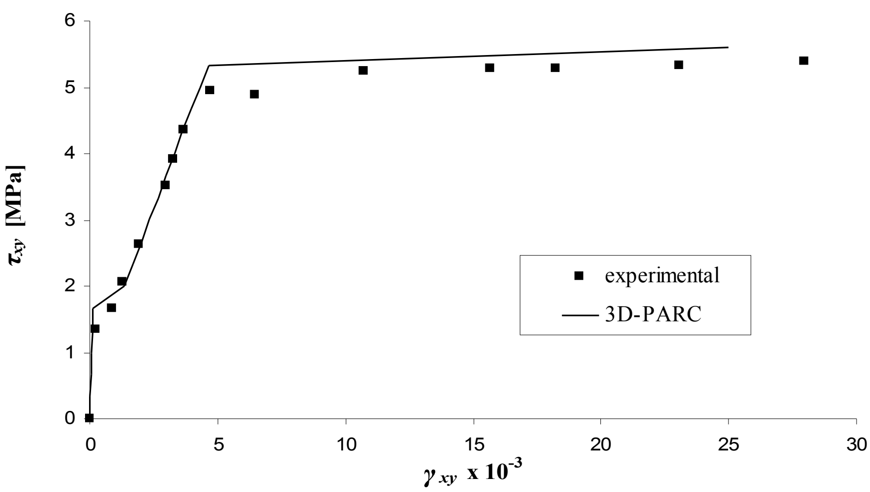

Figure 4.44 – Result comparison for panel A2.

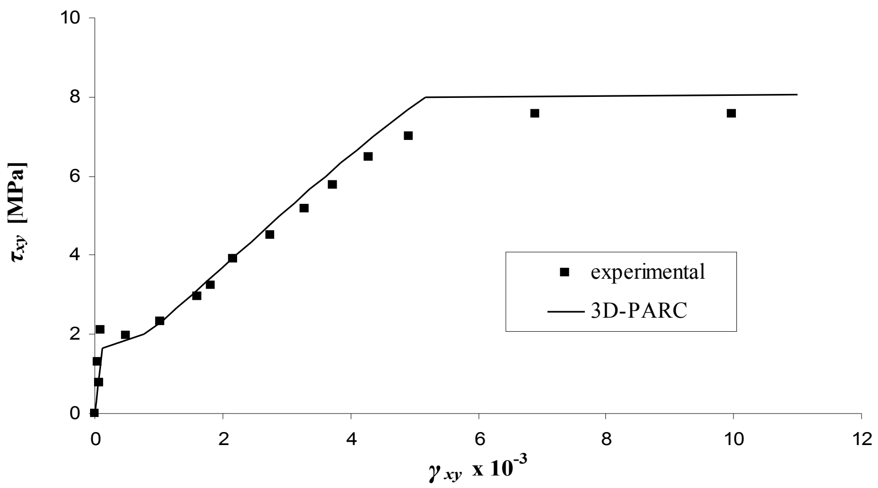

Figure 4.45 – Result comparison for panel A3.

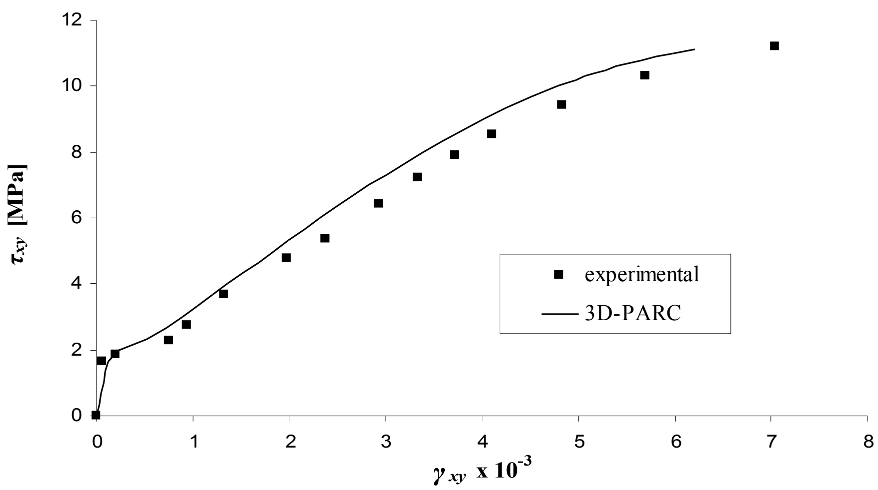

Figure 4.46 – Result comparison for panel A4.

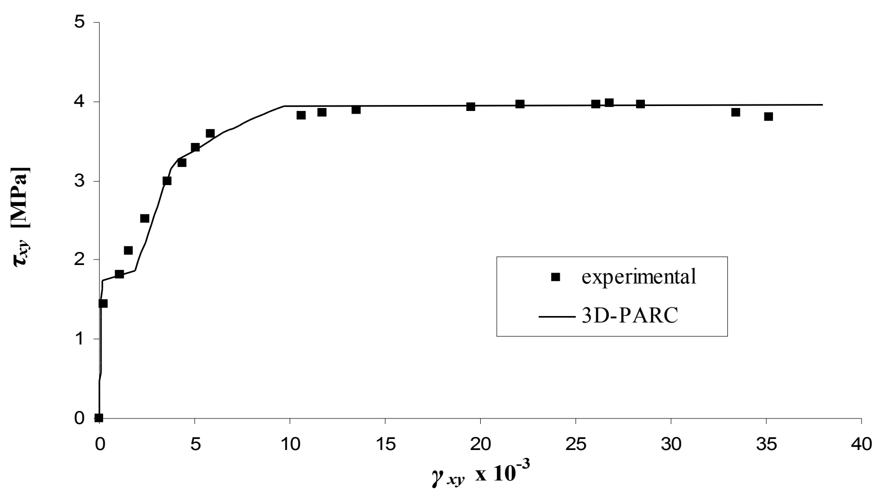

Figure 4.47 – Result comparison for panel B1.

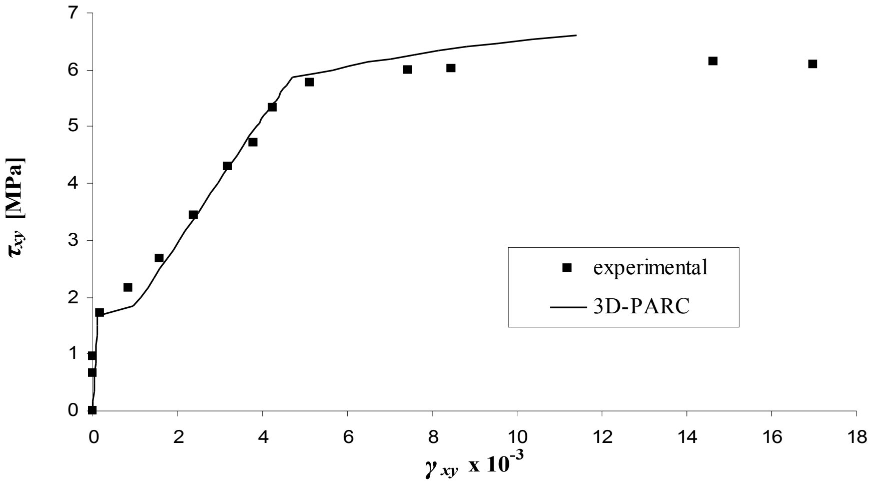

Figure 4.48 – Result comparison for panel B2.

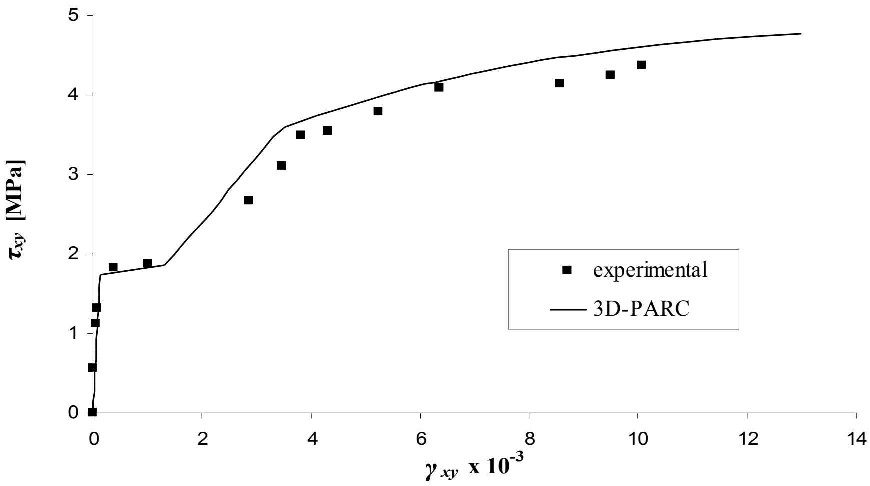

Figure 4.49 – Result comparison for panel B3.

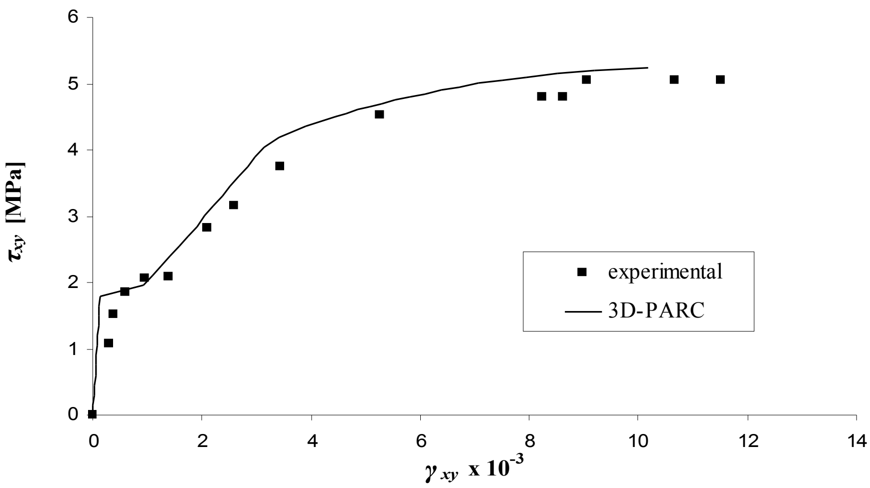

Figure 4.50 – Result comparison for panel B4.

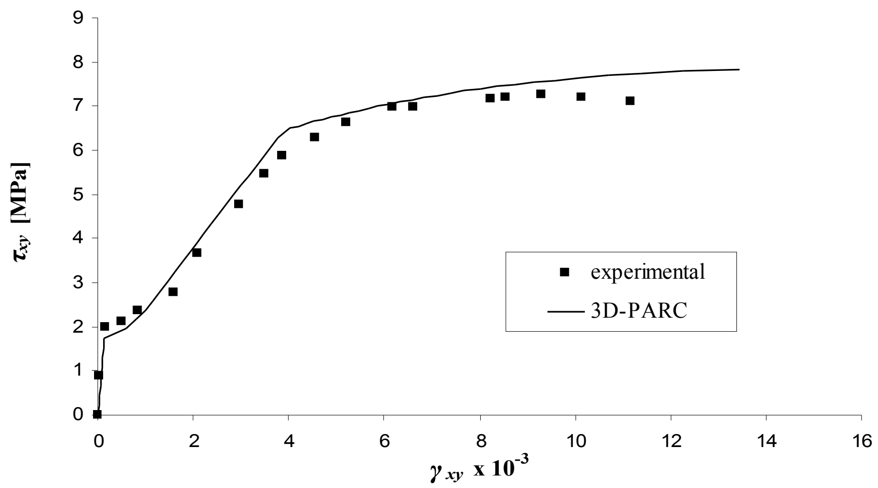

Figure 4.51 – Result comparison for panel B5.

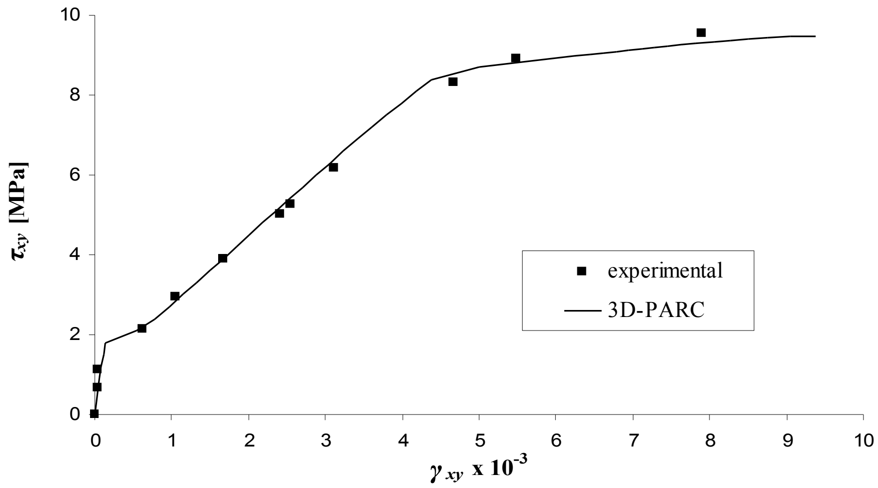

Figure 4.52 – Result comparison for panel B6.

These failure modes are evident from the stress-strain response: after cracking and after the linear part, the curves present a steep change with the loss of stiffness due to the first layer yielding but the load keeps on increasing up to the failure.

The panel behavior is summarized in terms of failure mode in the diagram of Figure 4.53. The diagram is based on panel A4 properties and it can be considered representative of all the panels. The boundaries are computed in two ways: the solid curves according to a simplified model neglecting the tension stiffening and the aggregate bridging. The dashed curves are produced by an improved and more sophisticated formulation.

The diagram, whose formulation will not be discussed, can be useful to immediately locate the panel behavior.

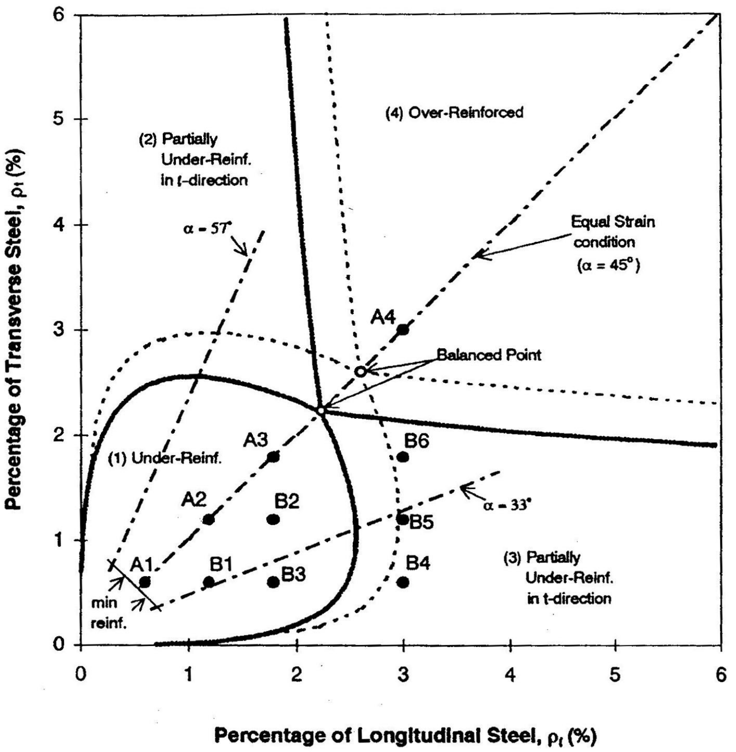

Figure 4.53 – Failure mode diagram.

4.8 – REINFORCED CONCRETE TIE

The investigation of a tensioned RC element is particularly interesting since it leads to a deep understanding of some basic problems such as crack opening, bond-slip laws, aggregate bridging and tension stiffening, which are usually part of the serviceable limit states of the structures. These phenomena are easier to capture in a simple tension experimental test than in more complicated configurations. What is more, from the numerical point of view, this comparison is a fundamental step to verify the model and its implementation.
The experimental test was already investigated by a numerical simulation which is here reported as a parameter for comparison [10].

4.8.1 – Experimental test and numerical modeling

The 200-mm long specimen is reinforced by a 8-mm steel bar in the center of the 40x40-mm square section (Figure 4.54). The uniaxial tensile and compressive concrete strength are f_t=3.66 MPa and f_c=56 MPa respectively, the concrete elastic modulus is E_{c0}=36300 MPa and the steel elastic modulus is E_s=200000 MPa.

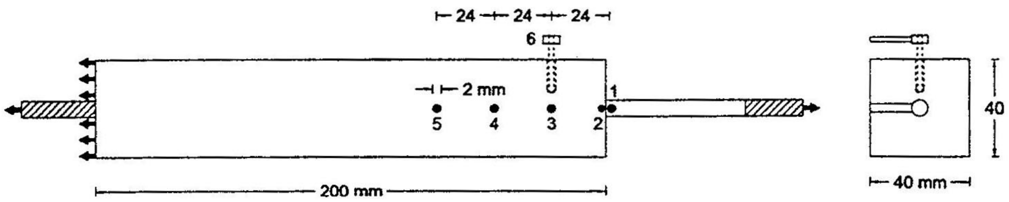

Figure 4.54 – Problem geometry.

The first specimen end is glued to the experimental setup in order to create a stage I situation: the stresses are transmitted by both steel and concrete. The test procedure is performed in a displacement control mode. The displacement is applied to the steel bar at the second specimen end. During the casting procedures, four 2-mm diameter steel bars are glued to the central bar and, emerging from the concrete, they allow to read the steel bar displacements in the related points. The concrete displacements are measured directly on the concrete external surface.
The experimental test is carried out with the speckle photography technique. This method, proposed in the '70s, provides a resolution near to 10^{-3} mm and therefore, it allows to investigate the very early cracking stages. Moreover, this technique allows to measure the displacement of some selected points without locally influencing the structural behavior. The

measuring setup is reported in Figure 4.55. The displacements are measured by using photographic and interferometric techniques. By comparing the Young fringes in the pictures taken before and after the load increment, it is possible to evaluate the direction and the amplitude of the displacement of the selected point.

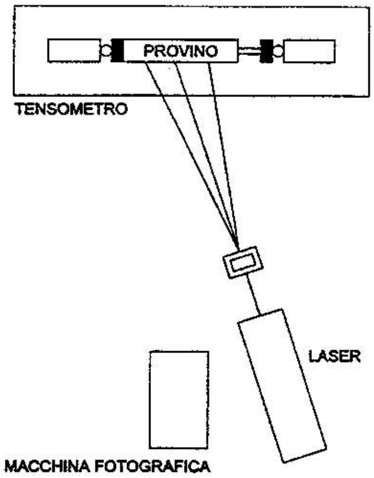

Figure 4.55 – Sketch of equipments for "speckle photography".

The specimen is modeled in ABAQUS with a 528-element mesh (Figure 4.56). Due to the double symmetry, only a quarter of the specimen is modeled. The 20-node quadratic reduced integration solid element C3D20R is used with two different constitutive models in order to simulate the plain concrete and the reinforced regions. Therefore, two different materials are used: the first one is plain concrete, the second one is the combination of concrete and smeared reinforcements. The external action is applied on the reinforced elements in order to simulate the real experimental procedure. The boundary conditions at the first end are simulated by constraining every node on the face not to move along the specimen axis.

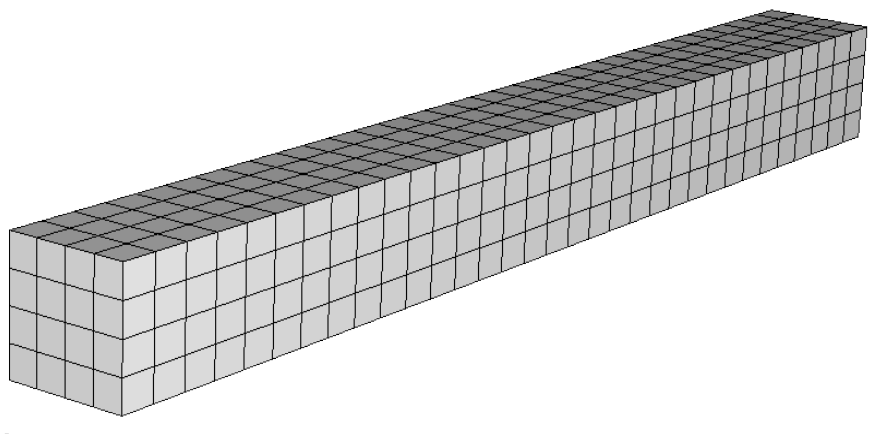

Figure 4.56 – FE discretization (a quarter of the specimen).

In order to investigate the model reliability, several analyses with different meshes are carried out and it appears that the outcomes are coincident. This demonstrates that the model has a good mesh independence.

In the previous numerical analysis [10], the tie is modeled as blocks in series separated by cracks. By using the planar section hypothesis, the problem is reduced to a uniaxial one and, afterwards, the equilibrium and the compatibility are imposed. After taking into account the constitutive models, the bond-slip relation and the boundary condition, the differential problem is written and solved by the multiple shooting method.

The proposed FE analysis presents some major differences compared to the previous one. The planar section hypothesis is not valid anymore and, in general, the problem is no longer uniaxial but fully 3D. In fact, the stresses are transferred from the reinforced elements to the plain concrete elements by the tangential stresses with a non-planar deformation and, due to the small specimen size, the problem cannot be modeled as axisymmetric.

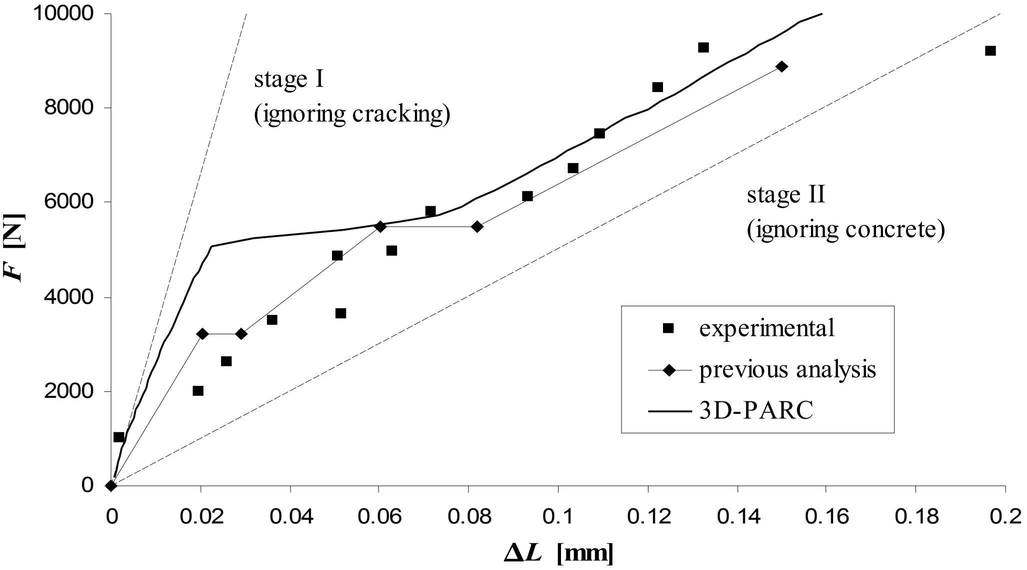

Figure 4.57 – Force-displacement result comparison.

4.8.2 – Results and comparisons

Figure 4.57 compares the FE analysis outcomes, the experimental data and the previous analysis results in terms of force-displacement curves. The global response computed by 3D-PARC is in good agreement with the experimental data and with the previous analysis results. The numerical investigation allows to evaluate the stiffness evolution and to trace it accurately. Moreover, the validity of tension stiffening and aggregate interlock formulations is demonstrated. Therefore, it can be concluded that the proposed model is able to capture the general structural behavior.

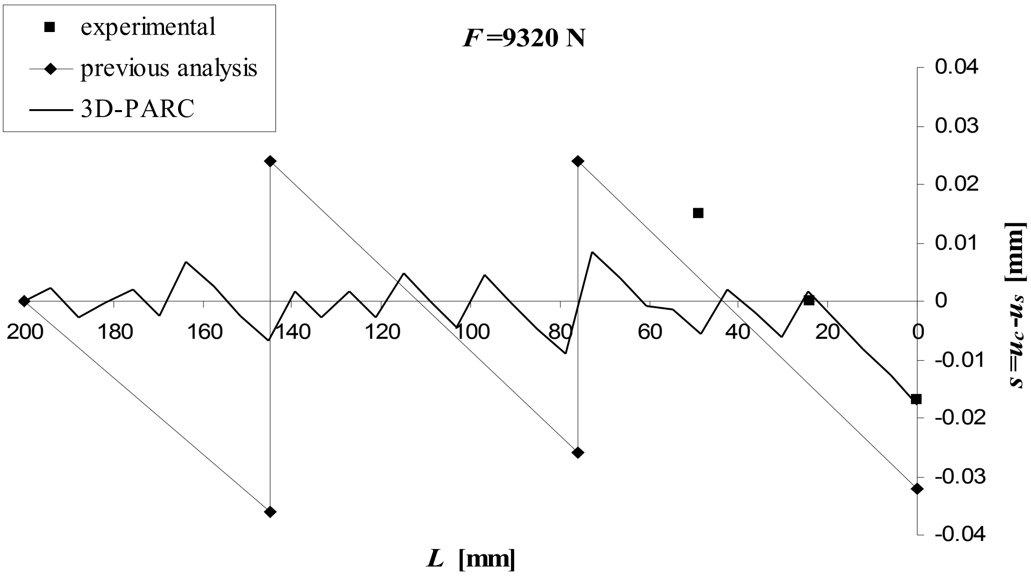

Figure 4.58 – Slip comparison.

Figure 4.58 shows the slip distribution along the specimen. The experimental values are limited to the measuring points 2, 3 and 4 indicated in Figure 4.54. The previous analysis is able to capture the effect of the two main cracks whereas the proposed model simulates the cracking phenomenon by a smeared crack distribution. However, the first two experimental points are perfectly fitted by the proposed model.

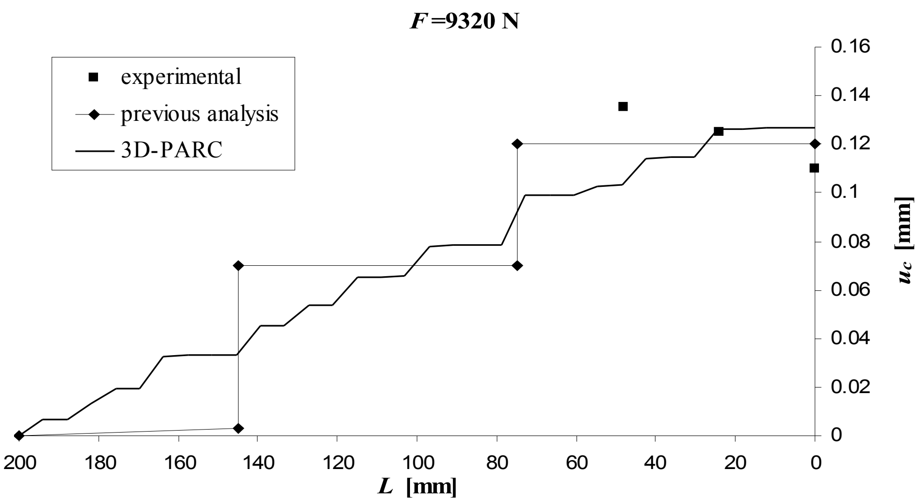

Figure 4.59 – Concrete displacement comparison.

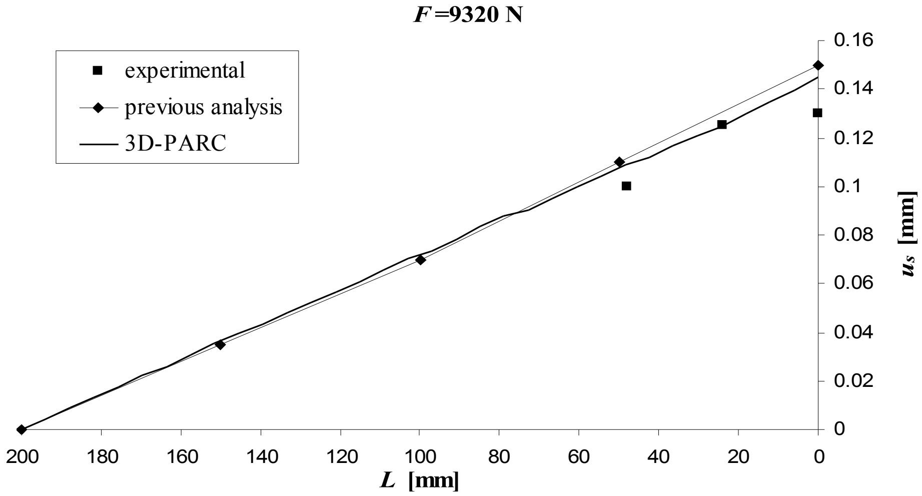

Figure 4.60 – Steel displacement comparison.

In figures 4.59 and 4.60 the concrete and steel displacements are separately plotted.
The main difference between the proposed model and the previous one lies in the function of the bond-slip law. In 3D-PARC, in fact, the bond-slip law is used only to compute the tension stiffening coefficient g. The crack spacing a_m, on the contrary, is an input parameter and does not depend on the bond-slip law.

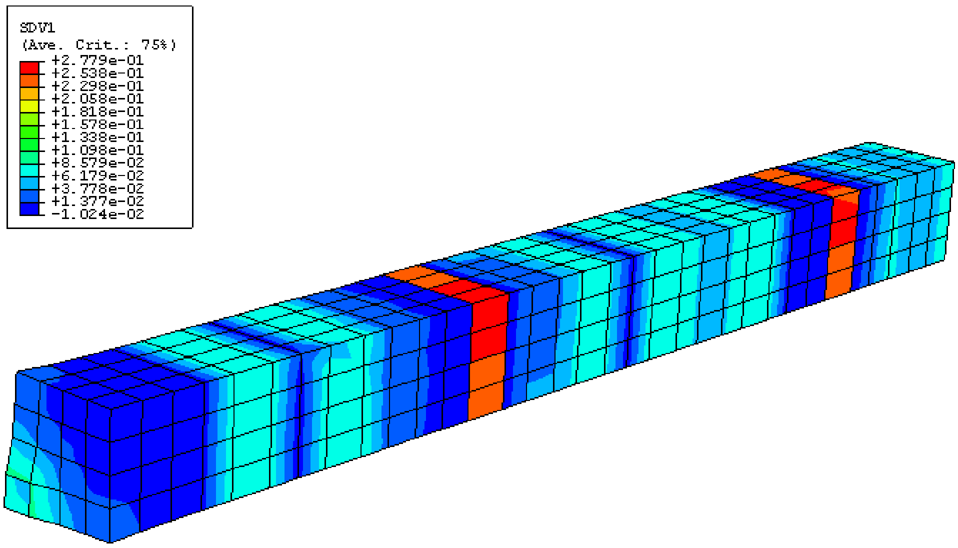

Figure 4.61 – Crack width distribution.

This means that the position of the two main cracks, defined in the previous analysis by the bond-slip law, is defined in the proposed model only by the stress diffusion. This leads to a distributed cracking along the specimen. However, it must be noted that the aggregate interlock can simulate a bond effect based on the shear transfer at the boundary between the reinforced and the unreinforced elements. In fact, as it can be clearly seen in the crack width distribution (Figure 4.61), two main cracks are located at L=73 and 163 mm from the second specimen end. This finding is in very good agreement with the experimental values of 76 and 144 mm. This effect can be deduced also from the stress distributions reported in figures 4.62 and 4.63.

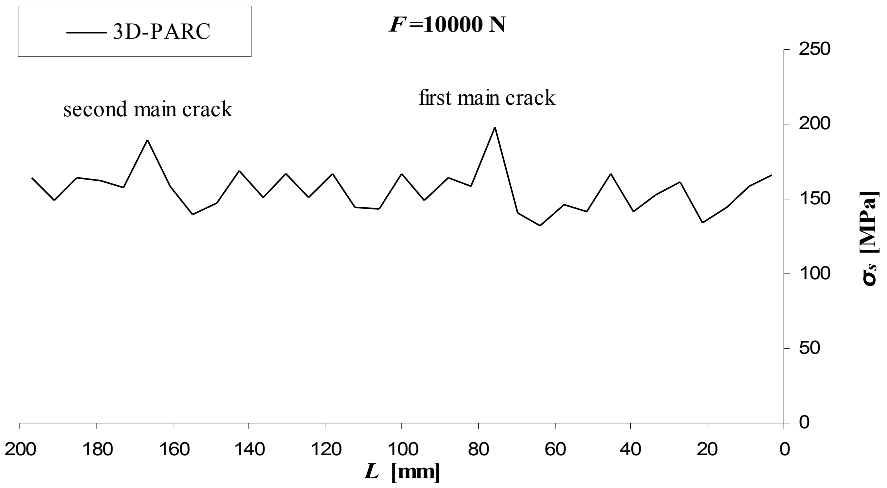

Figure 4.62 – Steel stress distribution.

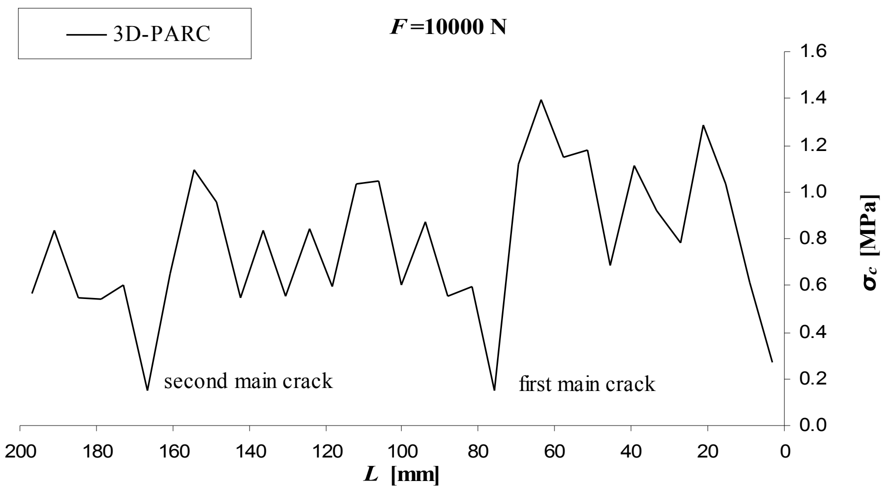

Figure 4.63 – Concrete stress distribution.

Finally, it can be concluded that the proposed model provides a good interpretation of the global physical phenomena, but it is less accurate than an application dedicated to the particular problem. On the other hand, 3D-PARC is characterized by a better flexibility, since, as a general purpose model, it can be applied to any type of structure through the FE method. Therefore, the achieved outcomes can be considered very satisfactory.

4.9 – TORSION OF PLAIN CONCRETE BEAMS

4.9.1 – Experimental tests and numerical modeling

This study analyzes two plain concrete members subjected to pure torsion in order to verify the theoretical model and the numerical implementation in the FE framework. These full 3D cases give the chance to check the concrete formulation in detail, since there are no steel, dowel action and tension stiffening effects.

Two 1500-mm long beams are selected from the experimental program [24]. The specimen A2 presents a rectangular, 254x381-mm section while the specimen A3 presents a square, 254x254-mm section.

The uniaxial compressive strength is f_c=28.6 MPa and the maximum aggregate size is 20 mm. The rest of the material properties such as the tensile strength, the elastic modulus and the fracture energy, are computed through the Model Code 90 suggestions [12].

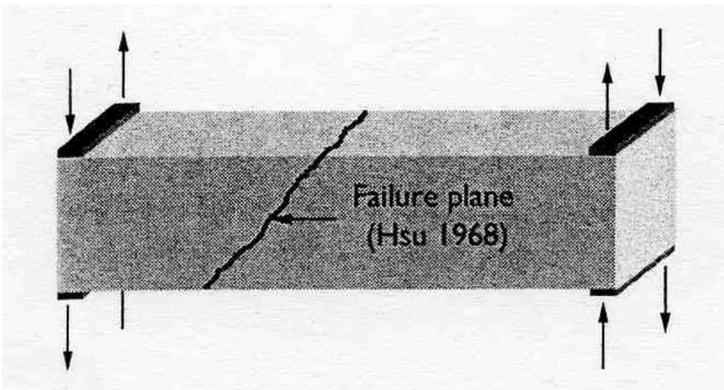

Figure 4.64 – Experimental setup and failure plane.

The experimental setup is shown in Figure 4.64. In the experimental tests, a load control procedure was chosen and therefore, no experimental data are available in the post peak region. On the contrary, in the numerical simulation, a displacement control method is adopted in order to capture the post peak behavior.

The displacements are imposed at both ends through two steel plates. The axial deformation is not restrained.

Both beams and plates are modeled in ABAQUS by using the 20-node quadratic reduced integration solid element C3D20R. In particular, the FE mesh contains 528/352 elements and 2909/2045 nodes for the beam A2 and A3 respectively. For the plates, a linear elastic material is used.

4.9.2 – Results and comparisons

Figure 4.65 represents the deformed mesh for the beam A3.

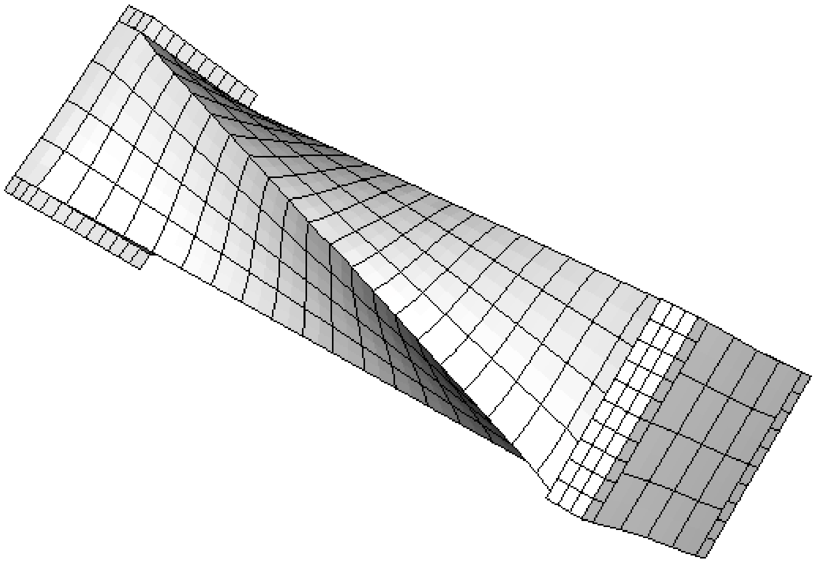

Figure 4.65 – Beam A3 deformed shape.

The torsional moment-torsional angle relationship is shown in figures 4.66 and 4.67. The agreement is very high for the beam A3, while the simulation is less accurate for the beam A2. However, 3D-PARC is able to capture the overall physical phenomenon as well as the post peak descending branch of the curve.

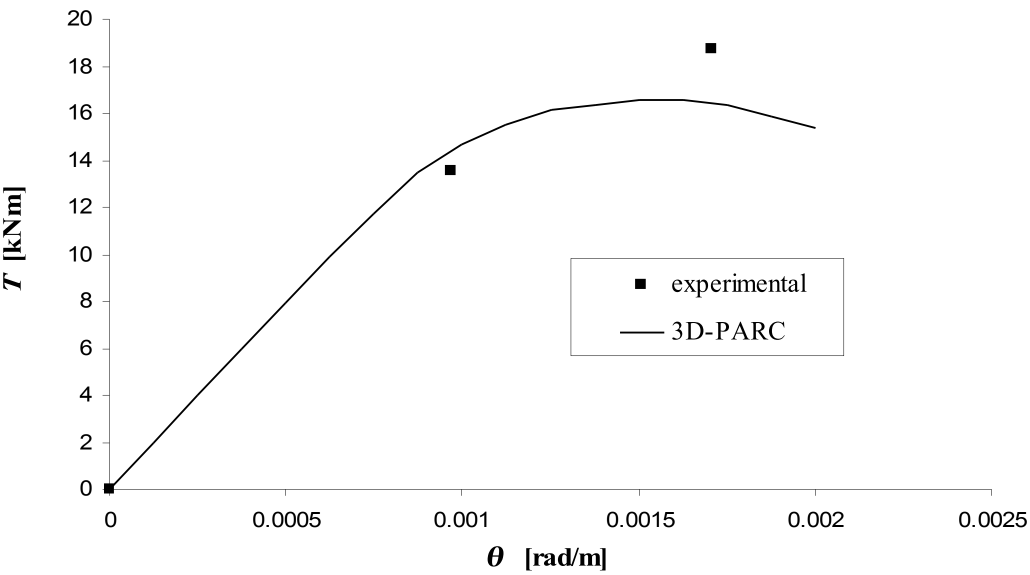

Figure 4.66 – Result comparison for the beam A2.

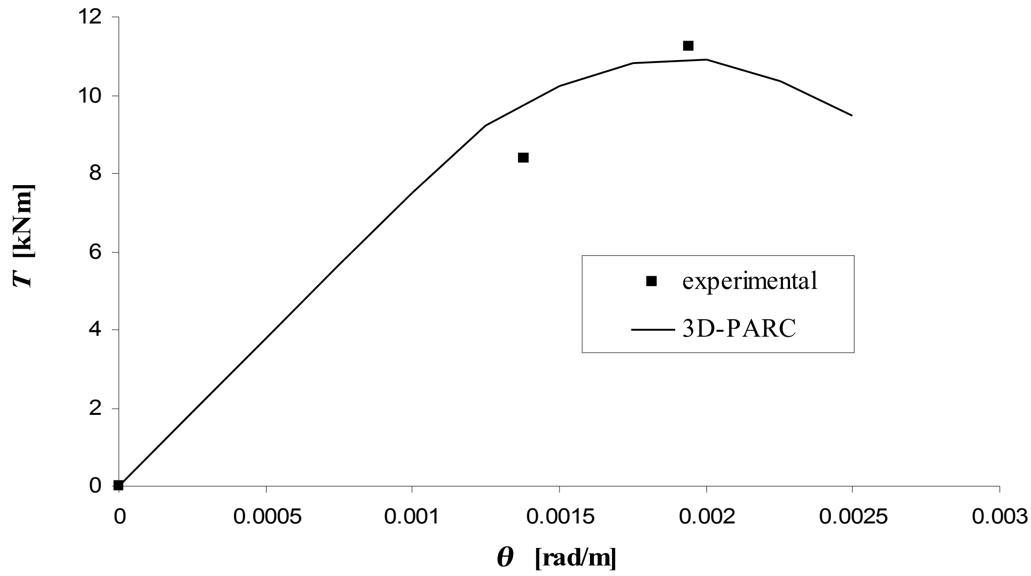

Figure 4.67 – Result comparison for the beam A3.

The investigated beams were studied from a numerical point of view by Maekawa, Pimanmas and Okamura [32]. The principal strain distribution at failure in the beam A3 obtained by that simulation is reported in Figure 4.68. This outcomes can be compared with the crack opening distribution obtained by using 3D-PARC shown in Figure 4.69.

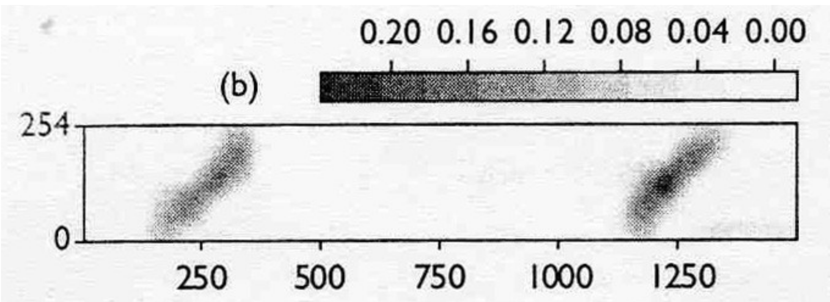

Figure 4.68 – Principal strain distribution [%] at failure in the beam A3.

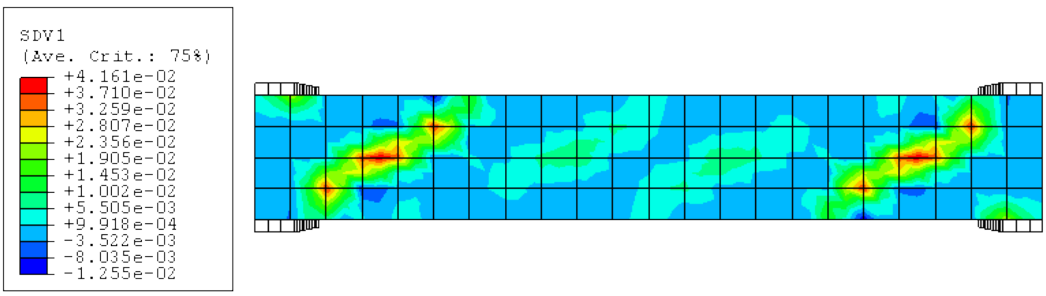

Figure 4.69 – Crack opening distribution [mm] at failure in the beam A3.

4.10 – TORSION OF REINFORCED CONCRETE BEAMS

4.10.1 – Experimental test and numerical modeling

Lampert and Thürlimann carried out a wide experimental program on a great number of beams subjected to torsion, bending and shear loading and their combinations. The program meant to develop a reliable analytical formulation for the beam computation based on empirical data. The experimental procedures are known to be performed very accurately and the outcomes, published in four volumes, are very detailed.

Up to now, the experimental programs were usually focused on small specimens with a rectangular solid section. Therefore, the authors decided to base the tests on a square hollow section, reinforced with ordinary steel, with a proper amount of transversal steel and a significant size which allows the results to be used for practical applications.

From November 1965 to February 1967, 15 square-section beams were tested at ETH institute in Zurich. Four beams were subjected to pure torsion [29]. The first three had a hollow section while the fourth was a solid section beam.

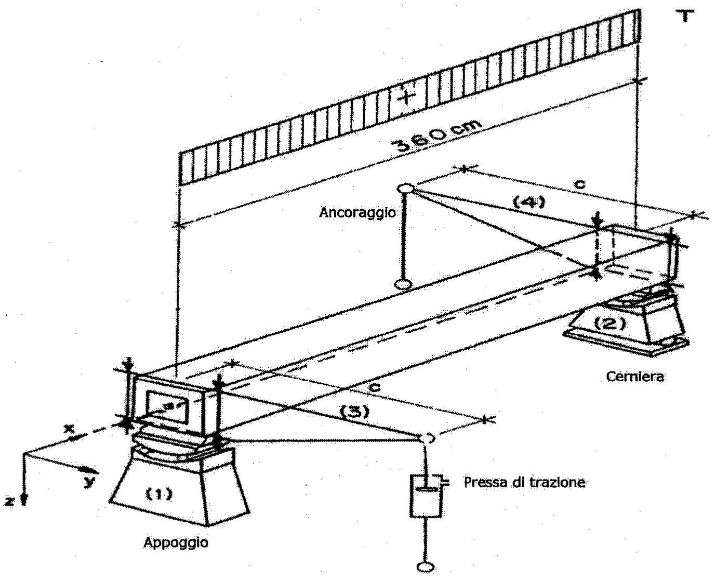

Figure 4.70 – Experimental setup.

The same amount of longitudinal and transversal reinforcements were used for all the beams while the reinforcement distribution was changed in the specimens. Since all the rest of the material properties were kept constant, the effect of the reinforcement location on structural behavior could be easily highlighted. In particular, the effect of the steel arrangement was

investigated in relation to the crack pattern evolution, to the ultimate load and to the internal stress distribution. Moreover, the influence of the central concrete core on the beam behavior could be determined.
The experimental facility, built for this program, is shown in Figure 4.70. A load control procedure was used by imposing increments of torsional moment. One beam end was fixed through an anchorage while, at the second end, the load was applied through a hydraulic press. The axial displacements were not restrained.
Since this program wanted to investigate not only the ultimate load but, overall, the involved physical phenomena, many different variables were recorded: torsional moment, torsional angle, stress in the longitudinal steel, stress in the transversal steel, crack opening, concrete strain.
Each load increment was carried out in three phases in order to correctly record the data. In fact, if the torsional moment had been kept constant during the measuring procedures, the data would have been affected by the viscosity. Therefore, after the load increment, in the first phase, (about 1 minute) the moment was kept constant and the moment itself and the torsional angle were recorded. Afterwards, the torsional angle was kept constant (from 7 to 80 minutes) and all the other measurements were performed. The third phase was analogous to the first one but the torsional moment recorded in this phase was smaller than the first one.
For each beam, several concrete and steel specimens were tested in order to obtain the values of the material properties. The concrete uniaxial compressive strength was about f_c=26 MPa, the steel yielding strength was f_{sy}=365 MPa and the steel elastic modulus was E_s=206000 MPa for all the beams.

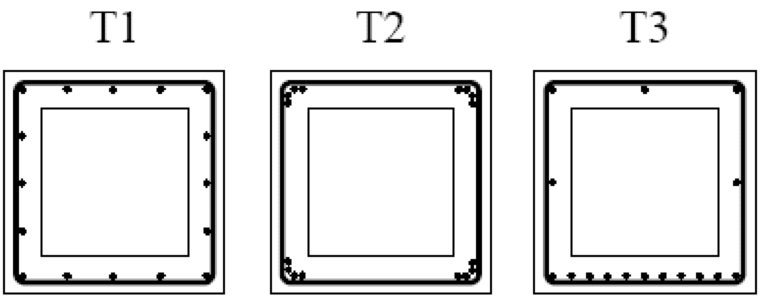

Figure 4.71 – Investigated beam sections.

Only the beams T1, T2 and T3 are considered in this study. All the beams are 3600-mm long and have a 500x500-mm hollow square section with 80-mm thick walls. The longitudinal reinforcements were 16 12-mm diameter bars and the stirrups were 12-mm diameter bars with a constant spacing equal to 110 mm. The steel amount is the same for all the beams while the reinforcement arrangement is different as it can be seen in figures 4.71 and 4.72. In the beam T1, the longitudinal steel is equally distributed along the walls, in the T2, it is concentrated at the angles and, in the T3, it is concentrated at the bottom side. The T3 adopts the typical reinforcement arrangement used in bended beams.

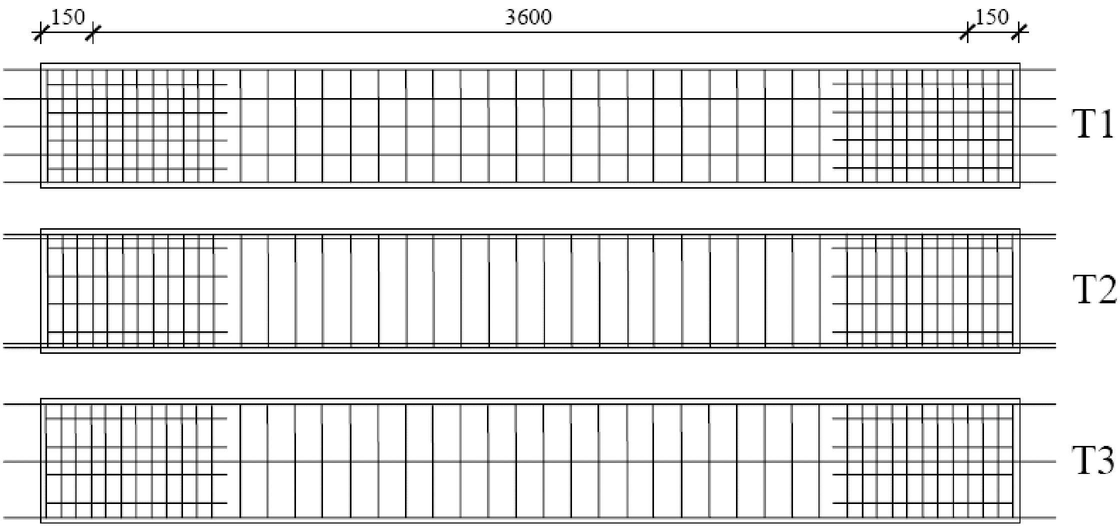

Figure 4.72 – Reinforcement arrangements.

The experimental program wanted to validate the 3D truss model for the calculation of beams subjected to pure torsion. The struts are the compressed diagonals which form in the concrete while the ties are the steel bars (Figure 4.73). By this formulation, it is possible to evaluate the internal stress distribution depending on the ratio between longitudinal and transversal steel. According to the Eurocode approach [13], the ultimate torsional moment can be computed through the following procedure.

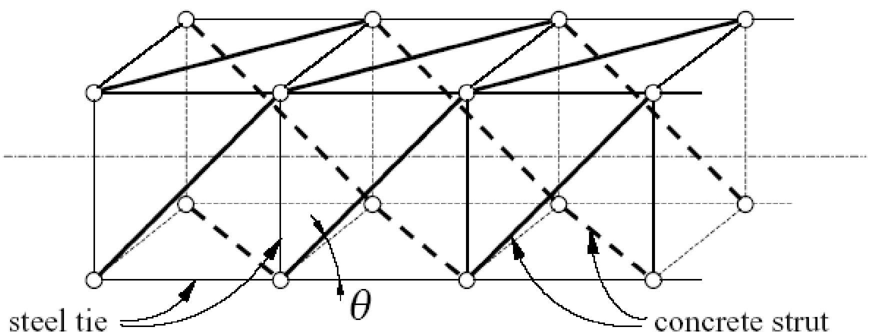

Figure 4.73 – The 3D truss model.

The torsional moment carried by the longitudinal steel is

$$T_l = 2A_k f_{sy} a_l \frac{1}{\cot\theta} \tag{4.8}$$

and the one carried by the transversal steel is

$$T_s = 2A_k f_{sy} a_s \cot\theta\,, \tag{4.9}$$

where

$$a_l = \frac{A_l}{u_k} \text{ and } a_s = \frac{A_s}{s}\,, \tag{4.10}$$

being A_k the area internal to the mean line of the section walls, θ the angle between the beam axis and the concrete struts, A_l the total longitudinal steel area, u_k the perimeter of the area A_k, A_s the area of a single stirrup and s the stirrup spacing.
The angle θ can be computed as

$$\cot\theta = \sqrt{\frac{a_l}{a_s}}\,. \tag{4.11}$$

In order to evaluate the longitudinal or the transversal steel failure, some empirical limits are chosen. If $0.4 \leq \cot\theta \leq 2.5$, the longitudinal and transversal steel are considered to be well balanced and to fail simultaneously. If $\cot\theta < 0.4$, the failure is caused by the longitudinal steel yielding and the constant value 0.4 is adopted. Finally, if $\cot\theta > 2.5$, the constant value 2.5 is used, since the transversal steel fails before the longitudinal steel.

Beam	***Experimental***		***Analytical***			***3D-PARC***		
	***T_{exp1}* [kN m]**	***T_{exp2}* [kN m]**	***T_{an}* [kN m]**	$\frac{T_{an}}{T_{exp1}}$	$\frac{T_{an}}{T_{exp2}}$	***T_u* [kN m]**	$\frac{T_u}{T_{exp1}}$	$\frac{T_u}{T_{exp2}}$
T1	*147*	*132*	*136*	*0.93*	*1.03*	*135*	*0.92*	*1.02*
T2	*146*	*134*	*136*	*0.93*	*1.01*	*135*	*0.92*	*1.01*
T3	*120*	*108*	*96*	*0.80*	*0.89*	*108*	*0.90*	*1.00*

Table 4.3 – Ultimate load comparison.

This model makes an attempt to consider the internal stress redistribution. The simultaneous steel failure is caused by the concrete strut orientation: θ is not fixed at 45 deg but varies in

the range 22-63 deg. The concrete struts are considered not able to orientate outside this range and, in that case, a constant value is used.
The ultimate load values computed by this analytical method are reported in Table 4.3. The “exp1” and “exp2” indicate the torsional moment measured at the beginning and at the end of the loading step respectively.

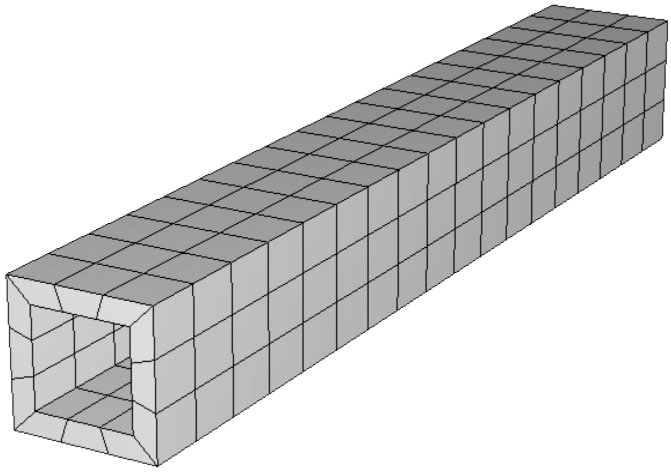

Figure 4.74 – Beam T1 FE discretization.

The beams T1, T2 and T3 are investigated through 3D-PARC. Figure 4.74 represents the FE discretization for the beam T1. For the other two beams a similar mesh is adopted. The 20-node quadratic reduced integration solid element C3D20R is used. The meshes consist of 216, 240, 240 elements and 1572, 1740, 1740 nodes for the beam T1, T2 and T3 respectively. Several different materials are used depending on the steel ratio and on the bar orientation. A load control method is applied.

4.10.2 – Results and comparisons

Several different variables are extracted from the numerical simulation and compared with the experimental data. In the following pages, the torsional moment-torsional angle curve, the stress in the longitudinal steel as well as in the stirrups, the concrete compressive strain and the mean crack opening are reported and discussed in detail.
The ultimate load values are reported in Table 4.3 and the torsional moment-torsional angle curves are shown in figures 4.75, 4.76 and 4.77 for the beams T1, T2 and T3 respectively.
The experimental outcomes are a very good validation of the 3D truss model for the beams T1 and T2. For these beams, the ultimate load can be captured with high accuracy by the analytical model, while, for the beam T3, the response cannot be computed with the same

precision. It must be considered that, for the beam T3, the analytical value is computed considering the longitudinal steel as made of only eight bars, neglecting the over-reinforcing steel of the bottom side. In other words, since only three bars are located in the weaker side, only three bars are considered active for each side. Probably, in the experimental test, some other mechanical phenomena are activated and the steel of the over reinforced side, through an internal stress redistribution, contributes to the ultimate load.

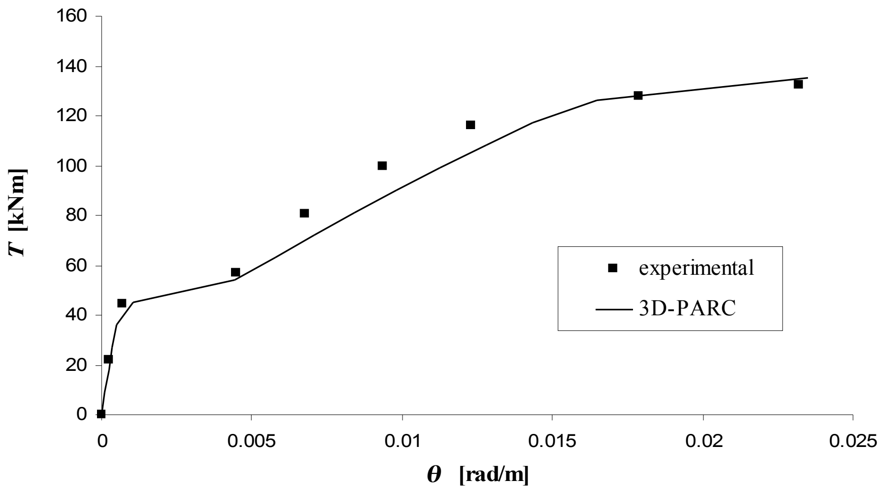

Figure 4.75 – Torsional moment-torsional angle result comparison for the beam T1.

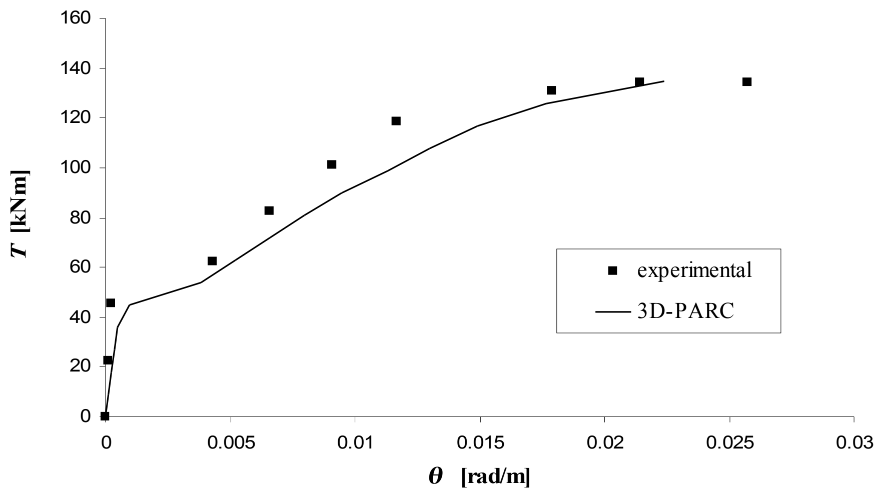

Figure 4.76 – Torsional moment-torsional angle result comparison for the beam T2.

The beams T1 and T2 are characterized by the almost simultaneous yielding of the longitudinal and transversal steel and they behave in a very similar way. Therefore, it can be concluded that the different reinforcement arrangements (distributed or concentrated at the angles) have a little influence on the response providing, in both cases, an effective support to the diagonal concrete struts. In the beam T2, the concrete struts are supported directly by the longitudinal steel in the angles, since there are no bars in the middle of the face.

After a first linear part, when the cracking is reached, the load is equally transferred to the longitudinal and to the transversal steel which were not previously loaded. This creates a sudden increment of torsional rotation. The equal contribute of the longitudinal and transversal steel is highlighted also by the concrete strut orientation θ=45 deg visible on the specimen. Moreover, the beam T2 exhibits a ductile response after the peak which is not reported in the figures since it is not possible to capture it in a load-controlled numerical simulation.

The 3D-PARC results are in very good agreement with the experimental data.

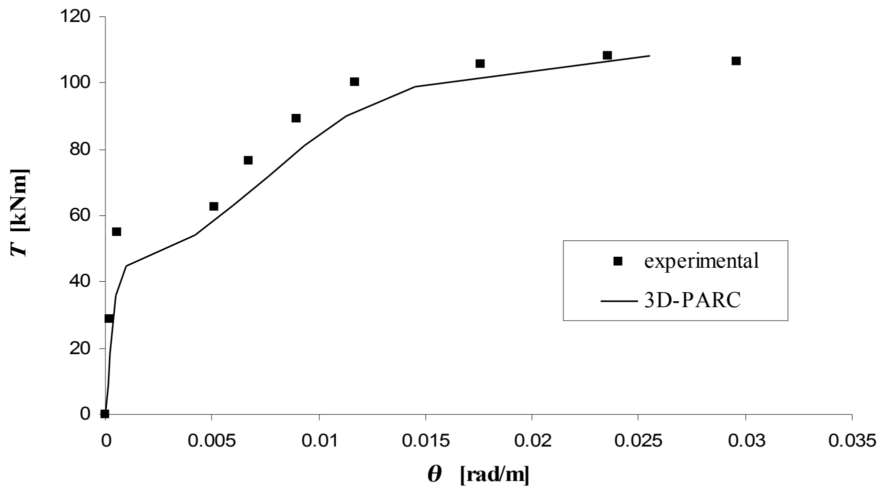

Figure 4.77 – Torsional moment-torsional angle result comparison for the beam T3.

The beam T3 is particularly interesting due to the strong asymmetry in reinforcement location. Due to the concrete strut orientation, the transversal steel equilibrates the lack of longitudinal steel in three of the four sides. Subsequently, the steel of the over-reinforced side gives a contribute increasing the ultimate load. Finally, the failure is caused by the yielding of three of the four beam sides. The strut orientation is also visible from the specimen crack pattern. Moreover, it can be noted that, in the beam T3, the experimental cracking moment is higher than the simulated one. Since the material properties were kept constant during the specimen preparation, it could be probably concluded that this behavior is related to an experimental scattering.

3D-PARC provides very good results for this beam: it is able to capture the concrete strut orientation and the consequent higher contribute given by the transversal steel. Moreover, the

strengthening effect, which cannot be captured by the analytical calculation, provided by the over-reinforced side, is detected through an higher ultimate load.
Figure 4.78 shows the deformed mesh of the beam T2. The other beams present a similar shape.

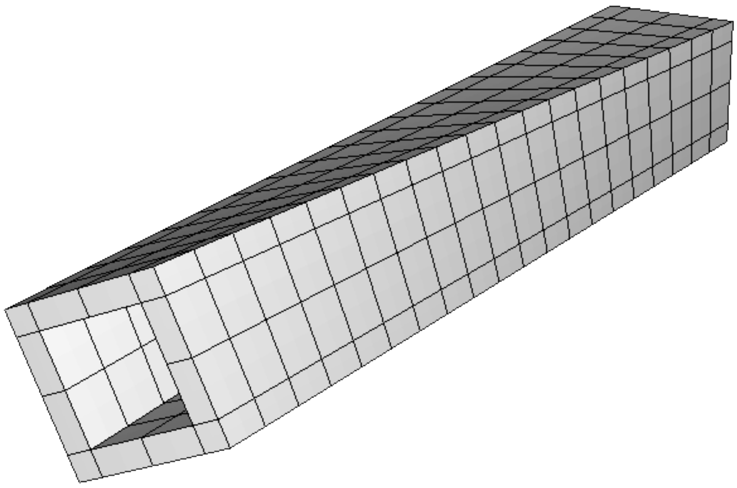

Figure 4.78 – Beam T2 deformed shape.

The longitudinal steel stresses are shown in figures 4.79, 4.80 and 4.81. Similarly, the transversal steel stresses are shown in figures 4.82, 4.83 and 4.84.
For the beams T1 and T2, since the stress difference at the top and at the bottom faces is negligible, a single line is plotted while, for the beam T3, three different curves related to the top, the bottom and the sides are specified. The agreement is generally good even if it can be noted that, as a general trend, the steel stresses are slightly under-estimated.

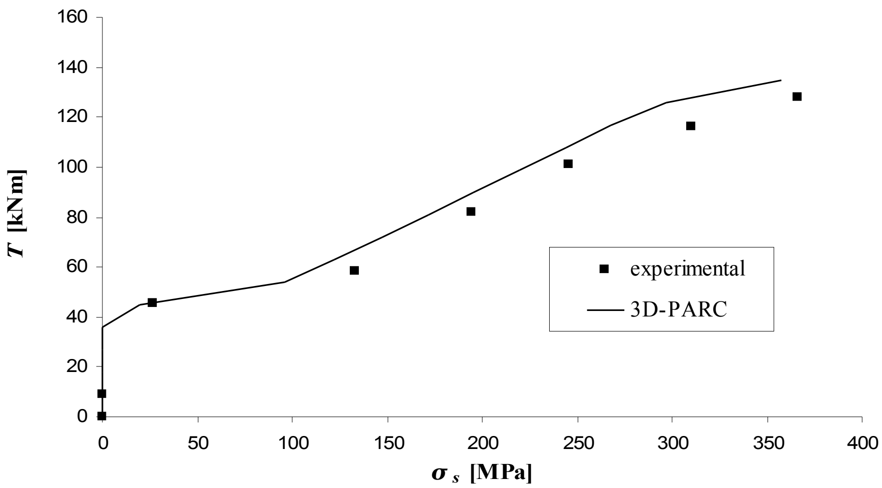

Figure 4.79 – Stress in longitudinal steel comparison for the beam T1.

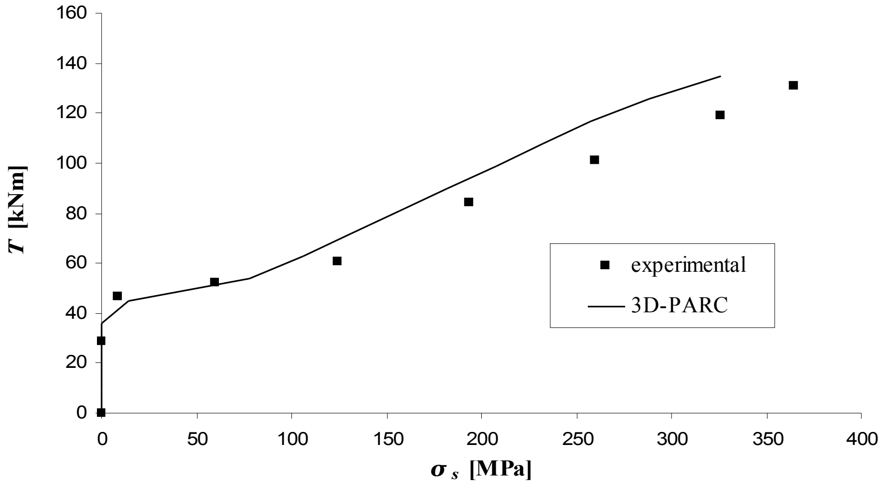

Figure 4.80 – Stress in longitudinal steel comparison for the beam T2.

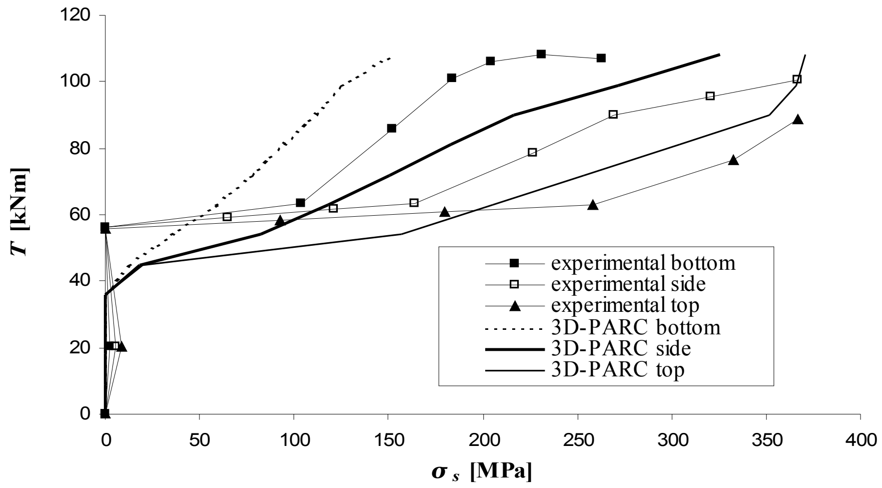

Figure 4.81 – Stress in longitudinal steel comparison for the beam T3.

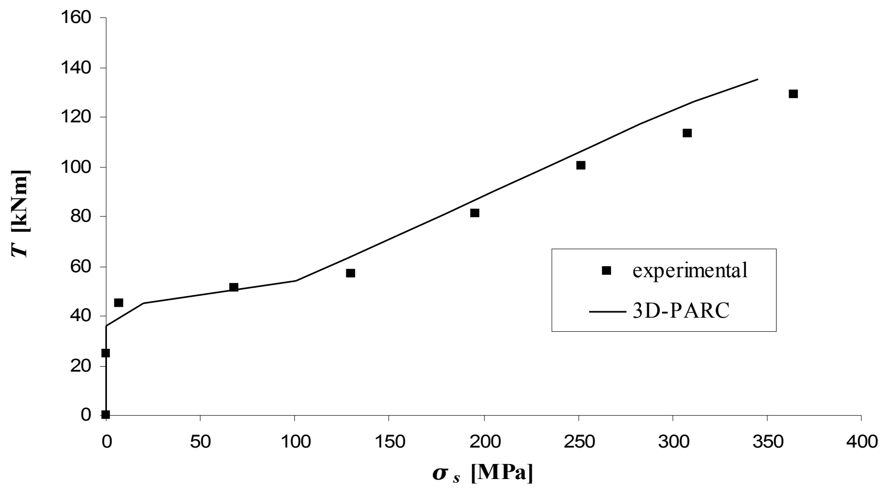

Figure 4.82 – Stress in transversal steel comparison for the beam T1.

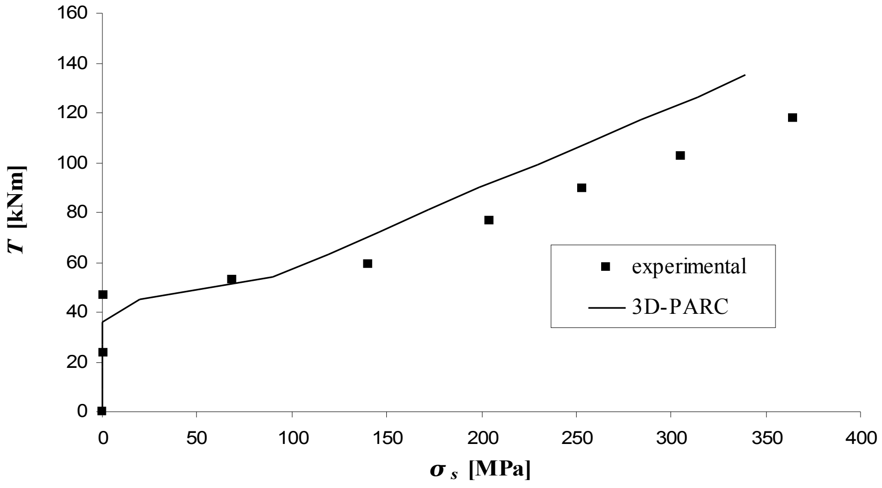

Figure 4.83 – Stress in transversal steel comparison for the beam T2.

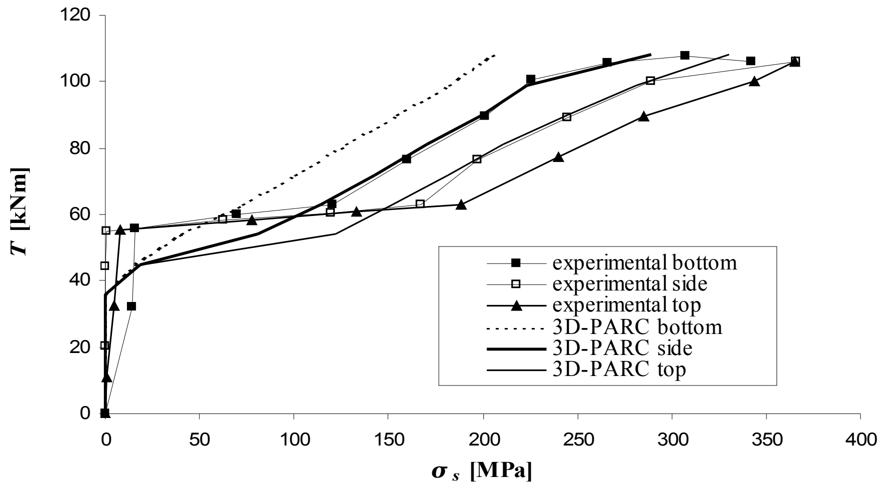

Figure 4.84 – Stress in transversal steel comparison for the beam T3.

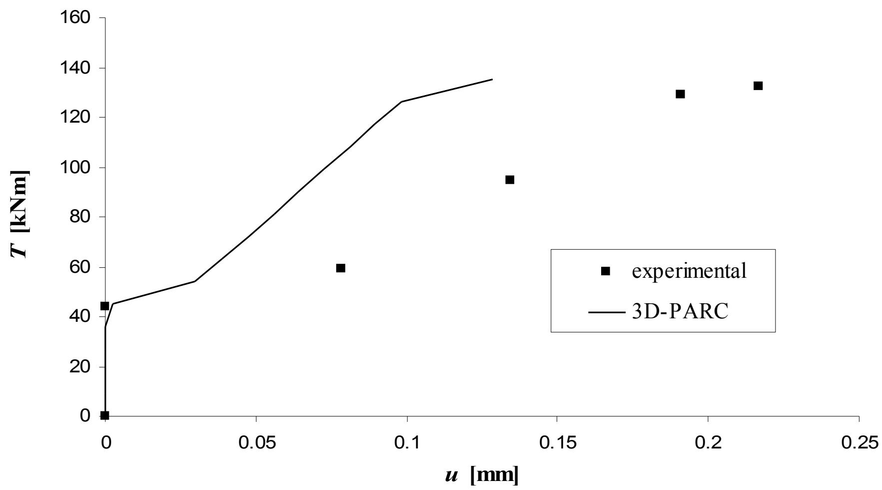

Figure 4.85 – Crack opening comparison for the beam T1.

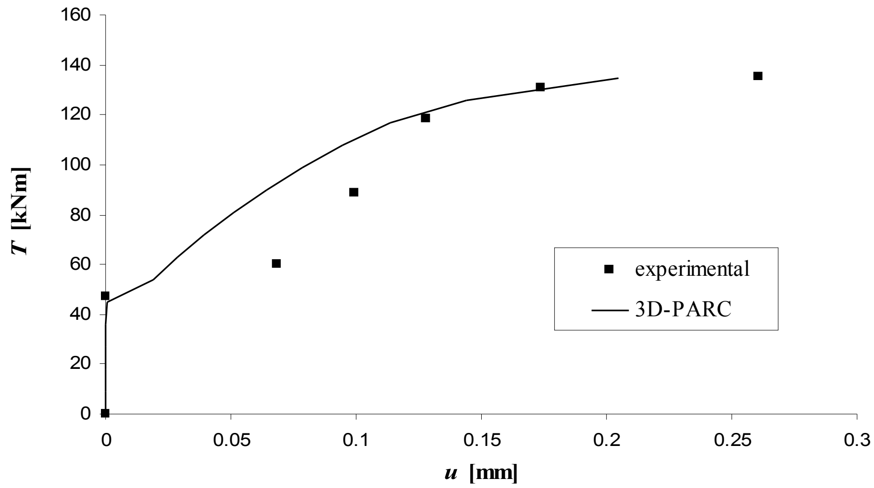

Figure 4.86 – Crack opening comparison for the beam T2.

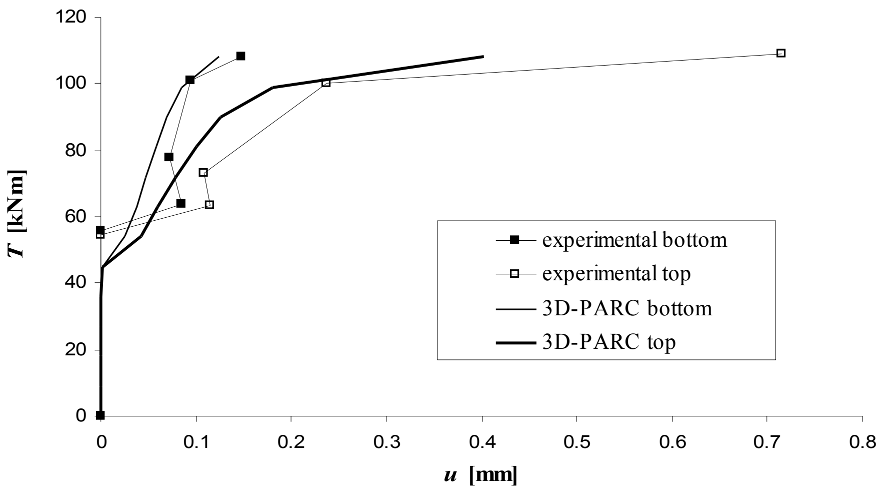

Figure 4.87 – Crack opening comparison for the beam T3.

Figures 4.85, 4.86 and 4.87 show the crack opening comparisons. In the beam T2, the crack opening in the middle of the faces is higher than in the other beams since no reinforcements are located in that region. For the beam T3, a strong difference can be noted between the top and the bottom face due to the different reinforcement arrangement.

Figures 4.88, 4.89 and 4.90 report the concrete compressive strain. In the experimental data, there are two main changes in the curve slope: at the cracking load level and at the steel yielding level when the concrete has to carry a bigger load to maintain the equilibrium. For all the beams, the strain increment due to the steel yielding is clearly detected by the proposed model, while the strain increment due to the cracking is less evident.

In general, for the crack opening as well as for the concrete strain, the simulated response is stiffer than the experimental one.

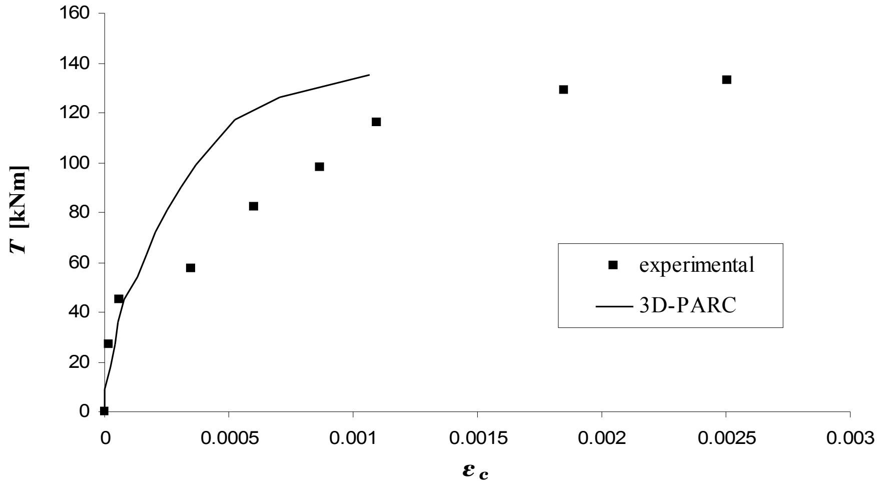

Figure 4.88 – Concrete compressive strain comparison for the beam T1.

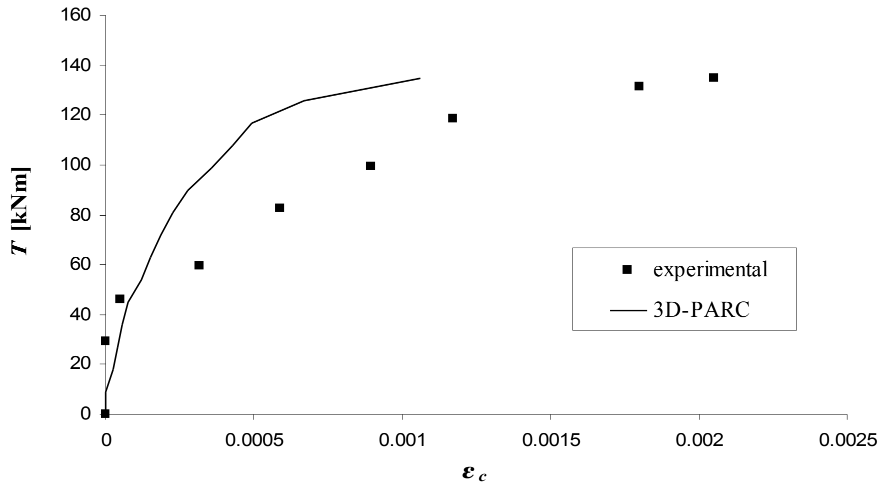

Figure 4.89 – Concrete compressive strain comparison for the beam T2.

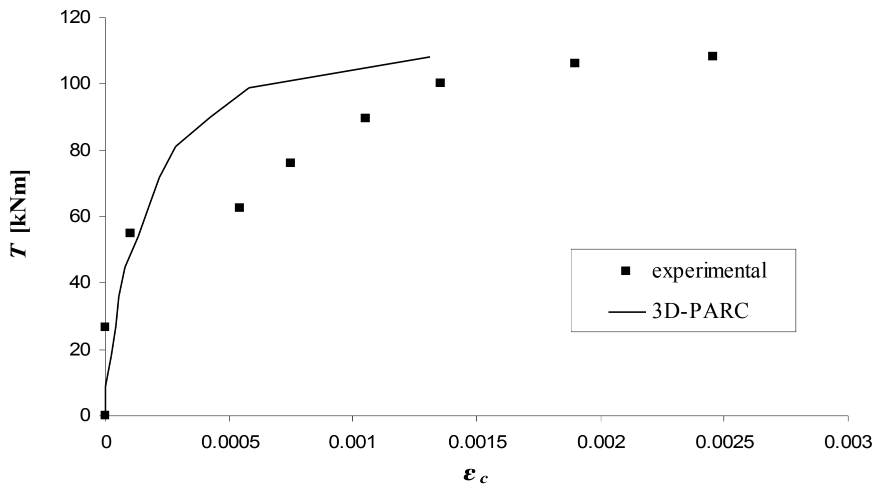

Figure 4.90 – Concrete compressive strain comparison for the beam T3.

The results achieved by the numerical simulations are very satisfactory. 3D-PARC is able to capture the beam structural behavior. The internal stress distribution due to the concrete strut orientation is clearly detected. Moreover, for the beam T3, the strengthening effect of the over-reinforced side is well highlighted.
Secondly, the proposed model formulation, inserted in the FE framework, allows to reveal also the local behaviors for any element in the structure. For these beams, the steel stresses, the crack opening and the concrete compressive strain are extracted from the FE model in some significant positions and compared to the experimental data obtaining a reasonable accuracy.
All these comparisons allows to conclude that 3D-PARC is able to capture the global structural behavior as well as the local phenomena.

CHAPTER 5 – ANALYSIS OF REINFORCED CONCRETE CORBELS

5.1 – INTRODUCTION

Corbels are widely used in precast concrete structures due to the main advantages of better concrete quality as well as improved speed and lower costs of construction. In the last century, many different theories have been proposed to describe the corbel behavior and several experimental programs have been carried out to investigate these structures from a practical point of view.

This chapter describes a numerical study of reinforced concrete (RC) corbels. The original work was carried out at the Institute of Structural Engineering (IKI) of the University of Natural Resourced and Applied Life Sciences – BOKU in Vienna, from October 2004 to March 2005 [35, 36]. The working plan is divided into three different phases.

- Two-dimensional (2D) deterministic analyses. Corbels from wide experimental programs are investigated by using the RC-oriented Finite Element (FE) code ATENA 2D. Several different specimens, including Steel Fiber Reinforced Concrete (SFRC) type, are simulated in order to find out whether the code is able to capture the structural behavior.
- 2D probabilistic analyses. A statistical study is carried out by using the software package SARA – Structural Analysis and Reliability Assessment. The uncertainties related to the materials are simulated by a randomization process. A 50-sample analysis based on an advanced Monte Carlo technique is used to find out the ultimate load distribution. Finally, the safety level is determined and compared with the one suggested by the Eurocode.
- Three-dimensional (3D) deterministic analyses. In the last step of the study, some of the corbels are investigated taking into account the full 3D behavior and inserting a different constitutive model for concrete.

The numerical simulations presented in this contribution are performed by the FE code ATENA which is an effective and reliable tool for non-linear analysis of RC structures. It is developed by Cervenka Consulting and it has been validated by many different applications and examples [18].

Advanced material models based on hypoelasticity or fracture-plasticity approaches are implemented within ATENA. Cracking phenomena are modeled by smeared crack approach. Fixed or rotating cracks can be assumed. Reinforcements can be modeled with smeared or discrete approach. In the latter case, the effect of reinforcement bond can be included by using several bond-slip laws. In addition, the constitutive models are fully customizable by modifying the material parameters or by introducing user-defined laws.

The FE model can be created in the CAD-like ambient which is capable of automatic meshing operations. Monitoring point can be specified in order to extract the required outcomes in some particular locations. Several advanced solving techniques such as Newton-Raphson, modified Newton-Raphson, arc length and line search, are implemented.

The structural behavior is strictly related to material and geometric properties. One of the main problems in numerical simulations is the uncertainty related to the structural properties. Therefore, in order to establish practical design techniques fulfilling the required safety level, a probabilistic approach is necessary.

In this contribution, the statistical procedures are performed by the multipurpose probability-based software FREET. The process is divided into three stages: stochastic modeling, sampling and assessment.

In the first stage, the uncertainties related to the materials are modeled by suitable Probability Density Functions (PDF). Moreover, a correlation matrix for the basic variables is defined. In the second stage, since non-linear FE calculation is usually a time-consuming process, an advanced Monte Carlo Latin Hypercube Sampling (LHS) technique is included in the sampling stage in order to decrease the number of simulations necessary to achieve accurate statistical results. Finally, in the third stage, the results from the FE simulations are evaluated in order to assess the reliability and the safety level of the structure.

The interaction between ATENA and FREET is managed by the software package SARA, which has been validated by many applications [11, 39, 40, 43].

In detail information about these softwares can be found in the related documentation [15, 16, 17].

5.2 – EXPERIMENTAL PROGRAMS

The corbels investigated in this study are taken from two wide experimental programs.
The first one is a very important reference for the study of corbels [26]. The work was carried out in 1964 at Research and Development Laboratories of the Portland Cement Association. A large number of specimen was tested – 124 corbels subjected to vertical load only and 71 corbels subjected to combined vertical and horizontal loads – divided in three series: exploratory test, vertical load, vertical and horizontal loads. The final objective of this study was to develop design criteria for these structures.
The exploratory tests were made to define testing procedures and reinforcing detailing; the other two series were a systematic investigation of the effect of several variables on corbel behavior.

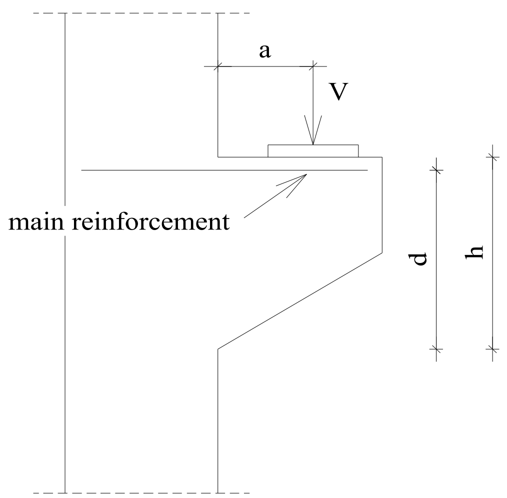

Figure 5.1 – Corbel sketch.

In particular, during the experimental program, the following properties were changed:

- reinforcement ratio;
- concrete strength;
- ratio of shear span to effective depth (*a*/*d*);
- amount and distribution of stirrup reinforcement;
- size and shape of corbel;
- ratio of the vertical to the horizontal load.

A corbel sketch with the main geometric properties is reported in Figure 5.1.
After the exploratory tests, it was possible to conclude that the corbel strength was not

significantly affected by the additional load carried by the column. Moreover, these preliminary tests provided useful observations about the reinforcement detailing: the compressive reinforcement in the corbel and the longitudinal bars in the column had little influence on the ultimate load. Furthermore, cross-bars welded to the main reinforcement ends could avoid bond failure and main reinforcements bent near the corbel outer edge could create a very weak zone. Therefore, in the subsequent tests, the reinforcements were set in order to obtain significant results.

All the specimens were built on a 203x305-mm column with two corbels arranged symmetrically to make the testing procedures easier. Three cylinders were taken for each specimen to determine the concrete compressive strength. For convenience, all the corbels were tested in an upside-down position (Figure 5.2).

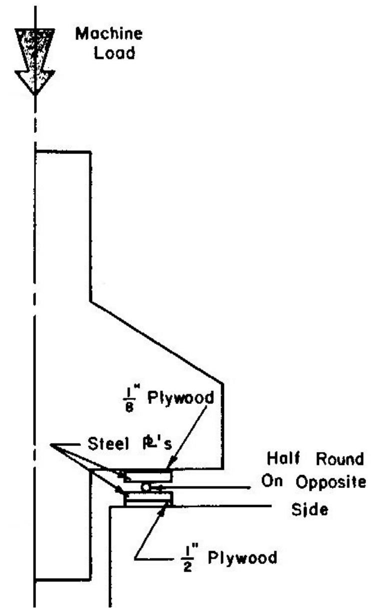

Figure 5.2 – Kriz-Raths test configuration.

SFRC is a material with improved properties regarding the post cracking behavior and the ductility. The second experimental program was focused on SFRC corbels in order to increase the amount of data regarding the application of this material to corbels and therefore, to achieve more general design criteria for these structures [22].

The tests were performed on 32 RC corbels subjected to vertical load. SFRC was used in 26 specimens as shear reinforcement in order to improve the strength and the ductility.

During the experimental program, the following properties were changed:

- the volume ratio of the fibers;
- the main reinforcement;

- the ratio of shear span to effective depth (*a*/*d*).

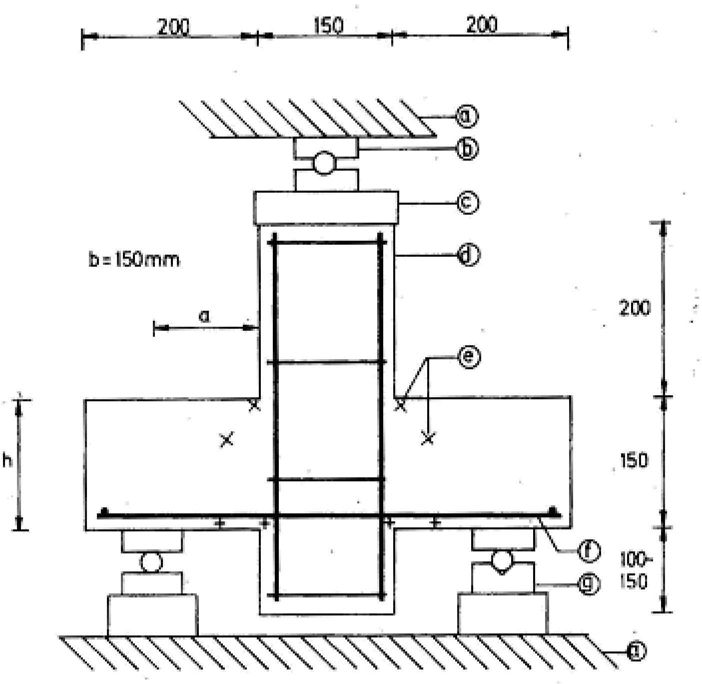

Figure 5.3 – Fattuhi test configuration.

The steel fibers used to reinforce the concrete were hooked, diameter 0.5 mm, length 30 mm, with an average tensile strength of 1100 MPa. Six different volume ratios from 1.0% to 2.5% were used. Seven different main reinforcements were used ranging from 101 mm^2 to 509 mm^2 in different diameter combinations, with an average yielding strength of 451, 454, 452 and 427 MPa for 8, 10, 12, 18 mm bars respectively. The shear span-to-depth ratio varied within a range from 0.40 to 0.92. All the columns were designed with a 150x150-mm cross section and were reinforced with four 12-mm longitudinal bars and four 6-mm lateral ties. Plastic spacers were used to ensure a 20-mm concrete cover for the main bars.

The casting procedures were set to produce the corbels and three 100-mm cubes, three 150-mm cubes and three 100-mm diameter by 200-mm long cylinders. Cubes and cylinders were tested to find out the concrete properties.

The experimental tests were carried out with an upside-down configuration as shown in Figure 5.3. All the corbels were vertically symmetrical to avoid bending effects.

The first test was performed with a load control mode, but the specimen failed suddenly with no possibilities to record its behavior near the peak load. Therefore, for all the other specimens, a displacement control was used. In this way, the post peak behavior could be properly investigated.

5.3 – TWO-DIMENSIONAL ANALYSIS

5.3.1 – Theoretical basics

In the 2D version of ATENA, the material is considered in a plane stress state, neglecting the full 3D behavior. Smeared cracking and discrete reinforcement approaches are used. This means that the modeling is realized by superimposing plain concrete elements and steel reinforcing bar elements. Each material is modeled separately. However, ATENA 2D provides also a smeared reinforcement approach.

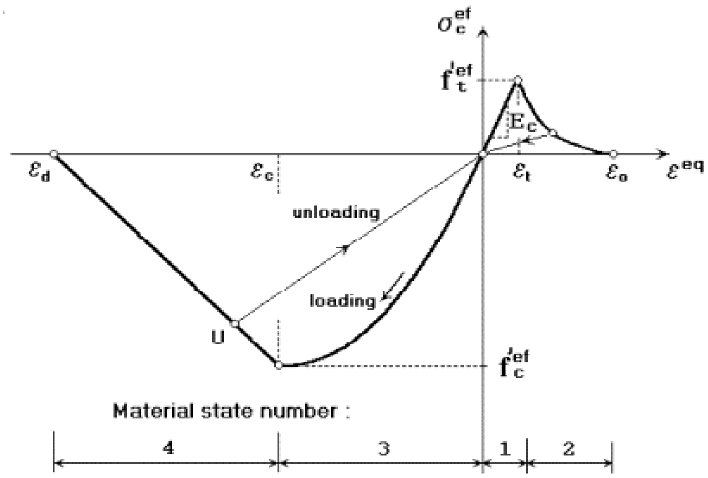

Figure 5.4 – Uniaxial constitutive model for concrete.

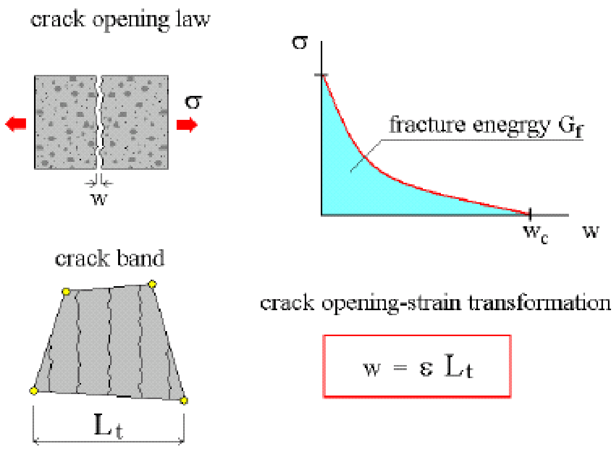

Figure 5.5 – Concrete behavior in tension.

Concrete is modeled by the SBETA material with standard parameters. The stress-equivalent strain curve is shown in Figure 5.4. A different number provided as output denotes every region and can be used to evaluate the concrete failure. In the ascending branch of the compressive field, the Model Code 90 [12] formulation is adopted, while the post peak behavior is assumed to be linearly descending.

In the tensile field, pre-cracking behavior is assumed to be linear elastic; after cracking, a fictitious crack band model based on a crack opening law and on fracture energy is used. Different laws can be specified; an exponential case is shown in Figure 5.5.

By this formulation, a real discrete crack is simulated by a band of localized strains. Since the crack strain is related to the FE size, a softening law in terms of strain is written for each element while the crack opening law is preserved.

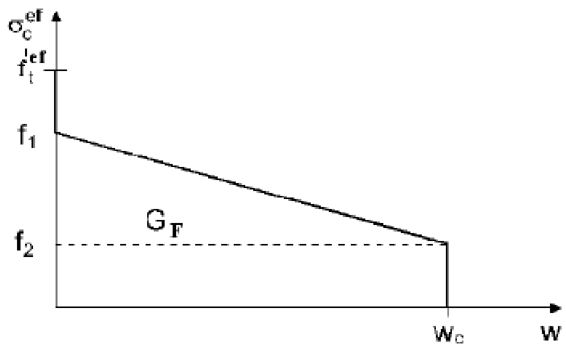

Figure 5.6 – SFRC law.

A different law is adopted to model the SFRC, as shown in Figure 5.6. In this case, the user is requested to introduce the values of f_1, f_2 and of fracture energy G_f.

In this work, f_1 is taken equal to the concrete tensile strength f_t while f_2 is calculated according to ACI committee 544 [2] by the equation

$$f_2 = 0.772F\frac{L}{D}V_f\,, \tag{5.1}$$

where F is a bond factor (ranging from 1 to 1.2), L is the fiber length, D is the fiber diameter and V_f is the fiber volume ratio. Finally, the fracture energy G_f is computed as the area under the curve.

Both fixed and rotating crack approaches are implemented.

The failure criterion, built according to experimental results, is shown in Figure 5.7. It is divided in tensile failure and compressive failure zones: if the domain is reached in a tensile zone, a crack occurs. Using the current stress state, the corresponding value on the domain can be found and used to build the uniaxial curve of Figure 5.4.

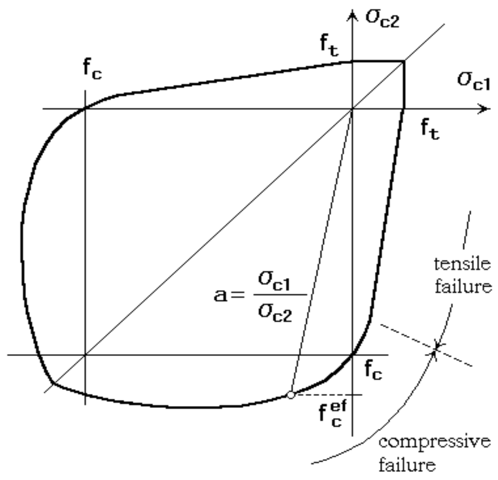

Figure 5.7 – Biaxial failure domain.

Concrete is discretized by the SBETA FE, a reduced integration quadrilateral element in which the material law is evaluated only at element centroid. The secant constitutive matrix is used.

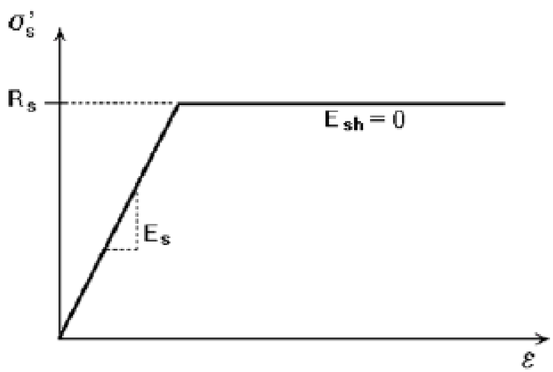

Figure 5.8 – Reinforcing bar uniaxial law.

As already mentioned, in ATENA, reinforcing bars can be inserted in two different ways, following the smeared or the discrete approach. In this work, the discrete approach is used with a bilinear elastic perfectly plastic uniaxial constitutive model (Figure 5.8). Uniaxial truss elements are used to model the reinforcing bars.

Furthermore, it is possible to include the effect of reinforcement bond by using several different bond-slip models such as CEB-FIB Model Code 90 law, Bigaj law and user-defined law (Figure 5.9). The law can be written as a function of the concrete compressive strength, reinforcement diameter and reinforcement type. Other important parameters like concrete confinement and quality can be included in this formulation.

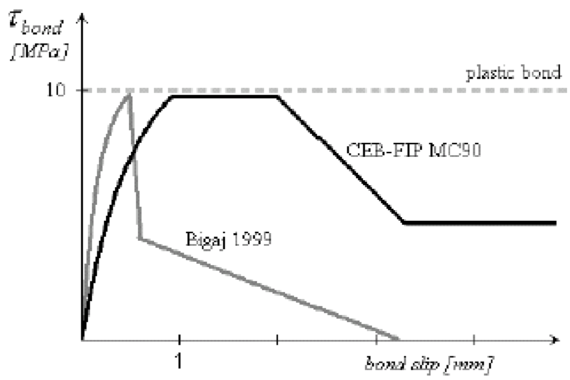

Figure 5.9 – Different ways to model reinforcement bond.

In this work, perfect connection with concrete mesh is assumed, therefore, no slip between steel and concrete is considered.

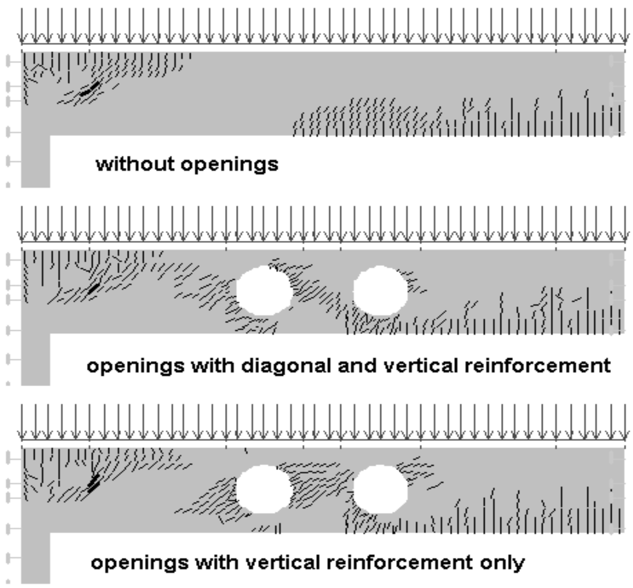

Figure 5.10 – Crack pattern of different design solutions.

The Cervenka's paper [18] shows at first some simple examples used to verify the model and then some applications to real cases difficult to solve by ordinary design tools.
The first problem is to design the reinforcements close to the openings for technical facilities in a large girder of a shopping center in Prague. The crack pattern of different design solutions is shown in Figure 5.10.
The study demonstrates that the beam with a good reinforcement arrangement can withstand the same load as the beam without openings (Figure 5.11).

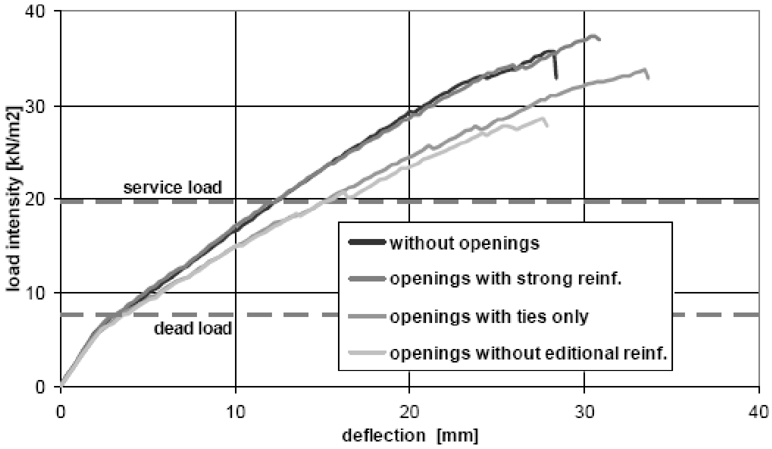

Figure 5.11 – Load-displacement curve for different design solutions.

Secondly, the axisymmetric problem of a column-slab joint is investigated in order to check whether the reinforcements are adequate to prevent a brittle punching failure (Figure 5.12). Several failure modes are taken into account and can be investigated by artificially modifying the material properties. For example, the column compressive ultimate load is computed by assigning the slab a linear elastic behavior.

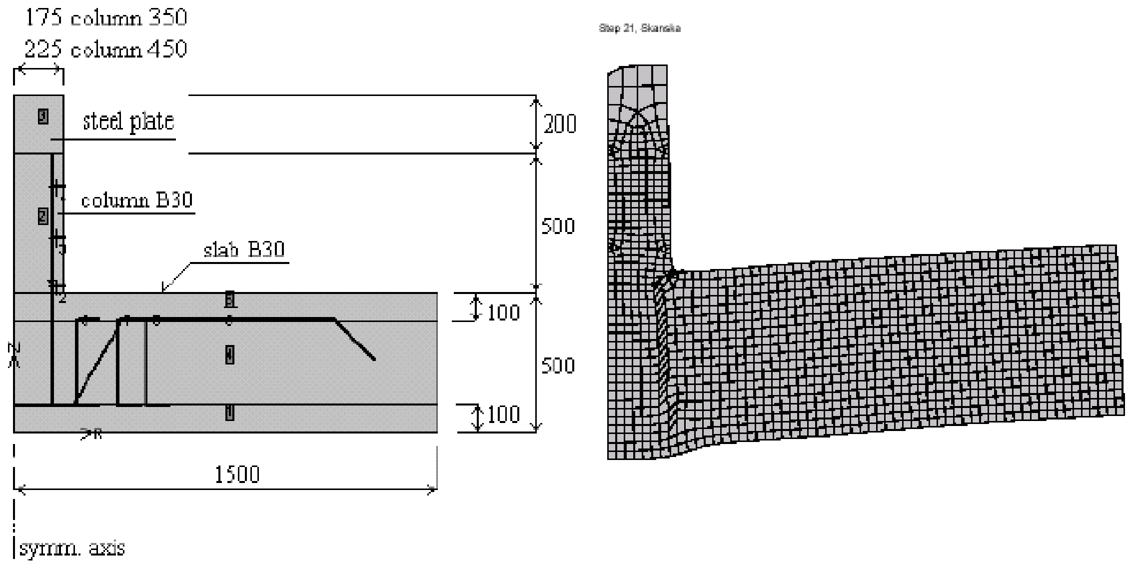

Figure 5.12 – Problem geometry and deformed shape.

In the full unconstrained analysis, where all the failure modes are allowed, the punching mode gives the lowest resisting load. Therefore, the study demonstrates that the reinforcements are inadequate to prevent the brittle punching failure but, by changing the location of the same amount of reinforcements, the load capacity can be highly increased.

5.3.2 – Structural modeling

Seven corbels from the Kriz-Raths program and five from the Fattuhi program, with different failure modes, are investigated in this work, performing both deterministic and probabilistic analysis. In the Kriz-Raths experimental program, the specimens were subjected to both vertical and horizontal loads; in the FE simulations, only the specimens with vertical load are tested. The corbel properties are reported in tables 5.1 and 5.2. The "fr" in the corbel name indicates a SFRC specimen. The fiber ratios used for the selected corbels are V=2.00% for corbel F23 and F37 and V=1.50% for corbel F35.

Corbel	Geometry					Concrete	Steel	
	a [mm]	h [mm]	b [mm]	d [mm]	a/h	f_{cm} [MPa]	f_{ym} [MPa]	A_s [mm^2]
KR13	152	559	203	513	0.27	31.6	352	260
KR14	152	660	203	615	0.23	31.3	352	260
KR21	152	660	203	615	0.23	27.0	298	400
KR55	254	559	203	513	0.45	27.7	312	396
KR80	152	559	203	513	0.27	16.8	300	510
KR91	121	457	203	406	0.26	28.0	322	1014
KR100	121	457	203	406	0.26	44.3	328	1014

Table 5.1 – Kriz-Raths corbel properties.

Corbel	Geometry					Concrete	Steel	
	a [mm]	h [mm]	b [mm]	d [mm]	a/h	f_{cm} [MPa]	f_{ym} [MPa]	A_s [mm^2]
F23fr	110	149	153	123	0.74	28.3	452	226
F25	110	149	154	123	0.74	30.7	452	226
F34	135	148	154	122	0.91	32.0	452	339
F35fr	135	149	155	123	0.91	30.4	452	339
F37fr	135	149	154	122	0.91	32.2	452	339

Table 5.2 – Fattuhi corbel properties.

An example of the FE discretization used in the numerical modeling is shown in Figure 5.13. The model contains about 1400 and 650 concrete elements for Kriz-Raths and Fattuhi corbels respectively and about 30 steel elements for both models. Due to the symmetry, only half of the specimen can be modeled within ATENA in order to save computational time.

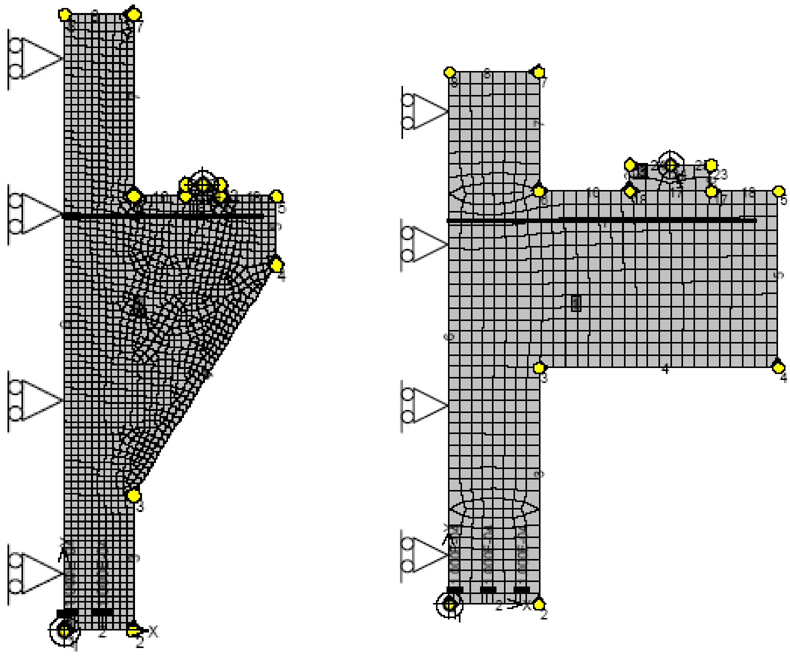

Figure 5.13 – Example mesh for Kriz-Raths (left) and Fattuhi (right) corbels.

In the numerical investigations, a displacement control method is applied. In particular, a displacement is imposed at the column base while the bearing plate is constrained not to move in the vertical direction.

For the selected specimens, a photograph after failure is available in the papers allowing to check the crack pattern numerically obtained. Moreover, since crack pattern and failure mode are strictly related, comparing these pictures is a good way of checking whether the numerical simulation is able to capture the experimental failure mode.

5.3.3 – Statistical modeling

The software package SARA integrates the FE code ATENA 2D and the statistical module FREET. Since non-linear FE analyses are usually time-consuming, an advanced Monte Carlo LHS technique is included in the software to decrease the number of simulations necessary to achieve accurate statistical results. The solution procedure within SARA is:

- modeling the deterministic problem within ATENA;
- randomization of material uncertainties according to well known distributions within FREET;
- starting from the chosen distributions, by using the LHS, several sets of input parameters are created for repeated ATENA analyses. In this work, 50 samples are used;
- running the repeated analyses of the randomized problem within ATENA;

- the results from the previous step are statistically evaluated in FREET. In particular, the outcomes are the histogram of the structural response, the sensitivity to the variables, the best numerical distribution to fit the structural response and the safety index assessment.

Material	***Variable***	***Distribution***	***COV***
concrete	E_c	*Lognormal 2-par.*	*0.08*
	f_t	*Lognormal 2-par.*	*0.12*
	f_c	*Normal*	*0.1*
	G_f	*Weibull min. 2-par.*	*0.17/0.25**
steel	E_s	*Normal*	*0.03*
	f_y	*Normal*	*0.05*

Table 5.3 – Distributions for randomized basic variables (SFRC).*

The randomized variables chosen to investigate the corbels are the elastic modulus E_c, the tensile strength f_t, the cylindrical compressive strength f_c and the fracture energy G_f for concrete, the elastic modulus E_s and the yielding strength f_y for steel.

For these basic variables, the stochastic models reported in Table 5.3 are used in the randomization process. The coefficient of variation *COV* is calculated as

$$COV = \frac{std}{m}, \tag{5.2}$$

where *std* is the standard deviation and *m* is the mean.

	E_c	f_t	f_c	G_f	E_s	f_y
E_c	*1*	*0.7*	*0.9*	*0.5*	*0*	*0*
f_t		*1*	*0.8*	*0.9*	*0*	*0*
f_c			*1*	*0.6*	*0*	*0*
G_f				*1*	*0*	*0*
E_s					*1*	*0*
f_y						*1*

Table 5.4 – Correlation matrix.

In order to capture the relation between the basic variables, a correlation matrix based on experimental results is used (Table 5.4).

For each corbel, the structural response provided by the numerical calculation is fitted by an analytical distribution in terms of PDF. What is more, a sensitivity study regarding the first four variables is performed and the outcomes of the first two variables are shown in figures. Finally, a comparison of the ultimate load safety index regarding the safety level proposed by the Eurocode is documented.

5.3.4 – Results and comparisons

The most important objective of the simulation is to test the code capabilities in capturing the real structural behavior.

Corbel	***Exp. failure***	***V_{exp} [kN]***	***ATENA (deterministic)***		***SARA (probabilistic)***	
			V [kN]	***Difference***	***V_m±std [kN]***	***Difference***
*KR13**	*T*	*266*	*279*	*4.9%*	*287 ± 14*	*7.9%*
KR14	*DS*	*374*	*367*	*-1.9%*	*359 ± 13*	*-4.0%*
KR21	*DS*	*423*	*405*	*-4.3%*	*411 ± 14*	*-2.8%*
KR55	*CE*	*269*	*255*	*-5.2%*	*255 ± 10*	*-5.2%*
KR80	*C*	*370*	*371*	*0.3%*	*372 ± 13*	*0.5%*
KR91	*S*	*546*	*585*	*7.1%*	*593 ± 29*	*8.6%*
KR100	*S*	*761*	*758*	*-0.4%*	*756 ± 31*	*-0.7%*

Table 5.5 – Kriz-Raths corbel result comparison.

** Corbel KR13 has a much higher experimental failure load and 266 kN is the steel yielding load. As this failure load seems to be related to the particular specimen and the corbel exhibits a steel failure, the steel yielding load is considered as ultimate load.*

Corbel	***Exp. failure***	***V_{exp} [kN]***	***ATENA (deterministic)***		***SARA (probabilistic)***	
			V [kN]	***Difference***	***V_m±std [kN]***	***Difference***
F23fr	*T*	*127*	*131*	*3.1%*	*131 ± 3*	*3.1%*
F25	*DS*	*109*	*103*	*-5.5%*	*103 ± 4*	*-5.5%*
F34	*DS*	*114*	*106*	*-7.0%*	*106 ± 5*	*-7.0%*
F35fr	*S*	*125*	*122*	*-2.4%*	*121 ± 3*	*-3.2%*
F37fr	*T*	*140*	*144*	*2.9%*	*144 ± 6*	*2.9%*

Table 5.6 – Fattuhi corbel result comparison.

Tables 5.5 and 5.6 show the results of this task regarding the ultimate load. In these tables, V_{exp} is the experimental ultimate load, V_m is the mean of the probabilistic distribution and *std* is the standard deviation. Moreover, the failure modes are indicated as: *T* for reinforcement tie tensile failure, *DS* for diagonal splitting, *CE* for corbel end failure, *C* for concrete strut compressive failure and *S* for shear failure.

The experimental results are compared with ATENA and SARA calculations. The former is a single deterministic analysis whereas the latter is a probabilistic evaluation based on the basic variables shown in Table 5.3.

The 50-sample ultimate load distribution is fitted, for every corbel, by an analytical distribution (tables 5.7 and 5.8). From these distributions, the 5% fractile V_5 is computed in the same table.

Corbel	*Fitting distribution*	*Mean [kN]*	*std [kN]*	*COV*	*Skewness*	V_5 *[kN]*
KR13	*Lognormal 3-par.*	*287*	*14*	*0.05*	*-0.22*	*264*
KR14	*Normal*	*359*	*13*	*0.04*	*/*	*337*
KR21	*Weibull max. 3-par.*	*411*	*14*	*0.03*	*-0.004*	*388*
KR55	*Weibull min. 2-par.*	*255*	*10*	*0.04*	*-0.96*	*236*
KR80	*Lognormal 3-par.*	*372*	*13*	*0.03*	*-0.41*	*350*
KR91	*Weibull min. 2-par.*	*593*	*29*	*0.05*	*-0.92*	*538*
KR100	*Weibull max. 3-par.*	*756*	*31*	*0.04*	*0.12*	*706*

Table 5.7 – Kriz-Raths corbel distribution properties.

Corbel	*Fitting distribution*	*Mean [kN]*	*std [kN]*	*COV*	*Skewness*	V_5 *[kN]*
F23fr	*Weibull max. 3-par.*	*131*	*3*	*0.02*	*0.22*	*126*
F25	*Weibull max. 3-par.*	*103*	*4*	*0.04*	*0.18*	*96*
F34	*Lognormal 3-par.*	*106*	*5*	*0.05*	*-0.02*	*98*
F35fr	*Weibull max. 3-par.*	*122*	*3*	*0.02*	*-0.68*	*116*
F37fr	*Weibull max. 3-par.*	*144*	*6*	*0.04*	*-0.41*	*134*

Table 5.8 – Fattuhi corbel distribution properties.

For Kriz-Raths corbels, the mean difference of the ultimate load regarding the experimental values is 3.4% for the deterministic and 4.2% for the probabilistic calculation. The corresponding values for Fattuhi corbels are 4.2% and 4.3% respectively. Therefore, the agreement is generally very high both for normal and SFRC corbels also considering that, as only one specimen was tested for each corbel, the experimental results could be scattered.

Moreover, the deterministic and the mean probabilistic values are mainly in good agreement.
It can also be observed that the material stochastic models of Table 5.3 lead to a ultimate load scattering of *COV*=0.02-0.05. Furthermore, the Weibull functions (minimum 2-parameter and maximum 3-parameter) are the best way to fit the resistance distribution of the investigated corbels.
ATENA allows extracting the model variable values for each step in order to investigate the mechanical behavior of the structure.
In Figure 5.14 the steel force vs. the vertical load is reported and compared with experimental data for Kriz-Raths corbels with *a*/*d*=0.30. The numerical simulations provide very good results and are capable to follow all the phases of the experimental tests.

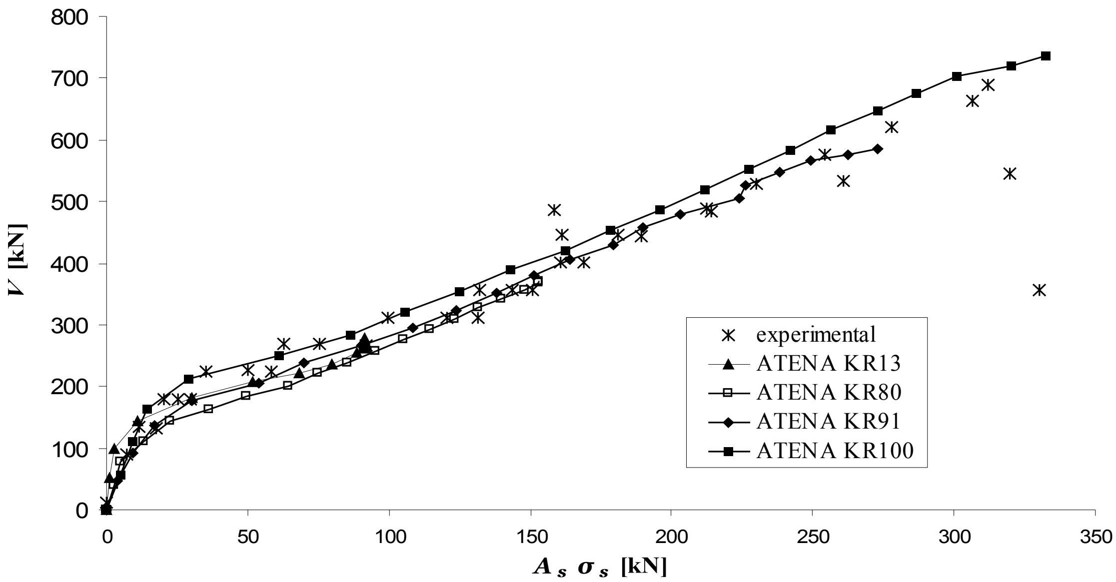

Figure 5.14 – Relation between applied load and steel force for corbels with a/d=0.30.

Furthermore, the crack pattern of the investigated structure can be extracted and compared with the experimental pattern for each corbel. Since the crack pattern is strictly related to the failure mode, comparing these pictures is a good way of checking the numerical outcomes.
Figures 5.15 and 5.16 show the crack pattern for corbels KR14 and F25. The numerical analysis can simulate the experimental response very accurately. Both corbels are characterized by diagonal splitting failure as can be clearly seen in the figures. At first, the flexural crack pattern is fully developed. Later, as the load increases, the compressed concrete fails by shear-compression and the diagonal splitting is revealed by a crack line extending from the bearing plate towards the end of the inclined bottom face of the corbel.
Therefore, it can be concluded that the numerical simulation is able to capture the

experimental failure mode. The crack patterns of all the corbels can be like wise interpreted.

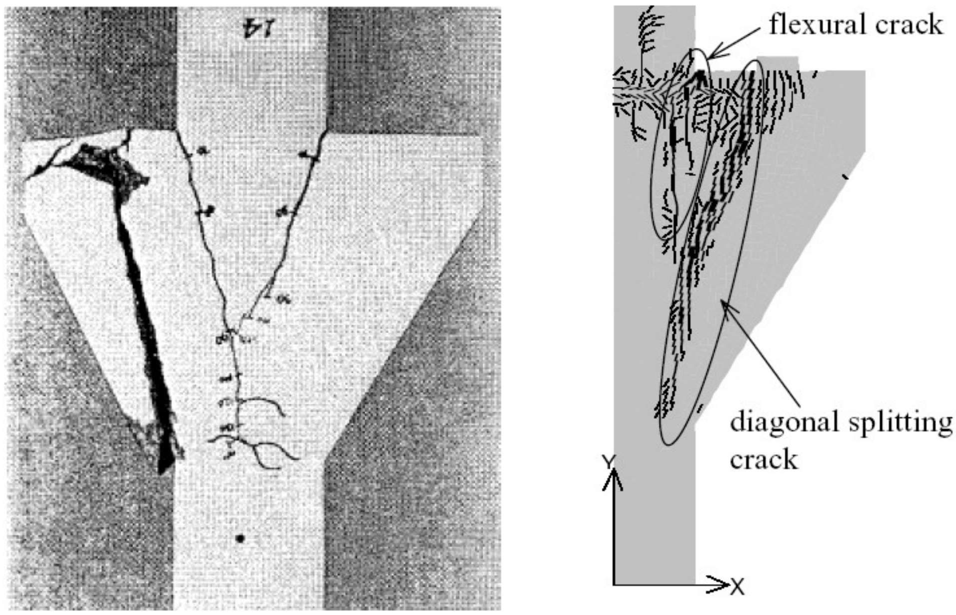

Figure 5.15 – Experimental and numerical crack pattern for corbel KR14.

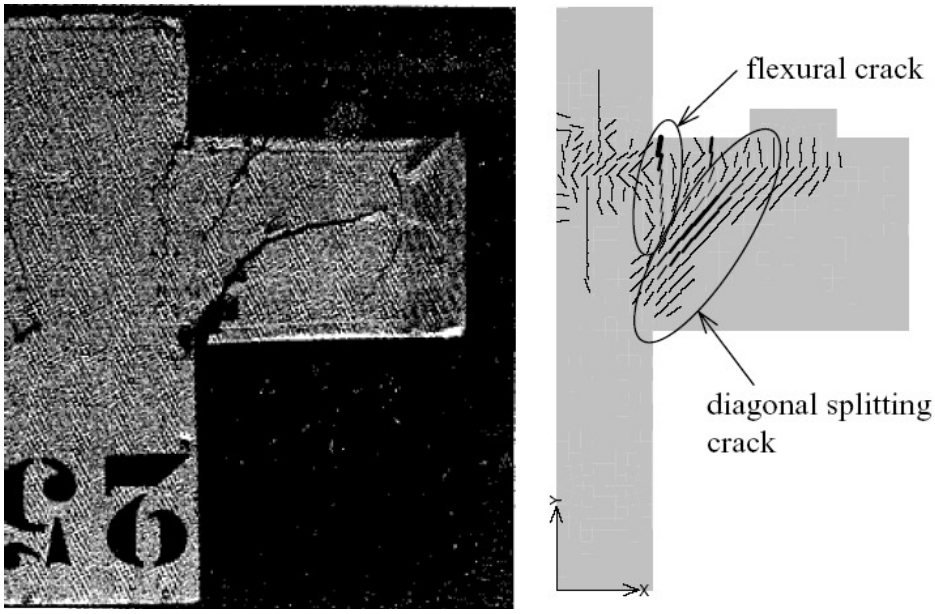

Figure 5.16 – Experimental and numerical crack pattern for corbel F25.

Finally, Figure 5.17 (Kriz-Raths corbels) and Figure 5.18 (Fattuhi corbels) give an insight of the corbel mechanical behavior for two different shapes. The minimum principal strain distribution clearly shows the main compressed zones highlighting the concrete strut and the singularity points. This demonstrates the power of the code in analyzing the concrete under complex stress states.

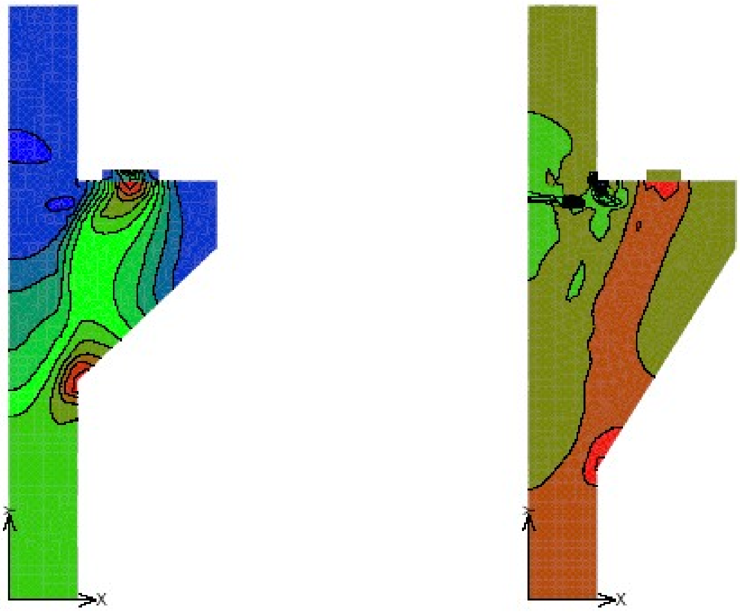

Figure 5.17 – Compressive principal strain for Kriz-Raths corbels.

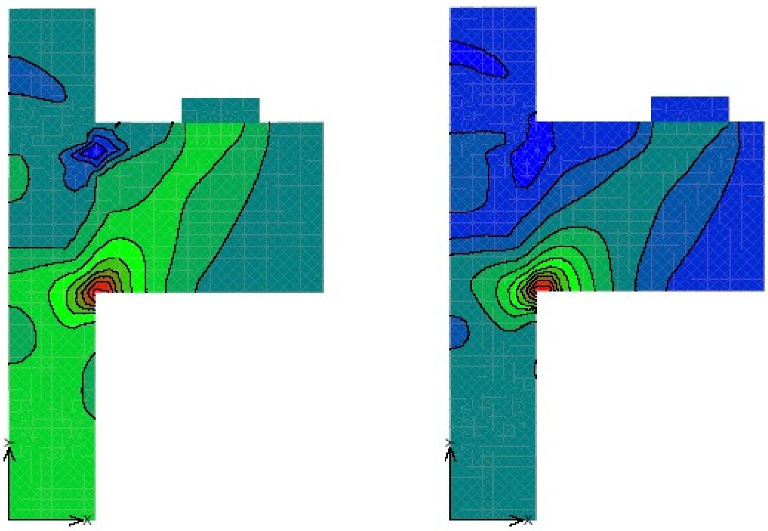

Figure 5.18 – Compressive principal strain for Fattuhi corbels.

In summary, it could be said that the global as well as the local response of the investigated structures can be captured very well by the FE code ATENA.

In the following pages, the load-displacement curve, the crack pattern, the ultimate load distribution, the sensitivity study and the safety index assessment are reported and discussed for each corbel. In the load-displacement curve, the displacement is measured at the column bottom whereas the load is measured at the bearing plate for all the specimens. Moreover, in the sensitivity analysis, since f_c has negative values, if the sensitivity is negative, its correlation is positive with the absolute value.

5.3.5 – Corbel Kriz-Raths 13

Figure 5.19 shows the load-displacement curve. The maximum load is 279 kN and it is in good agreement with the experimental load 266 kN. The post-peak branch of the curve shows a highly ductile behavior.

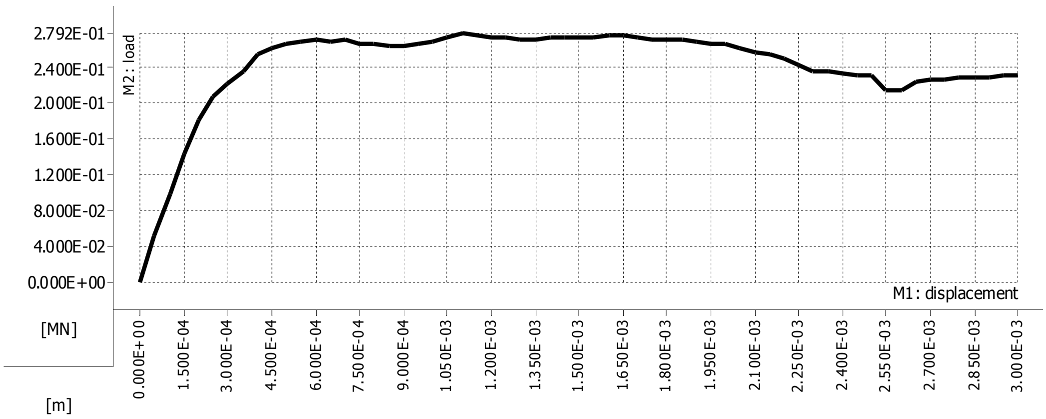

Figure 5.19 – Load-displacement curve for corbel KR13.

Figure 5.20 shows that the calculated crack pattern is very similar to the experimental one.

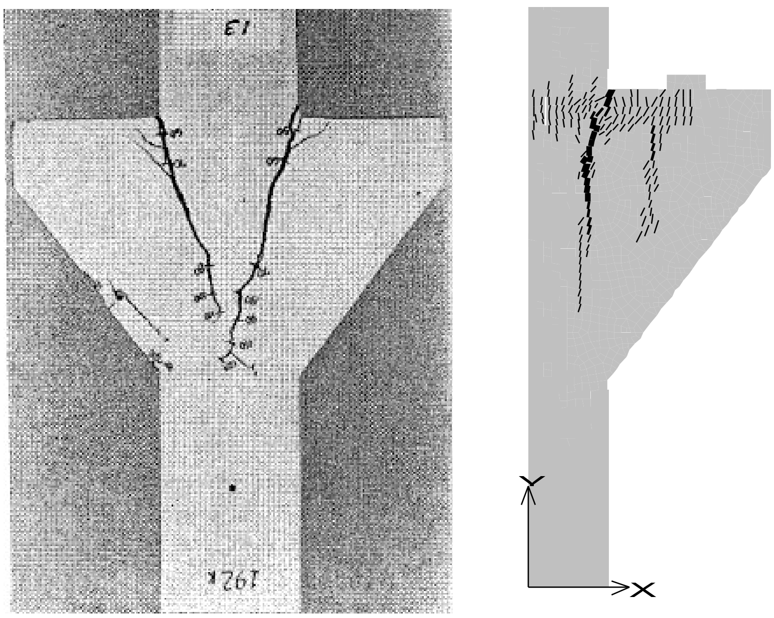

Figure 5.20 – Experimental and numerical crack pattern for corbel KR13.

A fitting procedure is performed on the numerical results. A Lognormal 3-parameter distribution proves to be a suitable function to describe the corbel ultimate load response (Figure 5.21). The fitting distribution properties are reported in Table 5.9.

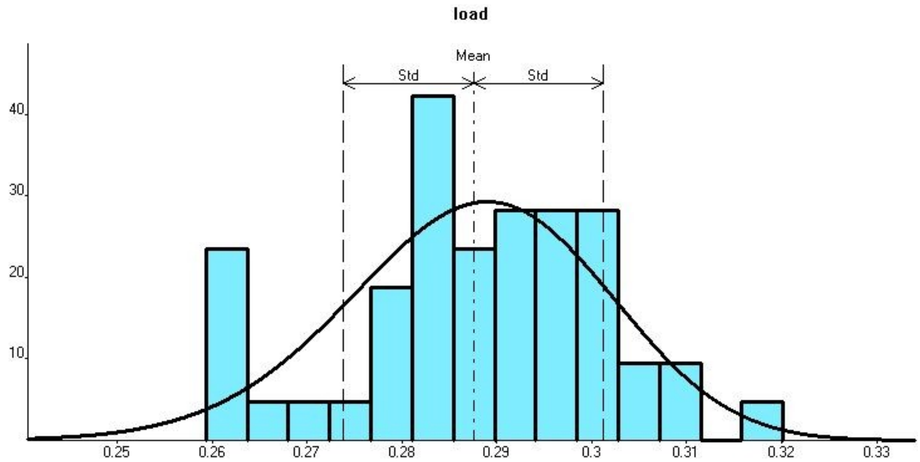

Figure 5.21 – Results and fitting distribution (PDF) for corbel KR13.

Variable	***Distribution***	***Mean [kN]***	***std [kN]***	***COV***	***Skewness***	***V_5 [kN]***
load	*Lognormal 3-par.*	*287*	*14*	*0.05*	*-0.22*	*264*

Table 5.9 – Fitting distribution properties for corbel KR13.

The sensitivity study leads to the ranking of Table 5.10. The numerical analysis shows that the variables E_c, f_c and f_t are nearly equally participating in the results. Figure 5.22 shows the sensitivity correlation between the load and the first two basic variables. As it can be seen by this plot, the variables have a moderate positive correlation to the load.

Variable	***Ultimate load sensitivity***
E_c	*0.35*
f_c	*0.33*
f_t	*0.31*
G_f	*0.25*

Table 5.10 – Sensitivity of ultimate load to variables for corbel KR13.

A further step in the corbel investigation is the evaluation of the allowable external load fulfilling a safety index of 4.7 (equal to a failure probability p_f=10^{-6}). This study is performed with a variable mean value of the load and four different *COV*.

Figure 5.23 shows the behavior of the safety index β related to the calculated ultimate load of the corbel and to a variable action, both expressed as PDF.

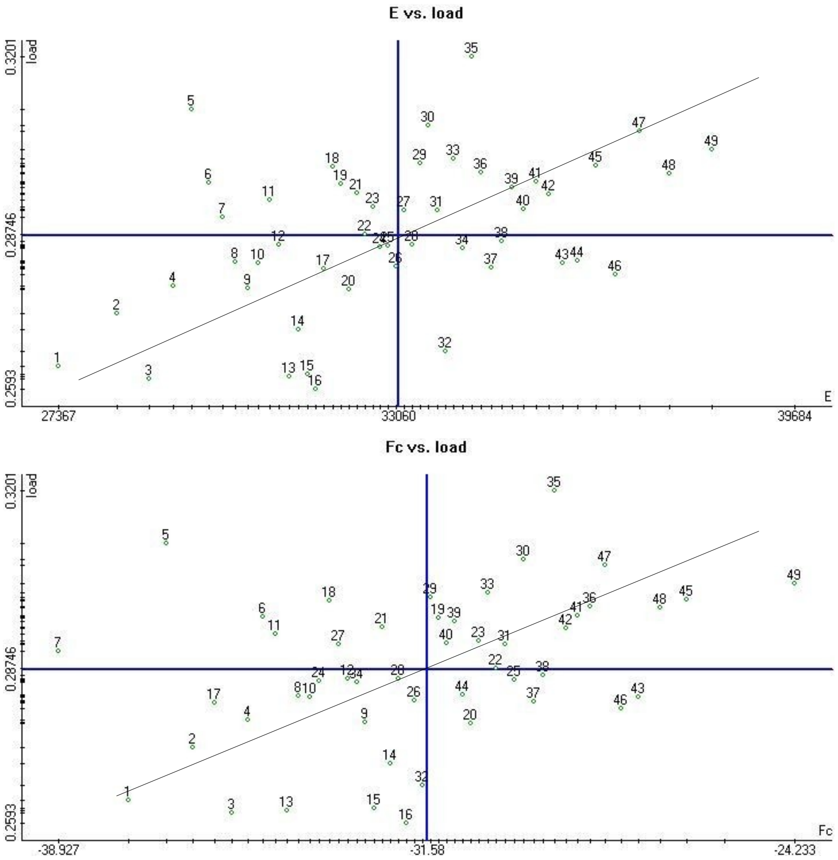

Figure 5.22 – Sensitivity plot for the first two variables for corbel KR13.

The investigation refers to different degrees of load scattering described by the *COV*. As it can be seen from the illustration, for a high *COV*=0.2 only a load of about 140 kN can be accepted by fulfilling the target limit of β=4.7. On the other hand, if it is possible to assure that the load scattering is smaller than *COV*=0.05, a load of about 205 kN is allowed.

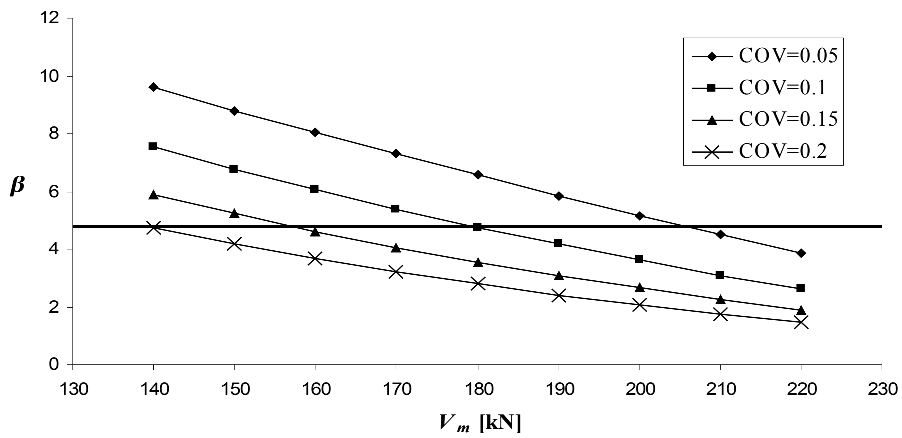

Figure 5.23 – Safety index assessment for corbel KR13.

5.3.6 – Corbel Kriz-Raths 14

Figure 5.24 shows the load-displacement curve. The maximum load is 367 kN and it is in very good agreement with the experimental load 374 kN. The post-peak branch of the curve shows a good ductile behavior.

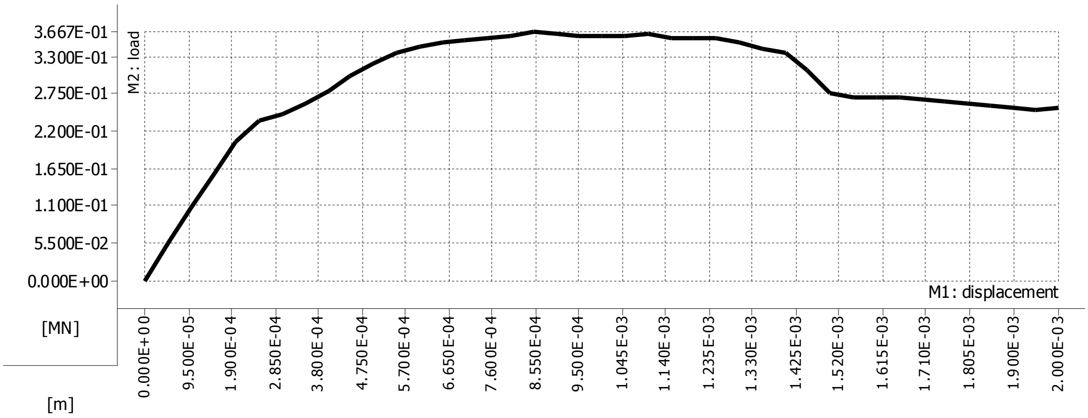

Figure 5.24 – Load-displacement curve for corbel KR14.

Figure 5.25 shows that the calculated crack pattern is very similar to the experimental one.

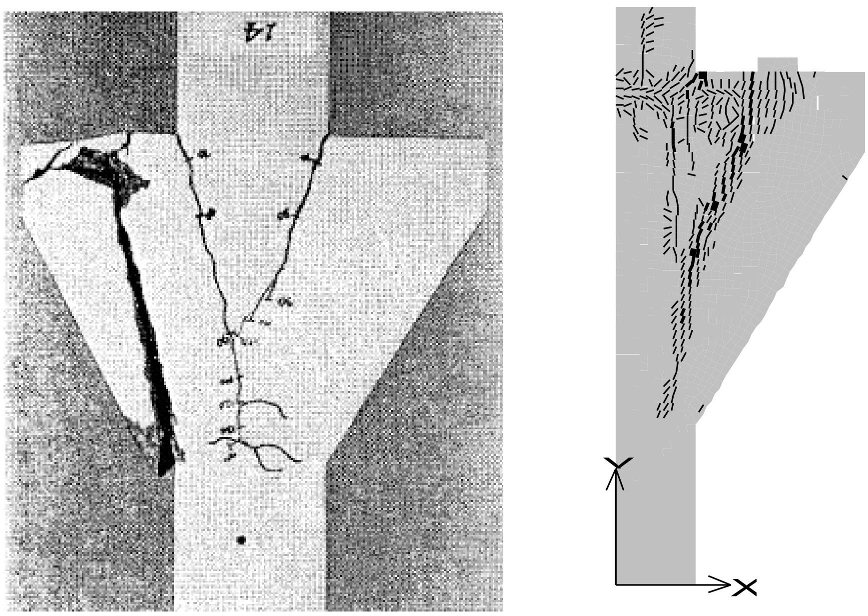

Figure 5.25 – Experimental and numerical crack pattern for corbel KR14.

A fitting procedure is performed on the numerical results. A Normal distribution proves to be a suitable function to describe the corbel ultimate load response (Figure 5.26). The fitting distribution properties are reported in Table 5.11.

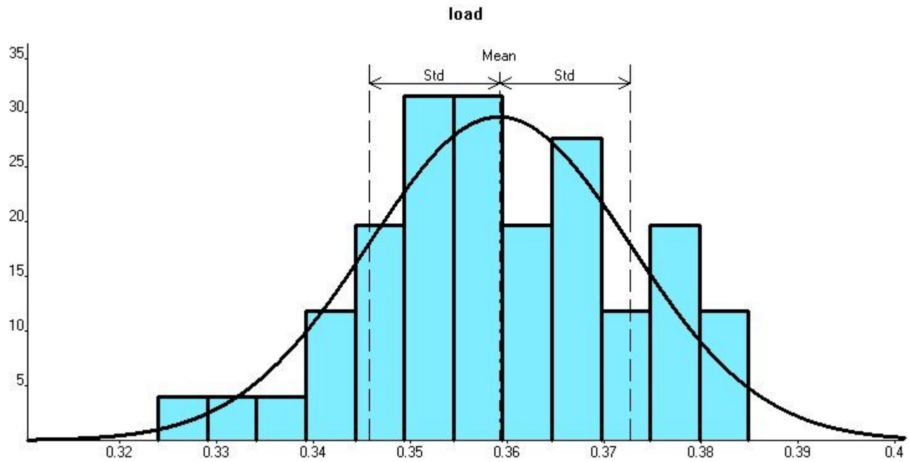

Figure 5.26 – Results and fitting distribution (PDF) for corbel KR14.

Variable	***Distribution***	***Mean [kN]***	***std [kN]***	***COV***	***Skewness***	***V_5 [kN]***
load	*Normal*	*359*	*13*	*0.04*	*/*	*337*

Table 5.11 – Fitting distribution properties for corbel KR14.

The sensitivity study leads to the ranking of Table 5.12. The numerical analysis shows that f_y is the most important variable. Then, G_f and f_t are nearly equally participating on the results. Figure 5.27 shows the sensitivity correlation between the load and the first two basic variables. As it can be seen by this plot, the first variable has a high positive correlation whereas the second has only a moderate positive correlation to the load.

Variable	***Ultimate load sensitivity***
f_y	*0.88*
G_f	*0.32*
f_t	*0.27*
E_c	*0.15*

Table 5.12 – Sensitivity of ultimate load to variables for corbel KR14.

A further step in the corbel investigation is the evaluation of the allowable external load fulfilling a safety index of 4.7 (equal to a failure probability p_f=10^{-6}). This study is performed with a variable mean value of the load and four different *COV*.

Figure 5.28 shows the behavior of the safety index β related to the calculated ultimate load of the corbel and to a variable action, both expressed as PDF.

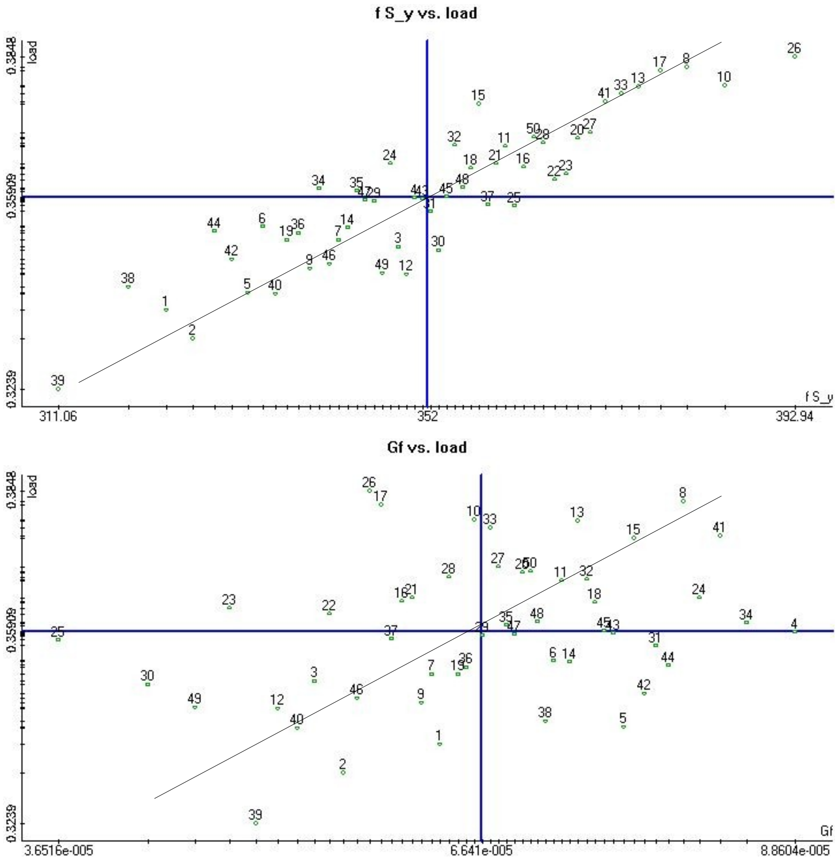

Figure 5.27 – Sensitivity plot for the first two variables for corbel KR14.

The investigation refers to different degrees of load scattering described by the *COV*. As it can be seen from the illustration, for a high *COV*=0.2 only a load of about 180 kN can be accepted by fulfilling the target limit of β=4.7. On the other hand, if it is possible to assure that the scattering of the load is smaller than *COV*=0.05, a load of about 265 kN is allowed.

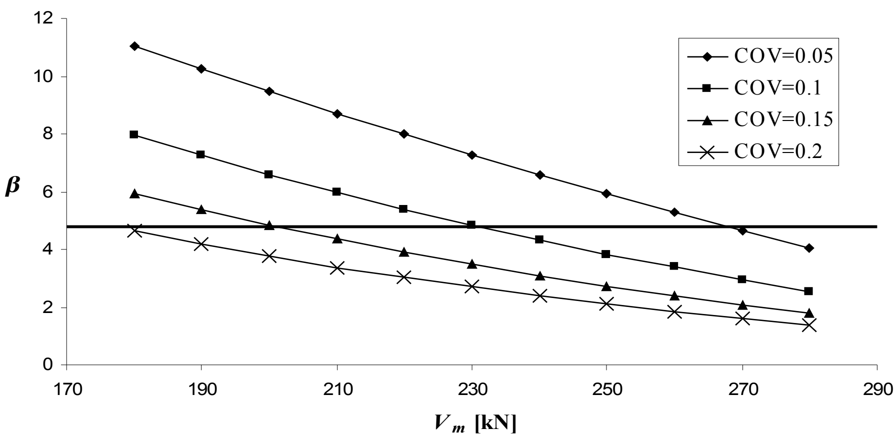

Figure 5.28 – Safety index assessment for corbel KR14.

5.3.7 – Corbel Kriz-Raths 21

Figure 5.29 shows the load-displacement curve. The maximum load is 405 kN and it is in good agreement with the experimental load 423 kN. The post-peak branch of the curve shows a good ductile behavior.

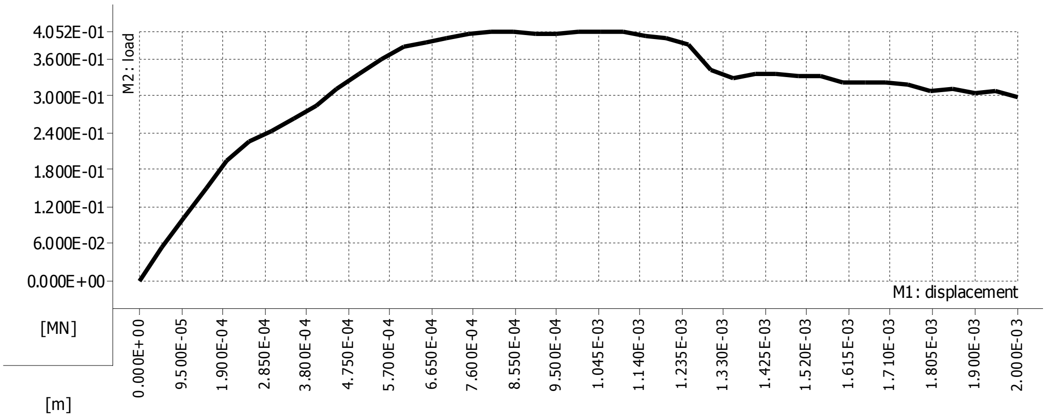

Figure 5.29 – Load-displacement curve for corbel KR21.

Figure 5.30 shows that the calculated crack pattern is quite similar to the experimental one.

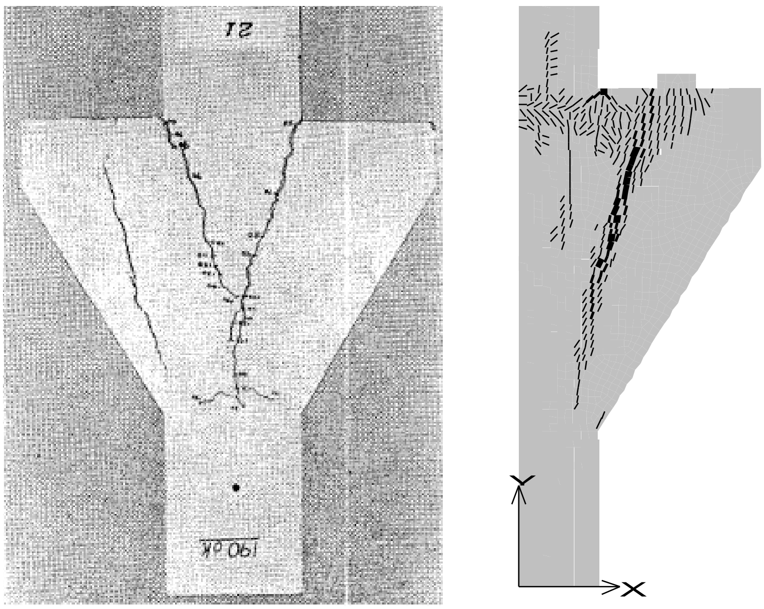

Figure 5.30 – Experimental and numerical crack pattern for corbel KR21.

A fitting procedure is performed on the numerical results. A Weibull maximum 3-parameter distribution proves to be a suitable function to describe the corbel ultimate load response (Figure 5.31). The fitting distribution properties are reported in Table 5.13.

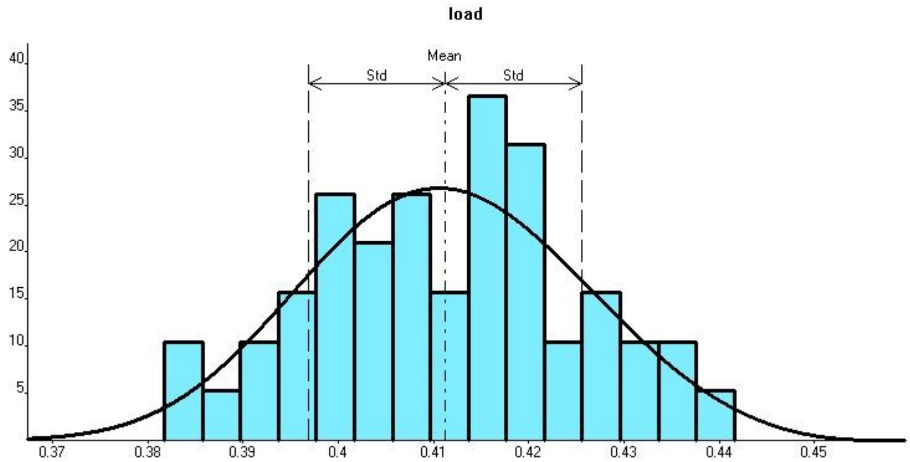

Figure 5.31 – Results and fitting distribution (PDF) for corbel KR21.

Variable	***Distribution***	***Mean [kN]***	***std [kN]***	***COV***	***Skewness***	***V_5 [kN]***
load	*Weibull max. 3-par.*	*411*	*14*	*0.03*	*-0.004*	*388*

Table 5.13 – Fitting distribution properties for corbel KR21.

The sensitivity study leads to the ranking of Table 5.14. The numerical analysis shows that all the first four variables are nearly equally participating on the results. Figure 5.32 shows the sensitivity correlation between the load and the first two basic variables. As it can be seen by this plot, the variables have a very low negative correlation to the load.

Variable	***Ultimate load sensitivity***
E_c	*-0.39*
f_c	*-0.32*
f_t	*-0.29*
f_y	*-0.28*

Table 5.14 – Sensitivity of ultimate load to variables for corbel KR21.

A further step in the corbel investigation is the evaluation of the allowable external load fulfilling a safety index of 4.7 (equal to a failure probability p_f=10^{-6}). This study is performed with a variable mean value of the load and four different *COV*.

Figure 5.33 shows the behavior of the safety index β related to the calculated ultimate load of the corbel and to a variable action, both expressed as PDF.

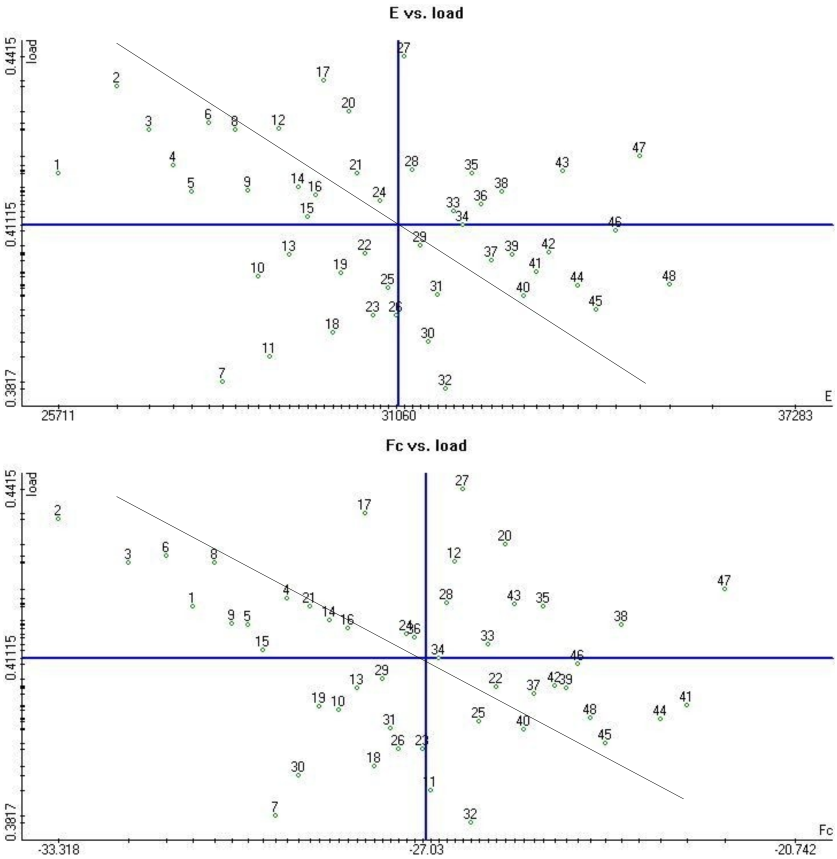

Figure 5.32 – Sensitivity plot for the first two variables for corbel KR21.

The investigation refers to different degrees of load scattering described by the *COV*. As it can be seen from the illustration, for a high *COV*=0.2 only a load of about 200 kN can be accepted by fulfilling the target limit of β=4.7. On the other hand, if it is possible to assure that the scattering of the load is smaller than *COV*=0.05, a load of about 310 kN is allowed.

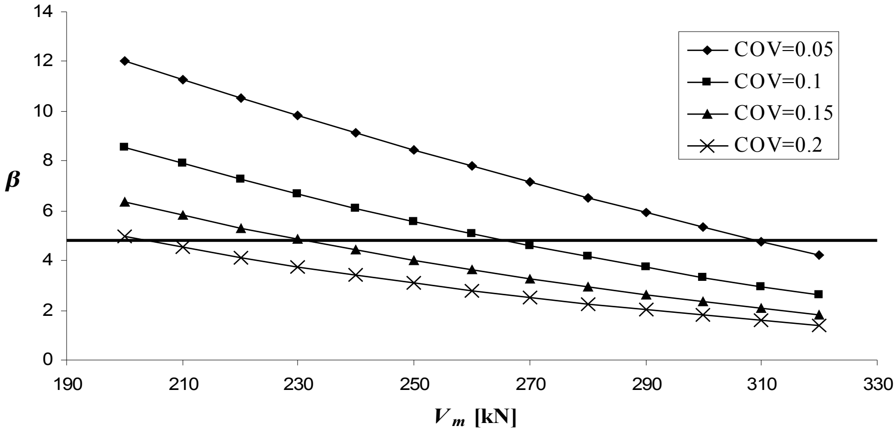

Figure 5.33 – Safety index assessment for corbel KR21.

5.3.8 – Corbel Kriz-Raths 55

Figure 5.34 shows the load-displacement curve. The maximum load is 255 kN and it is in good agreement with the experimental load 269 kN. The post-peak branch of the curve shows a highly ductile behavior.

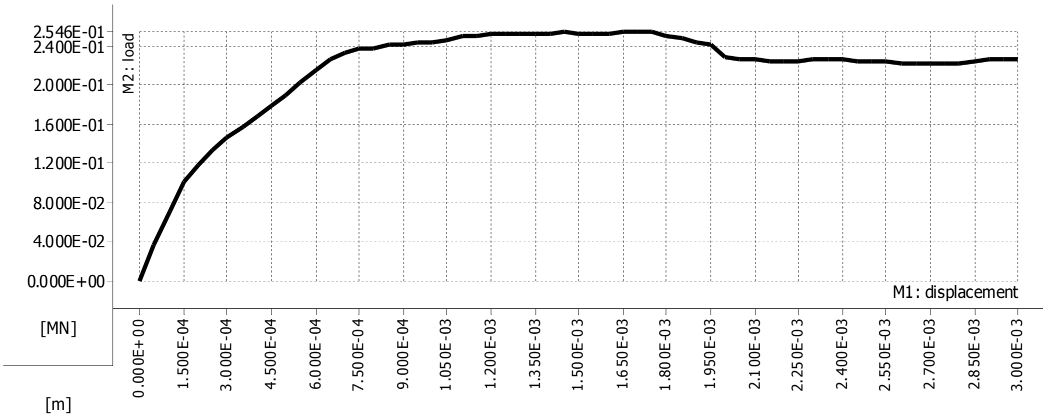

Figure 5.34 – Load-displacement curve for corbel KR55.

Figure 5.35 shows that the calculated crack pattern is very similar to the experimental one.

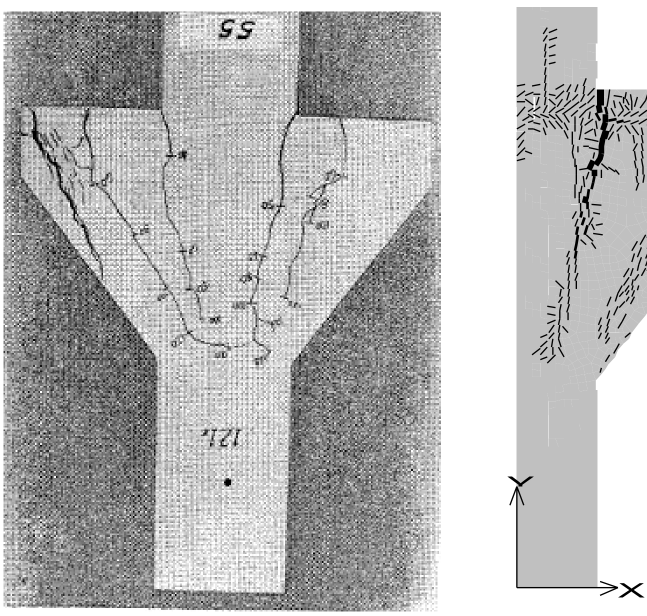

Figure 5.35 – Experimental and numerical crack pattern for corbel KR55.

A fitting procedure is performed on the numerical results. A Weibull minimum 2-parameter distribution proves to be a suitable function to describe the corbel ultimate load response (Figure 5.36). The fitting distribution properties are reported in Table 5.15.

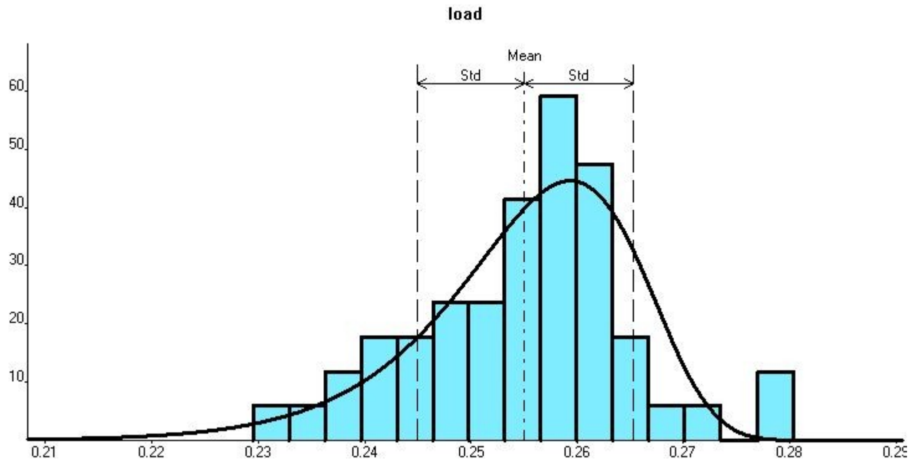

Figure 5.36 – Results and fitting distribution (PDF) for corbel KR55.

Variable	*Distribution*	*Mean [kN]*	*std [kN]*	*COV*	*Skewness*	V_5 *[kN]*
load	*Weibull min. 2-par.*	*255*	*10*	*0.04*	*-0.96*	*236*

Table 5.15 – Fitting distribution properties for corbel KR55.

The sensitivity study leads to the ranking of Table 5.16. The numerical analysis shows that f_y dominates the structural behavior. The other variables G_f, f_t and f_c have a very low influence. Figure 5.37 shows the sensitivity correlation between the load and the first two basic variables. As it can be seen by this plot, the first variable have a very high positive correlation to the load whereas the second variable correlation is negligible.

Variable	*Ultimate load sensitivity*
f_y	*0.96*
G_f	*0.09*
f_t	*0.06*
f_c	*-0.03*

Table 5.16 – Sensitivity of ultimate load to variables for corbel KR55.

A further step in the corbel investigation is the evaluation of the allowable external load fulfilling a safety index of 4.7 (equal to a failure probability p_f=10^{-6}). This study is performed with a variable mean value of the load and four different *COV*.
Figure 5.38 shows the behavior of the safety index β related to the calculated ultimate load of the corbel and to a variable action, both expressed as PDF.

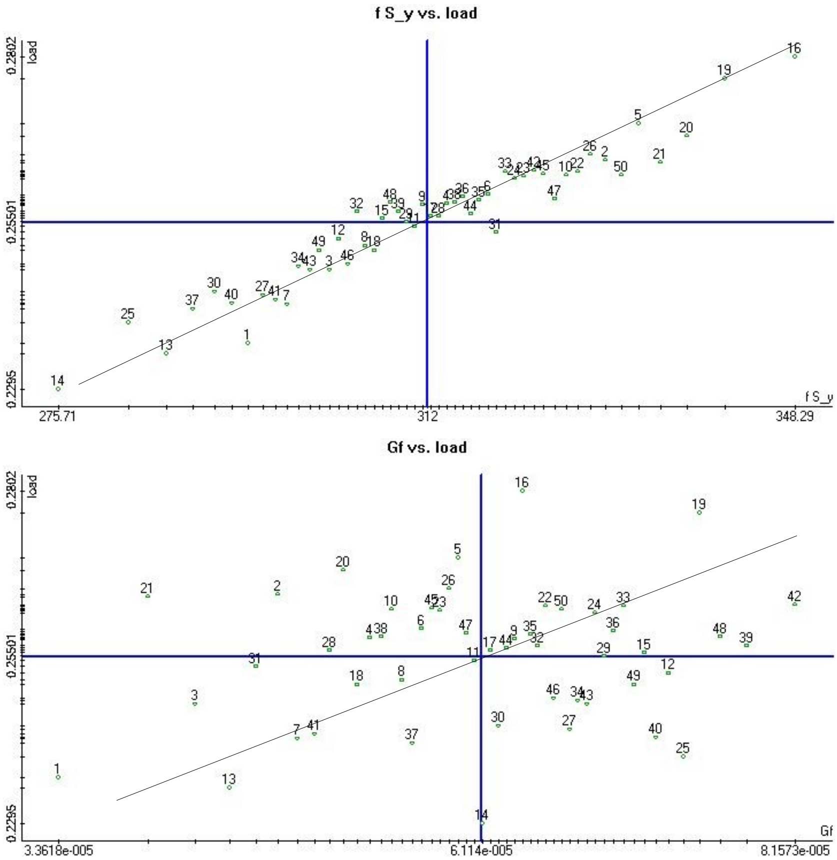

Figure 5.37 – Sensitivity plot for the first two variables for corbel KR55.

The investigation refers to different degrees of load scattering described by the *COV*. As it can be seen from the illustration, for a high *COV*=0.2 only a load of about 120 kN can be accepted by fulfilling the target limit of β=4.7. On the other hand, if it is possible to assure that the scattering of the load is smaller than *COV*=0.05, a load of about 190 kN is allowed.

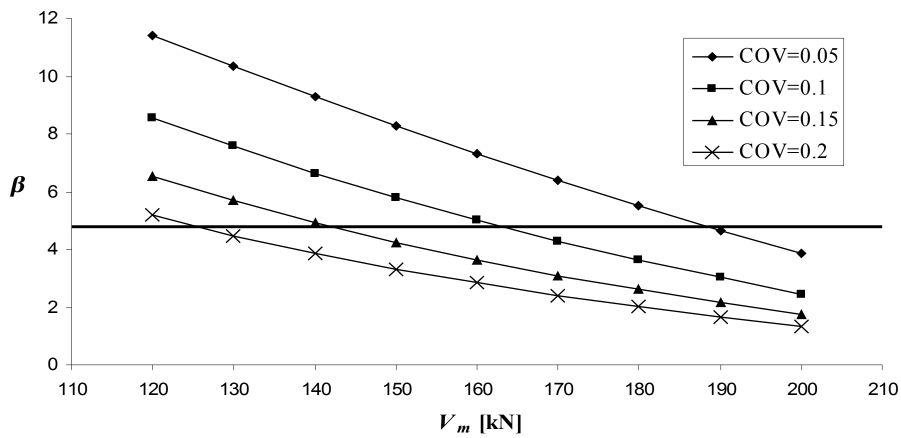

Figure 5.38 – Safety index assessment for corbel KR55.

5.3.9 – Corbel Kriz-Raths 80

Figure 5.39 shows the load-displacement curve. The maximum load is 371 kN and it is in very good agreement with the experimental load 370 kN. The post-peak branch of the curve shows a moderate ductile behavior.

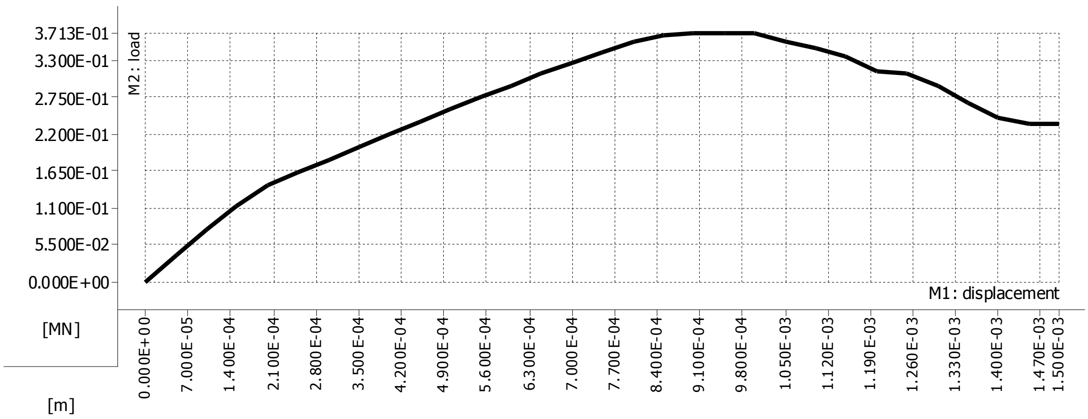

Figure 5.39 – Load-displacement curve for corbel KR80.

Figure 5.40 shows that the calculated crack pattern is very similar to the experimental one.

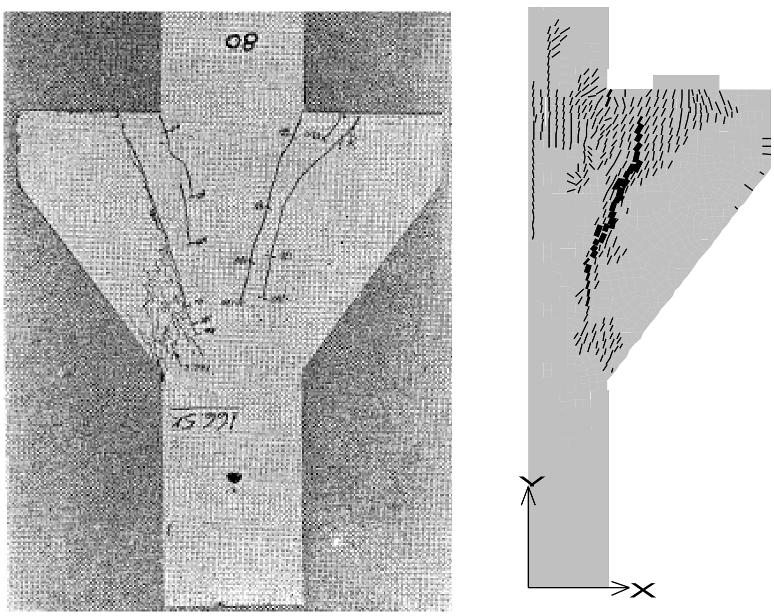

Figure 5.40 – Experimental and numerical crack pattern for corbel KR80.

A fitting procedure is performed on the numerical results. A Lognormal 3-parameter distribution proves to be a suitable function to describe the corbel ultimate load response (Figure 5.41). The fitting distribution properties are reported in Table 5.17.

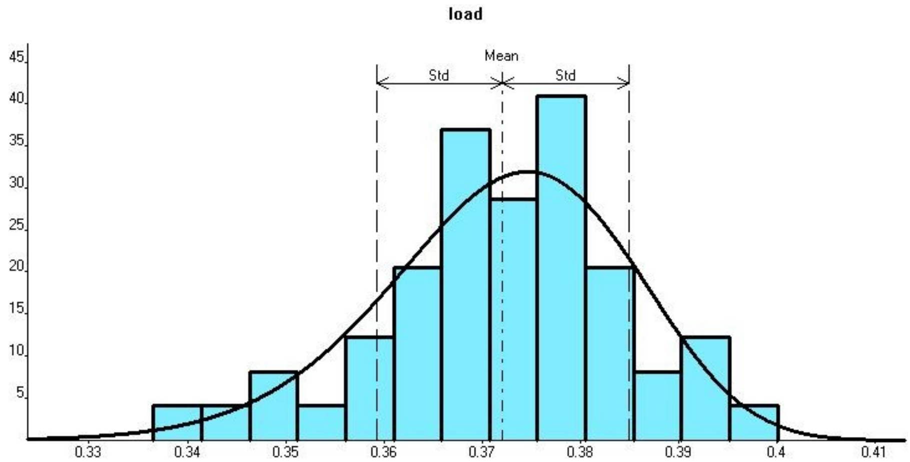

Figure 5.41 – Results and fitting distribution (PDF) for corbel KR80.

Variable	***Distribution***	***Mean [kN]***	***std [kN]***	***COV***	***Skewness***	***V_5 [kN]***
load	*Lognormal 3-par.*	*372*	*13*	*0.03*	*-0.41*	*350*

Table 5.17 – Fitting distribution properties for corbel KR80.

The sensitivity study leads to the ranking of Table 5.18. The numerical analysis shows that f_y is the most important variable. Then, f_c, f_t and E_c are nearly equally participating on the results. Figure 5.42 shows the sensitivity correlation between the load and the first two basic variables. As it can be seen by this plot, the first variable have a very high positive correlation to the load whereas the second variable correlation is lower and negative.

Variable	***Ultimate load sensitivity***
f_y	*0.76*
f_c	*-0.49*
f_t	*-0.40*
E_c	*-0.37*

Table 5.18 – Sensitivity of ultimate load to variables for corbel KR80.

A further step in the corbel investigation is the evaluation of the allowable external load fulfilling a safety index of 4.7 (equal to a failure probability p_f=10^{-6}). This study is performed with a variable mean value of the load and four different *COV*.

Figure 5.43 shows the behavior of the safety index β related to the calculated ultimate load of the corbel and to a variable action, both expressed as PDF.

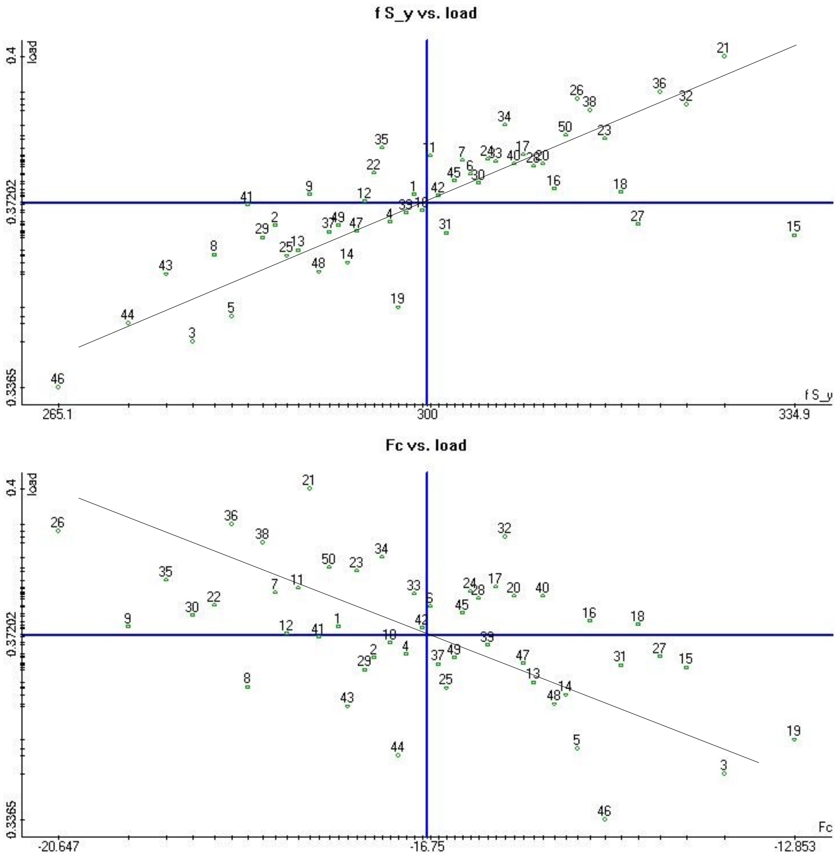

Figure 5.42 – Sensitivity plot for the first two variables for corbel KR80.

The investigation refers to different degrees of load scattering described by the *COV*. As it can be seen from the illustration, for a high *COV*=0.2 only a load of about 180 kN can be accepted by fulfilling the target limit of β=4.7. On the other hand, if it is possible to assure that the scattering of the load is smaller than *COV*=0.05, a load of about 280 kN is allowed.

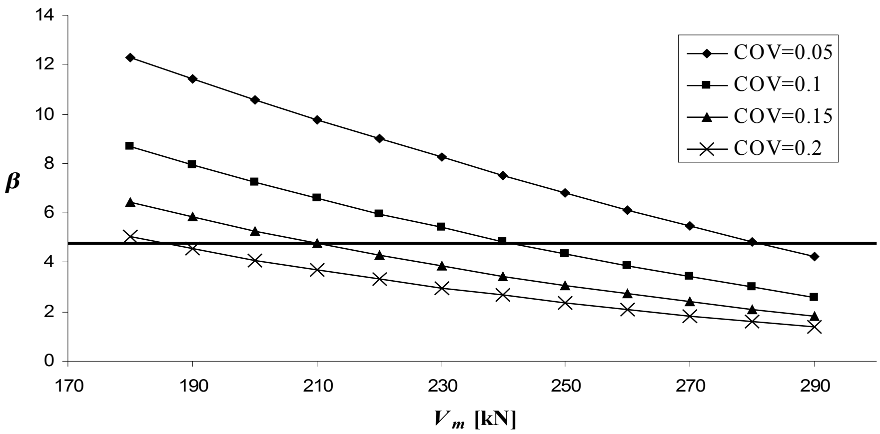

Figure 5.43 – Safety index assessment for corbel KR80.

5.3.10 – Corbel Kriz-Raths 91

Figure 5.44 shows the load-displacement curve. The maximum load is 585 kN and it is in good agreement with the experimental load 546 kN. The post-peak branch of the curve shows a highly brittle behavior.

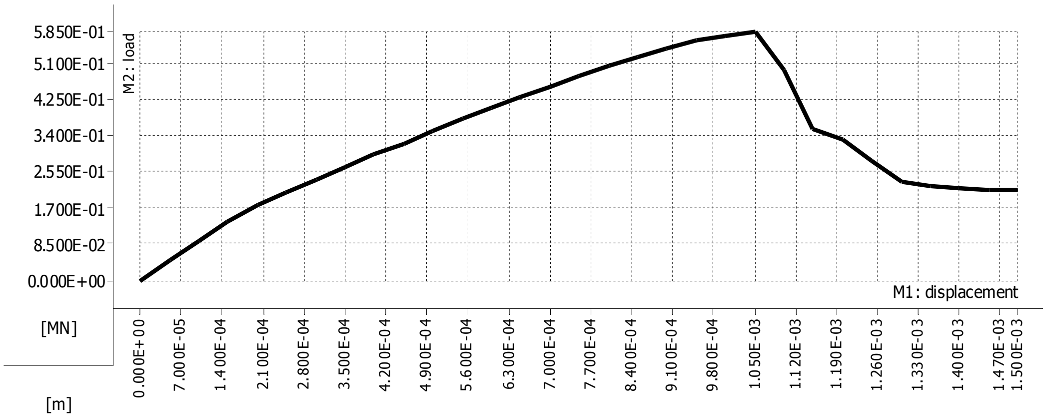

Figure 5.44 – Load-displacement curve for corbel KR91.

Figure 5.45 shows that the calculated crack pattern is very similar to the experimental one.

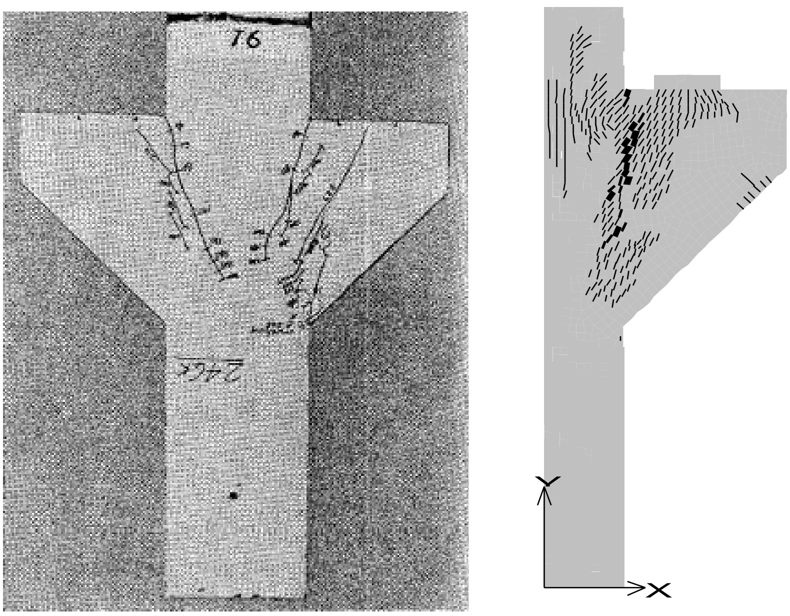

Figure 5.45 – Experimental and numerical crack pattern for corbel KR91.

A fitting procedure is performed on the numerical results. A Weibull minimum 2-parameter distribution proves to be a suitable function to describe the corbel ultimate load response (Figure 5.46). The fitting distribution properties are reported in Table 5.19.

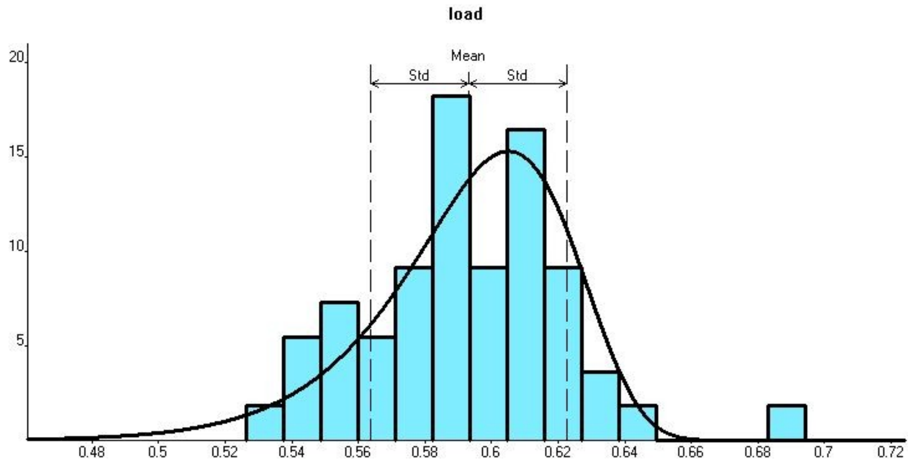

Figure 5.46 – Results and fitting distribution (PDF) for corbel KR91.

Variable	*Distribution*	*Mean [kN]*	*std [kN]*	*COV*	*Skewness*	*V_5 [kN]*
load	*Weibull min. 2-par.*	*593*	*29*	*0.05*	*-0.92*	*538*

Table 5.19 – Fitting distribution properties for corbel KR91.

The sensitivity study leads to the ranking of Table 5.20. The numerical analysis shows that f_c and E_c, are the most important variables, followed by f_t and G_f. Figure 5.47 shows the sensitivity correlation between the load and the first two basic variables. As it can be seen by this plot, the variables have a moderate negative correlation to the load.

Variable	*Ultimate load sensitivity*
f_c	*-0.57*
E_c	*-0.56*
f_t	*-0.30*
G_f	*-0.24*

Table 5.20 – Sensitivity of ultimate load to variables for corbel KR91.

A further step in the corbel investigation is the evaluation of the allowable external load fulfilling a safety index of 4.7 (equal to a failure probability p_f=10^{-6}). This study is performed with a variable mean value of the load and four different *COV*.

Figure 5.48 shows the behavior of the safety index β related to the calculated ultimate load of the corbel and to a variable action, both expressed as PDF.

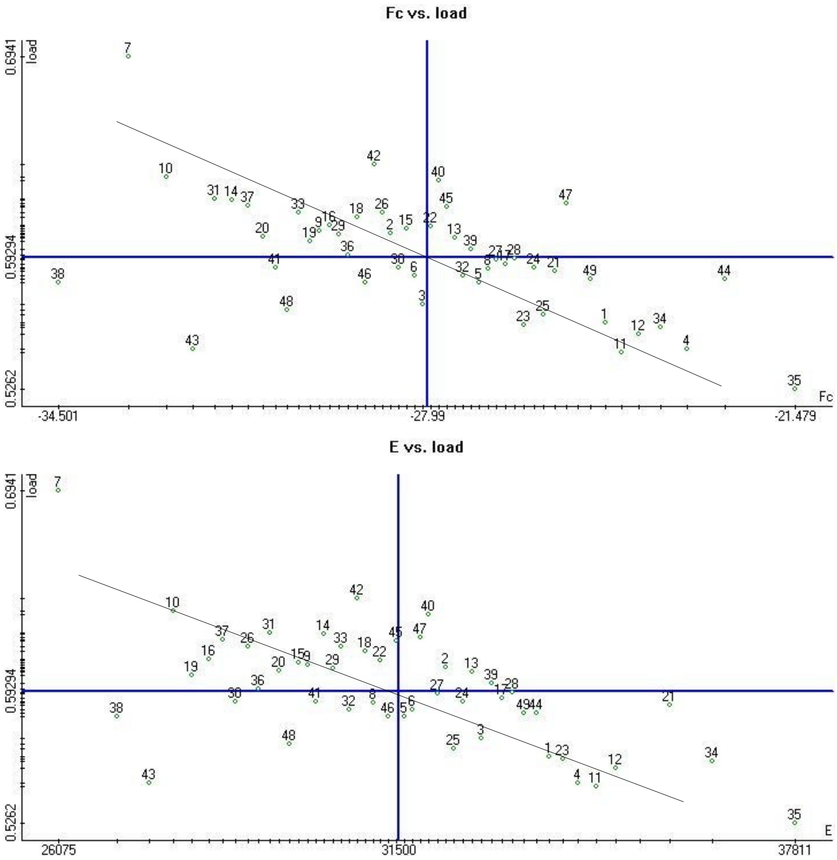

Figure 5.47 – Sensitivity plot for the first two variables for corbel KR91.

The investigation refers to different degrees of load scattering described by the *COV*. As it can be seen from the illustration, for a high *COV*=0.2 only a load of about 280 kN can be accepted by fulfilling the target limit of β=4.7. On the other hand, if it is possible to assure that the scattering of the load is smaller than *COV*=0.05, a load of about 420 kN is allowed.

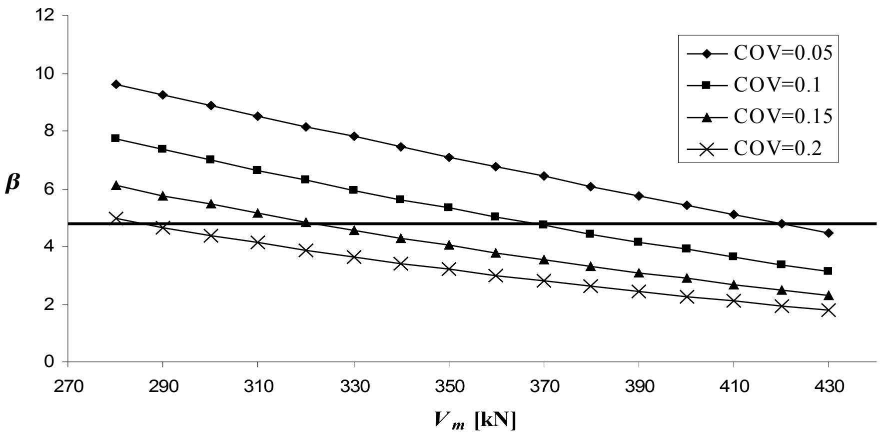

Figure 5.48 – Safety index assessment for corbel KR91.

5.3.11 – Corbel Kriz-Raths 100

Figure 5.49 shows the load-displacement curve. The maximum load is 758 kN and it is in very good agreement with the experimental load 761 kN. The post-peak branch of the curve shows a moderate brittle behavior.

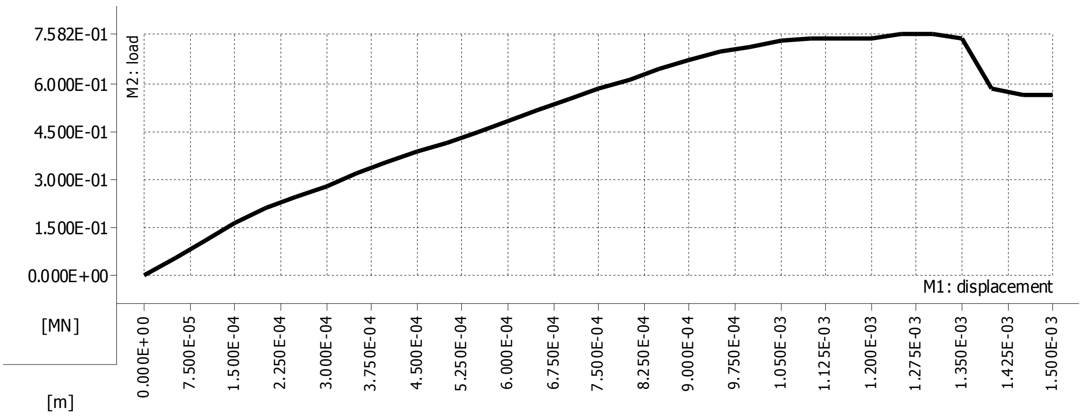

Figure 5.49 – Load-displacement curve for corbel KR100.

Figure 5.50 shows that the calculated crack pattern is very similar to the experimental one.

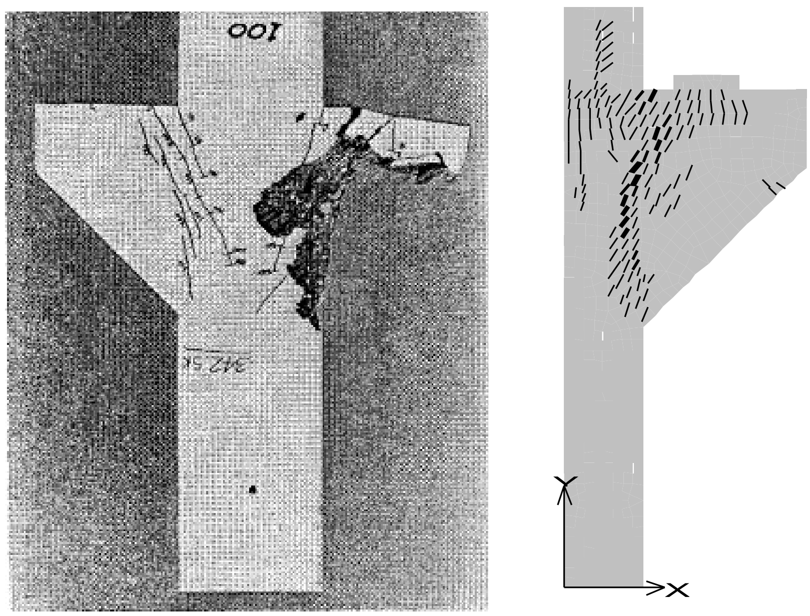

Figure 5.50 – Experimental and numerical crack pattern for corbel KR100.

A fitting procedure is performed on the numerical results. A Weibull maximum 3-parameter distribution proves to be a suitable function to describe the corbel ultimate load response (Figure 5.51). The fitting distribution properties are reported in Table 5.21.

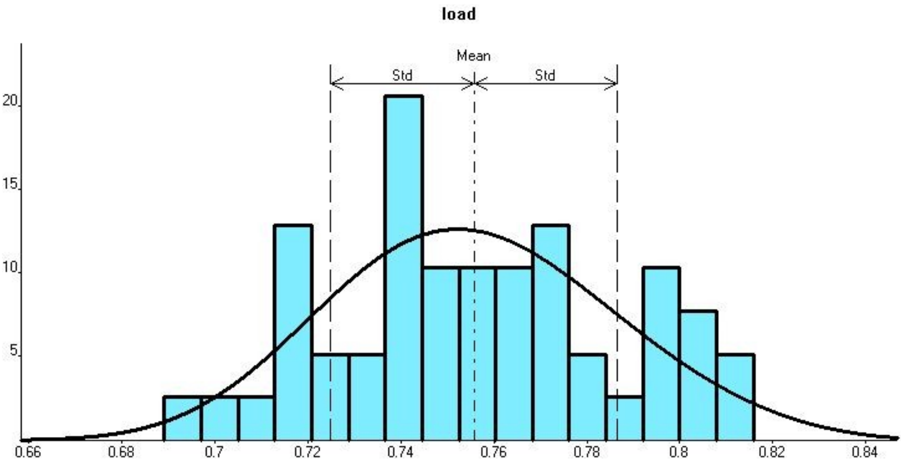

Figure 5.51 – Results and fitting distribution (PDF) for corbel KR100.

Variable	*Distribution*	*Mean [kN]*	*std [kN]*	*COV*	*Skewness*	*V_5 [kN]*
load	*Weibull max. 3-par.*	*756*	*31*	*0.04*	*0.12*	*706*

Table 5.21 – Fitting distribution properties for corbel KR100.

The sensitivity study leads to the ranking of Table 5.22. The numerical analysis shows that E_c is the most important variable, followed by f_c and then by f_y and f_t that are nearly equally participating on the results. Figure 5.52 shows the sensitivity correlation between the load and the first two basic variables. As it can be seen by this plot, the variables have a moderate negative correlation to the load.

Variable	*Ultimate load sensitivity*
E_c	*-0.37*
f_c	*-0.28*
f_y	*0.17*
f_t	*-0.16*

Table 5.22 – Sensitivity of ultimate load to variables for corbel KR100.

A further step in the corbel investigation is the evaluation of the allowable external load fulfilling a safety index of 4.7 (equal to a failure probability p_f=10^{-6}). This study is performed with a variable mean value of the load and four different *COV*.

Figure 5.53 shows the behavior of the safety index β related to the calculated ultimate load of the corbel and to a variable action, both expressed as PDF.

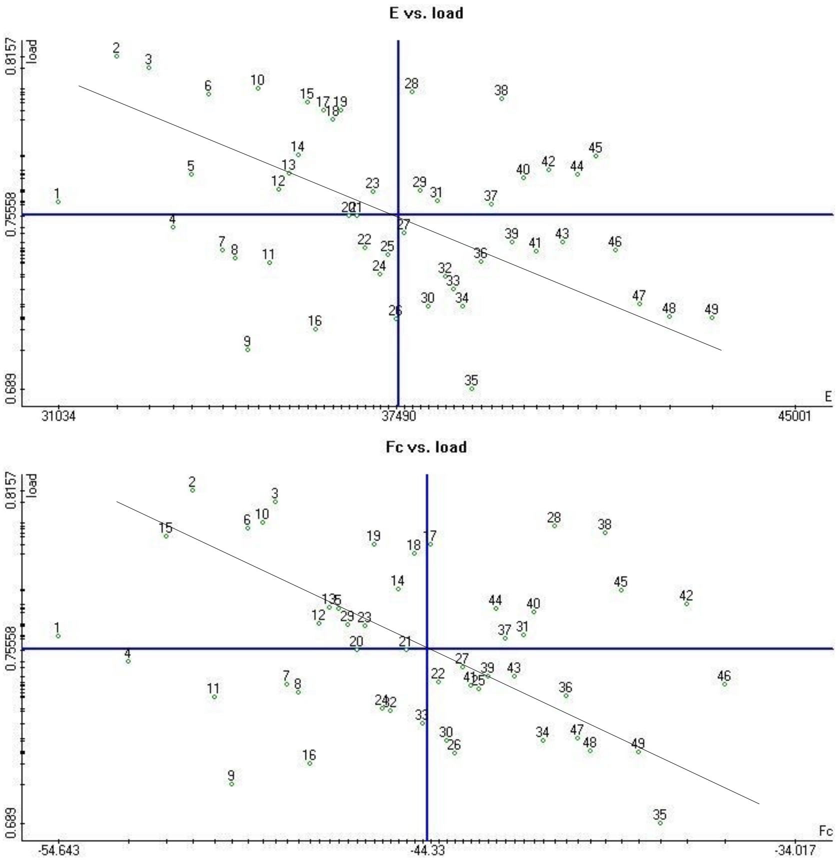

Figure 5.52 – Sensitivity plot for the first two variables for corbel KR100.

The investigation refers to different degrees of load scattering described by the *COV*. As it can be seen from the illustration, for a high *COV*=0.2 only a load of about 370 kN can be accepted by fulfilling the target limit of β=4.7. On the other hand, if it is possible to assure that the scattering of the load is smaller than *COV*=0.05, a load of about 550 kN is allowed.

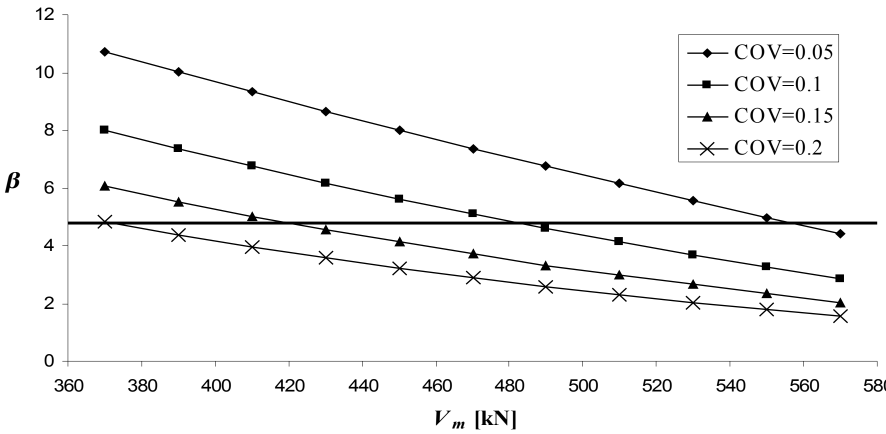

Figure 5.53 – Safety index assessment for corbel KR100.

5.3.12 – Corbel Fattuhi 23

Figure 5.54 shows the load-displacement curve. The maximum load is 131 kN and it is in good agreement with the experimental load 127 kN. The post-peak branch of the curve shows a brittle behavior.

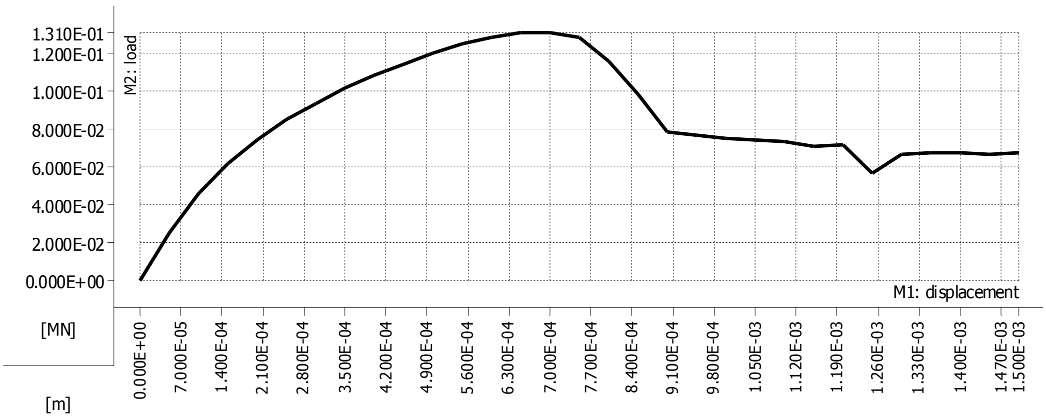

Figure 5.54 – Load-displacement curve for corbel F23.

Figure 5.55 shows that the calculated crack pattern is quite similar to the experimental one.

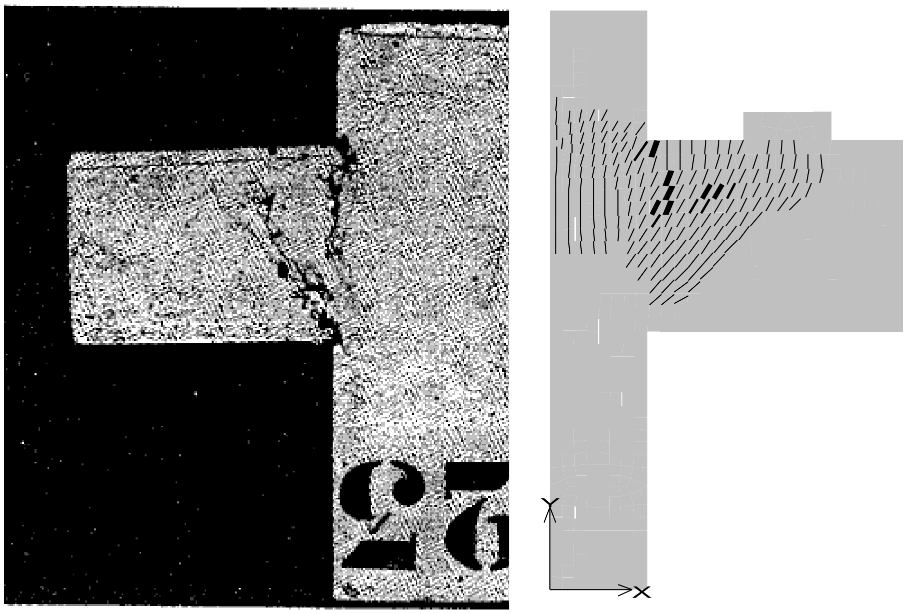

Figure 5.55 – Experimental and numerical crack pattern for corbel F23.

A fitting procedure is performed on the numerical results. A Weibull maximum 3-parameter distribution proves to be a suitable function to describe the corbel ultimate load response (Figure 5.56). The fitting distribution properties are reported in Table 5.23.

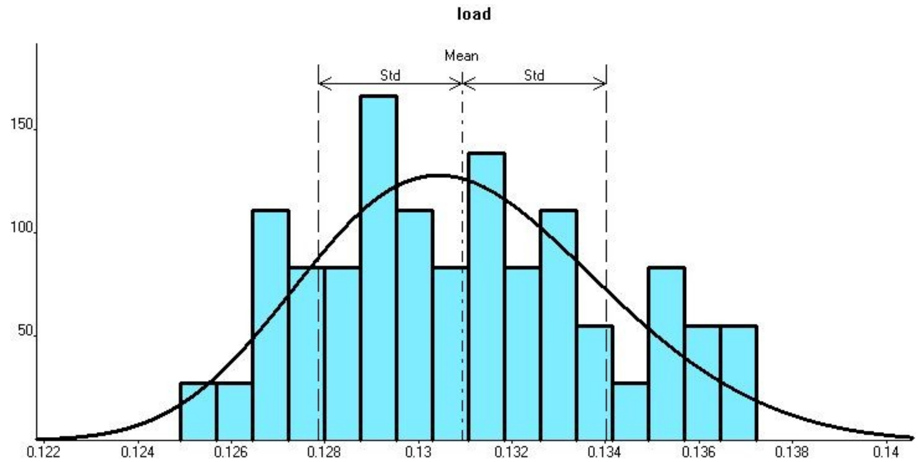

Figure 5.56 – Results and fitting distribution (PDF) for corbel F23.

Variable	***Distribution***	***Mean [kN]***	***std [kN]***	***COV***	***Skewness***	***V_5 [kN]***
load	*Weibull max. 3-par.*	*131*	*3*	*0.02*	*0.22*	*126*

Table 5.23 – Fitting distribution properties for corbel F23.

The sensitivity study leads to the ranking of Table 5.24. The numerical analysis shows that E_c and f_c are the most important variables whereas the other variables have a negligible influence. Figure 5.57 shows the sensitivity correlation between the load and the first two basic variables. Both the variables have a moderate negative correlation to the load.

Variable	***Ultimate load sensitivity***
E_c	*-0.65*
f_c	*-0.56*
f_t	*-0.14*
G_f	*0.06*

Table 5.24 – Sensitivity of ultimate load to variables for corbel F23.

A further step in the corbel investigation is the evaluation of the allowable external load fulfilling a safety index of 4.7 (equal to a failure probability p_f=10^{-6}). This study is performed with a variable mean value of the load and four different *COV*.

Figure 5.58 shows the behavior of the safety index β related to the calculated ultimate load of the corbel and to a variable action, both expressed as PDF.

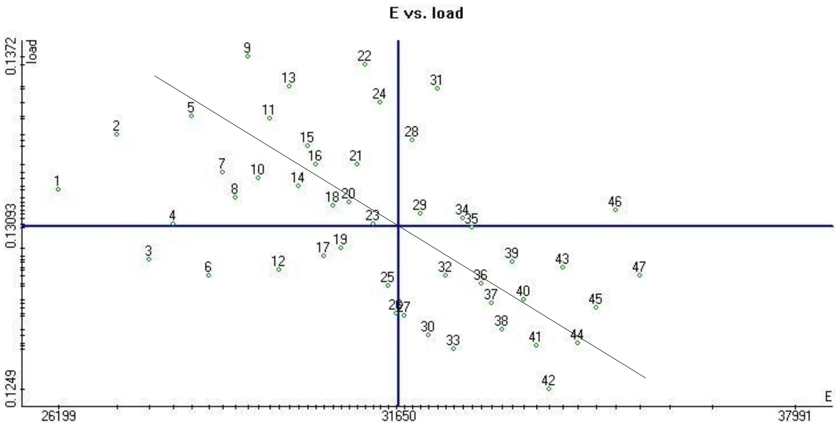

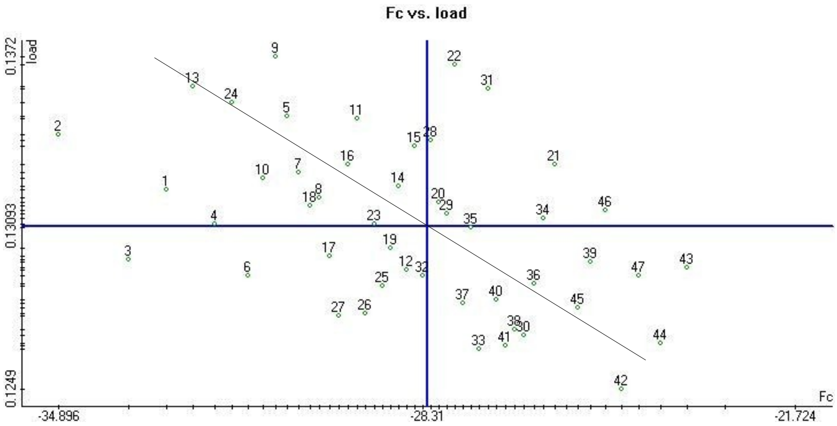

Figure 5.57 – Sensitivity plot for the first two variables for corbel F23.

The investigation refers to different degrees of load scattering described by the *COV*. As it can be seen from the illustration, for a high *COV*=0.2 only a load of about 65 kN can be accepted by fulfilling the target limit of β=4.7. On the other hand, if it is possible to assure that the scattering of the load is smaller than *COV*=0.05, a load of about 100 kN is allowed.

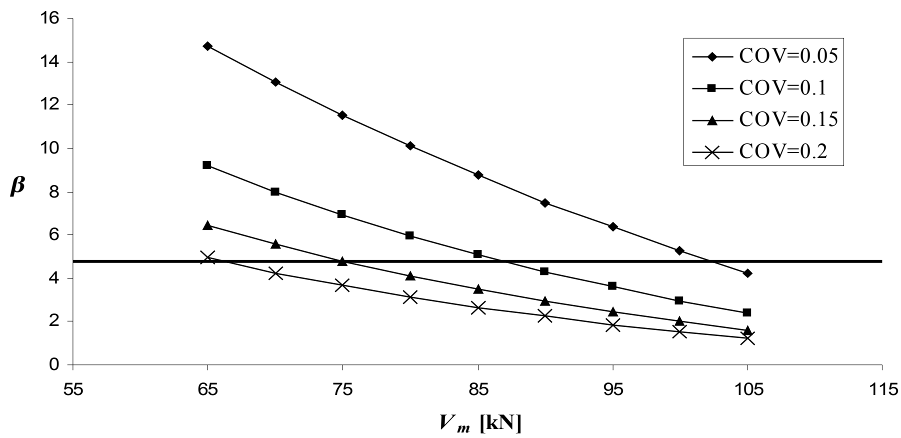

Figure 5.58 – Safety index assessment for corbel F23.

5.3.13 – Corbel Fattuhi 25

Figure 5.59 shows the load-displacement curve. The maximum load is 103 kN and it is in good agreement with the experimental load 109 kN. The post-peak branch of the curve shows a moderate ductile behavior.

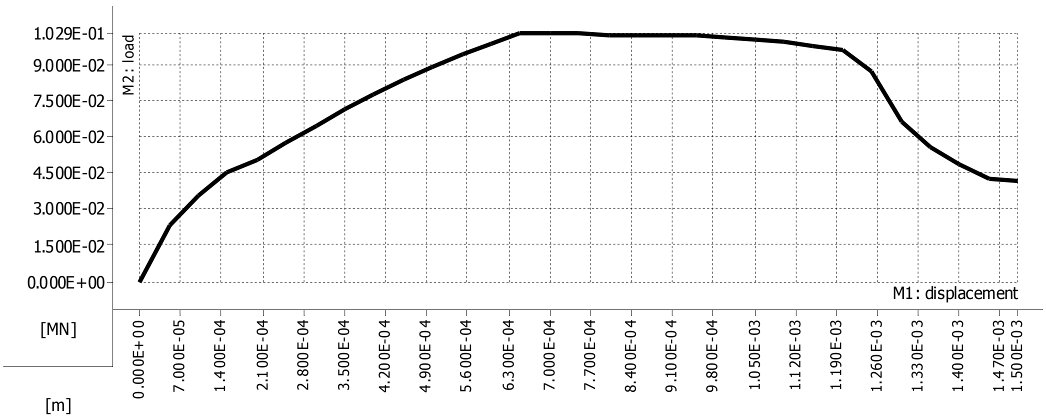

Figure 5.59 – Load-displacement curve for corbel F25.

Figure 5.60 shows that the calculated crack pattern is very similar to the experimental one.

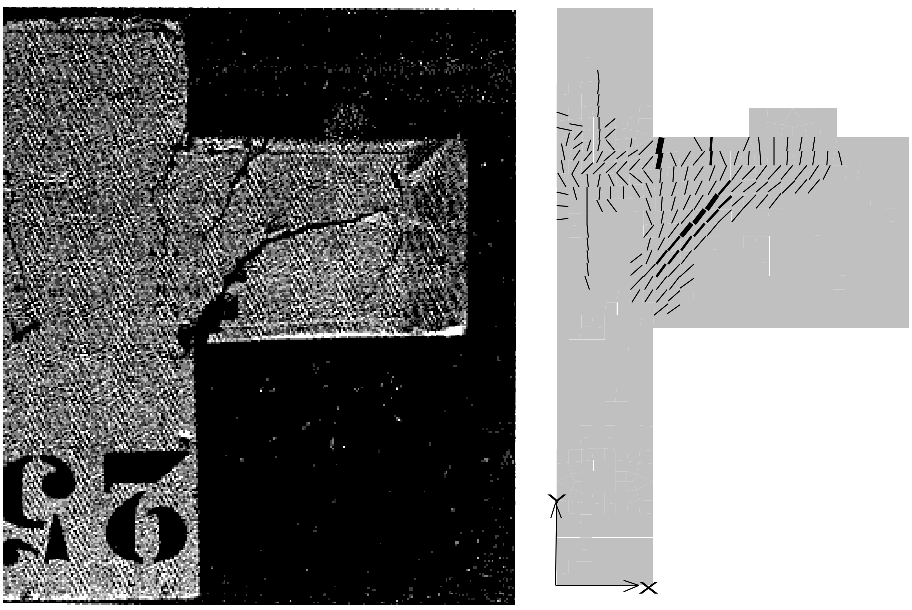

Figure 5.60 – Experimental and numerical crack pattern for corbel F25.

A fitting procedure is performed on the numerical results. A Weibull maximum 3-parameter distribution proves to be a suitable function to describe the corbel ultimate load response (Figure 5.61). The fitting distribution properties are reported in Table 5.25.

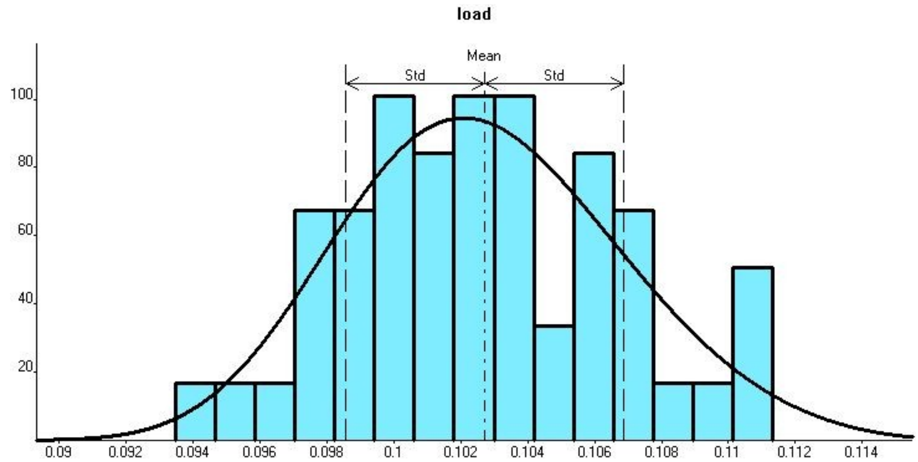

Figure 5.61 – Results and fitting distribution (PDF) for corbel F25.

Variable	***Distribution***	***Mean [kN]***	***std [kN]***	***COV***	***Skewness***	***V_5 [kN]***
load	*Weibull max. 3-par.*	*103*	*4*	*0.04*	*0.18*	*96*

Table 5.25 – Fitting distribution properties for corbel F25.

The sensitivity study leads to the ranking of Table 5.26. The numerical analysis shows that f_y has a very high influence on the results whereas f_c, E_c, and f_t are nearly equally participating on the results with a lower influence. Figure 5.62 shows the sensitivity correlation between the load and the first two basic variables. The first variable has a very high positive correlation to the load whereas the second variable has a lower negative correlation.

Variable	***Ultimate load sensitivity***
f_y	*0.88*
f_c	*-0.36*
E_c	*-0.34*
f_t	*-0.24*

Table 5.26 – Sensitivity of ultimate load to variables for corbel F25.

A further step in the corbel investigation is the evaluation of the allowable external load fulfilling a safety index of 4.7 (equal to a failure probability p_f=10^{-6}). This study is performed with a variable mean value of the load and four different *COV*.

Figure 5.63 shows the behavior of the safety index β related to the calculated ultimate load of the corbel and to a variable action, both expressed as PDF.

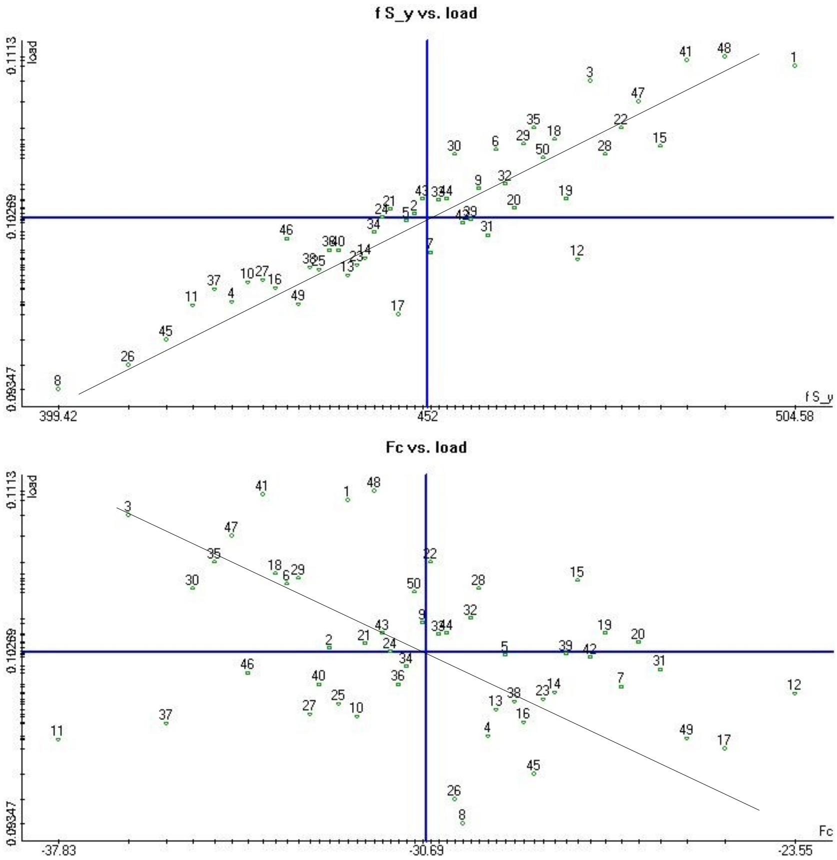

Figure 5.62 – Sensitivity plot for the first two variables for corbel F25.

The investigation refers to different degrees of load scattering described by the *COV*. As it can be seen from the illustration, for a high *COV*=0.2 only a load of about 50 kN can be accepted by fulfilling the target limit of β=4.7. On the other hand, if it is possible to assure that the scattering of the load is smaller than *COV*=0.05, a load of about 75 kN is allowed.

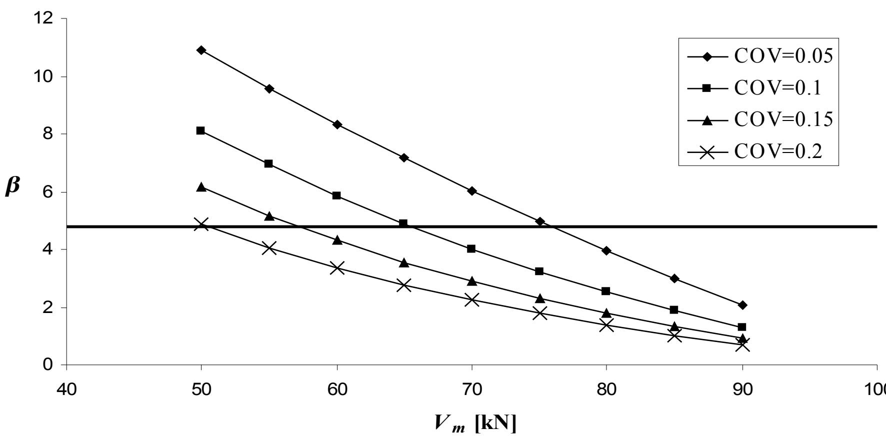

Figure 5.63 – Safety index assessment for corbel F25.

5.3.14 – Corbel Fattuhi 34

Figure 5.64 shows the load-displacement curve. The maximum load is 106 kN and it is in good agreement with the experimental load 114 kN. The post-peak branch of the curve shows a brittle behavior.

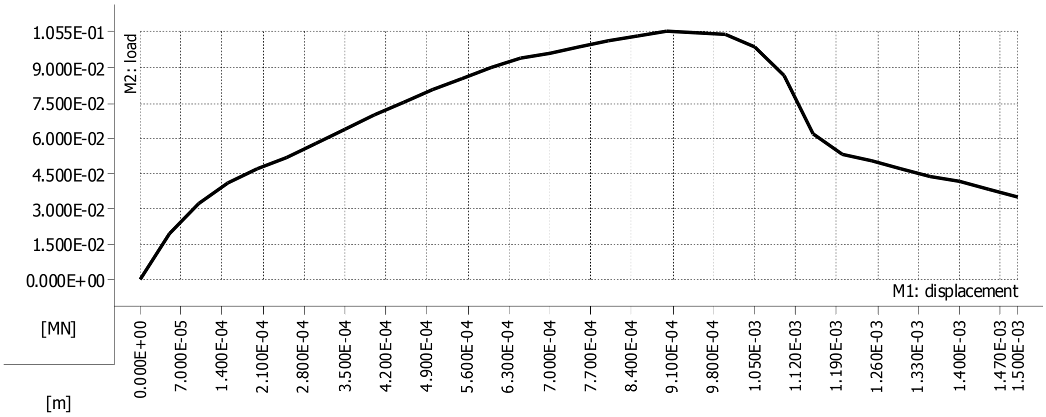

Figure 5.64 – Load-displacement curve for corbel F34.

Figure 5.65 shows that the calculated crack pattern is very similar to the experimental one.

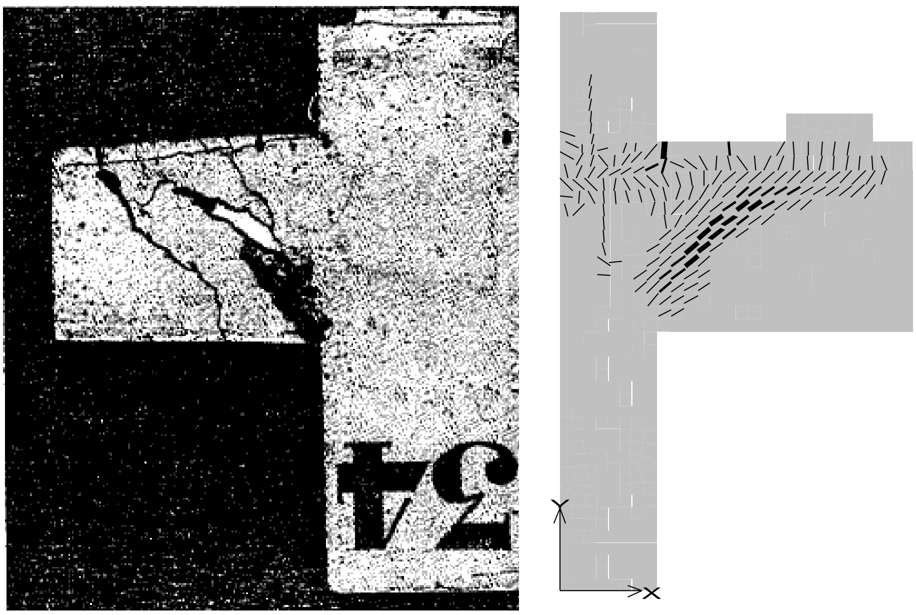

Figure 5.65 – Experimental and numerical crack pattern for corbel F34.

A fitting procedure is performed on the numerical results. A Lognormal 3-parameter distribution proves to be a suitable function to describe the corbel ultimate load response (Figure 5.66). The fitting distribution properties are reported in Table 5.27.

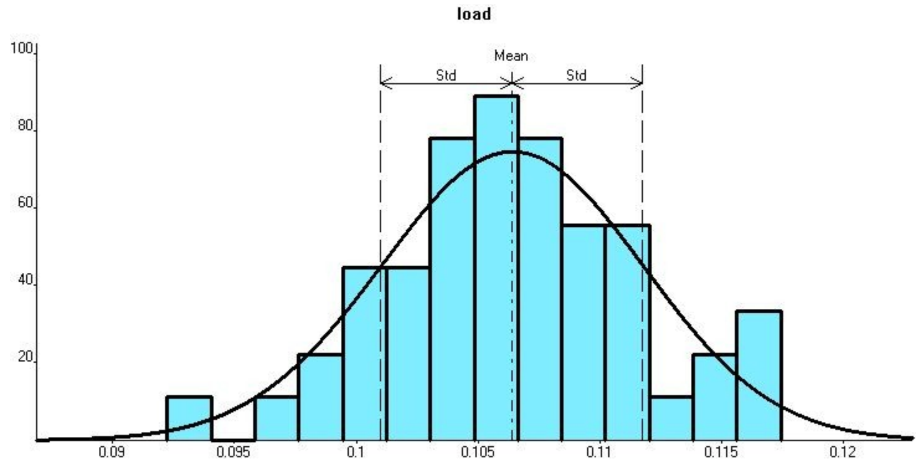

Figure 5.66 – Results and fitting distribution (PDF) for corbel F34.

Variable	*Distribution*	*Mean [kN]*	*std [kN]*	*COV*	*Skewness*	V_5 *[kN]*
load	*Lognormal 3-par.*	*106*	*5*	*0.05*	*-0.02*	*98*

Table 5.27 – Fitting distribution properties for corbel F34.

The sensitivity study leads to the ranking of Table 5.28. The numerical analysis shows that f_c and E_c are the most important variables with a high influence, followed by f_t and G_f. Figure 5.67 shows the sensitivity correlation between the load and the first two basic variables. As it can be seen by this plot, the variables have a strong negative correlation to the load.

Variable	*Ultimate load sensitivity*
f_c	*-0.95*
E_c	*-0.86*
f_t	*-0.67*
G_f	*-0.41*

Table 5.28 – Sensitivity of ultimate load to variables for corbel F34.

A further step in the corbel investigation is the evaluation of the allowable external load fulfilling a safety index of 4.7 (equal to a failure probability p_f=10^{-6}). This study is performed with a variable mean value of the load and four different *COV*.

Figure 5.68 shows the behavior of the safety index β related to the calculated ultimate load of the corbel and to a variable action, both expressed as PDF.

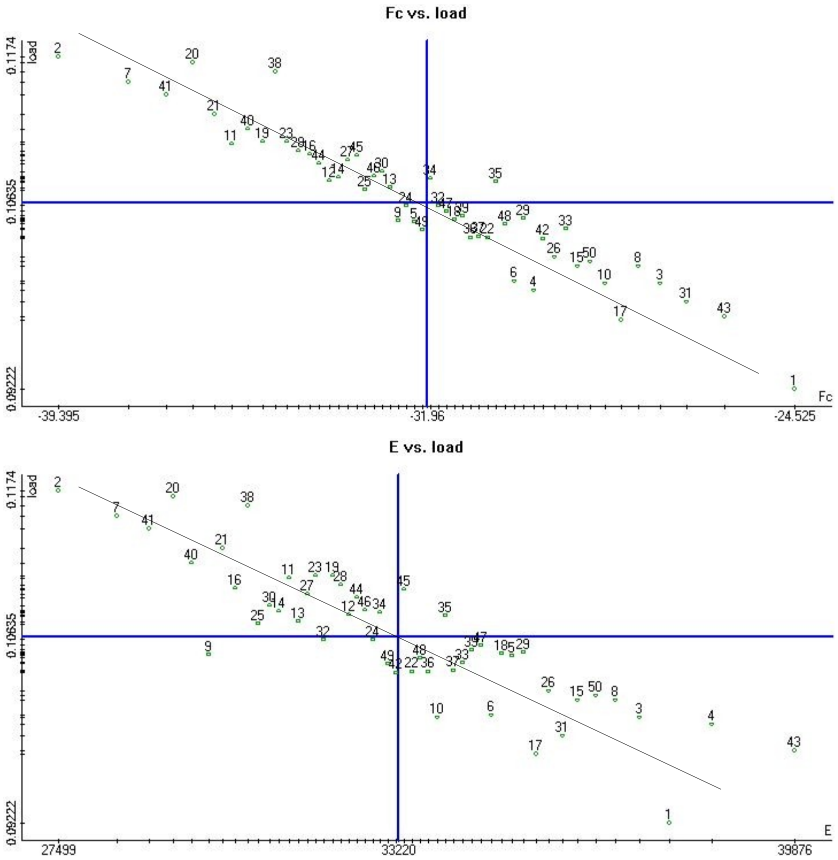

Figure 5.67 – Sensitivity plot for the first two variables for corbel F34.

The investigation refers to different degrees of load scattering described by the *COV*. As it can be seen from the illustration, for a high *COV*=0.2 only a load of about 50 kN can be accepted by fulfilling the target limit of β=4.7. On the other hand, if it is possible to assure that the scattering of the load is smaller than *COV*=0.05, a load of about 75 kN is allowed.

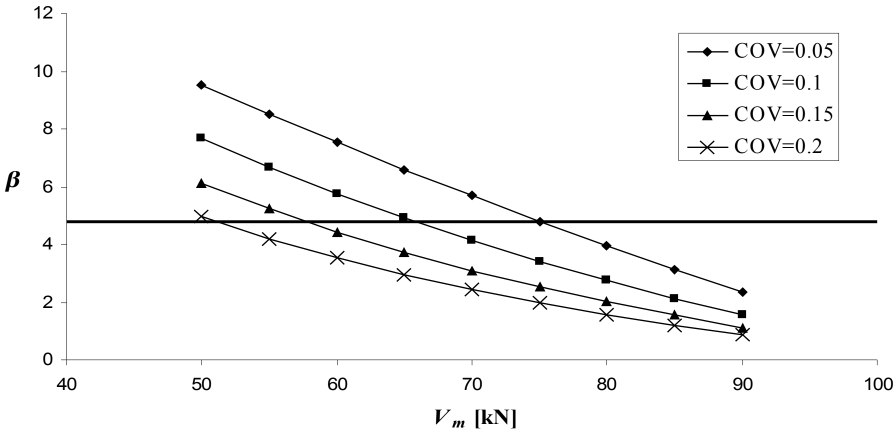

Figure 5.68 – Safety index assessment for corbel F34.

5.3.15 – Corbel Fattuhi 35

Figure 5.69 shows the load-displacement curve. The maximum load is 122 kN and it is in very good agreement with the experimental load 125 kN. The post-peak branch of the curve shows a moderate brittle behavior.

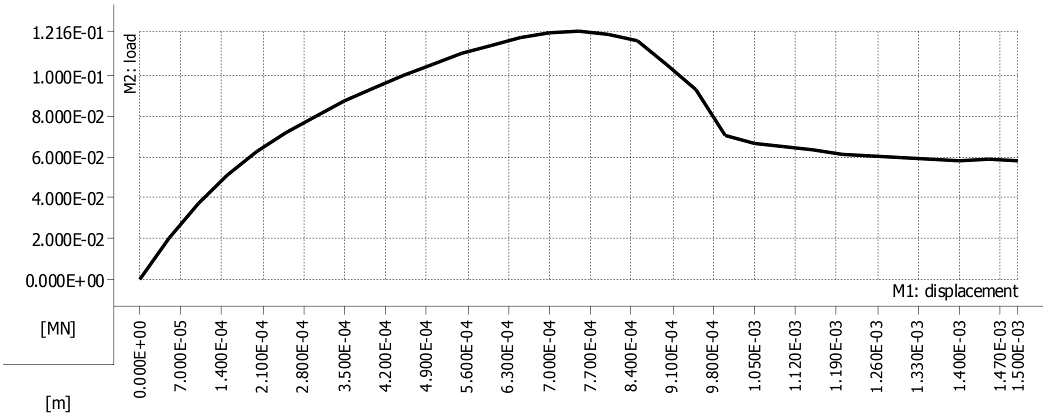

Figure 5.69 – Load-displacement curve for corbel F35.

Figure 5.70 shows that the calculated crack pattern is quite similar to the experimental one.

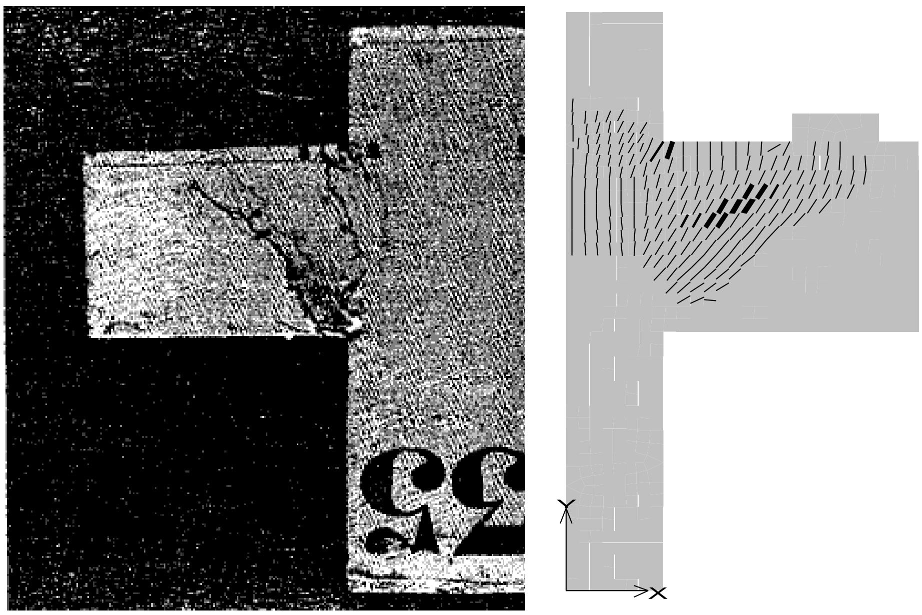

Figure 5.70 – Experimental and numerical crack pattern for corbel F35.

A fitting procedure is performed on the numerical results. A Weibull maximum 3-parameter distribution proves to be a suitable function to describe the corbel ultimate load response (Figure 5.71). The fitting distribution properties are reported in Table 5.29.

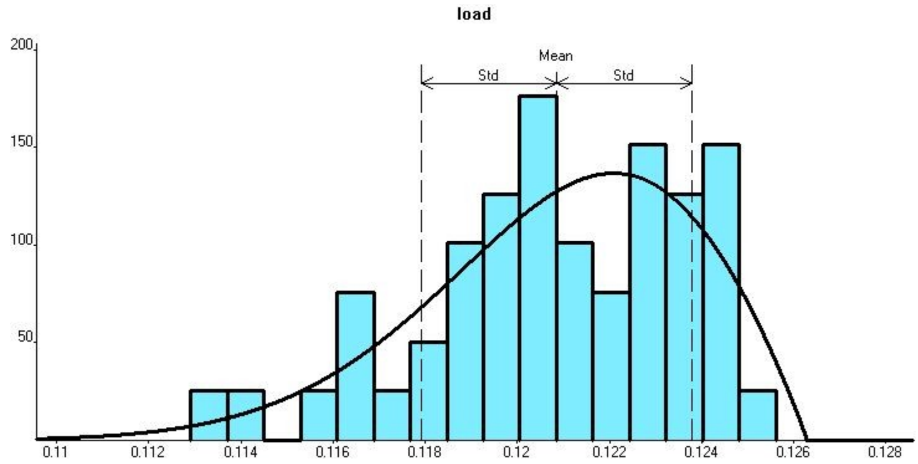

Figure 5.71 – Results and fitting distribution (PDF) for corbel F35.

Variable	*Distribution*	*Mean [kN]*	*std [kN]*	*COV*	*Skewness*	V_5 *[kN]*
load	*Weibull max. 3-par.*	*122*	*3*	*0.02*	*-0.68*	*116*

Table 5.29 – Fitting distribution properties for corbel F35.

The sensitivity study leads to the ranking of Table 5.30. The numerical analysis shows that G_f is the most important variable followed by f_t and E_s. Finally, the influence of f_c is negligible. Figure 5.72 shows the sensitivity correlation between the load and the first two basic variables. As it can be seen by this plot, the variables have a moderate positive correlation to the load.

Variable	*Ultimate load sensitivity*
G_f	*0.48*
f_t	*0.33*
E_s	*0.28*
f_c	*-0.14*

Table 5.30 – Sensitivity of ultimate load to variables for corbel F35.

A further step in the corbel investigation is the evaluation of the allowable external load fulfilling a safety index of 4.7 (equal to a failure probability p_f=10^{-6}). This study is performed with a variable mean value of the load and four different *COV*.

Figure 5.73 shows the behavior of the safety index β related to the calculated ultimate load of the corbel and to a variable action, both expressed as PDF.

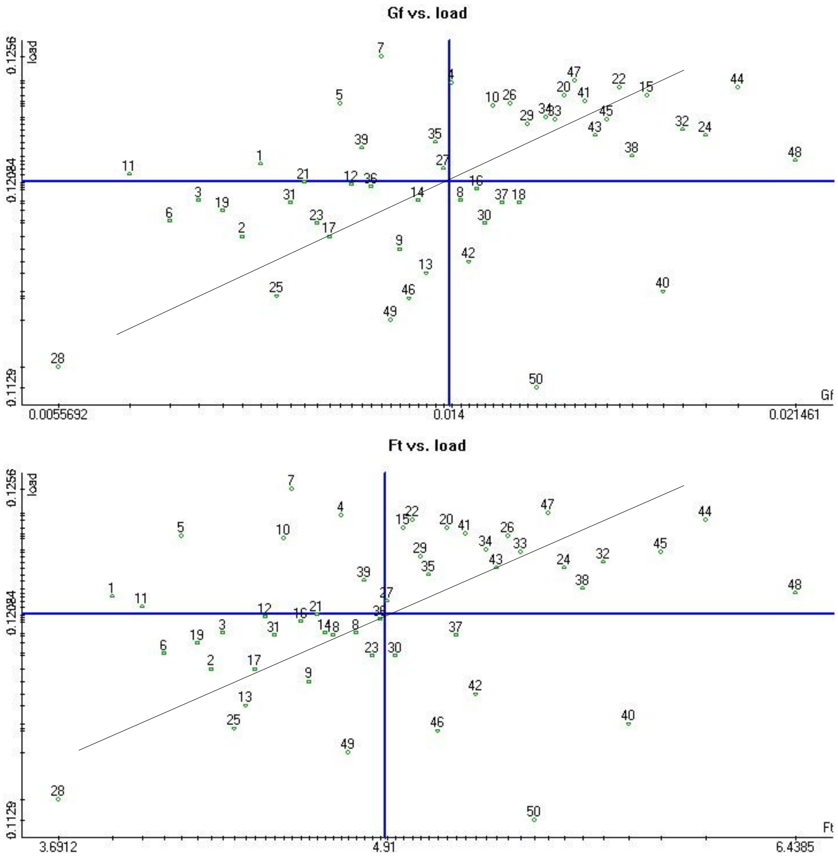

Figure 5.72 – Sensitivity plot for the first two variables for corbel F35.

The investigation refers to different degrees of load scattering described by the *COV*. As it can be seen from the illustration, for a high *COV*=0.2 only a load of about 60 kN can be accepted by fulfilling the target limit of β=4.7. On the other hand, if it is possible to assure that the scattering of the load is smaller than *COV*=0.05, a load of about 95 kN is allowed.

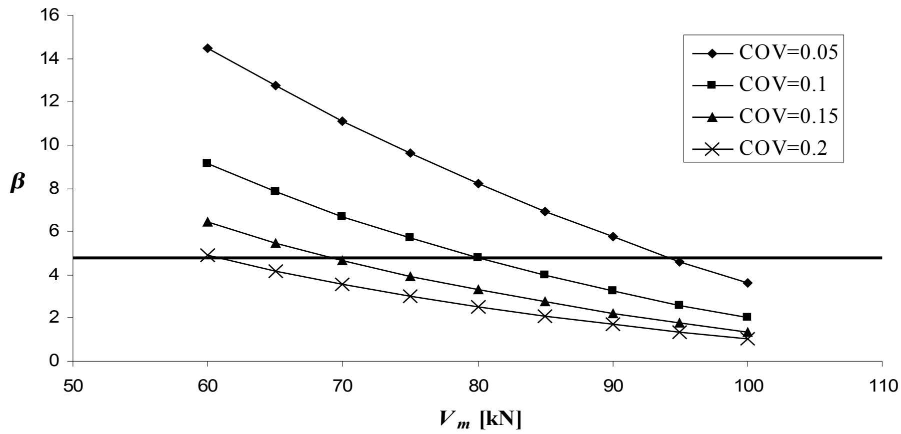

Figure 5.73 – Safety index assessment for corbel F35.

5.3.16 – Corbel Fattuhi 37

Figure 5.74 shows the load-displacement curve. The maximum load is 144 kN and it is in very good agreement with the experimental load 140 kN. The post-peak branch of the curve shows a brittle behavior.

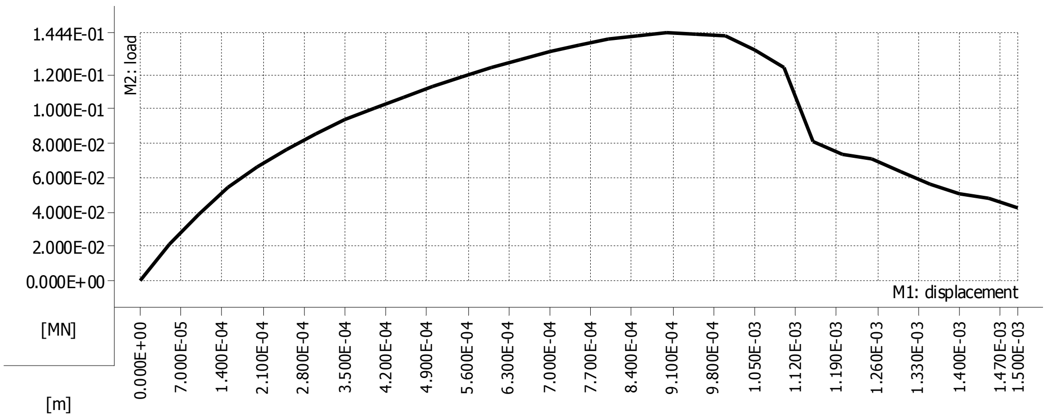

Figure 5.74 – Load-displacement curve for corbel F37.

Figure 5.75 shows that the calculated crack pattern is quite similar to the experimental one.

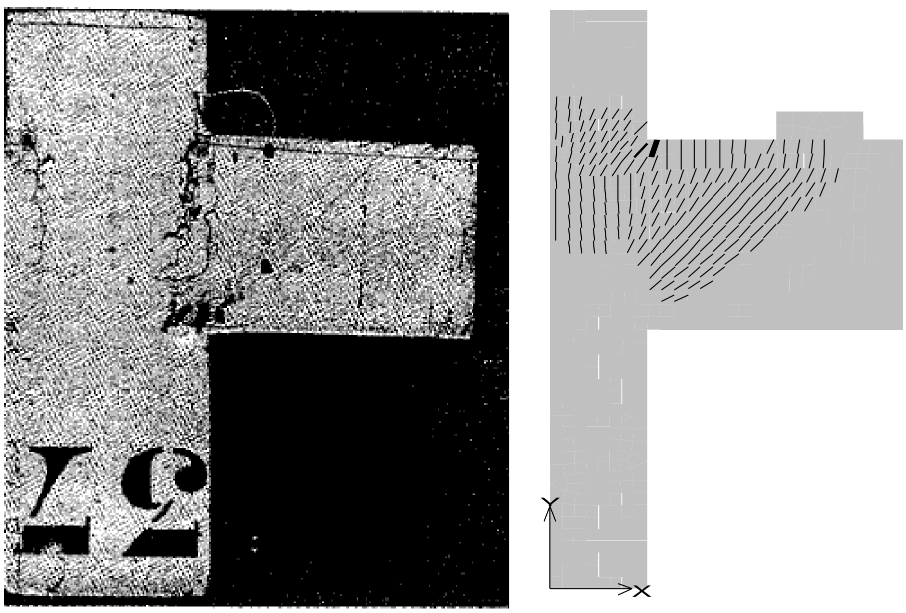

Figure 5.75 – Experimental and numerical crack pattern for corbel F37.

A fitting procedure is performed on the numerical results. A Weibull maximum 3-parameter distribution proves to be a suitable function to describe the corbel ultimate load response (Figure 5.76). The fitting distribution properties are reported in Table 5.31.

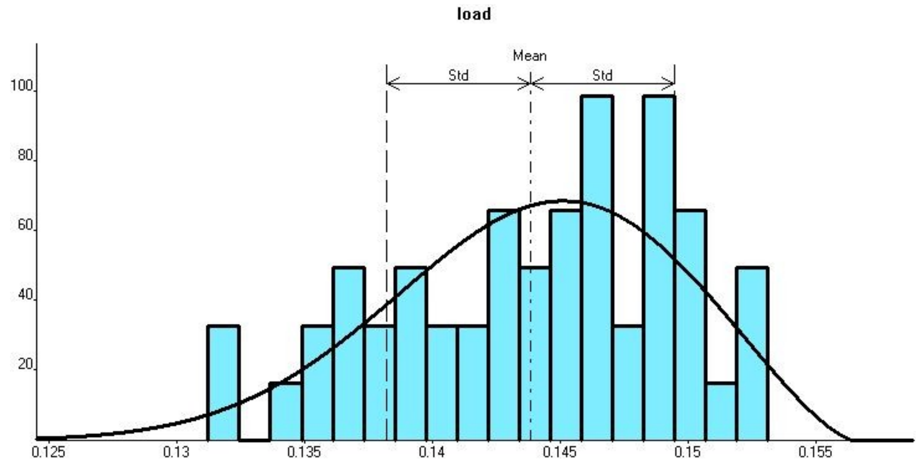

Figure 5.76 – Results and fitting distribution (PDF) for corbel F37.

Variable	***Distribution***	***Mean [kN]***	***std [kN]***	***COV***	***Skewness***	***V_5 [kN]***
load	*Weibull max. 3-par.*	*144*	*6*	*0.04*	*-0.41*	*134*

Table 5.31 – Fitting distribution properties for corbel F37.

The sensitivity study leads to the ranking of Table 5.32. The numerical analysis shows that f_c and E_c are nearly equally participating on the results with a very high influence. Then f_t and G_f have a lower influence. Figure 5.77 shows the sensitivity correlation between the load and the first two basic variables. As it can be seen by this plot, the variables have a strong negative correlation to the load.

Variable	***Ultimate load sensitivity***
f_c	*-0.92*
E_c	*-0.80*
f_t	*-0.50*
G_f	*-0.27*

Table 5.32 – Sensitivity of ultimate load to variables for corbel F37.

A further step in the corbel investigation is the evaluation of the allowable external load fulfilling a safety index of 4.7 (equal to a failure probability p_f=10^{-6}). This study is performed with a variable mean value of the load and four different *COV*.
Figure 5.78 shows the behavior of the safety index β related to the calculated ultimate load of the corbel and to a variable action, both expressed as PDF.

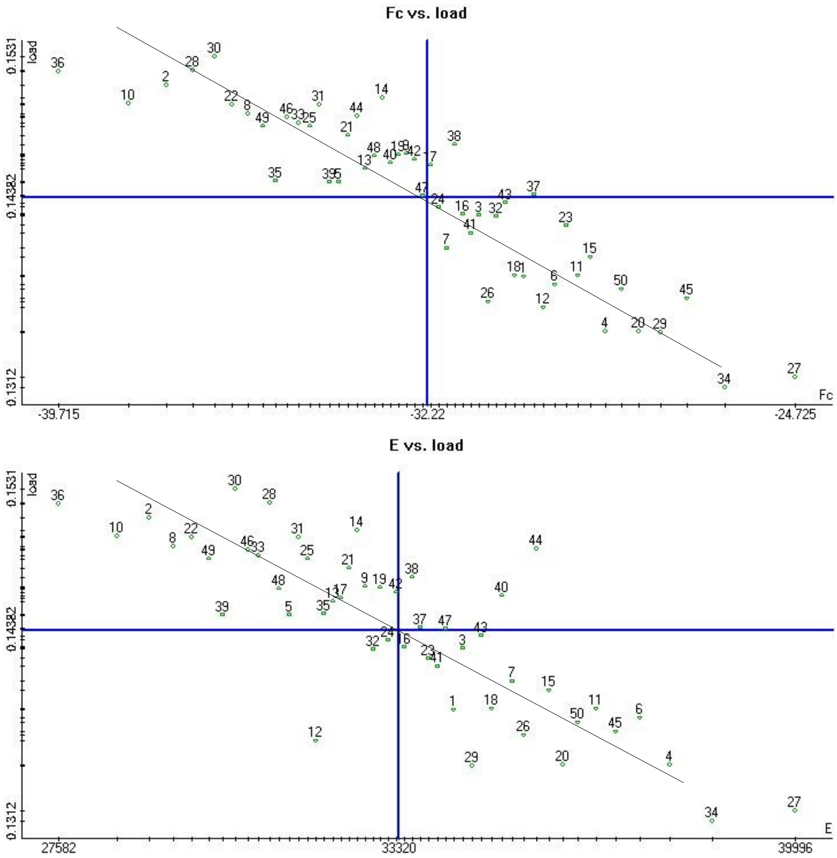

Figure 5.77 – Sensitivity plot for the first two variables for corbel F37.

The investigation refers to different degrees of load scattering described by the *COV*. As it can be seen from the illustration, for a high *COV*=0.2 only a load of about 70 kN can be accepted by fulfilling the target limit of β=4.7. On the other hand, if it is possible to assure that the scattering of the load is smaller than *COV*=0.05, a load of about 105 kN is allowed.

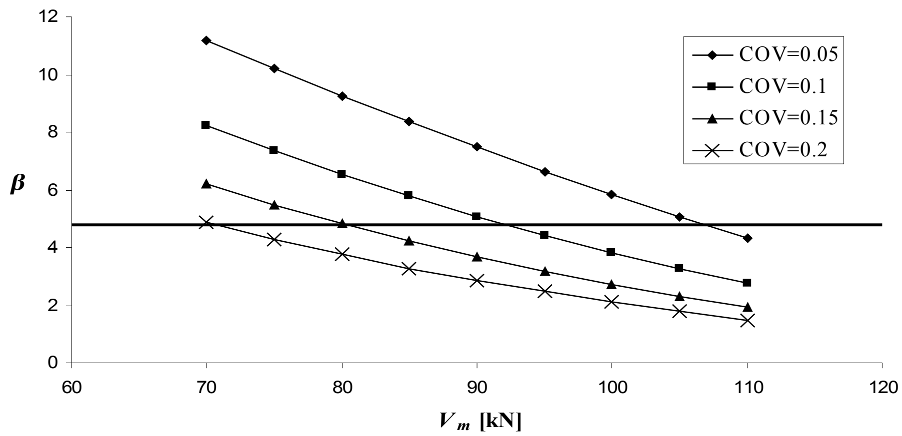

Figure 5.78 – Safety index assessment for corbel F37.

5.4 – COMPARISON WITH EUROCODE

The following calculations are performed according to Eurocode 2 (EC2) [13]. The design load is computed by using the Strut-and-Tie model shown in Figure 5.79. An additional horizontal force H=0.2 V is applied according to the code.

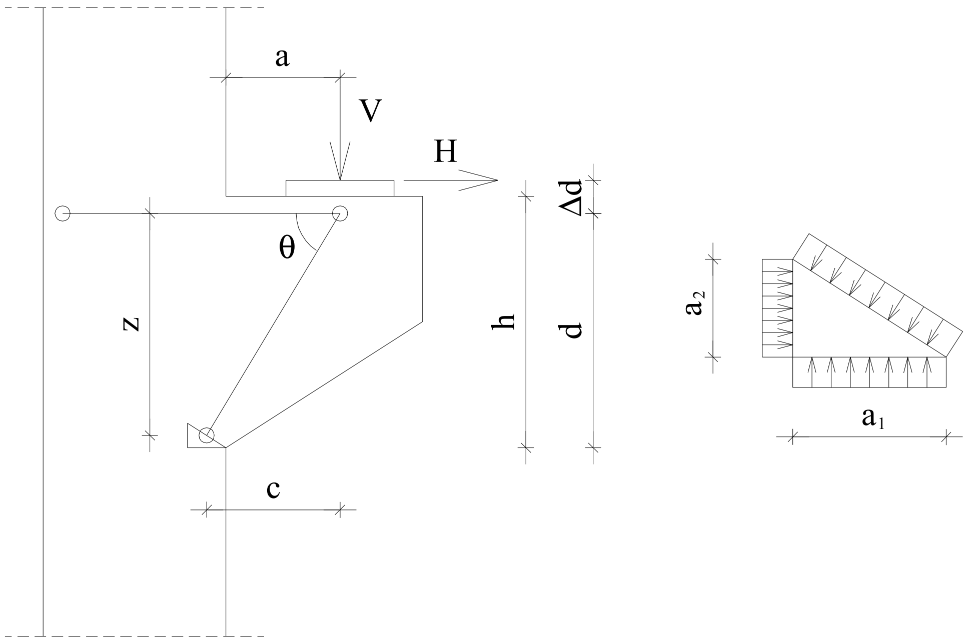

Figure 5.79 – Strut-and-Tie model.

The EC2 imposes the following limit for the span to height ratio:

$$0.4 \leq \frac{a}{h} \leq 1.0\,. \tag{5.3}$$

Some of the investigated corbels exceed this limit, but they are calculated with the same procedure as first approximation. Since the reinforcing fibers have a low influence on the ultimate load, the SFRC corbels are calculated as normal corbels. The geometric properties of the investigated corbels are reported in tables 5.1 and 5.2.

To calculate the design values for the materials, the following procedure is used. The characteristic values for steel and concrete strength f_{yk} and f_{ck} can be written as

$$f_{yk} = f_{ym} - 1.645 std_{steel} \text{ and } f_{ck} = f_{cm} - 1.645 std_{concrete}\,, \tag{5.4}$$

where f_{ym} and f_{cm} are the mean values for steel and concrete strength respectively and *std* is the standard deviation.

To calculate *std*, typical values of the coefficient of variation *COV* are used:

$$COV_{steel} = \frac{std_{steel}}{f_{ym}} = 0.035 \text{ and } COV_{concrete} = \frac{std_{concrete}}{f_{cm}} = 0.1. \tag{5.5}$$

Writing the *COV* according to (5.5) and substituting it into (5.4), the following equations are obtained:

$$f_{yk} = 0.94 f_{ym} \text{ and } f_{ck} = 0.84 f_{cm}. \tag{5.6}$$

The characteristic and the design values are related by

$$f_{sd} = \frac{f_{yk}}{1.15} \text{ and } f_{cd} = \frac{f_{ck}}{1.5}, \tag{5.7}$$

where f_{sd} and f_{cd} are the design values for steel and concrete strength respectively.

Therefore, the design values can be computed starting from the mean values with

$$f_{sd} = 0.82 f_{ym} \text{ and } f_{cd} = 0.56 f_{cm}. \tag{5.8}$$

The calculated values are reported in tables 5.33 and 5.34.

Corbel	***Concrete***			***Steel***		
	f_{cm} [MPa]	***f_{ck} [MPa]***	***f_{cd} [MPa]***	***f_{ym} [MPa]***	***f_{yk} [MPa]***	***f_{sd} [MPa]***
KR13	*31.6*	*26.5*	*17.7*	*352*	*331*	*288*
KR14	*31.3*	*26.3*	*17.5*	*352*	*331*	*288*
KR21	*27.0*	*22.7*	*15.1*	*298*	*280*	*244*
KR55	*27.7*	*23.2*	*15.5*	*312*	*293*	*255*
KR80	*16.8*	*14.1*	*9.4*	*300*	*282*	*245*
KR91	*28.0*	*23.5*	*15.7*	*322*	*303*	*263*
KR100	*44.3*	*37.2*	*24.8*	*328*	*308*	*268*

Table 5.33 – Material properties of Kriz-Raths corbels.

The angle θ between the strut and the tie is calculated by

$$\tan\theta = \frac{z}{c} = \frac{d-0.5a_2}{a+0.5a_1}, \tag{5.9}$$

where

$$a_1 = \frac{V}{0.6\alpha f_{cd} b} \text{ and } a_2 = d - \sqrt{d^2 - 2a_1 c}, \tag{5.10}$$

being b the corbel depth and α=0.85.

Corbel	***Concrete***			***Steel***		
	f_{cm} [MPa]	***f_{ck} [MPa]***	***f_{cd} [MPa]***	***f_{ym} [MPa]***	***f_{yk} [MPa]***	***f_{sd} [MPa]***
F23fr	*28.3*	*23.8*	*15.9*	*452*	*425*	*369*
F25	*30.7*	*25.8*	*17.2*	*452*	*425*	*369*
F34	*32.0*	*26.8*	*17.9*	*452*	*425*	*369*
F35fr	*30.3*	*25.5*	*17.0*	*452*	*425*	*369*
F37fr	*32.2*	*27.1*	*18.0*	*452*	*425*	*369*

Table 5.34 – Material properties of Fattuhi corbels.

After solving the Strut-and-Tie structure, the force in the steel F_s must be less than or equal to the design ultimate load:

$$F_s = \frac{1}{z}\left(H\left(z+\Delta d\right)+Vc\right) \le F_{Rd} = f_{sd} A_s. \tag{5.11}$$

Then, the verification for concrete is carried out according to shear design rules:

$$V \le V_{Rd2} = 0.6\alpha f_{cd} bz \sin\theta\cos\theta. \tag{5.12}$$

The calculated design loads, for steel and concrete failure, are reported in tables 5.35 and 5.36. The tables report the 5% fractile V_5 from the probabilistic analyses and compute the safety factor as

$$\gamma = \frac{V_5}{V_{EC2}}. \tag{5.13}$$

The safety factor values are compared with those proposed by the Eurocode, namely 1.15 for steel failure and 1.50 (variable loads) for concrete failure.

Corbel	$V_{EC2\ steel}$ **[kN]**	$V_{EC2\ concrete}$ **[kN]**	***Failure***	V_{EC2} **[kN]**	V_5 **[kN]**	γ
KR13	*125*	*352*	*steel*	*125*	*264*	*2.11*
KR14	*139*	*389*	*steel*	*139*	*337*	*2.42*
KR21	*170*	*336*	*steel*	*170*	*388*	*2.28*
KR55	*122*	*335*	*steel*	*122*	*236*	*1.93*
KR80	*169*	*187*	*steel*	*169*	*350*	*2.07*
KR91	*308*	*248*	*concrete*	*248*	*538*	*2.17*
KR100	*359*	*392*	*steel*	*359*	*706*	*1.97*

Table 5.35 – Design load and safety factor for Kriz-Raths corbels.

Corbel	$V_{EC2\ steel}$ **[kN]**	$V_{EC2\ concrete}$ **[kN]**	***Failure***	V_{EC2} **[kN]**	V_5 **[kN]**	γ
F23fr	*50*	*53*	*steel*	*50*	*126*	*2.54*
F25	*51*	*58*	*steel*	*51*	*96*	*1.87*
F34	*58*	*54*	*concrete*	*54*	*97*	*1.80*
F35fr	*57*	*52*	*concrete*	*52*	*115*	*2.21*
F37fr	*59*	*55*	*concrete*	*55*	*134*	*2.44*

Table 5.36 – Design load and safety factor for Fattuhi corbels.

The calculated safety factor is always greater than the one proposed by the Eurocode. In fact, if the 5% fractile of the ultimate load distribution computed by SARA is compared with the design value of the Eurocode, the demanded safety index is fulfilled by far. Considering the smallest safety margins of this study, it is possible to calculate the minimum $\Delta\gamma$ for steel and concrete failure. For steel failure $\Delta\gamma_{min}$=1.87-1.15=0.72 and for concrete failure $\Delta\gamma_{min}$=1.80-1.50=0.30 is obtained.

Finally, it can be stated that the non-linear numerical investigation allows a more accurate description of the material behavior and the activation of not used safety margins.

5.5 – THREE-DIMENSIONAL ANALYSIS

5.5.1 – Theoretical basics

Several different material models are implemented within the code ATENA 3D and the most of them are based on fracture-plasticity approach. In particular, in the simulations of this work, the CC3DNonLinCementitious2 material is used. The fracture-plastic model combines constitutive models for tensile (fracturing) and compressive (plastic) behavior.

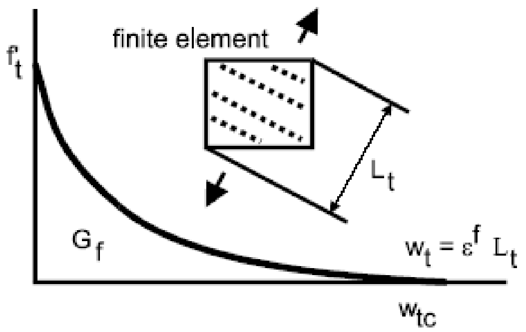

Figure 5.80 – Tensile softening and characteristic length.

The fracture model is based on the classical orthotropic smeared crack formulation and crack band model. It employs Rankine failure criterion, exponential softening (Figure 5.80) and it can be used as rotated or fixed crack model. It is assumed that strains and stresses are converted into the material directions. In case of rotated crack model, they correspond to the principal directions while, in case of fixed crack model, they are given by the principal directions at the cracking onset. The crack opening is the sum of the total fracturing strain and the current increment of fracturing strain multiplied by the characteristic length. Various methods were proposed for the characteristic length calculation in the FE framework. In ATENA, it is calculated as the FE size projected into the crack direction. This approach is satisfactory for low order linear elements, which are used throughout this study.

The hardening/softening plasticity model is based on Menetrey-Willam [33] failure surface (Figure 5.81), but Drucker-Prager formulation can be also used.

Both models use return mapping algorithm for the integration of constitutive equations. New stress state in the plastic model is computed using a predictor-corrector formulation where the plastic corrector is computed directly from the yield function by return mapping algorithm. Thus, the crucial aspect is the definition of the return direction. The position of failure surfaces is not fixed but it can move depending on the value of strain hardening/softening parameter. The strain hardening is based on the equivalent plastic strain. For Menetrey-Willam surface, the hardening/softening is controlled by a parameter, which evolves during the yielding/crushing process.

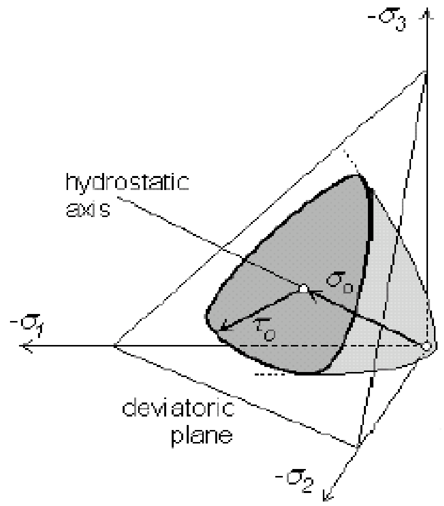

Figure 5.81 – 3D failure surface.

The hardening/softening law, which is based on the uniaxial compressive test, is shown in Figure 5.82, where the softening curve is linear and the ascending part is elliptical.

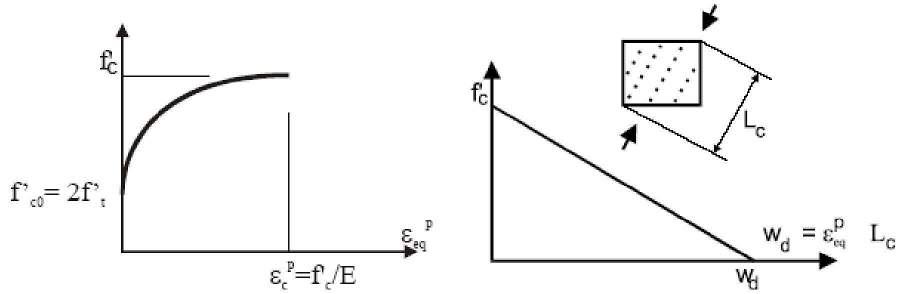

Figure 5.82 – Compressive hardening/softening and compressive characteristic length.

The law on the ascending branch is based on strains, while the descending branch is based on displacements to introduce mesh objectivity into the numerical solution. On the descending curve, the equivalent plastic strain is transformed into displacement through the length scale parameter. This parameter corresponds to the projection of FE size into the direction of the minimum principal stress. Return direction is given according to a plastic potential which contains β determining the return direction. If $\beta<0$, the material is being compacted during crushing, if $\beta=0$, the material volume is preserved, and if $\beta>0$, the material is dilating. In general, the plastic model is non-associated, since the plastic flow is not perpendicular to the failure surface.

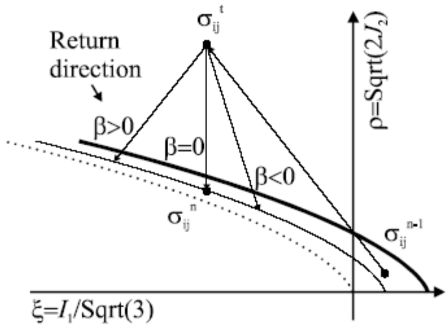

Figure 5.83 – Plastic predictor-corrector algorithm.

The return-mapping algorithm (Figure 5.83) for the plastic model is based on predictor-corrector approach. During the corrector phase of the algorithm, the failure surface moves along the hydrostatic axis to simulate hardening and softening. A secant algorithm is used to determine the stress on the surface, which satisfies both the yield condition and the hardening/softening law.

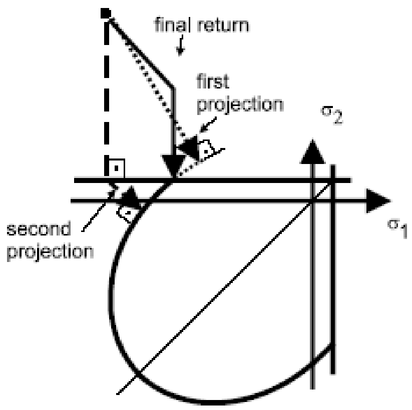

Figure 5.84 – Combination of plasticity and fracture model.

Special attention is given to the combination of fracture and plasticity models (Figure 5.84). The combined algorithm is based on a recursive substitution, and it allows for the two models to be formulated separately. However, both models are developed within the framework of return mapping algorithm which guarantees the solution for all magnitudes of strain increment. From an algorithmic point of view, the problem is then transformed into finding an optimal return point on the failure surface. The algorithm can handle cases when failure surfaces of both models are active, but also when physical changes, such as crack closure due to crushing in other material directions, occur. The combining algorithm must determine the separation of strains into plastic and fracturing components, while it must preserve the stress equivalence in both models. The problem can be generally stated as a simultaneous solution of two different inequalities. Each inequality depends on the output from the other one: therefore, an iterative scheme is developed.

An important condition for the procedure convergence is that the failure surfaces of the two models are intersecting in all possible positions even during the hardening or softening. Actually, concrete crushing in one direction affects the cracking in other directions. It is assumed, as a constraint, that after the plasticity yield criterion is violated, the tensile strength in all material directions is zero.

On the structural level, the secant matrix is used in order to achieve a robust convergence.

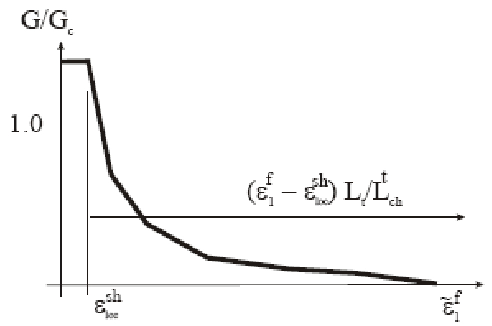

Figure 5.85 – User-defined shear retention factor.

ATENA allows the user to define the behavior of some selected parameters. In particular, it is possible to set the evolution laws for elastic modulus, tensile and compressive strength, shear retention factor for fixed crack approach (Figure 5.85) and reduction of tensile strength due to lateral compressive stress (Figure 5.86).

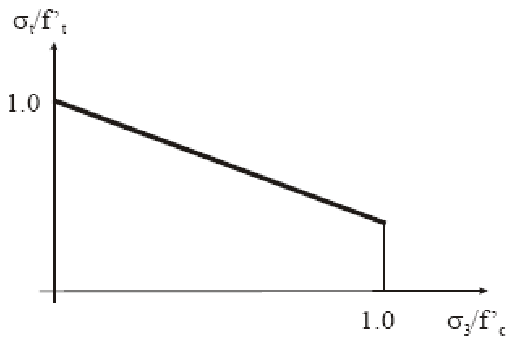

Figure 5.86 – Tensile strength degradation due to lateral compressive stress.

In heavily reinforced structures, or structures modeled with large elements, when many reinforcement bars are crossing each element, the crack band approach could provide too conservative results, and the calculated crack widths and consequently, the deflections may be overestimated. In fact, the crack band approach assumes that the crack spacing is larger than a FE size but, especially with shell/plate elements, it may occur that the crack spacing is smaller than the element size. In these cases, ATENA allows the user to manually define the crack spacing.

In RC structures, the cracks cannot fully develop and concrete contributes to the steel stiffness. This effect is called tension stiffening and it can be simulated by specifying a tension stiffening factor c_{ts}. This factor represents the relative limiting value of tensile strength in the tension-softening diagram. The tensile stress cannot drop below the value given by the product $c_{ts} f_t$ (Figure 5.87).

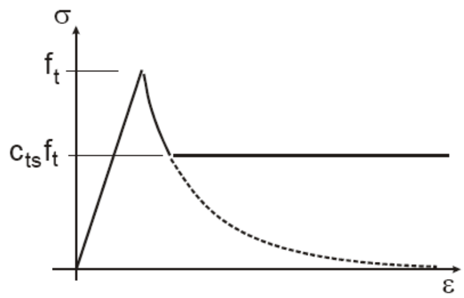

Figure 5.87 – Tension stiffening model.

The reinforcement modeling is realized by the same formulation already described in the 2D case.

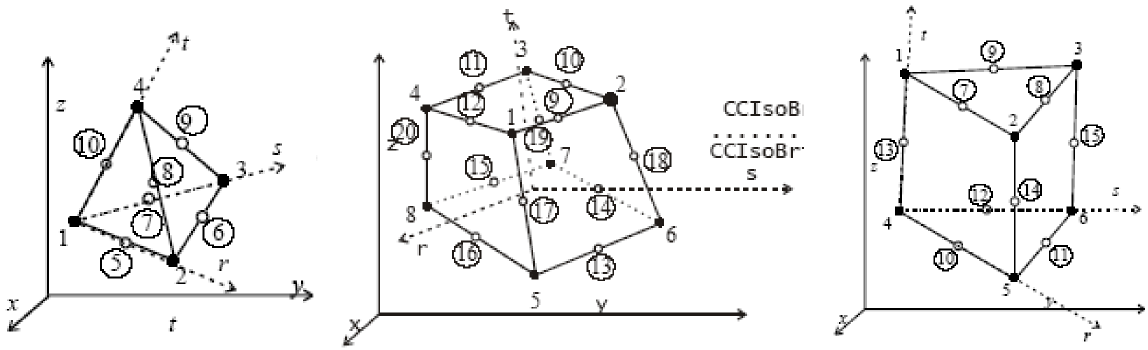

Figure 5.88 – ATENA solid element library.

ATENA 3D solid FE library includes tetrahedral, brick and wedge elements, all using linear isoparametric formulation (Figure 5.88).

In Cervenka's paper some 3D applications are shown [18]. The Nusle Bridge was built in

Prague in 1972. It is the largest bridge of the city with a six-lane highway on the top and a two-way subway inside the box (Figure 5.89).

The bridge is investigated in order to evaluate the safety of the structure, in particular regarding the effectiveness of the vertical prestressing cables which are expected to be damaged by corrosion.

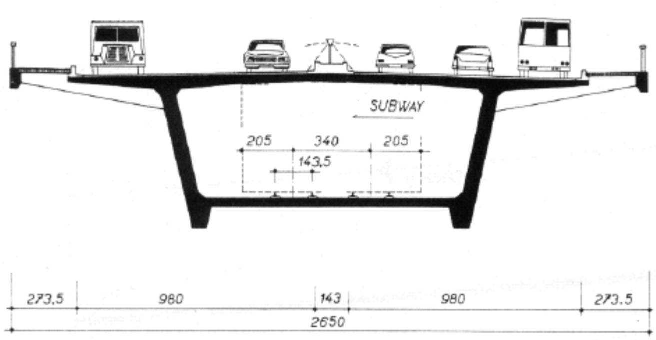

Figure 5.89 – Bridge cross-sectional geometry.

The computer model is rather complicated since the real geometry and the reinforcement location are represented with high accuracy (Figure 5.90). On the contrary, the construction process is not included in the model. Since the mechanical properties are difficult to estimate, a parametric study is required.

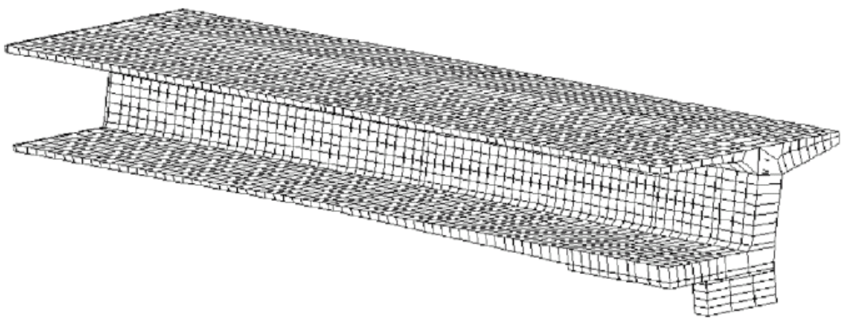

Figure 5.90 – FE discretization.

The main objective of the study is the evaluation of the structural behavior under the service and the ultimate load.

The analysis proves that the structural performance is satisfactory under the service load. What is more, the vertical prestressing cables have a high influence on the box wall behavior but not on the overall structural safety even if the prestressing is reduced near to zero.

Subsequently, the analysis is performed up to failure of the structure and a safety factor (ratio of the ultimate to the service load) of 1.99, coinciding with the safety level usually required, is found (Figure 5.91).

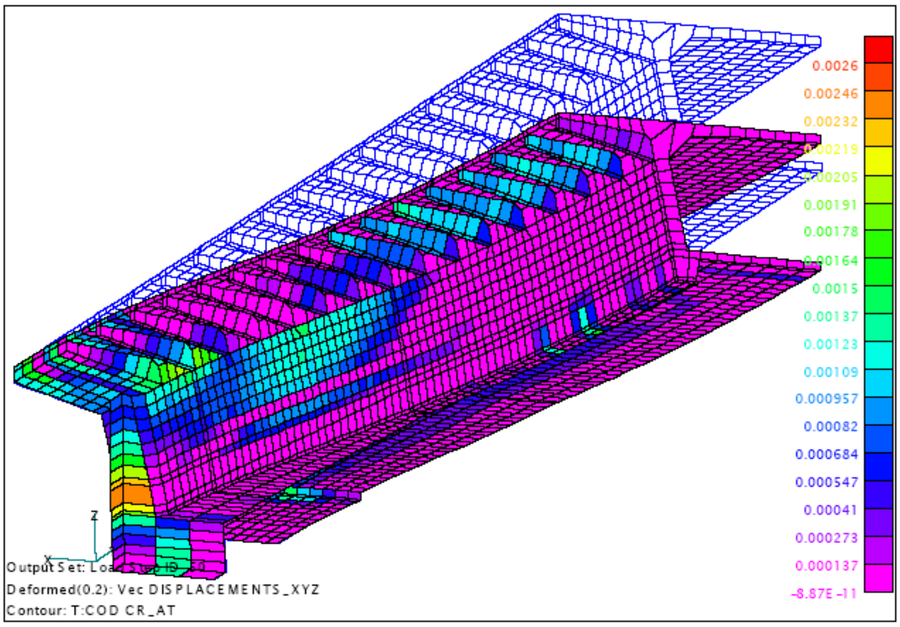

Figure 5.91 – Crack width and deformed shape at ultimate load.

5.5.2 – Structural modeling

The corbel properties for 3D analyses were already specified for the 2D case in tables 5.1 and 5.2.

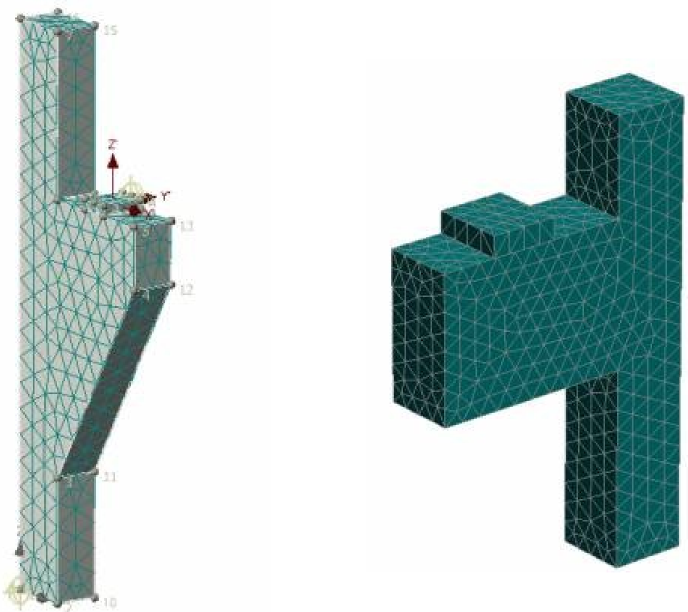

Figure 5.92 – 3D FE discretization for the investigated corbels.

The FE meshes for 3D analyses are shown in Figure 5.92. Linear tetrahedral elements are used with different size depending on the corbel. A fine mesh is more suitable for Fattuhi corbels whereas Kriz-Raths corbels require a less refined mesh. Due to double symmetry, only a quarter of the specimen is modeled.
With respect to the 2D case, concrete is modeled by using a different constitutive formulation based on fracture-plastic approach, as already discussed. On the contrary, for steel, the same formulation is adopted. Therefore, a bilinear elastic perfectly plastic uniaxial law is used together with a discrete reinforcement formulation. Perfect bond is assumed between concrete and steel
One of the main objectives of the simulations is the comparison of 2D and 3D outcomes, in order to understand if an approximate 2D analysis is sufficient or a more complete 3D analysis is necessary to capture the structural behavior.

5.5.3 – Results and comparisons

Numerical results for 3D analyses are reported in Table 5.37. The numerical simulations provide very good results for Kriz-Raths corbels, whereas the agreement is less accurate for Fattuhi specimens. In general, it can be stated that the ultimate load values are overestimated by the 3D analysis whereas they are underestimated, but with a lower error, by the 2D analysis.

Corbel	***Failure***	V_{exp} ***[kN]***	***ATENA deterministic***		***ATENA deterministic***	
			$V_{ATENA2D}$ ***[kN]***	***Difference***	$V_{ATENA3D}$ ***[kN]***	***Difference***
KR14	*DS*	*374*	*367*	*-1.9%*	*384*	*2.7%*
KR21	*DS*	*423*	*405*	*-4.3%*	*448*	*5.9%*
KR55	*CE*	*269*	*255*	*-5.2%*	*272*	*1.1%*
F23fr	*F*	*127*	*131*	*3.1%*	*142*	*11.8%*
F25	*DS*	*109*	*103*	*-5.5%*	*115*	*5.5%*
F34	*DS*	*114*	*106*	*-7.0%*	*129*	*13.2%*

Table 5.37 – 3D analysis result comparison.

In figures 5.93 and 5.94, the load-displacement curves for two of the investigated corbels are reported. The two specimens exhibit a ductile behavior with a long plastic plateau after the steel yielding.

In figures 5.95 and 5.96, some other outcomes from ATENA 3D are shown. In particular, on the base of the minimum principal strain, the compressive strut can be located in the corbel. Then, through the crack width, the crack pattern and therefore, the failure mode, can be evaluated. Finally, the corbel deformed mesh is visualized through the vertical displacement distribution.

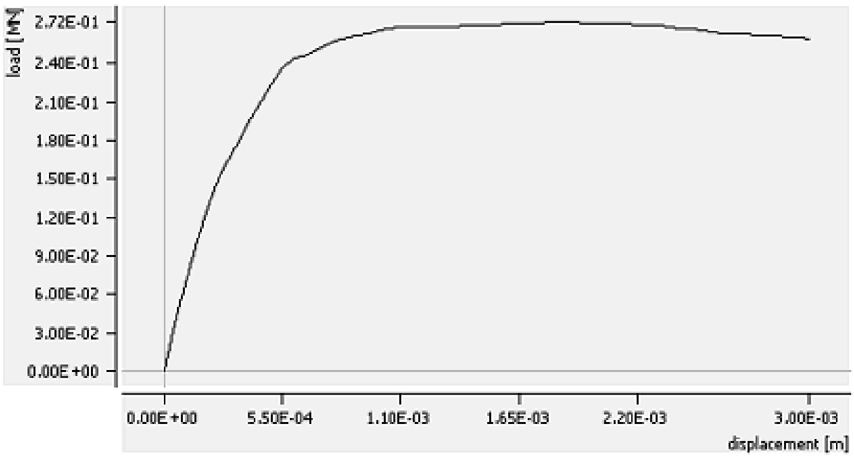

Figure 5.93 – Load-displacement curve for corbel KR55.

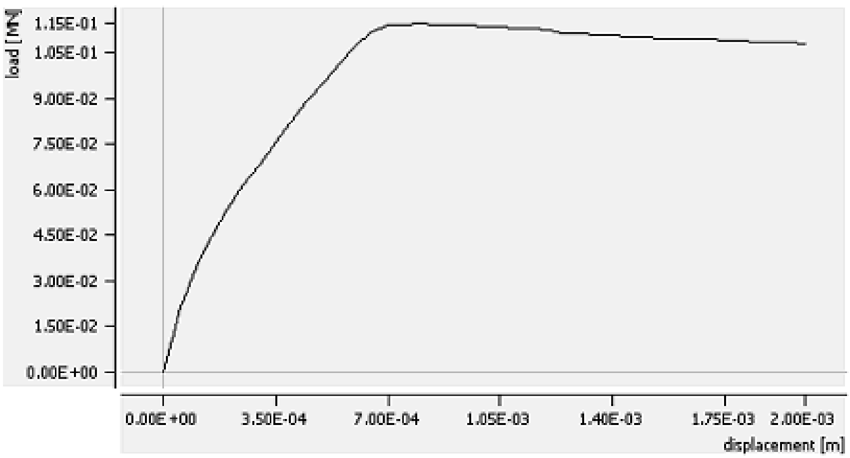

Figure 5.94 – Load-displacement curve for corbel F25.

The structural analysis can be performed in different ways according to the chosen accuracy level and to the required results.

The presented analysis demonstrates that the simple Strut-and-Tie model proposed by the Eurocode is sufficient to obtain safe results for design. The next level, the 2D analysis, can provide, besides the ultimate load, more information about the structural behavior such as the failure mode, the crack pattern, the stress in steel and the stress-strain distribution in concrete. Generally, the 3D analysis provides a high-level accuracy, capturing the real spatial unconstrained behavior. Obviously, the 3D model, namely the material formulation and the FE implementation, is more complicated and it can provide, in some cases, worse results than the simpler 2D analysis.

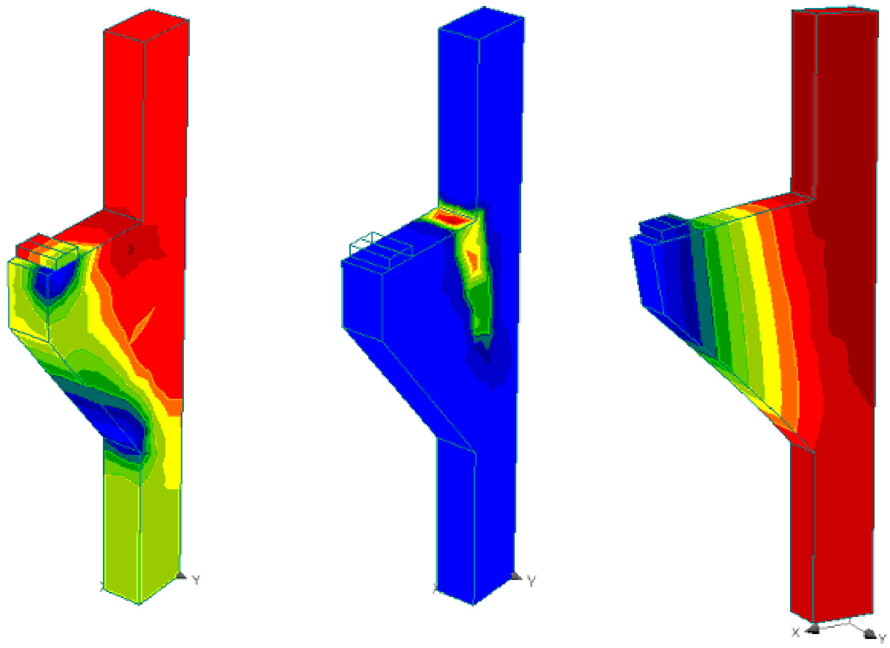

Figure 5.95 – Min. principal strain, crack width and vertical displacements for corbel KR55.

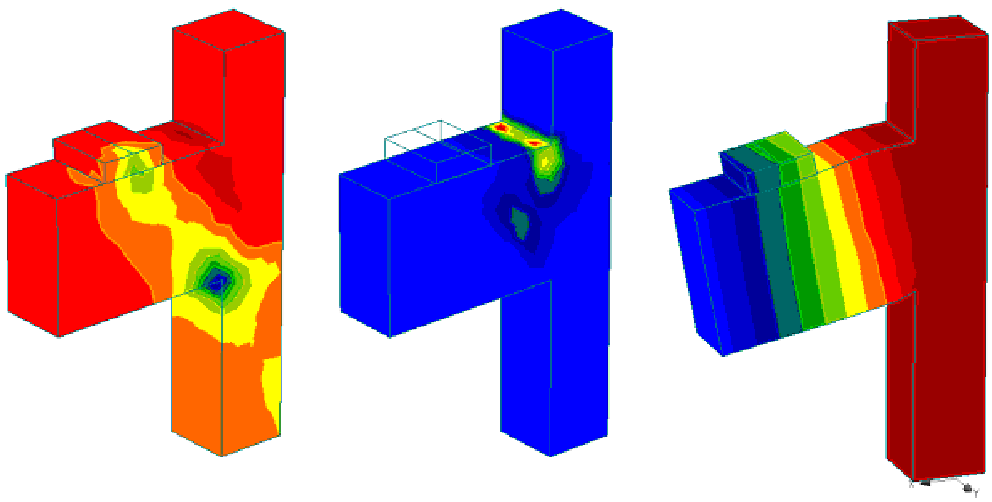

Figure 5.96 – Min. principal strain, crack width and vertical displacements for corbel F25.

In the study of the investigated corbels, in four out of six cases, the 3D analysis provides worse results than the 2D one. Moreover, the 2D calculation adopts a simplified model which is easier to manage and involves reduced computational time and modeling effort. Thus, it can be concluded that, even if the out of plane behavior is neglected, the 2D approximation is a very good way to investigate this type of structures.

5.6 – CONCLUSIONS

In this chapter, the deterministic and probabilistic FE analysis of RC corbels is presented. Deterministic analyses are performed using both 2D and 3D models with two different versions of the RC-oriented FE code ATENA. Probabilistic analyses are performed with SARA, a software package which integrates the code ATENA 2D and the probabilistic module FREET.

The deterministic analyses provide results in good agreement with the experimental data. Beside the ultimate load, ATENA allows to extract a great number of information from the model such as stresses, strains, reinforcement force and crack pattern. All these variables are compared with experimental outcomes and discussed in detail.

Concerning the probabilistic investigations, it can be concluded that the calculated ultimate load distributions can be very well described by the Lognormal and Weibull distributions. These fitting PDF allow to effectually describe the experimental results from the analytical point of view and therefore, they are suitable to perform the comparison with the Eurocode design values. The outcomes of this studies shows that in general, the non-linear probabilistic calculation can be used for activating additional safety margins not considered by the Eurocode.

Especially for corbel design, the probabilistic analysis provides a great advantage, since the sensitivity study gives the possibility to evaluate the most important material properties influencing the structural behavior. Therefore, the probability-based study offers the possibility of a professional and optimized design.

The comparison between 2D and 3D outcomes demonstrated that the 2D analysis provides better results with a simpler model which means reduced computational time and smaller modeling effort.

CHAPTER 6 – CONCLUSIONS

This doctorate dissertation presents the three-dimensional (3D) constitutive model for non-linear analysis of reinforced concrete (RC) structures 3D-PARC – Three-Dimensional Physical Approach for Reinforced Concrete. The 3D formulation, based on the author's graduate thesis [34], is the extension of the numerical model for membrane elements PARC developed at the Department of Civil Engineering of the University of Parma [8, 9]. The basic concepts of PARC were developed and applied in some previous works [25, 14].

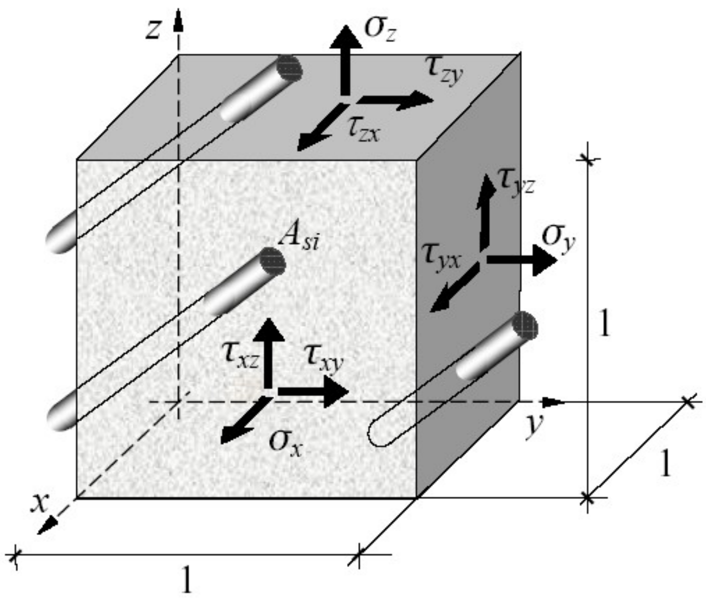

Figure 6.1 – Solid unitary RC element.

The study process which led to the development of the model, started from some basic investigations describing the physical phenomena. Following this philosophy, the theory of the model was created by combining single material contributes separately investigated: the constitutive models for concrete, steel and local effects (tension stiffening, dowel action, aggregate bridging and interlock) were studied through different publications and inserted in the model.

3D-PARC adopts fixed, multi-directional cracking and smeared reinforcement approaches. An unitary solid RC element is investigated (Figure 6.1). Three different phases are considered: the uncracked material, the singly cracked material and the doubly or multi-cracked material. In each phase, a different constitutive matrix is adopted depending on the strain field and on the physical properties of the materials.

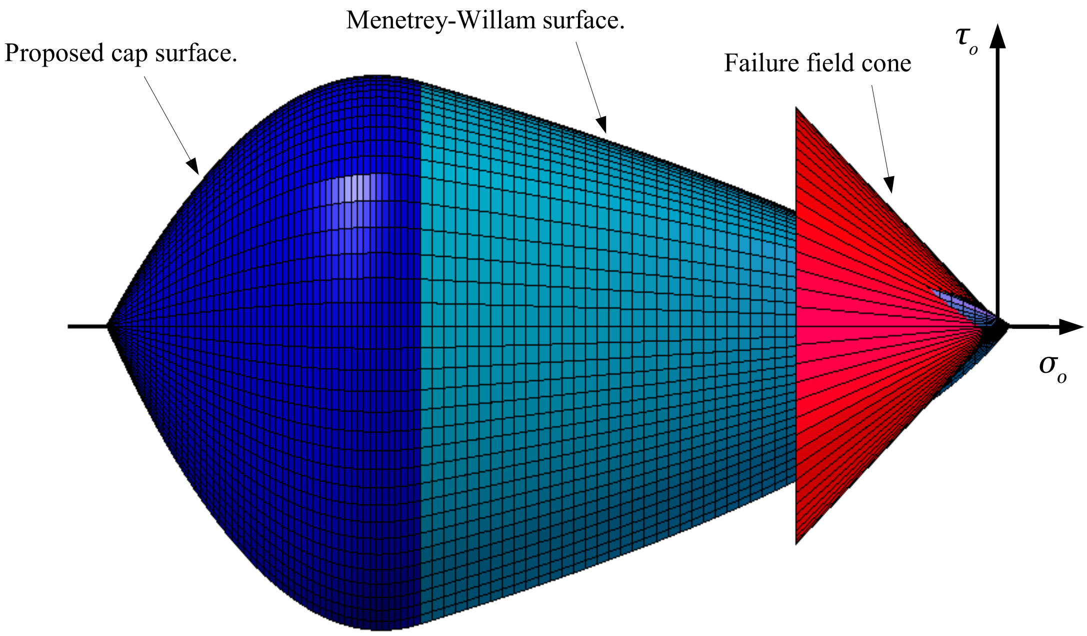

Figure 6.2 – The failure surface and the cone defining the failure fields.

In the uncracked phase, concrete and steel are supposed to be subjected to the same global strain field:

$$\left\{\varepsilon^{xyz}\right\} = \left\{\varepsilon_c^{xyz}\right\} = \left\{\varepsilon_s^{xyz}\right\}. \tag{6.1}$$

Therefore, the two material work in parallel and the following material stiffness matrix is obtained:

$$\left[D^{xyz}\right] = \left[D_c^{xyz}\right] + \left[D_s^{xyz}\right]. \tag{6.2}$$

In order to model the concrete behavior, the Balan-Spacone-Kwon failure surface [5], based on the previous Menetrey-Willam surface [33] is adopted. Furthermore, a new cap surface is proposed in order to close the surface in the region of high hydrostatic stresses. The tensile or compressive nature of the failure can be evaluated by dividing the surface into failure fields by a cone as shown in Figure 6.2. The Saenz stress-strain relation [42] and the equivalent uniaxial strain formulation [21] are used to compute the elastic moduli.

The steel behavior is modeled by a bilinear elastic-plastic curve equal in tension and compression. Any number of steel layers can be defined.

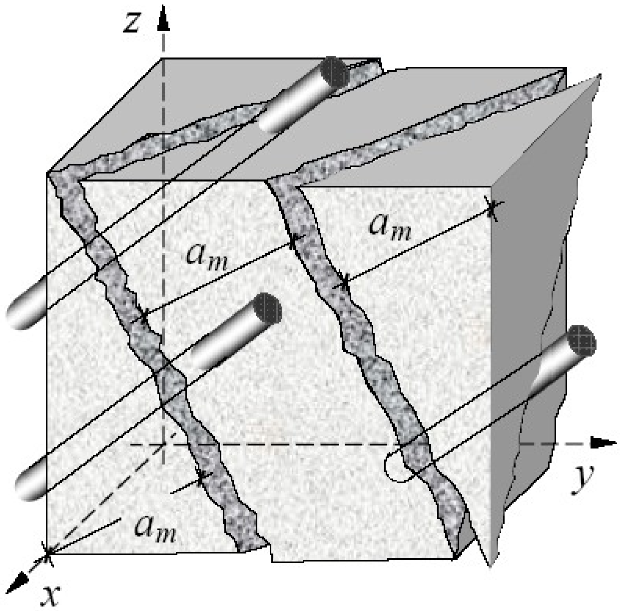

Figure 6.3 – Solid cracked RC element.

The cracks are assumed to form when the elastic tensile strain limit is exceeded. In the cracked phase (Figure 6.3), the total strain is decomposed into the strain between the cracks and in the crack:

$$\left\{\varepsilon^{xyz}\right\} = \left\{\varepsilon_c^{xyz}\right\} + \left\{\varepsilon_{cr}^{xyz}\right\}. \tag{6.3}$$

This leads to the following material stiffness matrix:

$$\left[D^{xyz}\right] = \left(\left(\left[I\right] + \left[D_c^{xyz}\right]^{-1}\left[D_s^{xyz}\right]\right)^{-1}\left(\left[D_c^{xyz}\right]^{-1} + \left[D_{cr}^{xyz}\right]^{-1}\right)\right)^{-1}, \tag{6.4}$$

where the concrete and the crack flexibility matrices are added.

The material between the cracks is assumed to be uncracked and it is modeled like in the uncracked phase. Nevertheless, the presence of the crack has a penalizing effect on the material properties which is modeled by a softening coefficient [7].
The crack matrix contains the contributes of the interface phenomena related to concrete and steel in the crack. In particular, in the concrete contribute, the aggregate bridging [12, 31] and interlock [23] are considered, while, in the steel contribute, the axial force in the reinforcing bar, the tension stiffening and the dowel action [46] are taken into account. A numerical procedure for the tension stiffening formulation is proposed.
In the doubly cracked phase, a similar approach is adopted: the total strain is the sum of the strain between the cracks, in the first crack and in the second crack:

$$\left\{\varepsilon^{xyz}\right\} = \left\{\varepsilon_c^{xyz}\right\} + \left\{\varepsilon_{cr1}^{xyz}\right\} + \left\{\varepsilon_{cr2}^{xyz}\right\}. \tag{6.5}$$

This leads to the following material stiffness matrix:

$$\left[D^{xyz}\right] = \left(\left([I] + \left[D_c^{xyz}\right]^{-1}\left[D_s^{xyz}\right]\right)^{-1}\left(\left[D_c^{xyz}\right]^{-1} + \left[D_{cr1}^{xyz}\right]^{-1} + \left[D_{cr2}^{xyz}\right]^{-1}\right)\right)^{-1}. \tag{6.6}$$

Similarly, it is possible to include any number of subsequent cracks just by adding their flexibility matrices.
3D-PARC is characterized by a physical approach to the problem: the model is focused on the basic causes which are locally studied and implemented. Sometimes, in fact, the modeling of physical phenomena, such as tension stiffening, aggregate interlock and dowel action, is carried out by numerical devices which are tuned in order to fit the general structural behavior. For example, the aggregate interlock is often modeled by the Shear Retention Factor and the tension stiffening is often implemented by modifying the tensile concrete behavior. On the contrary, the 3D-PARC formulation remains as close as possible to the physical reality avoiding these “unphysical” numerical devices.
The proposed model is based on a modular framework: the implementation of each contribute can be easily substituted and updated when an improved version is developed. For example, in this version of the model, the strain decomposition is introduced for the first time and the tension stiffening formulation is improved.
The model is implemented in a FORTRAN subroutine which can be run within the Finite Element (FE) program ABAQUS [1]. The theoretical formulation as well as the numerical

implementation are applied to the investigation of a wide range of structures: plain concrete specimens subjected to biaxial and triaxial stress states, membrane elements subjected to shear, one RC tie, plain concrete and RC beams subjected to torsion.

The model demonstrates to be very flexible since it can analyze real cases presenting very different stress fields. In fact, the model is formulated as a general purpose tool and it can be used with a wide range of elements in the FE implementation. This allows to apply it to the study of every kind of structure.

The results obtained from the numerical simulations are good in all cases. Therefore, it can be concluded that the model is able to capture the general structural response. Moreover, it is possible to extract from the FE model many variables such as steel stresses, concrete strains and crack displacements and to validate them through the comparison with experimental data, allowing a complete evaluation of the local behaviors.

The following pages report a brief review of the most significant results.

The simulations of plain concrete tests highlight the model capabilities to investigate the biaxial and triaxial stress regions where 3D-PARC is able to effectively reproduce the failure domain [27, 30].

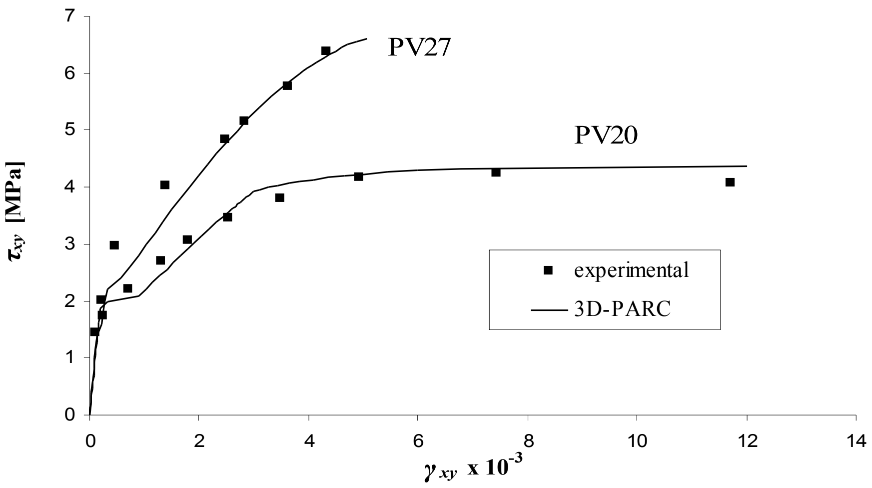

Figure 6.4 – Vecchio-Collins selected panels.

Many different shear panels, from different experimental programs, are investigated by 3D-PARC. The specimens present a wide range of size, concrete properties, steel yielding strength, reinforcement ratios and failure modes. In these biaxial tests, all the material contributes are activated by the testing procedures and therefore, it is possible to deeply verify the model theory as well as its numerical implementation. The model provides very good results in capturing the post-cracking behavior, the ultimate load, the deformability and the failure mode. Figure 6.4 shows the outcomes related to two panels selected from the Vecchio-Collins experimental program [45]. The PV27 presents a concrete failure, whereas, in the PV20, since the steel layers are asymmetrical, the failure is reached by non-simultaneous steel yielding.

Figure 6.5 compares two panels selected from the Pang-Hsu experimental program [37]. The A4 is symmetrically over-reinforced and the failure is caused by the crushing of the concrete between the cracks. On the contrary, the B4 is asymmetrically under-reinforced in both directions: the curve clearly shows the subsequent yielding of the two steel layers.

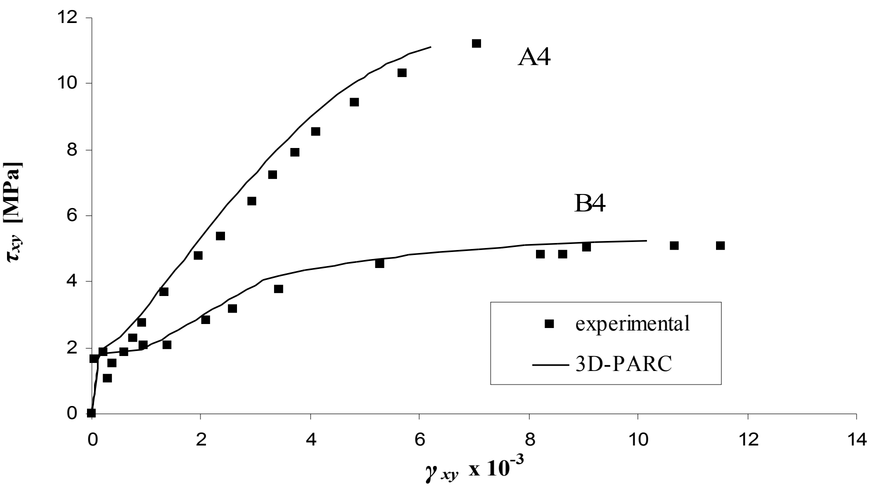

Figure 6.5 – Pang-Hsu selected panels.

Afterwards, some full-size structures subjected to complex 3D stress fields are investigated. The numerical analysis of a RC tie [10] gives the possibility to deeply test the model response in investigating the serviceability limit states. What is more, this simulation provides useful information about the tension stiffening formulation.

In the numerical simulation of two plain concrete beams subjected to pure torsion tested by Hsu [24], the model demonstrates to be able to capture the structural behavior in a case dominated by a complex, fully 3D stress state.

Finally, three RC beams subjected to pure torsion studied by Lampert and Thürlimann are investigated [29]. Since all the beam properties, except the longitudinal bar arrangement, were kept constant, these tests provide fundamental information about the effect of the steel reinforcement location. Figure 6.6 shows the results for the beams T1 and T3. Through this comparison, the effect of the longitudinal steel distribution can be highlighted.

The proposed model is able to capture the concrete strut reorientation during the loading process. The numerical outcomes are also compared to the analytical solution proposed by the Eurocode [13]. It has to be mentioned that 3D-PARC is able to capture the strengthening effect of the over-reinforced side of the beam T3 which cannot be capture by the Eurocode analytical formulation.

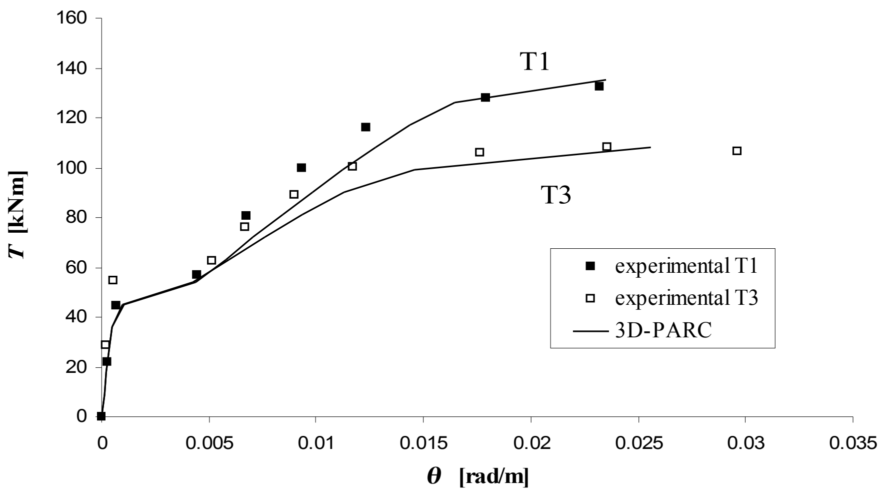

Figure 6.6 – Result comparison for the beams T1 and T3.

Furthermore, the FE implementation of 3D-PARC provides some local information about the longitudinal and transversal steel stresses, the crack opening and the concrete strain. The longitudinal steel stress for the beam T3 is reported in Figure 6.7.

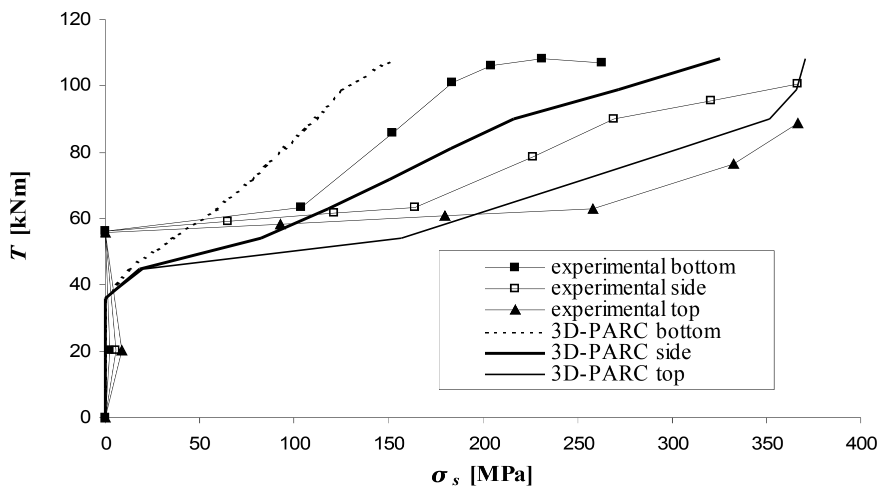

Figure 6.7 – Longitudinal steel stress for the beam T3.

This doctorate dissertation also contains the FE analysis of RC corbels developed during a six-month collaboration with the Institute of Structural Engineering (IKI) of the University of Natural Resources and Applied Life Sciences – BOKU in Vienna. The deterministic and probabilistic analyses were performed with the software package SARA which includes the RC-oriented FE code ATENA and the statistical module FREET. Since, in RC structures, materials and geometry are characterized by a high level of uncertainty, this contribution highlights the importance of a probabilistic approach. What is more, this practical experience, combining a high-level FE modeling with a sophisticated probabilistic formulation, represents an important development of the basic concepts of numerical analysis applied to RC structures.

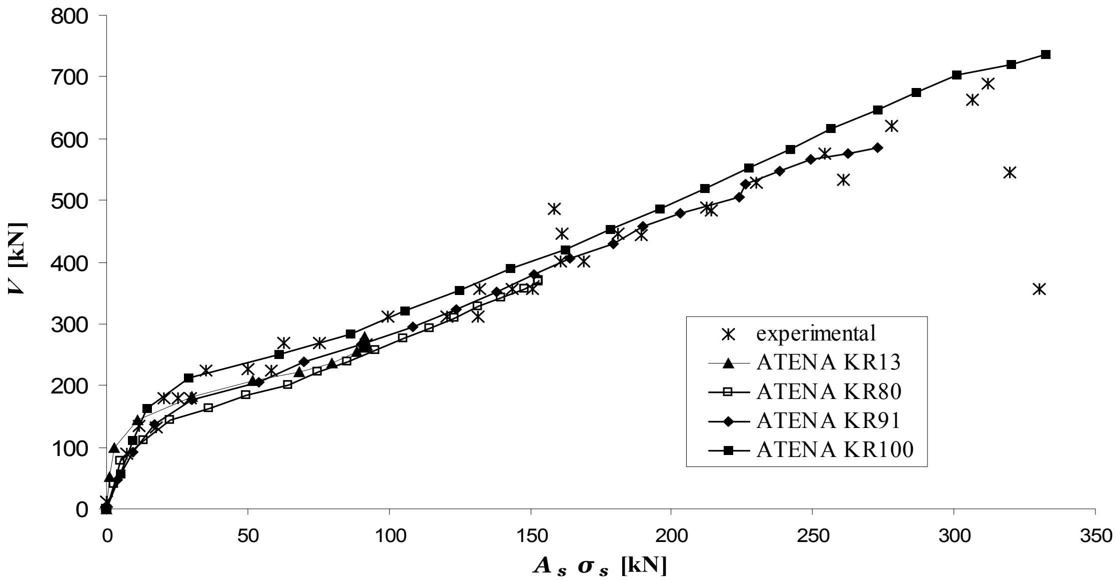

Figure 6.8 – Relation between applied load and steel force for corbels with a/d=0.30.

From the deterministic analyses, the ultimate load, the steel force and the crack pattern are extracted and compared with the experimental data. In Figure 6.8, the steel force in the main reinforcements of the corbels is reported as a function of the external load. Moreover, as it can be seen in Figure 6.9, the numerical crack pattern provides an important indication of the failure mode.

In the probabilistic procedure, some selected variables are randomized according to analytical distributions and repeated FE simulations are performed. The outcomes are statistically evaluated: first of all, the numerical results are fitted by an analytical distribution in terms of Probability Density Function (PDF). Subsequently, the sensitivity analysis as well as the safety level assessment are performed. The first one allows the evaluation of the most important variables affecting the structural behavior. The second one provides the safety index evaluation as a function of the mean value and of the coefficient of variation *COV* of the external load (Figure 6.10).

Finally, the safety level suggested by the Eurocode [13] is compared with the one obtained from the probabilistic calculations.

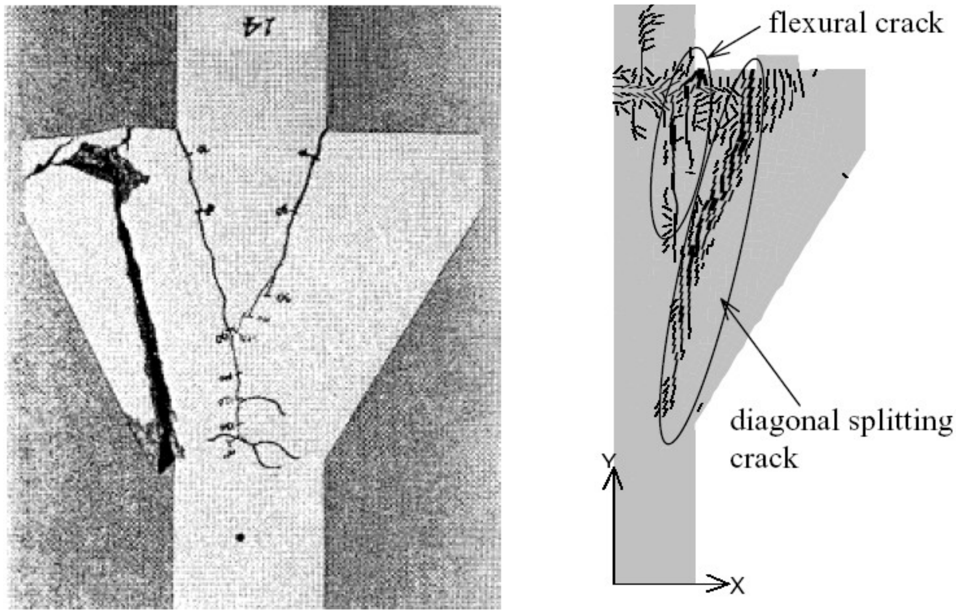

Figure 6.9 – Experimental and numerical crack pattern for corbel KR14.

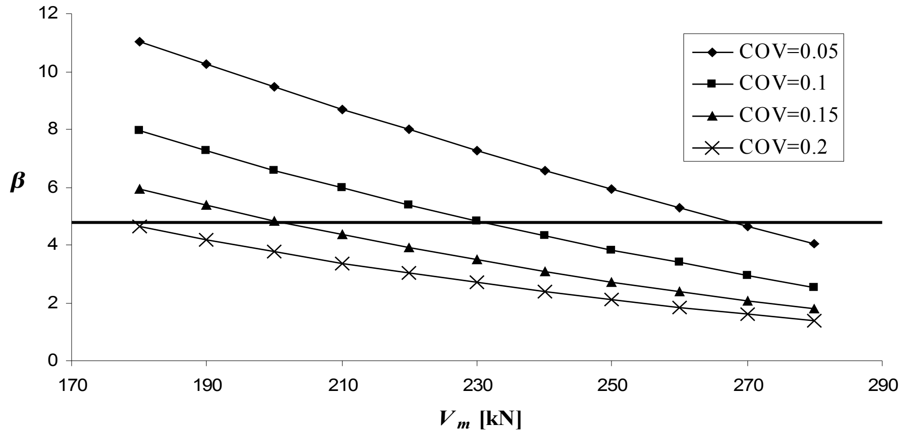

Figure 6.10 – Safety index assessment for corbel KR14.

By evaluating the two different but related activities carried out during the doctorate course, it can be concluded that an effective approach for the study of RC structures should be based on two main concepts.

First of all, reliable theoretical models and robust numerical implementations are required. The RC response is very complicated and, in order to capture the real structural behavior, all

the physical phenomena should be taken into account. Furthermore, the non-linear calculations are usually time-consuming and efficient numerical techniques are fundamental.
Secondly, if the problem depends on input parameters which are known with a low confidence level, the solution loses its significance even if sophisticated models are implemented. Above all, this is important for the existing structures, where the deterioration processes make it very difficult to estimate the basic parameters. Therefore, a probabilistic formulation should be adopted. The statistical approach, in fact, provides the sensitivity study as well as the safety level assessment which can be very useful in applications like the analysis of existing structures and the optimized design procedures for mass production.
The combination of these two approaches provides high-level effective tools satisfying the requirements of reliability and accuracy nowadays demanded in the numerical analysis of RC structures.

REFERENCES

[1] ABAQUS, *ABAQUS Version 6.5 Documentation*, ABAQUS Inc., 2004.

[2] ACI Committee 544, *Design considerations for steel fiber reinforced concrete (ACI 544.4R-88)*, Manual of Concrete Practice, Part 5, American Concrete Institute, Detroit, MI, 563-590, 1998.

[3] ADINA, *ADINA System 8.1 Documentation*, ADINA R&D Inc., 2003.

[4] ANSYS, *ANSYS Release 9.0 Documentation*, SAS IP, Inc., 2004.

[5] Balan T. A., Spacone E., Kwon M., *A 3D hypoplastic model for cyclic analysis of concrete structures*, Computers & Structures, 23, 2001, pp 333-342.

[6] Bathe K. J., Walczac J., Welch A., Mistry N., *Nonlinear analysis of concrete structures*, Computers & Structures, Vol. 32, No. 3/4, 1989, pp 563-590.

[7] Belarbi A., Hsu T. T. C., *Constitutive Laws of Softened Concrete in Biaxial Tension-Compression*, ACI Structural Journal, Vol. 92, No. 5, Sep-Oct 1995, pp 562-573.

[8] Belletti B., *Un modello numerico per elementi piani in conglomerato armato*, Doctorate dissertation in Structural Mechanics, XIII Cycle, Politecnico di Torino, December 2000.

[9] Belletti B., Cerioni R., Iori I., *A Physical Approach for Reinforced-Concrete (PARC) Membrane elements*, Journal of Structural Engineering, ASCE, December 2001, pp 1412-1426.

[10] Belletti B., Fantilli A. P., Ferretti D., Iori I., *Analisi numerico-sperimentale di un elemento in conglomerato armato semplicemente teso*, atti del 12° Congresso C.T.E. Collegio dei tecnici della industrializzazione edilizia, Padova, 5-6-7 November 1998.

[11] Bergmeister K., Strauss A., Eichinger E. M., Kolleger J., Novak D., Pukl R., Cervenka V., *Structural analysis and safety assessment of existing concrete structures*, The First fib Congress, Osaka, Japan, 2002.

[12] CEB, Comite Euro-International du Beton, *CEB – FIP Model Code 90*, Bulletin d'Information No. 213/214, 1993.

[13] CEN, European Committee for Standardization, *EN1992 Eurocode 2: Design of concrete structures*, Bruxelles, 1998.

[14] Cerioni R., Iori I., *Sul comportamento di elementi bidimensionali a lastra, in conglomerato armato e soggetti ad azioni taglianti ai bordi*, Studies and Researches, Graduate School in Concrete Structures F.lli Pesenti, Politecnico di Milano, Italia, Vol. 16, 1995, pp. 151-171.

[15] Cervenka Consulting, *SARA – Structural Analysis and Reliability Assessment, User's manual*, 2003.

[16] Cervenka Consulting, *FREET – program documentation*, 2004.

[17] Cervenka Consulting, *ATENA program documentation – Theory*, 2005.

[18] Cervenka V., *Computer simulation of failure of concrete structures for practice*, Proceedings of the First fib Congress, Osaka, Japan, Session 13, 2002, pp 289-304.

[19] Cook R. D., Malkus D. S., Plesha M. E., *Concepts and applications of finite element analysis*, John Wiley & Sons, third edition, 1989.

[20] Darwin D., Pecknold D. A., *Non-linear biaxial stress-strain law for concrete*, Journal of the Engineering Mechanics Division, Vol. 103, No. EM2, April 1977, pp 229-241.

[21] Elwi A. A., Murray D. W., *A 3D hypoelastic concrete constitutive relationship*, Journal of the Engineering Mechanics Division, Vol. 105, No. EM4, August 1979, pp 623-641.

[22] Fattuhi N.I., *Strength of SFRC corbels subjected to vertical load*, ASCE, Journal of Structural Engineering, Vol. 116, No. 3, March 1990.

[23] Gambarova P. G., *Sulla trasmissione del taglio in elementi bidimensionali piani di c.a. fessurati*, Atti delle Giornate AICAP, Bari, 1983, pp. 141-156.

[24] Hsu T. T. C., *Torsion of structural concrete – plain concrete rectangular sections*, Torsion of Structural Concrete, SP-18, ACI, Detroit, 1968, pp 203-238.

[25] Iori I., Dei Poli S., *Sulla torsione di elementi strutturali in cemento armato*, L'Industria Italiana del Cemento, Vol. 2, 1985.

[26] Kriz L. B., Raths C. H., *Connections in precast concrete structures – strength of corbels*, PCI Journal, Vol. 10, No. 1, February 1965.

[27] Kupfer H., Hilsdorf H. K., Rusch H., *Behavior of concrete under biaxial stresses*, ACI journal, American Concrete Institute, Proceedings, Vol. 66, No. 8, Aug 1969, pp 656-666.

[28] Kwon M., Spacone E., *Three-dimensional finite element analyses of reinforced concrete columns*, Computers & Structures, 80, 2002, pp 199-212.

[29] Lampert P., Thürlimann B., *Torsionsversuche an Stahlbetonbalken*, Institut für Baustatik ETH, Bericht Nr. 6506-2, Zürich, 1968.

[30] Launay P., Gachon H., *Strain and ultimate strength of concrete under triaxial stress*, ACI SP 34, Am. Concrete Inst., Paper 13, American Concrete Institute (ACI), Detroit, Mich, 1972, pp 269-282.

[31] Li V. C., Stang H., Krenchel H., *Micromechanics of crack bridging in fibre-reinforced concrete*, Materials and Structures, 26, 1993, pp 486-494.

[32] Maekawa K., Pimanmas A., Okamura H., *Nonlinear Mechanics of Reinforced Concrete*, SPON Press, London, 2003.

[33] Menetrey P., Willam K. J., *Triaxial Failure Criterion for Concrete and Its Generalization*, ACI Structural Journal, Vol. 92, No. 3, May-June 1995, pp 311-317.

[34] Mordini A., *Un modello non lineare per l'analisi tridimensionale di elementi in calcestruzzo armato*, Graduate Thesis at the University of Parma, 2002.

[35] Mordini A., Strauss A., *Deterministic and Probabilistic Finite Element Analysis of Reinforced Concrete Corbels*, Internal report of Institute of Structural Engineering, University of Natural Resources and Applied Life Sciences, Vienna, March 2005.

[36] Mordini A., Strauss A., Bergmeister K., *Deterministic and Probabilistic Finite Element Analysis of Reinforced Concrete Corbels*, submitted for publication to Computer & Concrete, 2005.

[37] Pang X. D., Hsu T. T. C., *Behavior of Reinforced Concrete Membrane Elements in Shear*, ACI Structural Journal, Vol. 92, No. 6, Nov-Dec 1995, pp 665-679.

[38] Popovics S., *Numerical approach to the complete stress-strain relation for concrete*, Cement Concrete Res., 3 (5), 1973.

[39] Pukl R., Cervenka V., Strauss A., Bergmeister K., Novak D., *An advanced engineering software for probabilistic-based assessment of concrete structures using nonlinear fracture mechanics*, Applications of Statistics and Probability in Civil Engineering, Der Kiureghian, Madanat & Pestana (eds), Millpress, Rotterdam, 2003.

[40] Pukl R., Novak D., Bergmeister K., *Reliability assessment of concrete structures*, Computational modeling of concrete structures: Euro-C 2003, March 17-20, 2003, St. Johann im Pongau, Austria, 2003, pp 817 – 825.

[41] Rots J. G., Blaauwendraad J., *Crack models for concrete: discrete or smeared? Fixed, multi-directional or rotating?*, Heron, Vol. 34 No. 1, 1989.

[42] Saenz L. P., Discussion of *Equation for the stress-strain curve of concrete*, by Desayi and Krishnan, ACI journal, American Concrete Institute, Proceedings, Vol. 61, No. 3, Mar 1964, pp 1229-1235.

[43] Strauss A., Bergmeister K., Santa U., Pukl R., Cervenka V., Novák D., *Non destructive reliability analysis of concrete structures numerical concepts and material models for existing concrete structures*, Deutsche Gesellschaft für Zerstörungsfreie Prüfung: International Symposium (NDT-CE 2003) Non-Destructive Testing in Civil

Engineering 2003, Berlin, September 16-19, 2003.

[44] Timoshenko S., *Strength of Material, Part I, Elementary Theory and Problems*, 3rd Edition, D. Van Nostrand Co., Inc., New York, NY, 1955, pg. 221, article 48.

[45] Vecchio F. J., Collins M. P., *The modified compression-field theory for reinforced concrete elements subjected to shear*, American Concrete Institute Struct. Journal, ACI, Proc. Vol. 83, No. 2, 1986, pp 219-231.

[46] Walraven J. C., Reinhardt H. W., *Theory and experiments on the mechanical behaviour of cracks in plain and reinforced concrete subjected to shear loading*, Heron, Concrete Mechanics, part A Vol. 26, 1981.

[47] Willam K. J., Warnke E. P., *Constitutive model for the triaxial behaviour of concrete*, International Association for Bridge and Structural Engineering Proceeding, seminar on “Concrete structures subjected to triaxial stresses”, May 1974, ISMES, Bergamo, Italy.

ACKNOWLEDGMENTS

I would like to start thanking the people who supported me the most in the development of this dissertation: my parents. They encouraged me every step of the way and gave me the freedom to make my own choices.

Many people at the Department of Civil Engineering of the University of Parma have been very helpful during my doctorate course. I want to thank my supervisors Prof. Roberto Cerioni and Prof. Ivo Iori. I enjoyed working with you and learning from you. I would like to thank you for the opportunity you gave me to develop my work in the best possible conditions. I have also appreciated a lot your support during the time I spent in Vienna.

Furthermore, I would like to thank Prof. Iori for his two precious books: the study of the history of scientific and technical thought is something we share and that has increased my passion for my work.

Finally, I would like to mention Prof. Daniele Ferretti for his friendship, his help and our stimulating discussions in his office.

Writing the dissertation would have been harder without Marta: thank you for your help in reviewing my English and for your kisses!

During my doctorate, I spent an eleven-month period in Vienna. In the first six months, I was enrolled in two different projects at the Institute of Structural Engineering (IKI) of BOKU University: the European Community INDEPTH project and the SARA project which is included in this thesis.

I am especially grateful to Prof. Konrad Bergmeister who gave me the chance to work in his Institute. During that time, I particularly enjoyed my close collaboration with Dr. Alfred Strauss in both projects. I also want to mention Ing. Vladimir Cervenka and Ing. Radomir

Pukl of Cervenka Consulting and Prof. Drahomir Novák of Brno University of Technology, who kindly agreed to let me use SARA, ATENA and FREET.
Thanks to all the people who made my time at IKI enjoyable from every point of view: I really felt like one of you!
In Vienna I worked also at VCE – Vienna Consulting Engineers. I am particularly grateful to my project leader Dr. Helmut Wenzel. Thank you to Konstantin Savov for our productive collaboration and your deep friendship. I would also like to mention Prof. Hiroshi Tanaka of the University of Ottawa for our interesting conversations and for that excellent book.
Finally, my greetings go to all the people of VCE research & development staff: it was really nice and stimulating to spend five months with you!

Modena, March 3, 2006